Grain Boundary Character Distributions In Isostructural Materials

Submitted in partial fulfillment of the

requirements for the degree of

Doctor of Philosophy

in

Materials Science and Engineering

Sutatch Ratanaphan

B.S., Physics,
Mahidol University

M.S., Materials Science and Engineering,
University of California, Los Angeles

Carnegie Institute of Technology
Carnegie Mellon University
Pittsburgh, PA

Acknowledgements

Gregory S. Rohrer, my advisor is a great Professor, it is honor to be one of his students. I would like to thank him for his advice, encouragement, and support. It has been my pleasure to work under his supervision at Carnegie Mellon. It is his invaluable guidance that helps me to be who I am today as a scientist. I am also grateful to my committee members, Prof. Anthony D. Rollett, Prof. Elizabeth A. Holm, and Dr. Vasily V. Bulatov for numerous discussions, interesting questions, and continuous help. Interestingly, they have different areas of expertise, but they have the same (isostructural) character of the great scientist, which I am hoping to achieve as well. I thank Prof. David Kinderlehrer for the afternoon discussion on "An Entropy Based Theory of the Grain Boundary Character Distribution". I am indebt to Prof. David E. Laughlin and Prof. Jian-Gang (Jimmy) Zhu for a critical thinking and advice during my second year in graduate school. Many sincere thanks to the staff of the Department of Materials Science and Engineering for the great help. Thanks to Suzy Smith, Marygrace Antkowski, William Pingitore, F.H. Rogan, Adam Wise, Angela Pusateri, and Anita Connelly for help and support. I would also like to thank Neetha Khan and Jeanna Pekarcik for delicious cupcake and cookies. I am indebt to Jason Wolf, who encouraged me when I was struggled with my graduate study, I will never forget it. I greatly appreciated the generous help on the microstructure characterization from Tom Nuhfer. I would like to thank all of people in the Department of Materials Science and Engineering. Specially, I would like to acknowledge the members of Rohrer's group, Herb Miller, Andy Schultz, Li Li, Debashis Kar, Harry Chien, Lisa Chan, Yiling Zhang, Jia Li, William Frazier, Yisi Zhu, Noey Ratiporn, Stephanie Bojarski, and Brian Lin. Thanks to Ben Anglin, Clay Stein, Ellen Reifler, Ranga Kamaladasa, Jingxi Wu, Xuan Liu, Clare Mahoney, Lily Nguyen, Sudarshan Narayanan, Rachel Ferebee, Ray Miaolei Yan, Anya Prasitthipayoung, Aswin Tejasukmana, Soyoung Park, Lu Yan, Reeju Pokharel, and Tetsuya Kaneko for making my graduate study an enjoyable one.

I wish to express my gratitude to Anusorn Seubsai, Tang Kritsanu, Yoo Supachai, Adolfo Anta, Viriya Darmindra, Daow, Kanok, Proud Pitirat, Amm Saiyavath, Jib Chalalai, Tubtim, and all of my friends. Special thanks to Cho, Sira, Namtoey, Kong, IInk, Kii, and Eve (Kun poo and gang lok moos), for great help, encouragement, and for all happy time we shared during my stay in Pittsburgh. Special thanks to my landlord Ken Tew for critical review of papers, a day trip to Akron only for Church's Chicken, and Thanksgiving Turkey. I acknowledge financial support form the Royal Thai Government Scholarship. This work would not be possible without financial and technician supports from MRSEC program of the National Science Foundation under Award Number DMR-0520425.

I also thank James and Tina Palanchai for the late night talk, which has inspired me to pursue my dream as a scientist. Last but not the least, I want to express my deep gratitude to my family, without their love, endless support, and understanding through out my life, I could not reach this far.

Sutatch Ratanaphan

Pittsburgh, PA

September 2013

Abstract

Anisotropic grain boundary character distributions (GBCDs), which influence macroscopic materials properties, are thought to be controlled by the grain boundary energy anisotropy. Structurally, grain boundary could be viewed as two free surfaces joined together. Grain boundary energy could be simply defined by the total excess energy for creating two free surfaces minus the energy gained when new bonds are formed between these surfaces. This implies that different crystal structure should have different GBEDs and GBCDs. It was recently discovered that grain boundary energy distributions (GBED) in isostructural materials, a class of materials that share the same crystal structure, are directly related to one another. This suggests that GBCDs in isostructural materials might also be related in a similar way. To test this hypothesis, electron backscatter diffraction (EBSD) was used to map grain orientations in Ag, Au, Cu, Fe, and Mo. The GBCDs were determined from the stereological interpretation of EBSD maps containing on the order of 100,000 grains. It was found that the GBCDs of face-centered cubic (FCC) metals are statistically correlated, while the GBCDs of body-centered cubic (BCC) Fe and Mo are not correlated to the GBCD of FCC metals. The degree of the correlations among the FCC metals is weaker if there are significant differences in grain shape or texture. For example, Ag has the weakest correlation to the other FCC materials and also has quantitatively different grain shapes and texture. The relationship between the populations and energies of grain boundaries was also studied. By comparing the GBCDs of Al, Au, Cu, and Ni to the energies of 388 grain boundaries previously calculated by the Embedded Atom Method (EAM), we observed a moderately inverse correlation between the relative areas of grain boundaries and their energies. Interestingly, there are strong inverse correlations between the energies and populations of the most common grain boundaries (Σ3, Σ9, and Σ27). Because the enhancement of twin related boundaries due to the prevalence Σ3 boundaries results in a decrease in the grain boundary populations for the other boundary types, this inverse correlation is influenced by the

crystallographic constraints at triple junctions. In other words, having an anisotropic misorientation distribution with strong maxima for certain boundaries biases the inverse correlation between grain boundary population and energy for other boundaries and causes different slopes at each misorientation. Interestingly, the inverse correlation at each misorientation is consistent with the Boltzmann distribution. Based on our results, it is possible to predict the GBCDs and GBEDs in isostructural polycrystalline materials by using a single GBCD and GBED. This principle is demonstrated by predicting the GBCD and GBED of Actinium (Ac).

To investigate the GBED in the isostructural BCC metals, the energies of 408 grain boundaries in Fe and Mo were computed using atomistic simulations based on the embedded-atom method (EAM) potential. We found that the calculated boundary energies in Fe and Mo were strongly correlated and scaled with the ratio of the cohesive energy divided by the square of the lattice constant (E_{coh}/a_0^2). We would expect that the GBCD of Fe and Mo might be correlated in a similar manner to that of FCC metals. To test this hypothesis, we compared the GBCDs of Fe and Mo. We found that the GBCDs of Fe and Mo are moderately and strongly correlated when all boundary types and only Σ3 boundaries were considered, respectively.

In this thesis, the results demonstrated that the GBCDs of isostructural materials are correlated with one another and the magnitudes of correlation coefficients varied. Reduced correlations were observed when there were differences in the microstructure and crystallographic texture. The inverse relationship between grain boundary population and energy is more strongly correlated at each misorientation than over the entire five macroscopic parameters of grain boundary, especially when there is significant misorientation texture. This relationship leads to GBCDs of isostructural materials that are also more strongly correlated at each misorientation than over the entire grain boundary space.

Table of contents

List of Tables

List of Figures

Chapter 1

1. Introduction

1.1 Motivation

Engineered solid materials, which are used in a wide range of applications, are usually polycrystalline. Polycrystalline materials are composed of single crystal aggregates joined by a network of internal interfaces, also known as the grain boundary network. The characteristics of the grain boundary network, such as the grain size, grain shape, crystallographic orientation distribution, and grain boundary misorientation distribution, influence many macroscopic properties. Because of this, efforts have been made to improve and enhance materials' properties by engineering the microstructure. It is widely recognized that grain boundary energies influence the distributions of grain boundaries [1][2]. However, the grain boundary energy distribution (GBED) is not known for most materials and, because it depends on five independent parameters, remains difficult to measure. The grain boundary character distribution (GBCD), on the other hand, is much easier to measure, but it is still not practical to measure the GBCD of every material. Therefore, a simple principle to relate GBEDs and GBCDs in different materials is needed to provide a building block for materials design. For this reason, it is necessary to investigate the correlations between the GBEDs and GBCDs of isostructural polycrystalline materials. Assuming such correlations exist, it should be possible to construct provisional GBCDs and GBEDs for isostructural materials.

1.2 Hypothesis

It has been observed that grain boundary populations are inversely correlated to grain boundary energies [1][2][3][4][5][6][7][8]. Furthermore, a previous study has shown that the distribution of grain boundary planes, averaged over all misorientations in annealed $SrTiO_3$ remained constant during grain growth [9]. The resultant GBCD could reasonably be viewed as a fingerprint of the polycrystalline material. Holm et al. showed that the calculated grain boundary energies of four face-centered cubic (FCC) metals (Al, Au, Cu, and Ni) are strongly correlated [10]. More recent studies have shown that the GBCDs of Al and Ni have strong inverse correlations to the calculated grain boundary energies [3][4]. These findings suggest the possibility that the relative populations of grain boundaries could be directly deduced from the calculated grain boundary energies and that grain boundary energies can be derived from observed populations.

The central hypothesis of this dissertation is that the relative grain boundary populations of isostructural materials with similar microstructures are correlated. If this is the case, it should then be possible to predict the GBCDs and GBEDs of isostructural polycrystalline materials using only a single GBCD or GBED. One can imagine arguments for or against this hypothesis. For example, because the grain boundary energy is related to the microscopic structure of the interface, and the only parameter that is changing is the atomic size, then within the limits of a hard sphere model, isostructural materials should have the same boundary structure and relative grain boundary energies that scale with the strength of the interatomic bonds. On the other hand, atoms of different sizes undoubtedly have different electronic structures and this might lead to completely different grain boundary structures and energies. In cases where there is extensive twinning, it is possible that crystallographic constraints could change the correlation between the grain boundary energies and the grain boundary populations. For example, if there is a large population of Σ3 boundaries, then a high population of Σ9 boundaries may be

created simply by the intersection of these boundaries. As a result, the relative areas of grain boundaries in isostructural materials might not be as strongly correlated as the calculated boundary energies of FCC metals that were recently reported in reference [10]. Finally, it should be noted that the hypothesis is expected to be true only under the condition that the crystallographic texture is approximately random and there is little anisotropy in the grain shape. As an example of how these factors influence the GBCD, **Figure 1.1** shows a schematic illustration of a polycrystalline material with columnar grains and a strong [111] texture along the sample's normal direction. Because of the texture and grain shape, most of the grain boundaries in this polycrystal will be [111] tilt grain boundaries, regardless of the GBED. Understanding the limits on the allowable texture and grain shapes is one of the goals of this work.

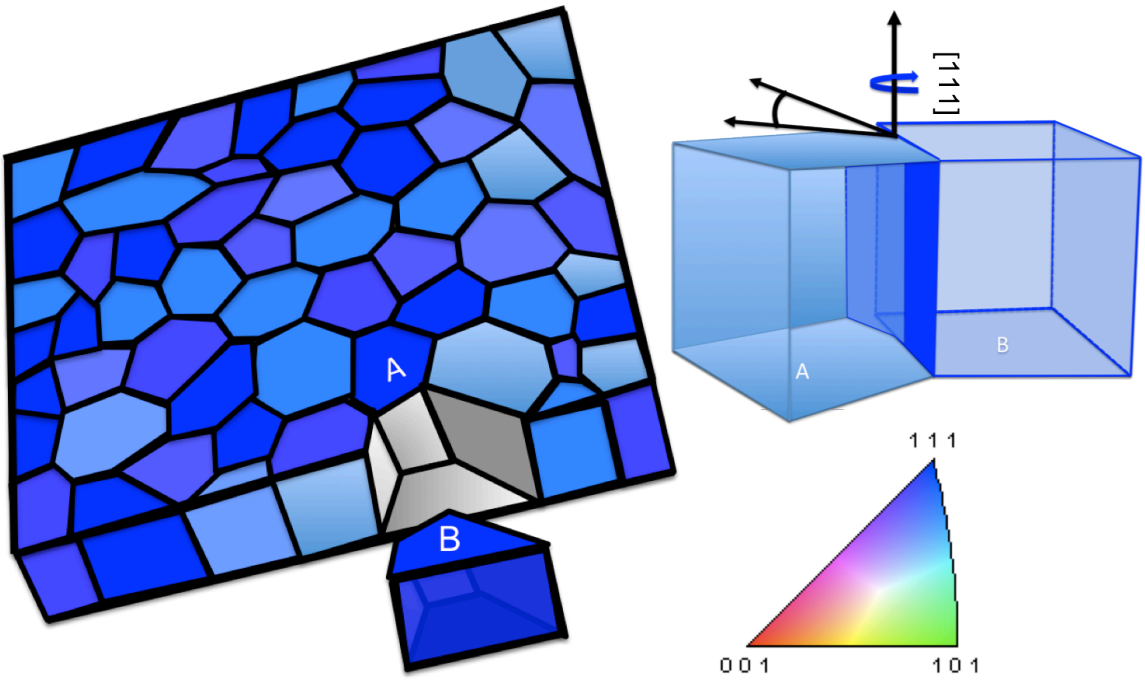

Figure 1.1. Diagram shows a polycrystalline material with columnar grains and a [111] fiber texture along the normal direction of the sample. Because of the texture and grain shape, the grain boundary between grain A and grain B can only be a tilt grain boundary with a [111] misorientation axis.

1.3 Method

To test this hypothesis, it is necessary to compare isostructural materials prepared to have microstructures that are as similar as possible. For example, it is known that segregating impurities and processing methods can influence the GBCD [11][12][13], so these factors must be controlled as much as possible. We select FCC metals as model materials, because of their wide use in industrial applications and our ability to obtain the specimens from commercial sources with high and known purities. Metals with a range of stacking fault energy are deliberately selected, as this characteristic influences the amount of anisotropy in the GBCD. To validate whether or not this hypothesis could be generalized to other isostructural materials, we examine two body-centered cubic (BCC) metals (Fe and Mo). All of the microstructures were prepared by a thermal annealing processes, using experimental conditions that are as nearly the same as possible. The details of the materials and sample preparation will be discussed in §3.2. It also follows from the hypothesis that the GBCDs of non-isostructural materials should not be correlated with those of isostructural materials. To test this idea, the GBCD of Ni is compared to the relative areas of the grain boundaries in the BCC metals.

A scanning electron microscope equipped with an electron backscatter diffraction (EBSD) detector is used to map the crystal orientations of the specimens. A stereological method is then used to determine the GBCD from planar EBSD maps [14][15]. The step size of the EBSD scans as well as the number of line segments will be optimized so that reliable measurements can be made in a reasonable amount of time. These issues will be addressed in detail in §3.3. To determine the inverse correlation between grain boundary populations and grain boundary energies, we compare the measured GBCDs to grain boundary energies that were calculated earlier (Al, Au, Cu, and Ni) [10] or as part of the present thesis (Fe and Mo).

Throughout this study, correlations will be examined over the full five-parameter grain boundary space. Pearson product-moment correlation coefficients and Spearman's rank correlation coefficients will be used as statistical metrics of the correlations and, thus, be used to draw conclusions. These metrics will be addressed in §3.4.

Chapter 2

2. Background

2.1 Introduction

In the field of materials science and engineering, the fundamental goal is to understand the connections between structure, properties, and processing. It is essential to have a good understanding of the relationship between structure and properties at a level that is sufficient to design suitable processing methods. For this reason, it raises an important question of how the structures of grain boundaries in polycrystalline materials are linked to their properties. However, until the last decade, it was not possible to characterize the populations of grain boundaries as a function of all crystallographic parameters. Using high speed EBSD and a stereological interpretation of the data, this is now routinely possible [15]. The survey of background knowledge is arranged in the following way. First, the experimental five parameter grain boundary character distribution (GBCD) will be described. Next, computational predictions and experimental measurements of the grain boundary energy distribution (GBED) are reviewed. Finally, we shall briefly discuss how to correlate the relative areas of grain boundaries, which are calculated using a stereological interpretation of planar EBSD maps, to the calculated boundary energy [10] using the Boltzmann distribution.

2.2 Grain Boundary Character Distribution (GBCD)

A grain boundary is a transition region between adjacent grains of two different crystal orientations. The transition region that accommodates the change of crystal orientation might be ordered or disordered [1]. The structure of a grain boundary is parameterized by three microscopic degrees of freedom $(\vec{t}_1,\vec{t}_2,\vec{t}_3)$ and five macroscopic degrees of freedom $(\varphi_1,\Phi,\varphi_2,\theta,\phi)$. The microscopic degrees of freedom $(\vec{t}_1,\vec{t}_2,\vec{t}_3)$ characterize relative translations between the adjacent crystals. If $\vec{t}_1,\vec{t}_2$, and $\vec{t}_3$ are always those that minimize the total energy at fixed temperature, pressure, and chemical potential, then the five macroscopic degrees of freedom are sufficient to describe the structure of grain boundary. Here, we assume this is true and define the GBCD, $\lambda(\Delta g,n)$, as the relative areas of grain boundaries where the misorientation (Δg) is specified by three Euler angles $(\varphi_1,\Phi,\varphi_2)$ and the plane normal (n_{ij}) is specified by two spherical angles (θ,ϕ). The discretization of the system is illustrated in **Figure 2.1**.

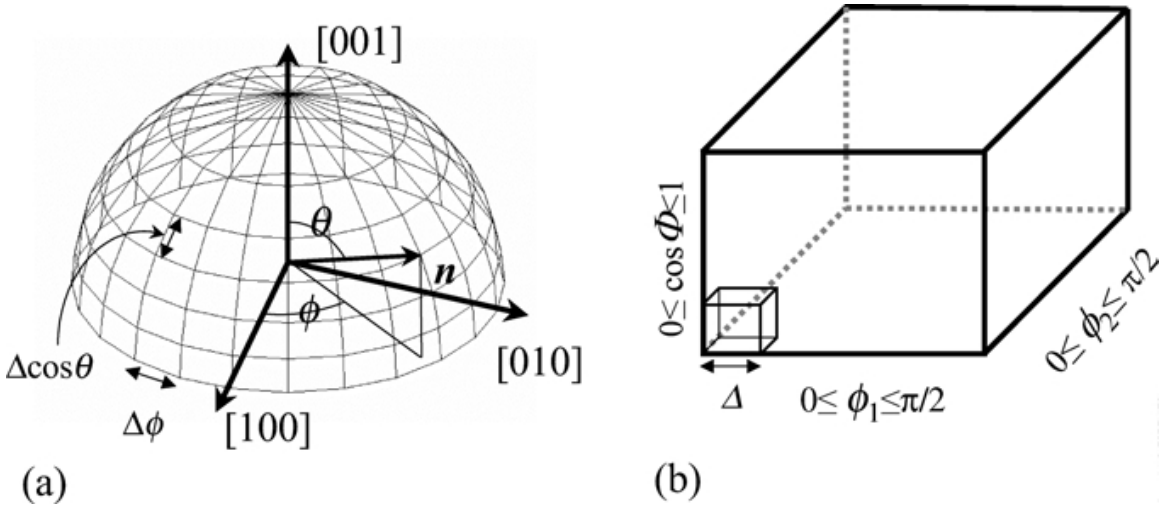

Figure 2.1. The schematic diagram shows the parameterization of five macroscopic degrees of freedom, $\lambda(\Delta g,n)$ to (a) two boundary plane orientation parameters and (b) three lattice misorientation parameters. This figure was reproduced from reference [14].

In cubic system, the domain of grain boundary parameters $(\varphi_1,\Phi,\varphi_2,\theta,\phi)$ ranges from 0 to 2π, π, 2π, π and 2π, respectively[14][16]. The number of distinguishable boundary types (N) for a cubic material in the domain is given by: $N = \frac{8\pi^5}{4 \times 24 \times 24 \times \Delta^5}$ [14], where the angular resolution is Δ. With an angular resolution of 10° ($0.5\pi/9$), there are 6,561 distinguishable grain boundary types, which is indeed significantly large. We could directly obtain the GBCD from three-dimensional techniques such as high energy diffraction microscopy [17][18][19], transmission electron microscopy [20], or electron backscatter diffraction combined with focused ion beam sectioning [5][6][7][21][22][23][24]. However, these methods are relatively difficult and have stringent limitations with respect to grain size and resolution. The stereological interpretation of planar EBSD data is much more flexible and efficient and allows us to accumulate more data.

An EBSD map provides four of the five parameters that specify the grain boundary structure; the only unknown parameter is the angle between the observation plane and the grain boundary plane. Using the stereological method, this distribution of grain boundary inclinations can be statistically determined [14][15][16]. Relative areas of grain boundaries are derived from relative lengths of grain boundaries. Because the GBCD is discretized into a finite number of types or "bins", the relative area of a boundary is influenced by the binning resolution [25]. A schematic diagram in **Figure 2.2** illustrates an ideal case. In this example, there are a total of 400 observations, assumed to have equal area, distributed among 10 bins in **Figure 2.2a**. In this case, we have an average number of 40 observations per bin. The 400 observations are placed into two bins so that the first one contains 320 observations and the second one contains 80 observations. Because the relative areas are calculated by dividing the total observed area in a single bin by the average area per bin, the first and the second bin will have observed populations of 8 and 2 MRD (multiple of random), respectively. If the peak width is smaller than the binning resolution, the observed populations will double when doubling the resolution.

In the case where the peak width is larger than the binning resolution, the observed population will not differ from the one with the original binning. In practice, the distribution of relative grain boundary areas may contain many maxima with different widths as illustrated in **Figure 2.2**. The fact that different peaks may be affected differently by the selected resolution will contribute some uncertainty to the experimental observations and this must be considered when comparisons are made to the grain boundary energy distributions.

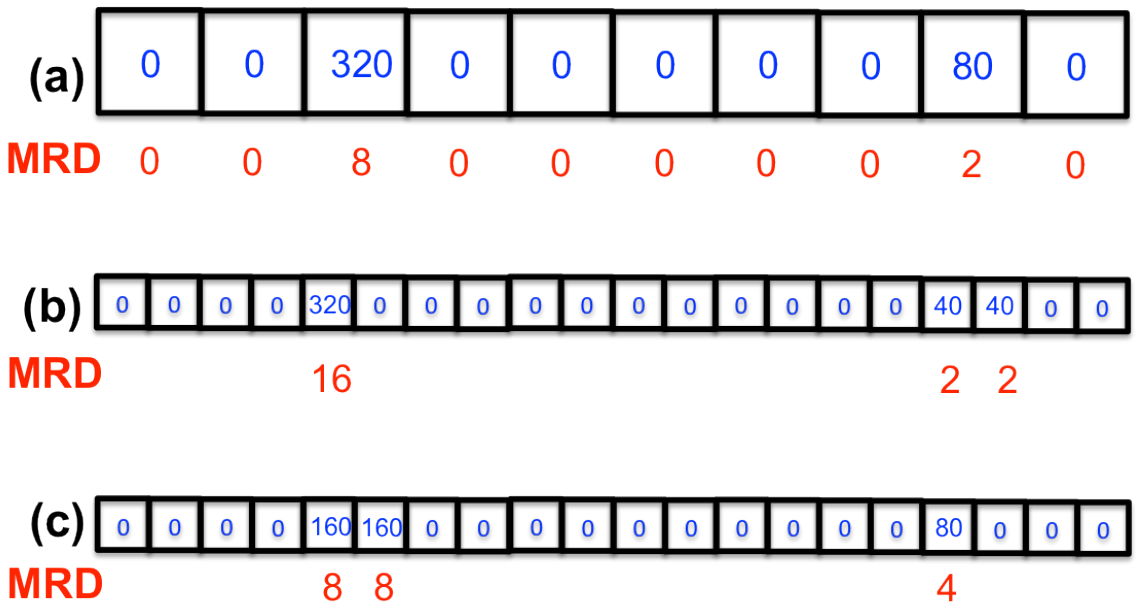

Figure 2.2. Diagram shows the effect of binning resolution on observed populations. 400 observations are placed into two bins, one with 320 observations and the other with 80 observations, leading to observed populations of 8 and 2 MRD, respectively. When doubling the resolution in (b) and (c), the observations will increase if the width of the observations is narrower than the binning resolution. On the other hand, if the observations are divided between two bins, the population will be independent of the binning resolution.

The stereological GBCD method has been validated and tested with simulated data as well as 3D-EBSD data [14][15][16]. The method has successfully characterized anisotropic distributions in a variety of polycrystalline materials [11][12][13][16][26][27][28][29][30][31][32][33][34][35][36][37][38][39][40][41].

The GBCDs of FCC materials (Al [28], Cu [16][26], Ni [6][26], Pb [39], brass [13][31][32][33], CuZr alloy [22], and stainless steel [40][41]) share a number of similarities, including maxima at the orientations of low index planes. The coherent twin boundary, which is a 60 ° misorientation about the [111] axis with (111) planes on either side of the boundary, is the most highly populated grain boundary. As an example, the grain boundary plane and energy distributions of Ni for boundaries with a misorientation of 60° about the [111] axis are shown in **Figure 2.3**.

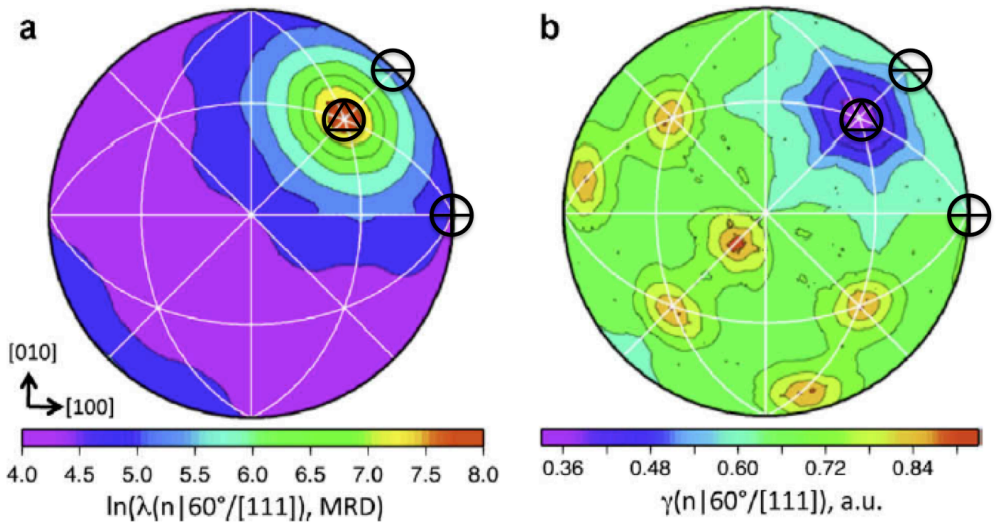

Figure 2.3. Grain boundary character distribution (GBCD) of Ni with a misorientation of 60° about [111] (a), is compared to the grain boundary energy distribution (b). The data are plotted in the equal-area projection along [001] and the (100), (110), and (111) poles, marked with a circled "+", "-", and triangle, respectively. This figure was reproduced from reference [6].

In materials with a high concentration of twins, such as Cu, Ni, brass, and stainless steel, the highly populated Σ3 boundary could enhance the concentration of Σ9 and Σ27 grain boundaries as a result of the crystallographic constraint at triple junctions [13][42]. Nevertheless, it was reported that the high populations of Σ9 boundary in Ni were consistent with their low energies [6]. The anisotropic distribution of grain boundaries is inversely correlated to the anisotropy of the grain boundary energy (see **Figure 2.3**). Recall that solid-state grain growth in dense polycrystalline materials favors low energy surface planes [21]. In other words, grain boundary habit planes develop analogously to the growth of an isolated crystal [5][27]. With sufficient annealing time, a steady-state distribution of grain boundaries is reached that is inversely correlated to the energy distribution [5][6][9][43][44]. Computer simulations have shown that the steady state GBCD is strongly affected by the energy anisotropy and influenced very weakly by the mobility anisotropy [45][46]. It is therefore reasonable to consider only the influence of grain boundary energy on the steady state GBCD. Based on these observations, the critical event model proposed by Rohrer [47] predicts a steady state GBCD from the rate of boundary creation and annihilation. While the rate of generation of a specific grain boundary type is determined by the orientation distribution, the rate of annihilation for each boundary type is proportional to the number of those boundaries and inversely proportional to the average area of that type of grain boundary. The areas of grain boundaries are described as a function of grain boundary energies, which are based on the experimental observation that a grain boundary with a larger energy is more likely to be decreasing in area and a grain boundary with a smaller energy is more likely to be increasing in area [43]. As shown in **Figure 2.4**, the model can predict the anisotropic steady state GBCD from an initially isotropic distribution, and capture the correlation between the logarithm of the populations and energies, which correspond to the experimental results in **Figure 2.11**. [6]. It should also be noted that the anisotropy of the grain boundary population is correlated to the energy anisotropy (ε).

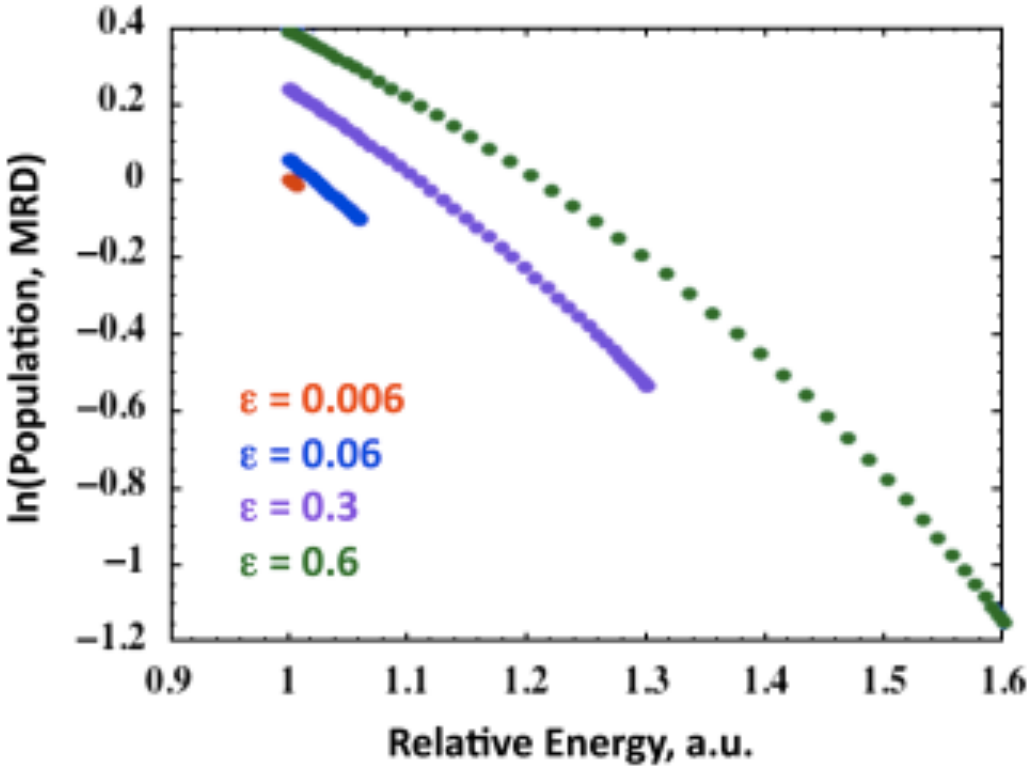

Figure 2.4. The steady state grain boundary populations for four different energy anisotropies (ε), predicted by the critical event model, are plotted as a function of grain boundary energy. This figure was reproduced from reference [2].

2.3 Grain Boundary Energy Distribution (GBED)

The grain boundary is a planar defect and its presence raises the total excess free energy. Thermodynamics predicts that the grain boundary is unstable and should spontaneously be eliminated from the system. However the elimination of grain boundaries is a dynamic process, which is in general slow at low temperature. At high temperature, the excess free energy provides the capillary driving force for grain growth [48]. However, the capillary driving force decreases as the grain size increases. In addition, the substantially low mobility of smooth grain boundaries could lead to grain-growth stagnation [49][50]. Therefore, grain boundaries are nearly always found in solid materials. Experimental values of grain boundary

energies are difficult to measure and only available for a few particular grain boundary types. Many models have been formulated to predict grain boundary energies, as reviewed in references [9] and [51]. The "Read-Shockley" or dislocation model is one of the earliest attempts to predict grain boundary energies [52]. The model assumed that dislocations could render the structure of a low angle grain boundary. The grain boundary energy is the sum of the dislocation energies and the interaction energy, which is the excess energy when those dislocations are brought together to form the low angle grain boundary. In this model, the grain boundary energy is proportional to $\theta - \theta \ln \theta$, where θ is the misorientation angle [52]. At a high misorientation angle, $\theta > 6°$, the boundary energy is not well-approximated by the dislocation model because of the complex interactions that occur when the dislocation cores are atomically close. For that reason, the dislocation model only provides a good approximation of the energies of low angle grain boundaries with misorientation angles less than about 6° [53].

Coincident site lattices (CSL) are labeled by the inverse of the fraction of coincident sites for two misoriented crystals. The angular range around the exact CSL misorientation within which the boundaries are assumed to be equivalent (Brandon's criterion) is derived from the concept of using dislocations to compensate for small misorientation differences [54][55]. Some low-Σ CSL boundaries are considered "special" because of their properties, although the use of this term is far from universal. Furthermore, it is not clear that the CSL number alone is sufficient to designate a boundary as special. For example, it has been found that Σ3 twin boundaries enhance resistance to crack initiation and intergranular corrosion in austenitic steels, however not all grain boundaries with the Σ3 misorientation improve these properties [56][57]. Only coherent Σ3 twin boundaries (those with {111} boundary planes) play a critical role in enhancing the properties of grain boundary engineered materials [57]. The creep rate of grain boundaries with the Σ7 misorientation (38.2° about [0001]) in alumina also depend on the grain boundary plane orientation [58].

In addition, the experimental measurement of grain boundary energy for Σ3 boundaries in Ni (see **Figure 2.3b**) showed that there are a wide range of boundary energies for the Σ3 misorientation [4][6]. The results demonstrate that lattice coincidence alone, which is specified by three degrees of freedom $(\varphi_1, \cos\Phi, \varphi_2)$, is not sufficient to characterize grain boundary energy [59]. Therefore, the grain boundary energy has to be specified in term of five crystallographic parameters. Wolf used atomistic methods to calculate grain boundary energies over a wide range of grain boundary types, including symmetrical twist/tilt-boundaries and asymmetrical twist-boundaries [60][61][62][63][64][65]. These studies show that asymmetrical twist-boundaries with a low-index plane on one side of the boundary have lower energies than symmetrical twist boundaries with high-index planes [63]. A grain boundary could be simply viewed as two free surfaces joined together. The total energy is the excess energy for creating two free surfaces, $\gamma_s^{tot} = \gamma^1(hkl) + \gamma^2(h'k'l')$, minus the energy gained (B) when new bonds are formed between these two free surfaces [9][65][66]. The grain boundary energy (γ_{gb}) is simply given by

$$\gamma_{gb} = \gamma_s^{tot} - B \qquad \text{Equation 2.1}$$

Wolf also purposed that grain boundary energies could be related to the number of broken bonds in a similar manner to free surface energies [66]. To illustrate the relationship between these quantities, **Figure 2.5** compares the free surface energies, the energies of symmetrical tilt grain boundaries (STGB) calculated by an empirical Lennard-Jones (LJ) pair potential, and the energies of random-grain boundaries (RGB) calculated by a broken bond model. The broken bond model is a better predictor for the energies of high angle grain boundaries than low angle boundaries where the strain field from dislocations contributes to the energy. Specifically, to the first order, the lattice is generally unperturbed except for the strain energy associated with the dislocations for low angle grain boundaries.

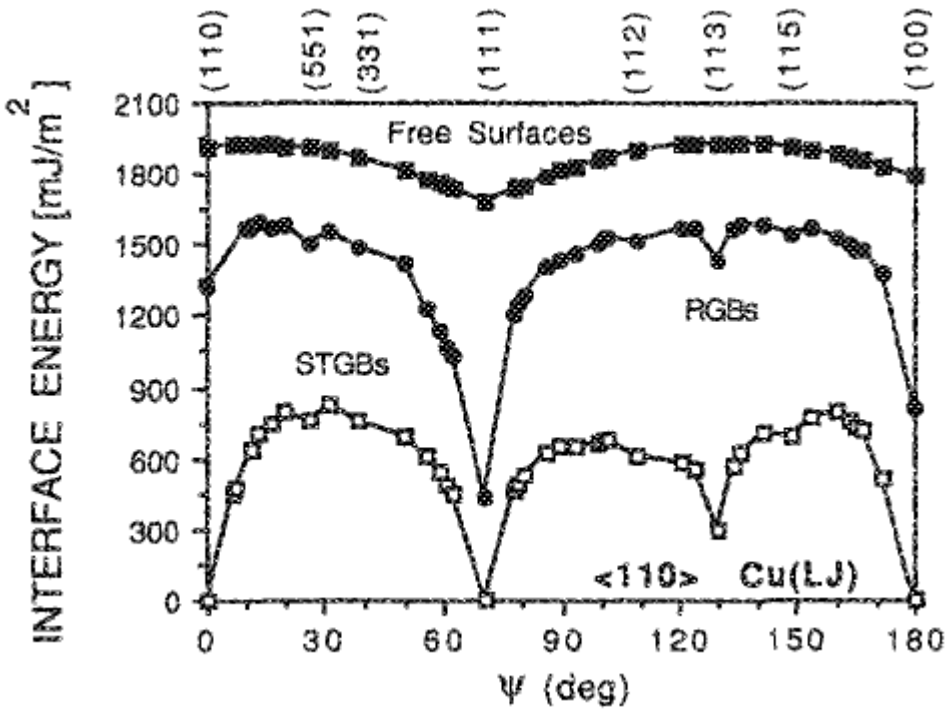

Figure 2.5. Interface energy (mJ/m^2) of planes perpendicular to <110> pole axis as a function of tilt rotation angle (Ψ). This figure was reproduced from reference [66].

The embedded-atom method (EAM), which is semi-empirical, was first developed by Daw and Baskes to study surfaces and defects in FCC metals[67][68]. The inter-atomic potential consists of a pair potential, $U_{ij}(R_{ij})$, and an embedding energy, $G(\rho_j^a)$.

$$E_{total} = \sum_i G_i(\sum_{j \neq i} \rho_j^a(R_{ij})) + \frac{1}{2} \sum_{i,j(j \neq i)} U_{ij}(R_{ij}) \qquad \text{Equation 2.2}$$

Where ρ^a is the averaged atomic electron density and R_{ij} is the distance between two atoms. The total energy, E_{total}, is determined from the interatomic distances and the local background electron density, $\sum \rho_j^a(R_{ij})$. Because this method assumes an angular independent potential, it is therefore valid for FCC metals with nearly empty or nearly full d-bands. Holm et al. recently used EAM inter-atomic

potentials to calculate grain boundary energies of FCC metals, Al, Au, Cu, and Ni [10]. A broad crystallographic domain of 388 distinct grain boundaries were constructed within a periodic cell of $15a_0/2$, where a_0 is the lattice parameter [10][69]. The 388 boundaries are the set of all grain boundaries with periodic length less than $15a_0/2$. There are 72 distinct misorientations for those 388 boundaries. For each grain boundary, several hundred to several thousand initial configurations with different microscopic degrees of freedom were constructed. The global minimum energy was obtained by minimization using the conjugate-gradient method in the LAMMPS code [70]. It is important to note that there were a large number of microscopic configurations that were minimized to nearly the same low energy for each grain boundary; the lowest energy configuration therefore provides a reasonable estimate of the grain boundary energy. As shown in **Figure 2.6**, the grain boundary normal has a significant influence on the grain boundary energy. The energies of <111> and <100> twist boundaries, plotted with disorientation angle, are both distinct from one another and also consistent with the Read-Shockley dislocation model [69][71]. However, for all other grain boundaries, the Read-Shockley dislocation model could not explain the variation of grain boundary energy with disorientation angle. Moreover, for Σ3 boundaries with a misorientation angle of 60° around [111], the spread in energies reflects the significant influence of the grain boundary plane orientation on the grain boundary energy.

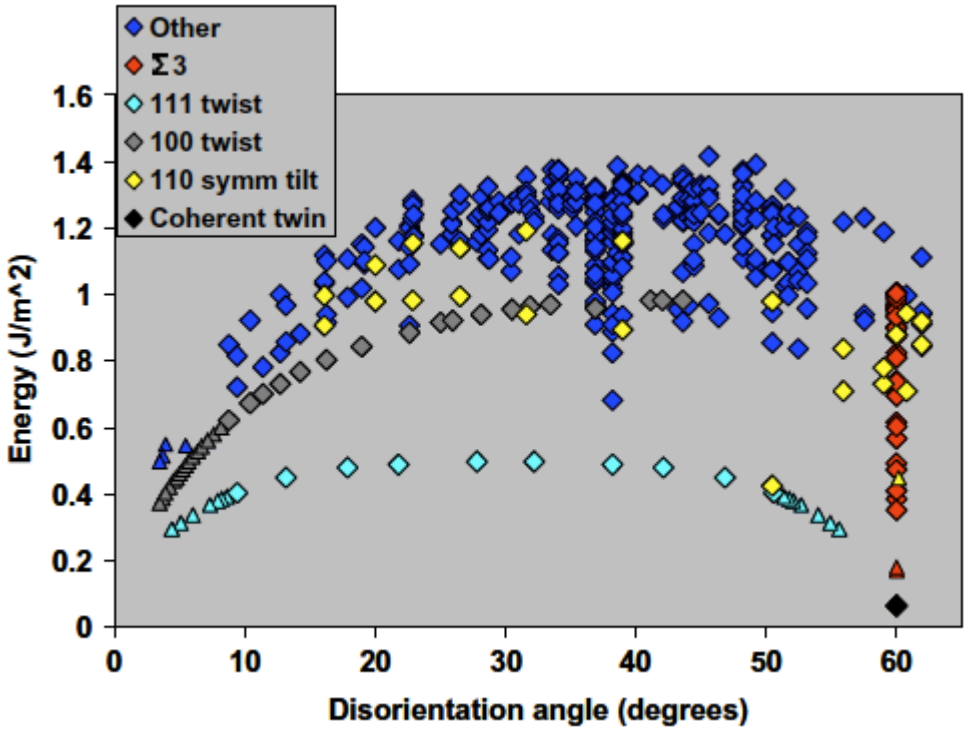

Figure 2.6. The diagram shows the calculated grain boundary energies of Ni versus disorientation angle. Triangles correspond to selected grain boundaries to fill the gap in the data set of the 388 boundaries. This figure was reproduced from reference [69].

It should also be noted that the calculated grain boundary energies with the same macroscopic structure in different FCC metals (Al, Au, Cu, and Ni) are proportional and linearly correlated [10], as shown in **Figure 2.7**. The linear correlation represents the similarity of microscopic configurations for the same macroscopic structure in different FCC metals. The relative grain boundary energies are linearly scaled with the ratios of a_0C_{44} or $a_0\mu$. Where a_0, C_{44}, and μ are lattice constant, shear modulus, and Voigt shear modulus respectively. This shows that there is a plausible scaling factor, related to the strength of interatomic bonding. for grain boundary energies in isostructural materials.

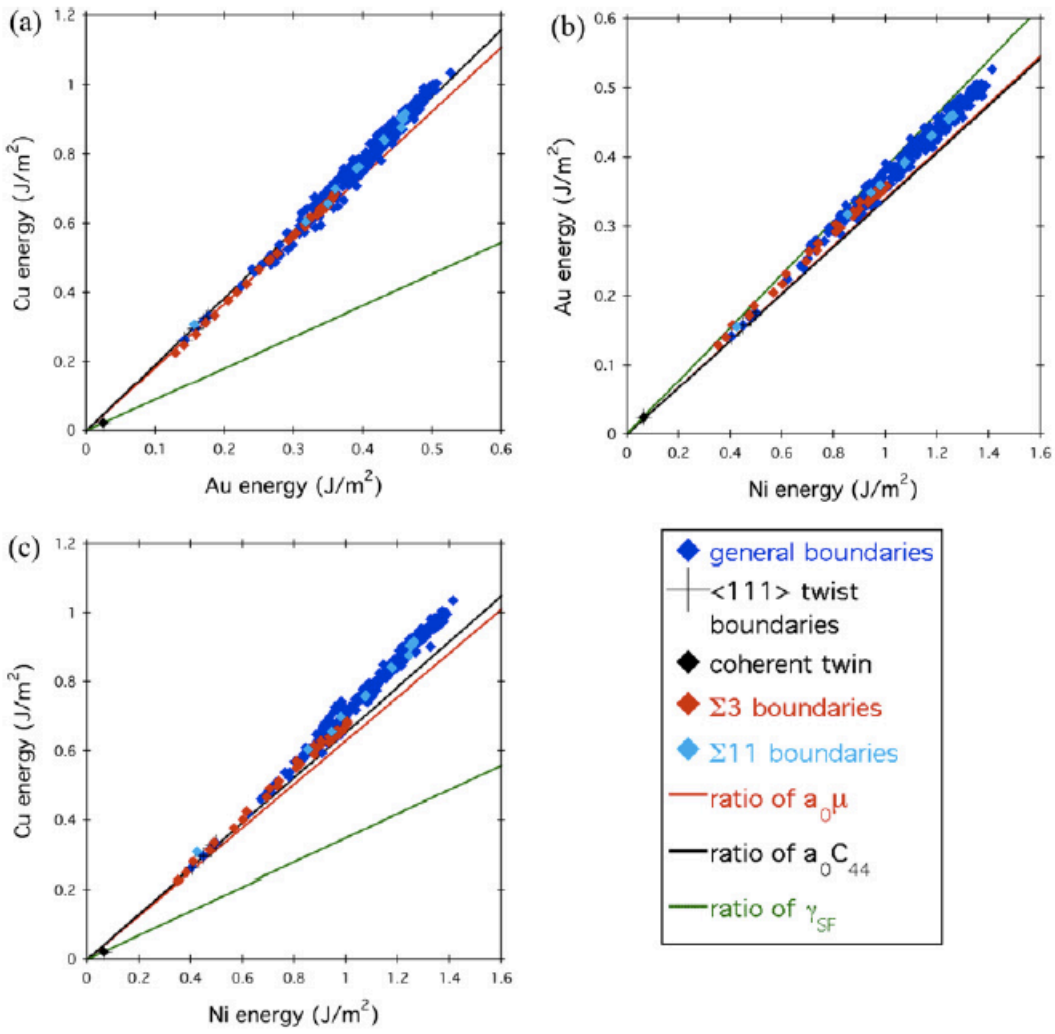

Figure 2.7. Schematic diagram represents pairs of calculated grain boundary energies that share the same macroscopic structure, (a) Cu vs Au, (b) Au vs Ni, and (c) Cu vs Ni. Lines show scaling factors predicted by the various materials parameters. This figure was reproduced from reference [10].

Grain boundary energies can be experimentally measured using the geometries of grain boundary triple junctions, which are assumed to be in a local thermodynamic equilibrium and described by the Herring relation [72].

$$\gamma_i \vec{t}_i + \frac{\partial \gamma_i}{\partial \beta} \vec{n}_i = 0 \qquad \text{Equation 2.3}$$

As shown in **Figure 2.8a**, γ_i is the energy of i^{th} grain boundary. The triple junction is in equilibrium when the tangential ($\vec{t}_i$) forces and normal ($\vec{n}_i$) forces are balanced. The Herring equation can be simplified by assuming that the differential of the energy terms with respect to the rotation angle ($\partial\gamma_i/\partial\beta$) are small and can be neglected. In this case, only the tangential forces need to be balanced. The simplified Herring relation or Young's equation is given by:

$$\frac{\gamma_1}{\sin\theta_{2,3}} = \frac{\gamma_2}{\sin\theta_{1,3}} = \frac{\gamma_3}{\sin\theta_{1,2}} \qquad \text{Equation 2.4}$$

Where the terms are defined in **Figure 2.8b**. This equation has been used to determine the grain boundary energy of Al by measuring the dihedral angles (θ) between the grain boundaries of a tricrystal [73][74].

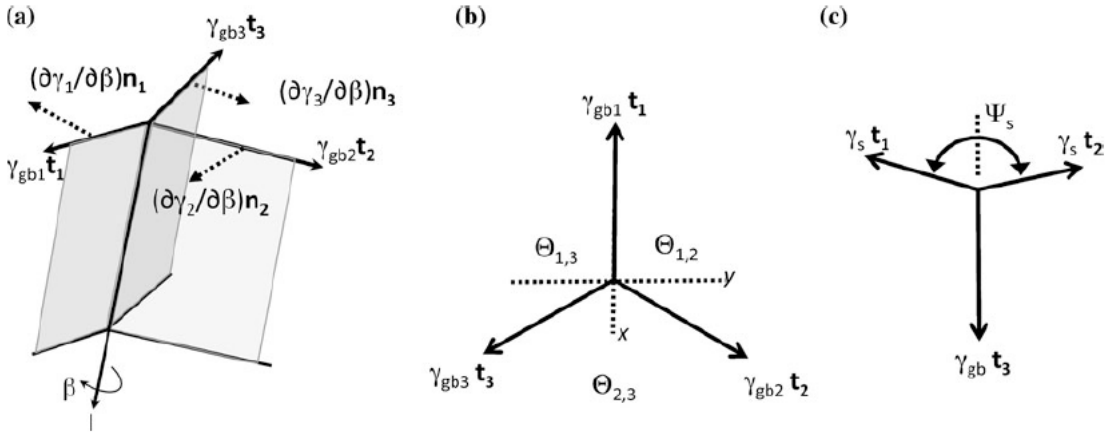

Figure 2.8. The diagram shows the balance of interfacial energies at triple junctions (a) Herring relation corresponding to Equation 2.3, (b) Young's Equation 2.4, and Mullins' Equation 2.5. This figure was reproduced from reference [1].

In the case of thermal groove measurements, where a grain boundary meets a free surface, the equation can be simplified further by assuming that the free surfaces have the same energy. The grain boundary energies (γ_{gb}) are then deduced from the geometry of the thermal groove according to the Mullins' equation [75].

$$\gamma_{gb} = 2\gamma_s \cos(\frac{\Psi}{2}) \qquad \text{Equation 2.5}$$

Referring to **Figure 2.8c**, γ_s is the surface energy (assumed to be constant) and Ψ is the grain boundary dihedral angle. Grain boundary energies of Al [73][74] and Cu [53][76] measured using the tricrystal and thermal groove method are compared in **Figure 2.9**. Although the relative grain boundary energies are slightly different for different elements, the energy anisotropies follow the same trend. Interestingly, this experimental evidence is consistent with the calculations of Holm et al. [10] and provides support for the idea that the grain boundary energies in FCC metals are correlated. Only a relatively small number of grain boundary energies have been measured by the tricrystal and thermal groove methods. All possible grain boundary energies can be obtained from three-dimensional electron backscatter diffraction (3D-EBSD) measurements, in which a focused ion beam or manual polishing has been used for serial sectioning [5][6][7][77][78]. By assuming that the interface junctions are in local thermodynamic equilibrium, the grain boundary energy distribution (GBED) is extracted from the geometry of grain boundaries according to Herring equation [72], as described in [79]. This method has been used to determine the GBED of Ni [6][44] and several ceramics [5][7][77][78]. A recent comparison between calculated and measured grain boundary energies in Ni indicates the limitations of each method [4]. The reliability of measured grain boundary energies depends on the observation frequency. While the calculated grain boundary energies are not subject to this limitation, they are limited by computational capabilities. For the case of low symmetry boundaries, the size of the periodic cell representing the boundary can be so large that it is impossible to perform the calculation in a reasonable time.

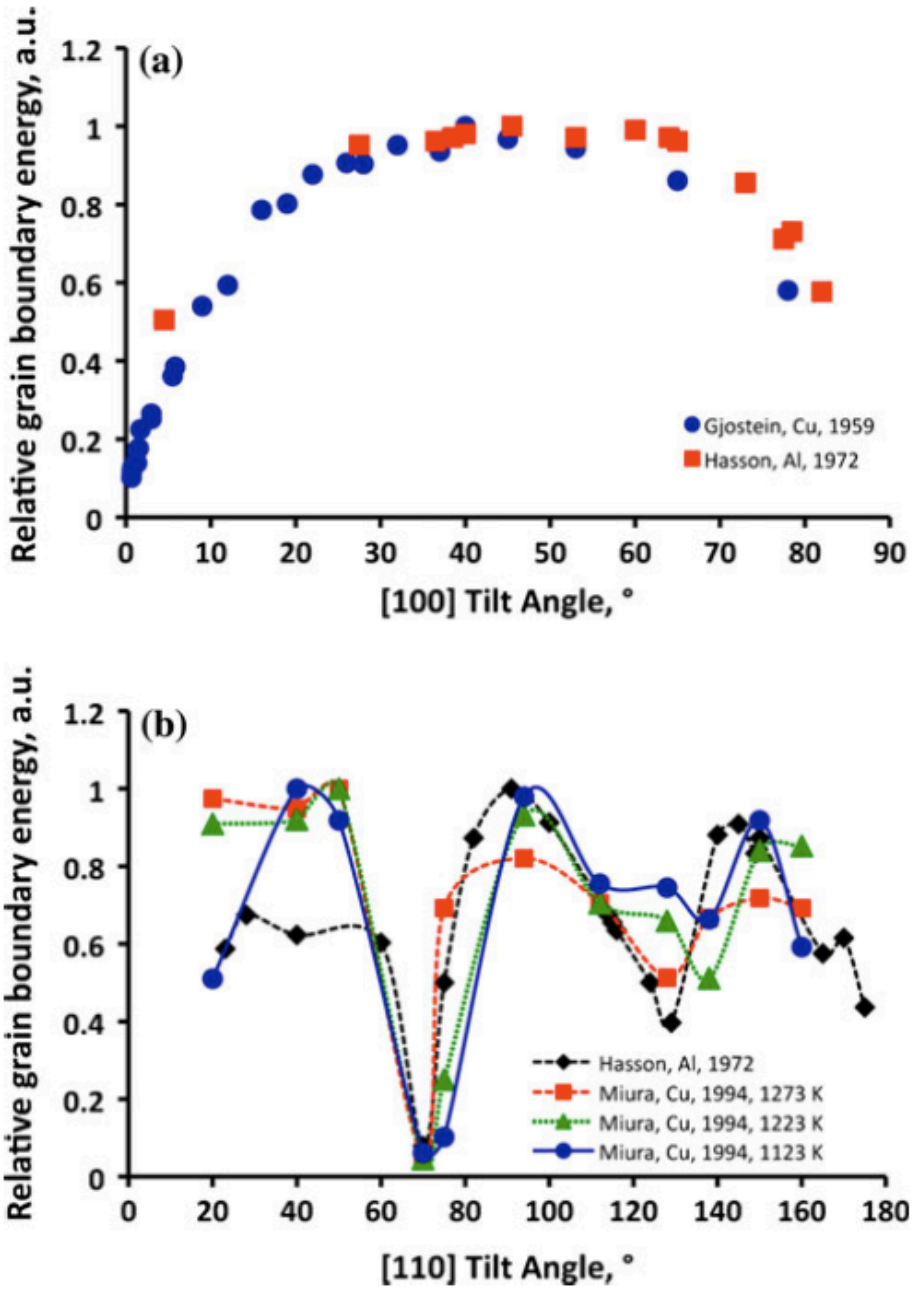

Figure 2.9. The measured grain boundary energies of (a) symmetric <100> tilt grain boundaries in Al and Cu, (b) symmetric <110> tilt grain boundaries in Al and Cu. This figure was reproduced from reference [1].

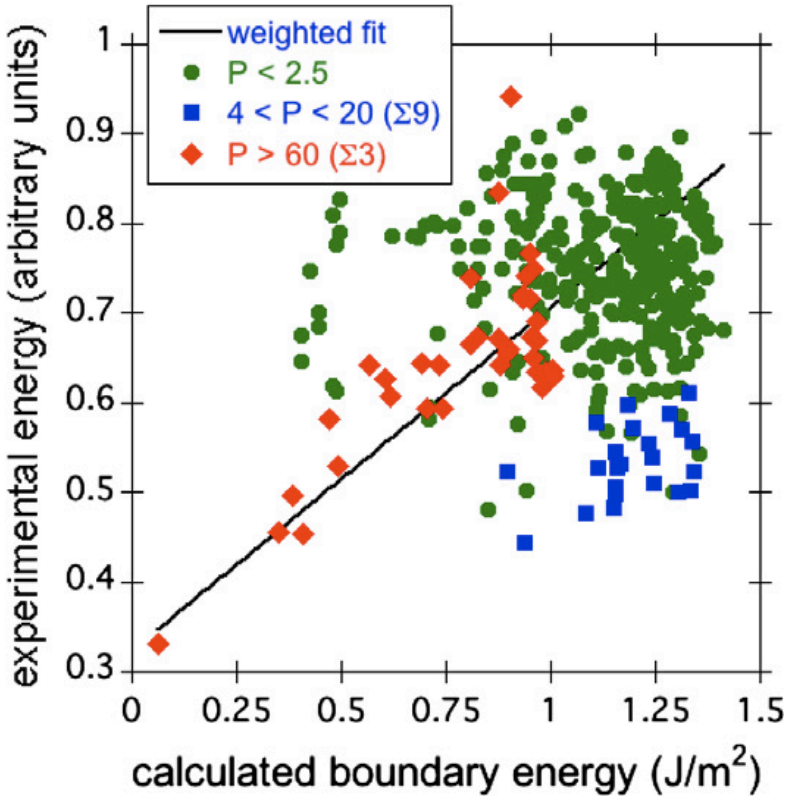

Figure 2.10. The relationship between experimental and calculated grain boundary energy in Ni weighted by boundary population (P). The data are plotted with their population groups, red diamond for P > 60, blue square for 4 < P< 20, and green circles for P < 2. This figure was reproduced from reference [4].

The experimental observations can be used to select the most important grain boundaries to include in the calculations. It should be emphasized that there is excellent agreement between calculated and measured grain boundary energies for the prevalent Σ3 boundaries (see **Figure 2.10**). Experimental [6][7][5][21] and computational [46][47] studies show that there is an inverse relationship between grain boundary populations and grain boundary energies. **Figure 2.11** compares the experimental population and calculated boundary energy in Ni. As shown in the plot, there is an excellent correlation for the high population grain boundaries and a poor correlation for the low population grain boundaries. This poor correlation could be the result of inaccurate measurements of the population because of a limited number of observations.

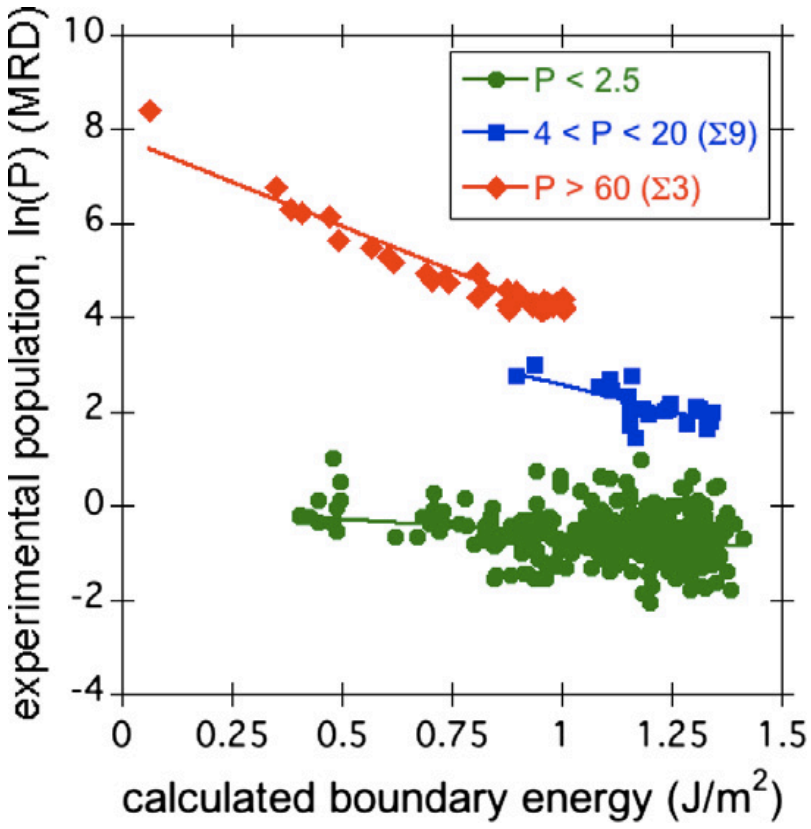

Figure 2.11. Grain boundary population plotted as a function of calculated grain boundary energy in Ni. The data are plotted by population group, red diamonds for P > 60, blue squares for 4 < P < 20, and green circles for P < 2. This figure was reproduced from reference [4].

If grain boundary populations obey a fixed relationship between the energy and population, grain boundary energies could then be extracted directly from the grain boundary character distribution (GBCD) [3][6]. The direct measurements of grain boundary populations are more accurate than the grain boundary energies derived from 3D-EBSD measurements, and could extend to all observed grain boundary types, which is not possible by atomistic simulation. Therefore, it is possible to obtain a more complete and accurate GBED from the experimental GBCD data. Recall that the grain boundary energies are correlated in FCC metals [10], the GBCDs of FCC metals should be correlated in a similar manner.

The data in **Figure 2.12** indicates that for selected Σ3 boundaries in Al and Ni, the correlation is strong. In this case, it should be noted that the GBCDs were

calculated at different discrete bin resolutions because of differences in the sizes of the data sets. Therefore, more studies on other FCC metals with comparable amounts of data are needed to generalize this critical finding.

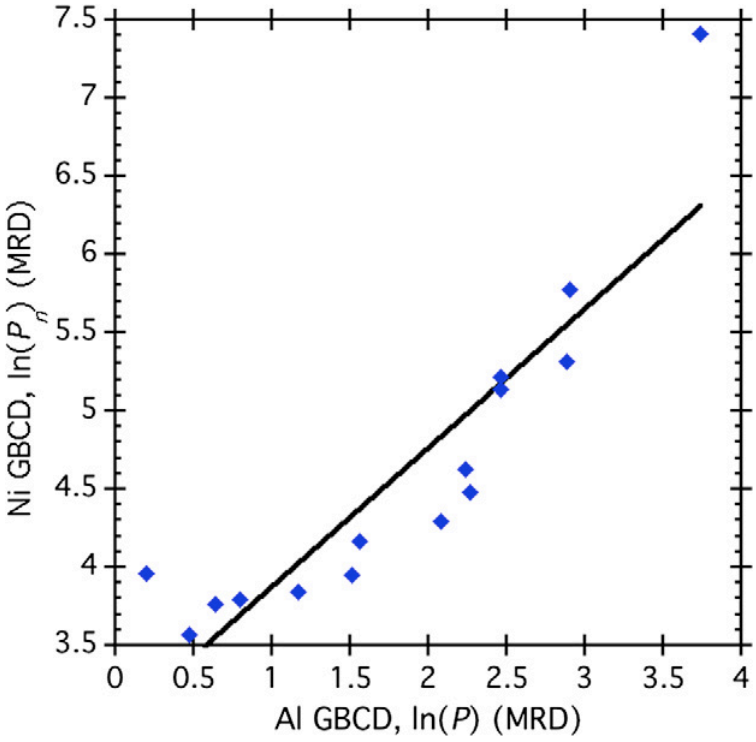

Figure 2.12. Comparison between GBCDs in Ni and Al for Σ3 boundaries, using those boundaries that were also in the set of 388 EAM simulated GBs [10]. Solid line indicates the linear correlation. This figure was reproduced from reference [3].

2.4 Boltzmann Distribution of Grain Boundary Populations

Previous studies demonstrated that grain boundary populations are inversely correlated to the grain boundary energies [4][5][6][43][44][45][46][47].

Barmak et al. recently developed an entropy-based theory to explain the inverse relationship [80][81]. According to the theory, the GBCD evolution is described by a Fokker-Planck type equation. The GBCD derived from this equation has a functional form similar to the Boltzmann distribution. Specifically, the temperature-like parameter (λ), which is determined from the minimization of the relative entropy over a long period time for a specific grain boundary energy distribution, was assigned as the denominator for the boundary energy (E_i) in the Boltzmann distribution, $\exp(-E_i/\lambda)$ [80][81]. It was assumed in this theory that the GBCD is the consequence of the grain boundary coarsening process that drives grain boundaries to the Boltzmann distribution [80][81]. The GBCD simulated from large-scale two-dimensional simulations of grain coarsening employed the local evolution law and space-filling constraints was consistent with the results obtained from the entropy-based theory [80][81]. The grain boundary energy distributions in these two-dimensional simulations are modeled by considered only misorientation angles (Δg). Therefore, it is of interested to investigate this Boltzmann relationship between the experimental GBCDs and the grain boundary energy specified by misorientation angles and grain boundary normal, $\lambda(\Delta g, n)$, the five macroscopic parameters of grain boundary space.

In this study, an analogy is suggested that links the distribution of grain boundaries among a set of structural states with different energies and the distribution of classical particles among a set of possible energy states. It should be noted that the Boltzmann distribution describes the distribution of distinguishable classical particles over various energy states when in thermal equilibrium. If the arrangement of atoms at the grain boundary is analogous to a distinguishable classical particle [82][83], it is then reasonable to assume that the GBCDs can be described by Boltzmann statistics. Although there are an unlimited number of different grain boundary types in the five dimensional space, we can limit the number of grain boundary types by assuming that grain boundaries which are crystallographically close (in the same bin of the 5D space of grain boundary types), occupy the same energy state [69]. Therefore, the possible energy states of systems

are limited to N = 6,561 for a binning resolution of 10° (see §2.2). We also assume that the energy states for the 6,561 bins might be close, but are not exactly the same; therefore, there are no degenerate states. Furthermore, we assume that when polycrystalline materials are annealed for a sufficiently long time, a steady-state distribution of grain boundaries is reached and remains constant during grain growth. Miller reported that the grain boundary plane distribution of strontium titanate is constant during grain growth in which the average grain size increased by a factor of ten [9]. This result supports the assumption that the GBCD is scale invariant during grain growth. In addition, annealed strontium titanate has a steady state GBCD that is inversely correlated to the grain boundary energy anisotropy and is consistent with the steady state GBCD predicted by the critical event model [47].

The critical event model assumed grain boundary lengthening at the triple junction obeys Young's equation and the possibility that the GBCD changes when a critical event occurs is determined by the rates of boundary creation and annihilation [47]. While the rate of creation is obtained from a random distribution (or existing orientation distribution), the rate of annihilation is proportional to the grain boundary energies. The steady state, in which the rate of creation and annihilation of grain boundary are equal, is analogous to the equilibrium of a system of particles described by Boltzmann statistics. Because the geometry and grain boundary energy at a triple junction in equilibrium must satisfy interfacial equilibrium, it implies that grain boundaries interact in the grain boundary network via the local equilibrium at a triple junction. We could therefore make an analogy between the interaction at the triple junction and the transfer of energy that occurs when particle collide. Further, the critical events that occur when a grain disappears or two grow to the point of contact could also be considered analogous to energy transfer between particles. For the analogy with the Boltzmann distribution to be complete, this interaction must be weak so that in most cases, the boundaries can act independently.

Considering an isotropic GBCD, 6,561 distinguishable grain boundary types are uniformly distributed over 6,561 bin with equal probability, leading to a

population of N_i=1 MRD. In this case, if we assigned each bin as a single particle, the total number of particles in the system would be 6,561 distinguishable particles. The numbers of configurations, where N_i is the number of particles with energy state E_i, are constrained by the total number of particles $\sum_{i=1}^{6,561} N_i = 6,561$, and the total energy $\sum_{i=1}^{6,561} E_i N_i = E_{total}$. The numbers of configurations subjected to these constraints are described by $\Omega(N_i) = \frac{N!}{N_1!N_2!N_3!...N_N!}$ [82][83]. There are many configurations that satisfy both constraints, but only the most predominant configuration, which has the greatest number of configurations for specified N_i , is assigned as the system configuration. From statistical mechanics, the probabilistic description of entropy (S) is defined from Boltzmann's postulate [82][83].

$$S \equiv k_B \ln \Omega \qquad \text{Equation 2.6}$$

Where k_B is the Boltzmann constant and the number of configurations $\Omega(N_i)$ can be regarded as an effectively continuous function. Therefore, the predominant configuration is derived from differential calculus. The logarithm of the total number of configurations is given by [82][83]

$$\log \Omega(N_i) = \log N! - \sum_{i=1}^{N} \log N_i! \qquad \text{Equation 2.7}$$

The application of Stirling's approximation then yields:

$$\log \Omega(N_i) \approx N \log N - \sum_{i=1}^{N} N_i \log N_i \qquad \text{Equation 2.8}$$

Using the method of Lagrange multipliers with the total number of particles and the of total energy as constraints [82][83], the maximum number of configuration $\log \Omega(N_i)$ is:

$$\frac{\partial}{\partial N_i}\frac{[\log\Omega(N_i) - \delta\,\Sigma_{i=1}^{N}\,N_i - \beta\,\Sigma_{i=1}^{N}\,E_i N_i]}{} = 0 \qquad \text{Equation 2.9}$$

Where δ, β are Lagrange multipliers that maximize the number of configurations $\Omega(N_i)$. After differentiating, we obtain

$$\sum_{i=1}^{N}\left[-(\log N_i + 1) - \delta - \beta E_i\right]dN_i = 0 \qquad \text{Equation 2.10}$$

The solution is then given by $\log N_i = -1 - \delta - \beta E_i$

$$N_i(E_i) = e^{-1-\delta}e^{-\beta E_i} \qquad \text{Equation 2.11}$$

To determine the Lagrange multipliers (δ and β) as a function E_i, we use the constraint that the total number of particle is fixed. Therefore it must be true that

$$\sum_{i=1}^{N}N_i(E_i) = \sum_{i=1}^{N}e^{-1-\delta}e^{-\beta E_i} = N$$

$$\sum_{i=1}^{N}N_i(E_i) = e^{-1-\delta}\sum_{i=1}^{N}e^{-\beta E_i} = N$$

$$\sum_{i=1}^{N}e^{-\beta E_i} = \frac{N}{e^{-1-\delta}} = Z(\beta)$$

or

$$e^{-1-\delta} = \frac{N}{Z(\beta)} \qquad \text{Equation 2.12}$$

From the Boltzmann postulate and the second law of thermodynamics, $\beta = \frac{1}{k_B T}$ [82][83]. The partition function is defined as $Z(T) = \sum_{i=1}^{N}e^{-E_i/k_B T}$ and T is an experimental temperature in K. The probability of observing a grain boundary with energy E_i, is then given by use of Equation 2.11 and Equation 2.12.

$$P(E_i) = \frac{N(E_i)}{N} = \frac{e^{-E_i/k_B T}}{Z(T)} \qquad \text{Equation 2.13}$$

It should be noted that the grain boundary energy is defined as energy per unit area. To investigate the relationship between grain boundary populations and boundary energies using the Boltzmann distribution, the grain boundary energy needs to be multiplied by unit area variable $\alpha_i =< area >_i$. Equation 2.13 is then defined by

$$N_i = N \times \frac{e^{-E_i \alpha_i / k_B T}}{Z(T)} \qquad \text{Equation 2.14}$$

And the partition function is redefined as $Z(T) = \sum_{i=1}^{N} e^{-E_i \alpha_i / k_B T}$. It should be noted that grain boundary energy, E_i is convoluted with temperature. It was reported that the temperature dependence of the surface energy $\gamma_s(T)$ could be written as [84]

$$\gamma_s(T) = \gamma_s(T_0) - \int_{T_0}^{T} \frac{S}{A} dT$$

$$\gamma_s(T) = \gamma_s(T_0) - \frac{S}{A}(T - T_0) + \xi(\mathrm{O}) \qquad \text{Equation 2.15}$$

Where T_0, S, A are temperature at 0 K, the total surface entropy from vibrational and configurational contributions, and the surface area per mole of surface atoms [84]. We shall assume a constant surface entropy, S, when $0 < \frac{T}{T_m} < 0.5$ and the error $\xi(\mathrm{O})$ from approximation is negligible. The temperature dependence grain boundary energy, $\gamma_{gb}(T)$, which composed of two surfaces, $\gamma_s^{tot} = \gamma^1(hkl) + \gamma^2(h'k'l')$, is then simply given by

$$\gamma_{gb}(T) = \gamma_s^1(T_0) - \frac{S^1}{A^1}(T - T_0) + \gamma_s^2(T_0) - \frac{S^2}{A^2}(T - T_0) - B$$

$$\gamma_{gb}(T) = \gamma_{gb}(T_0) + C - mT; \qquad \text{Equation 2.16}$$

Where $C = \left(\frac{S^1}{A^1} + \frac{S^2}{A^2}\right) T_0$ and $m = \left(\frac{S^1}{A^1} + \frac{S^2}{A^2}\right)$. The influence of temperature on the boundary energy described in Equation 2.16 is similar to simulated grain boundary

energies as a function of temperature in Cu [85] and Ni [86]. If the C and m parameters for every boundary are approximately the same for all boundaries, Equation 2.14 is then given by

$$N_i = N \times \frac{e^{-\left[\frac{(E_i(T_0)+C-mT)\alpha_i}{k_B T}\right]}}{\sum_{i=1}^{N} e^{\left[\frac{(E_i(T_0)+C-mT)\alpha_i}{k_B T}\right]}} = N \times \frac{e^{-\left[\frac{(C-mT)\alpha_i}{k_B T}\right]} \times e^{-\left[\frac{E_i(T_0)\alpha_i}{k_B T}\right]}}{e^{-\left[\frac{(C-mT)\alpha_i}{k_B T}\right]} \times \sum_{i=1}^{N} e^{-\left[\frac{E_i(T_0)\alpha_i}{k_B T}\right]}}$$

$$N_i = N \times \frac{e^{-\left(\frac{E_i(T_0)\alpha_i}{k_B T}\right)}}{\sum_{i=1}^{N} e^{-\left(\frac{E_i(T_0)\alpha_i}{k_B T}\right)}} \qquad \text{Equation 2.17}$$

Therefore the probability of observing a grain boundary with energy E_i at temperature T can be deduced from the boundary energy simulated at T = 0 K.

Chapter 3

3. Experiment

3.1 Introduction

In this chapter, we shall describe the preparation and analysis of the polycrystalline specimens. Electron backscatter diffraction (EBSD) is discussed as a technique for the spatial mapping of crystal orientations. The procedures for cleaning the EBSD maps and reconstructing the grain boundaries are described. Next, the procedures for calculating the GBCD from the EBSD measurements will be presented. Finally, the statistical measures used to quantify the correlations are described.

3.2 Sample preparation

We deliberately selected FCC metals with a wide range of stacking fault energies, as listed in **Table 3.1**. The BCC polycrystalline specimens used in this study were Fe and Mo. The high purity polycrystalline specimens were purchased from commercial sources, specified in **Table 3.2**. The specimens were cut and then annealed in a hydrogen flow furnace to avoid oxidation and contamination. We varied annealing conditions in an attempt to achieve specimens with similar microstructures as well as weak textures. The details of annealing conditions are listed in **Table 3.2**. Appropriate surfaces were prepared by using the LaboPol-4/LaboForce-1 combination polisher (Struers Inc.). A summary of sample preparations is presented in **Table 3.3**. The specimens were initially ground with SiC papers and then polished with diamond suspensions, Green lubricant, a water-

based solution, was used with a diamond suspension (Struers Inc.). Finally the samples were fine polished using colloidal silica slurry (OP-S). It is important to note that the colloidal silica has to be appropriate for the polishing system and the force has to be carefully adjusted to be as small as possible, but high enough to remove material in a reasonable time. Ag and Au are extremely soft; therefore, the samples have to be carefully polished with a low force.

Table 3.1. Materials and material properties of the polycrystalline specimens.

Materials	Al	Ag	Au	Cu	Ni	Fe	Mo
Atomic Number	13	47	79	29	28	26	42
Lattice cont. (Å)	4.03	4.09	4.08	3.615	3.52	2.86	3.15
Stacking Fault EAM (mJ/m^2)	104 [b]	21 [a]	30.7 [b]	44.4 [b]	127 [b]	-	-
Voigt average Shear Modulus (GPa)	33 [b]	37.5 [a]	29.1 [b]	55.2 [b]	90 [b]	89.28 [d]	125.98
E (111) (J/m^2)	0.870 [b]	0.842 [a]	1.094 [b]	1.239 [b]	1.953 [b]	2.685 [c]	3.429 [c]
E (100) (J/m^2)	0.942 [b]	0.983 [a]	1.176 [b]	1.345 [b]	2.06 [b]	2.565 [c]	3.261 [c]
E (110 (J/m^2)	1.037 [b]	1.01 [a]	1.282 [b]	1.475 [b]	2.375 [b]	2.370 [c]	2.920 [c]

[a]Reference [87], [b]Reference [10], [c]Reference [88], [d]Reference [89] [d]

Table 3.2. Characteristics of samples and accumulated grain boundary data. T_H is a homologous temperature.

	Purity (%)	Commercial Sources	Annealing (°C)	T_H	Annealing (Hours)	Number of segments	Step size (μm)	Steps per line
Al	>99.50	Commercial Alloy 1050	400	0.72	1	76,707	2.0	6.5
Ag	99.9985	Alfa Aesar Premion	200	0.39	2	300,875	0.4	6.6
Au	99.999	Alfa Aesar Premion	300	0.43	2	312,183	0.4	6.3
Cu	99.9999	Alfa Aesar Puratronic	300	0.43	2	308,062	1.0	6.5
Ni	99.999	Alfa Aesar Puratronic	416	0.40	24	293,609	1.0	7.3
Fe	99.995	Alfa Aesar Puratronic	550	0.46	2 4 8 16	48,133 81,685 71,889 279,212	1.0	11.5 9.9 9.2 11.4
Mo	99.95	Alfa Aesar	1050	0.46	2	297,494	1.0	7.1

Note Al and Ni data sets recorded by Miller [25] were also included in this study.

Table 3.3 Surface preparation.

Materials	Surface	Polishing	Lubricant	Speed [Rpm]	Force (N)	Time (Min)
Ag/ Au	SiC-paper	#1200	Water	120	2.5	-
	SiC-paper	#2400	Water	120	2.5	15
	SiC-paper	#4000	Water	120	2.5	30
	MD-Mol	3μm diamond	Green	120	2.5	45
	MD-Nap	1μm diamond	Green	120	2.5	60
	MD-Chem	40 nm colloidal silica	Soap	120	2.5	180
Cu	SiC-paper	#1200	Water	120	5.0	-
	SiC-paper	#2400	Water	120	5.0	15
	SiC-paper	#4000	Water	120	5.0	30
	MD-Mol	3μm diamond	Green	120	5.0	60
	MD-Chem	40 nm colloidal silica	Soap	120	5.0	180
Fe/Mo	SiC-paper	#1200	Water	120	7.5	-
	SiC-paper	#2400	Water	120	7.5	15
	SiC-paper	#4000	Water	120	7.5	30
	MD-Mol	3μm diamond	Green	120	5.0	45
	MD-Mol	1μm diamond	Green	120	5.0	60
	MD-Chem	40 nm colloidal silica	Soap	120	5.0	120

Note MD-Mol, MD-Nap, and MD-Chem are polishing cloths (Struers Inc.). MD-Mol (Taffeta wool) and MD-Nap (short synthetic nap) are cloths for diamond polishing. MD-Chem is a final cloth for final polishing with colloidal silica slurry (OP-S).

3.3 Measuring the Grain Boundary Character Distribution (GBCD)

3.3.1 Electron Backscatter Diffraction (EBSD)

Electron backscatter diffraction (EBSD) is a characterization technique to determine local crystal orientations. EBSD orientation maps can be collected from planar surfaces by using an automated EBSD system in a scanning electron microscope (SEM). We use a field-emission gun SEM (Quanta 200, FEI Company) for EBSD measurements. The microscope geometry is shown in **Figure 3.1**. When an electron beam is focused on a crystalline material, electrons undergo inelastic and elastic scattering while penetrating through a volume of material. Elastic scattering obeys Bragg's law and therefore reveals crystallographic information from the interaction volume. Optimal intensity for the electron backscattering effect occurs when the sample is tilted to about 70° with respect to the electron beam, as shown in **Figure 3.1a**. The diffracted electrons produce an EBSD pattern on a phosphor screen, which is connected to a high gain intensified charge coupled device (CCD) camera (see **Figure 3.1b**). The geometry of the EBSD pattern is used to determine the local orientation of the crystal [90]. EBSD patterns are collected and analyzed by TSL/OIM software. Errors in absolute orientation and misorientation are estimated to be ±5° and ±0.5°, respectively [91][92][93]. The electron beam can be programmed to move on a fixed grid until the orientations in a predetermined area of the sample are mapped. The reliability of indexing is determined by the confidence index (CI). The crystal orientations with respect to the sample normal are defined by colors in the standard stereographic triangle (see **Figure 3.1c**). It should be noted that there are mis-indexed points at grain boundaries and at triple junctions where the diffraction patterns are superimposed. Mis-indexed points can also arise because of flaws in the surface preparation. Therefore it is necessary to correct mis-indexed pixels by clean up methods.

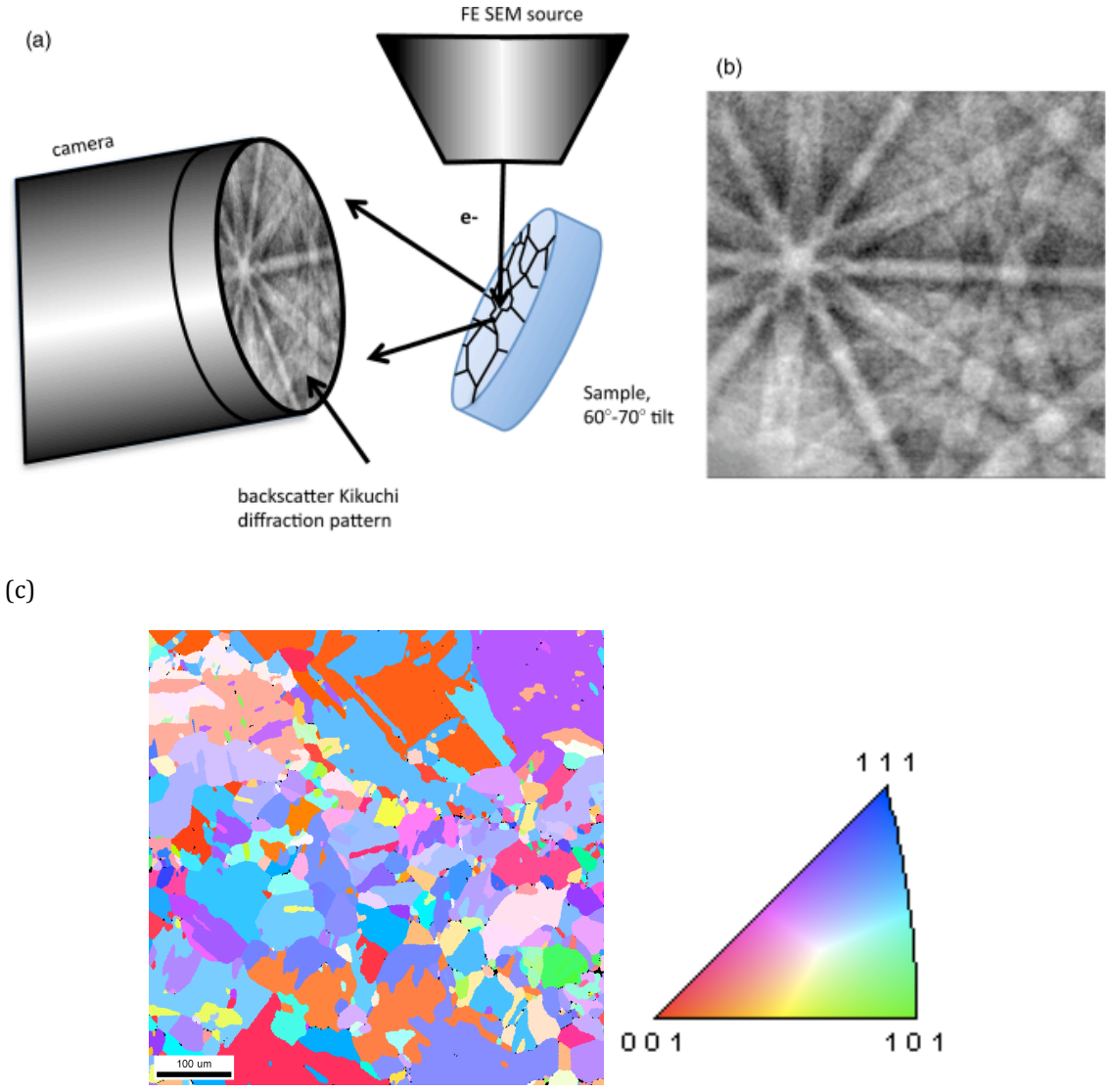

Figure 3.1. Schematic diagram shows the EBSD system. The electron beam from the FE SEM source is focused on the tilted sample (a). A backscatter Kikuchi diffraction pattern or EBSD pattern (b) is captured by the CCD camera [2]. The crystal orientation is then plotted in an [001] inverse pole figure map (c), color coded according to the standard triangle.

The confidence index (CI), which is generated from the voting scheme patented by TSL, indicates the confidence of indexed crystal orientation. The CI =1 represents the maximum confidence in the orientation solution, while CI = 0 indicates that the point is likely to be mis-indexed. All of the EBSD maps were "cleaned-up" using algorithms that are parts of the TSL OIM software. Clean up parameters were varied from experiment to experiment based on the raw data. As an example, the clean up for the copper data is illustrated in **Figure 3.2**. We first performed a neighbor CI correction. In this correction, all of the pixels with CI less than 0.1 were changed to the orientation and CI of the neighbor with the highest CI. The map in **Figure 3.2b** depicts the inverse pole figure (IPF) map of the resultant data. Second, we performed grain CI standardization. The CIs of all points in a grain, where a grain is defined as two or more pixels with misorientation less than than 5°, are changed to the maximum CI found in the grain.

It should be noted that this step only changes the CI but not the orientation. In **Figure 3.2b**, some pixels that appear to be incorrectly assigned are marked by a black circle. These pixels are removed by a single iteration grain dilation in which single pixels were reassigned a new orientation to that of the nearest grain, as shown in **Figure 3.2c**. Approximately 2 % of the data was changed with this clean up method. At this point, we could see significant improvement from the raw data (**Figure 3.2a**). However there are orientation gradients inside grains, as clearly shown in the red and orange grains at the bottom left corner in **Figure 3.2c**. These orientation gradients are less than 5° in a single grain. We replace the individual orientations inside the grain with the average crystal orientation by applying the single orientation per grain method. The map in **Figure 3.2d** represents the data that was processed with this single orientation per grain method. After extensive clean up procedures, there are clusters of small grains with grain size less than 20% of the average grain size. A comparison with the raw data suggests that these are actually unresolved areas that have been converted to very small false grains by the clean-up procedure.

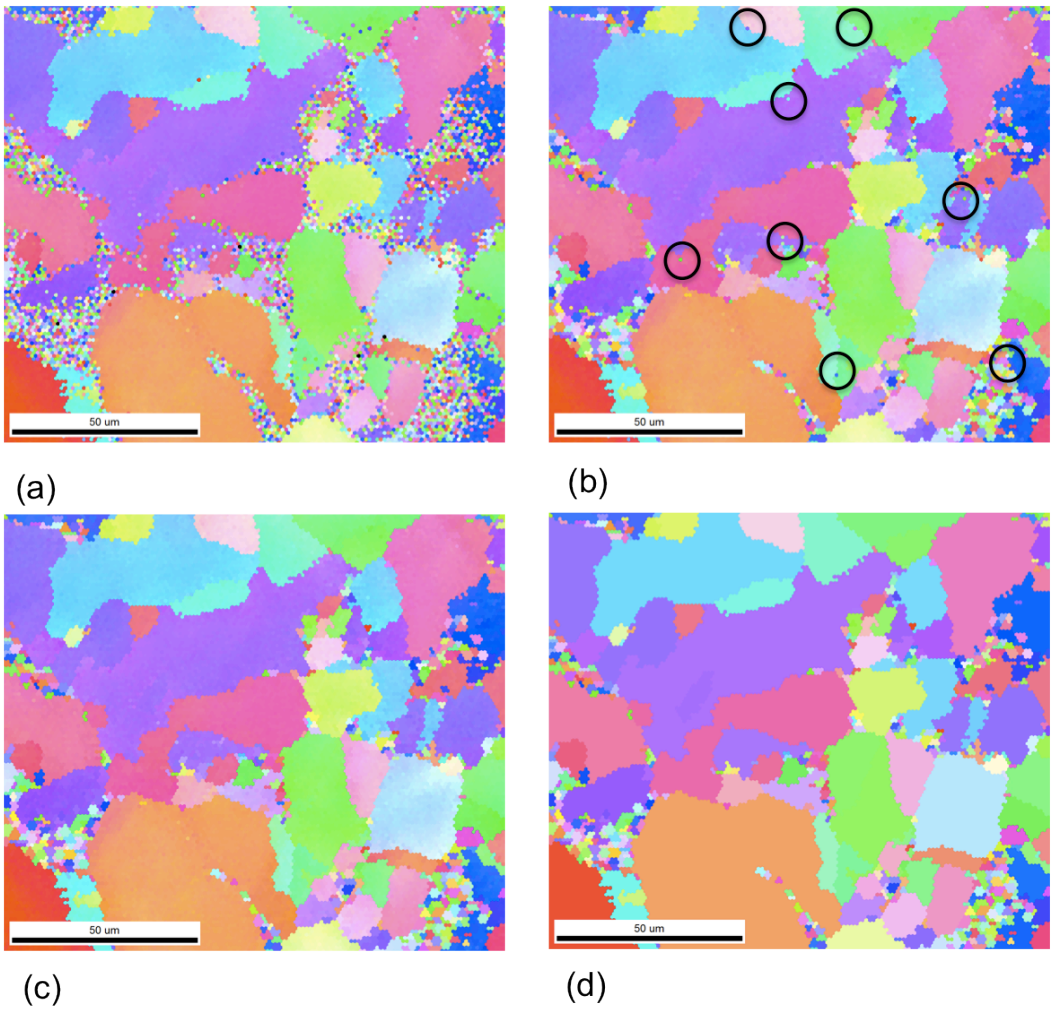

Figure 3.2. Inverse pole figure (IPF) maps for Cu illustrating the multi-step clean up procedures (a) raw data, (b) neighbor CI correction and grain CI standardization, (c) Grain dilation, and (d) average orientation per grain. Artifact pixels are highlighted by black circles.

The unresolved areas are regions of damage inherent in the sample preparation. Therefore, we shall consider these grains as artifacts. To remove these artifacts (**Figure 3.3a**), we partition the data and select only grains with CI greater

than 0.1 and grain size larger than 20% of the average grain size. The IPF map in **Figure 3.3b** represents the partitioned EBSD map, which is approximately 90% of the data. To reconstruct grain boundary line segments for the GBCD calculation, we used TSL software to extract line segments from the partitioned EBSD map (see **Figure 3.3b**). The software first identifies triple junctions and then estimates the in plane grain boundary geometry [94]. Straight lines are first used to connect all of the triple points, as in **Figure 3.3c**. If these segments deviate from the boundary position by more than two pixels, the segments will be divided to better match the curvatures of grain boundaries, as depicted in **Figure 3.3d**. From the reconstructed boundaries, four of five parameters that specify the character of a grain boundary are determined, three for crystal orientation and one for the in-plane boundary orientation. The unknown parameter, the boundary plane inclination with respect to the section plane, is estimated using a stereological procedure developed at Carnegie Mellon University [14][16][95].

The relative areas of the grain boundaries or the grain boundary character distribution (GBCD) are calculated from the relative lengths of grain boundaries. In this study, the program calc_gbcd_stereo, version 05/14/2010 was used to calculate the GBCD [95]. Cubic crystal symmetry and the TSL default reference frame were chosen for the GBCD calculation. The GBCD was calculated using the same discretization for the misorientations (Euler angles) and boundary plane orientations (spherical angles). Each calculation was carried out twice, once using a 10° discretization and once using a 8.2° discretization. The stereographic projections of grain boundary plane distributions (GBPD) and GBCD are calculated using the program graph_gbcd, version 03/16/2010 [95]. All of the projections are created using generic mapping tools (GMT) driven by the script "draw_stereograms".

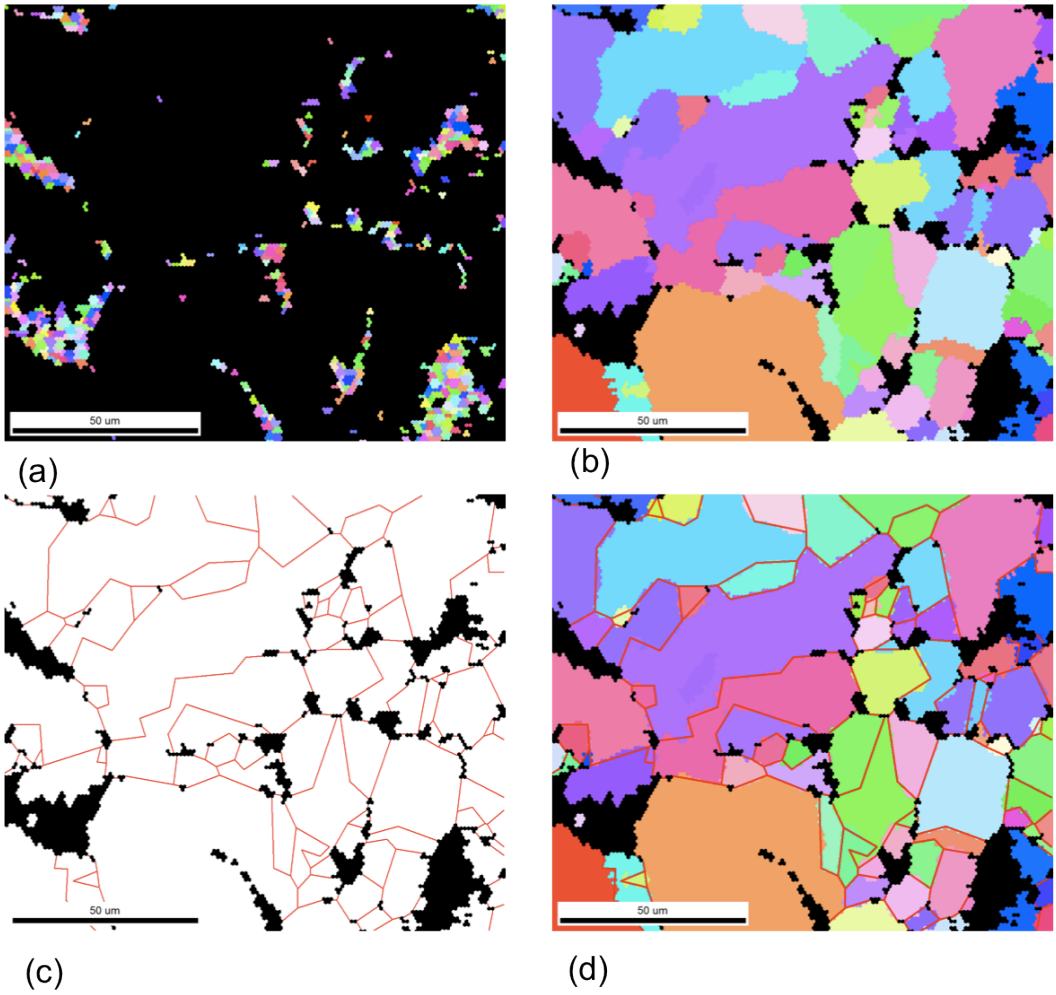

Figure 3.3. Inverse pole figure (IPF) maps for Cu, (a) cluster of false grains, (b) partitioned EBSD map excluding those grains, (c) reconstructed grain boundary map, and (d) IPF map plotted with reconstructed boundaries marked by red lines and false grains are colored black.

3.3.2 Guidance for EBSD measurements and GBCD calculations

The GBCD is calculated from a stereological interpretation of the reconstructed grain boundaries; therefore, the GBCD calculation has inherited uncertainties from the reconstructed grain boundaries. EBSD maps are discrete measurements on a grid; as a result, there are uncertainties in the grain boundary reconstruction associated with the step size in the EBSD measurements [25]. As clearly seen in **Figure 3.3d**, the reconstructed line segments deviate most significantly from the boundary position in small segments. To reduce this source of uncertainty, we deliberately use a step size that is approximately one tenth of average grain size for all EBSD measurements. In strongly textured materials, the bicrystal orientations are not random (**Figure 1.1**) and this leads to a bias in the sampling of boundary segments that can influence the results of the GBCD calculation. To ensure a fair comparison of GBCDs, we therefore processed the specimens to yield weak texture. It should also be noted that for those grain boundaries with highly populated misorientations, the relative areas are calculated with higher accuracy for the more common boundaries than for the ones of rarely observed boundaries. In other word, the GBCDs of highly populated grain boundaries are more accurate than the ones of less populated boundaries. For cubic materials, at least 50,000 reconstructed grain boundaries are needed for a reliable GBCD calculation with a bin resolution of 10° [14][16]. This assumes that all misorientations are equally distributed. However, our specimens are highly twinned and as many as 50 % of all the boundaries may be of the Σ3 type. To accurately sample the entire space, it is therefore necessary to have approximately 50,000 non-Σ3 boundaries. It should also be mentioned that the number of distinguishable boundary types is controlled by the binning resolution of the five dimensional space, as addressed in §2.2. Hence for a GBCD calculation with a bin resolution of 8°, at least 300,000 reconstructed grain boundaries are needed for a reliable GBCD.

3.4 Correlation Coefficients

To investigate the correlation of GBCDs in isostructural materials, we need statistical tools to quantify any correlations that exist. In this thesis, we use the Pearson product-moment correlation and the Spearman's rank-order correlation coefficients (r_{xy}) to characterize the magnitude and direction of the relationship [96]. Both approaches characterize the degree of correlation from the correlation coefficient, which ranges from -1 to 1. Positive and negative correlations are determined by the sign of the correlation and $|r_{xy}|= 1$ represents a perfect correlation, while $r_{xy} = 0$ shows no correlation. The Pearson product-moment correlation is generally used in determining the correlation between N pairs of measurements (x_i, y_i). The correlation coefficient is defined as:

$$r_{xy} = \frac{\sum_i^N (x_i - \bar{x})(y_i - \bar{y})}{\sqrt{\sum_i^N (x_i - \bar{x})^2 (y_i - \bar{y})^2}} \qquad \text{Equation 3.1}$$

The Spearman rank-order correlation assigns ranking values and uses the ranking values to calculate the correlation coefficient, which defined as

$$r_{xy} = 1 - \frac{6\sum_i^N (R_i - S_i)^2}{N(N^2 - 1)} \qquad \text{Equation 3.2}$$

Where R_i and S_i are the rank orders in x and y, respectively. The Pearson product-moment correlation is calculated by using Microsoft Excel 2008 for Mac. The Spearman rank-order correlation is calculated by using Wolfram Mathematica8. As an example, we calculated the correlation coefficients of relative areas for Σ3 boundaries among Au, Cu, and Ni in **Figure 3.4** (reproduced from data in **Figure 4.19**).

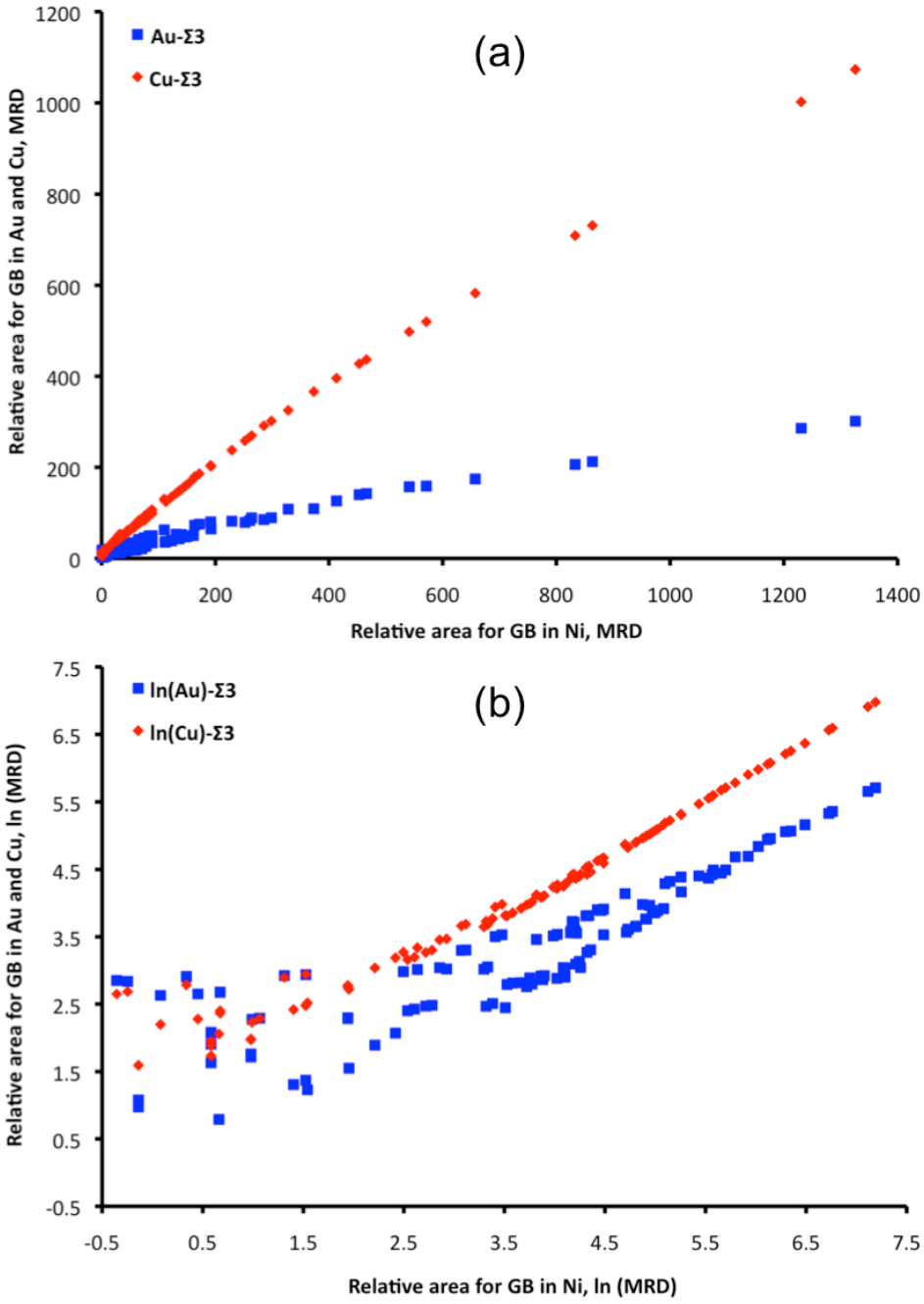

Figure 3.4. Comparison of GBCDs for Σ3 boundaries in Au, Cu, and Ni, linear plot in (a) and logarithmic plot in (b). Each point corresponds to two identical grain boundaries in two materials. The horizontal axis shows the relative area in Ni and the vertical axis shows the relative area in Cu or Au for the same boundary.

Figure 3.4 shows the comparison between the relative areas of Σ3 boundaries in Au, Cu, and Ni. The horizontal axis shows the relative area in Ni and

the vertical axis shows the relative areas for the same boundary in Au and Cu. In **Figure 3.4a**, grain boundary populations of Au and Cu fall along straight lines, this reveals nearly perfect correlations, which are consistent with the Pearson correlation coefficients in **Table 3.4**. Based on this plot and the correlation coefficients, the GBCD of Σ3 boundaries in Au, Cu, and Ni are perfectly correlated. However, there is more scatter in the correlation between Au and Ni (see **Figure 3.4a**). This indicates that the correlation is not uniform throughout the dynamic range of the data and that the strong correlation at higher populations will have a dominant influence on the correlation coefficient. Because the values of grain boundary population span several orders of magnitude, we can use the natural logarithmic plot and recalculate the Pearson correlation coefficients. In **Figure 3.4b**, the scatter of grain boundary population at the low values leads to the lower Pearson correlation coefficients (see **Table 3.4**). These results suggest that the Pearson correlation is not robust in quantifying the correlation of GBCD. On the other hand, the Spearman rank-order correlation coefficients have intermediate values between the Pearson correlation coefficients of linear and logarithmic data sets (**Table 3.4**). Therefore, the Spearman correlation coefficient described by Equation 3.2 is more robust in describing the correlation of GBCDs that spans more than three orders of magnitude.

Table 3.4. The correlation coefficients and slopes for GBCDs of Σ3 boundaries in Ni, Au, and Cu.

Σ3 only	Pearson Correlation	Spearman Correlation		Pearson Correlation
Au-Ni	0.98	0.94	ln(Ni)-ln(Au)	0.89
Cu-Ni	1.00	1.00	ln(Ni)-ln(Cu)	0.98
Cu-Au	0.99	0.96	ln(Au)-ln(Cu)	0.95

Chapter 4

4. Grain Boundary Character Distributions in FCC metals

4.1 Introduction

In this chapter, the microstructures and textures of the annealed polycrystalline specimens are described. Grain boundary character distributions (GBCDs) are extracted from the electron backscatter diffraction (EBSD) maps using the stereological technique described in §2.2. It was hypothesized that the GBCDs of isostructural polycrystalline materials are correlated. To test the hypothesis, we compare the GBCDs of annealed FCC metals: Ag, Au, and Cu. We also use data for Al and Ni recorded by Miller [25]. Finally, qualitative and quantitative comparisons of the GBCDs will be presented.

4.2 Microstructure

High purity metal foils were recrystallized at about 40% of the melting points in a hydrogen flow furnace, as described in §3.2. The goal of the processing was to achieve materials with comparable microstructures. Roughly 300,000 line segments were extracted from the EBSD maps. In an effort to keep the experimental conditions as nearly the same as possible, the step sizes of the EBSD measurements were carefully optimized to achieve a comparable step size per line segments for all of the FCC specimens (see **Table 3.2**). **Figure 4.1** shows the nominal

microstructures of the specimens. Au, Cu and Ni have similar microstructures. Those FCC microstructures have parental twin grains with multiple twin lamellae. The microstructure of Ag differs significantly from those of Au, Cu, and Ni. The Ag microstructure consists of much finer twin lamellae within large grains separated by curved boundaries. This is consistent with what was reported in the literature [97] and, despite several attempts, we were not able to produce microstructures similar to Au, Cu, and Ni.

The crystallographic textures were calculated using the WTS2POP code written by A.D. Rollett. As shown in the pole figures (see **Figure 4.2**), Au, Cu, Ni, and Al have weak texture, while Ag has a significantly stronger texture. The strengths of the textures can also be depicted in the inverse pole figures (see **Figure 4.3**). Ag has a strange pole figure, which could originate from only a few large parental grains with small twin lamellae as depicted in **Figure 4.1a**. Au has a (110)[112] brass texture. Cu has (001)[100] cube texture, which is in agreement with the previous studies of annealing texture of cold rolled Cu foils [98][99]. Ni has a very weak texture. Annealed Al alloy 1050 has (001)[100] cube texture and (123)[412] R texture, which is the characteristic texture influenced by the present of iron and silicon in the Al alloy [100][101]. It was reported that in annealed high purity FCC metals, Ag (low stacking fault energy) has a brass texture, while Cu, Ni, and Al (high stacking fault energy) have cube textures [98][99][102][103].

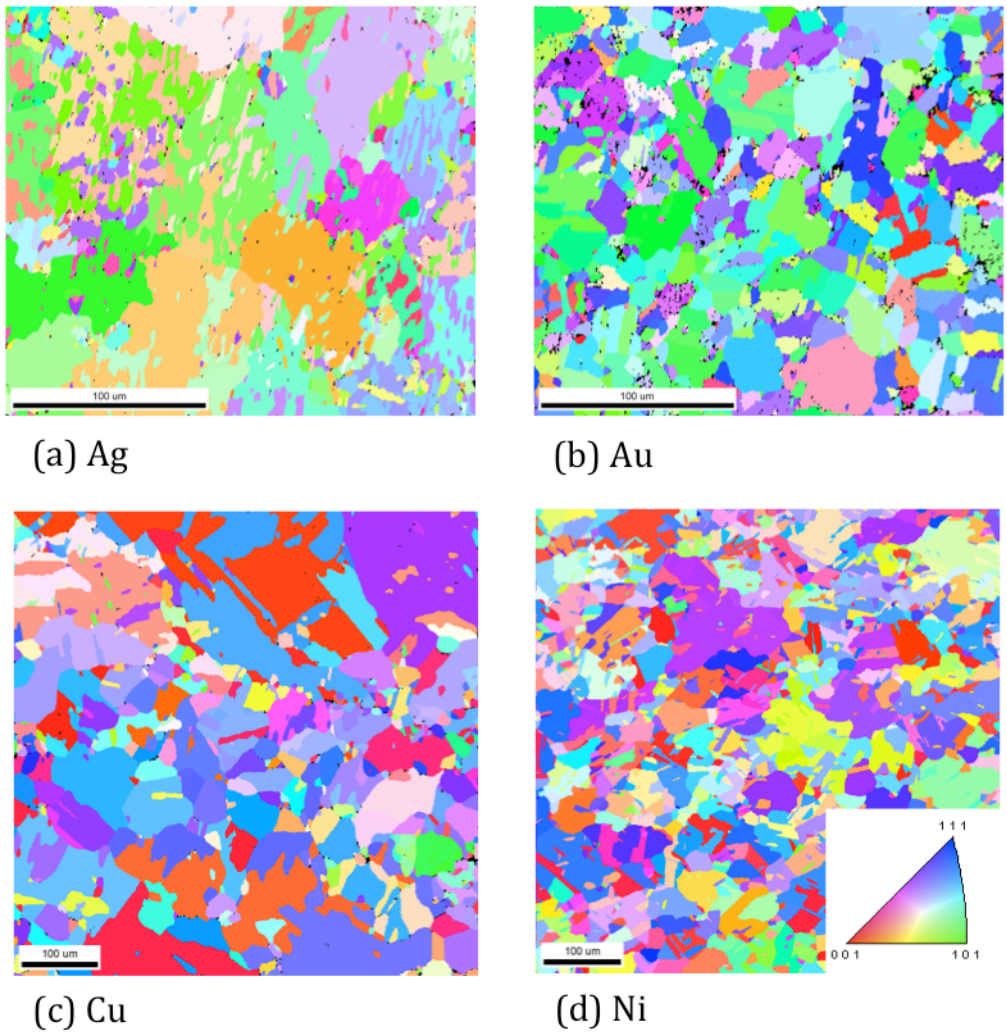

Figure 4.1. Representative [001] inverse pole figure maps for the specimens.

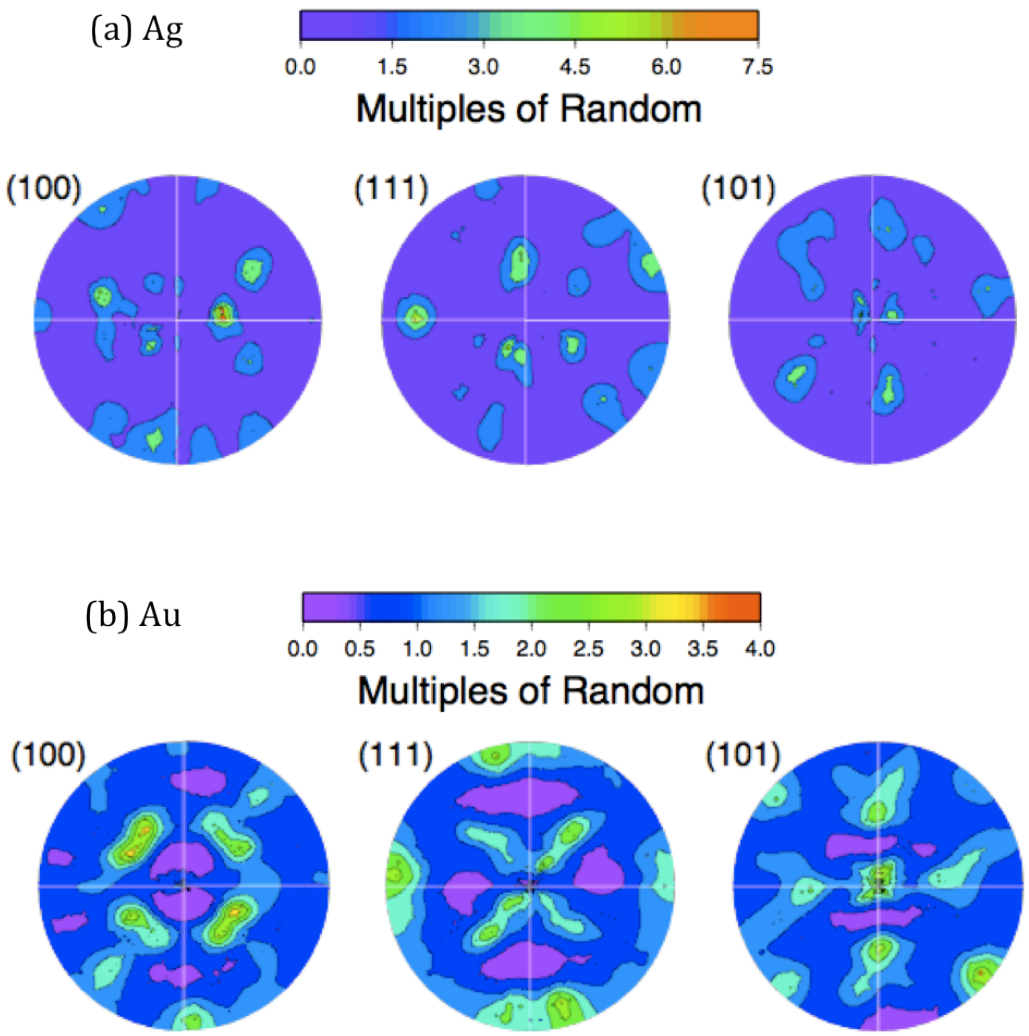

Figure 4.2. Pole figures for the specimens, (a) Ag, (b) Au (c) Cu, (d) Ni, and (e) Al.

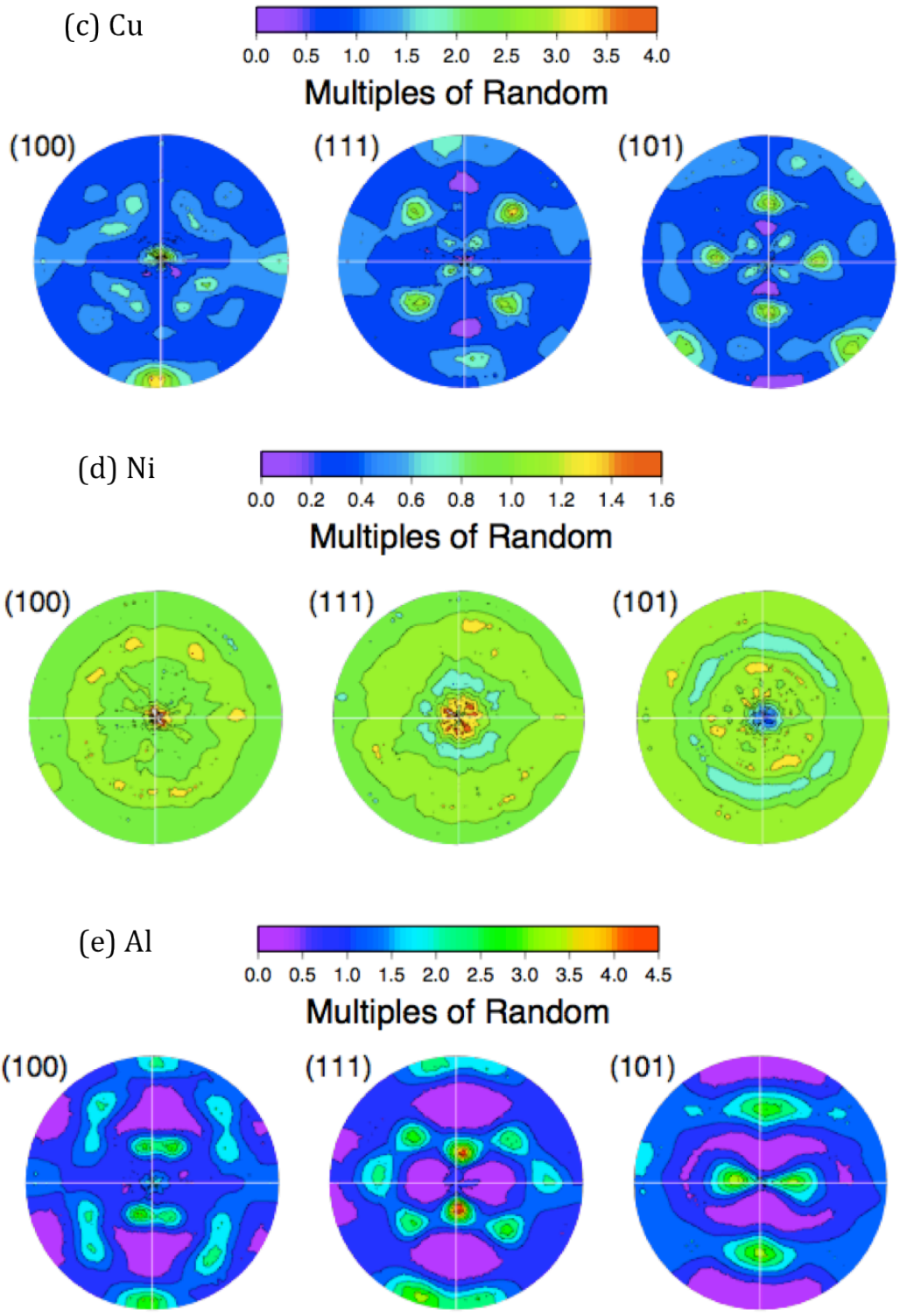

Figure 4.2, continued. Pole figures for the specimens, (c) Cu, (d) Ni, and (e) Al.

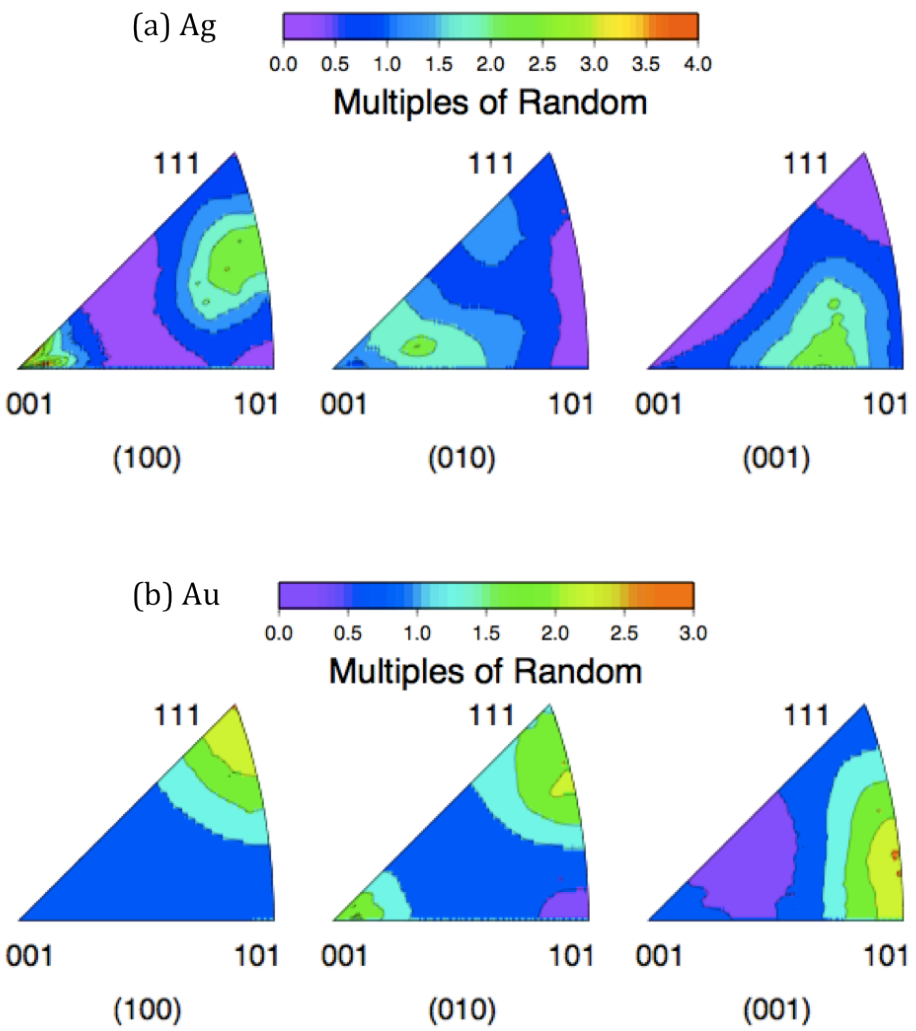

Figure 4.3. Inverse pole figures for the specimens, (a) Ag, (b) Au, (c) Cu, (d) Ni, and (e) Al.

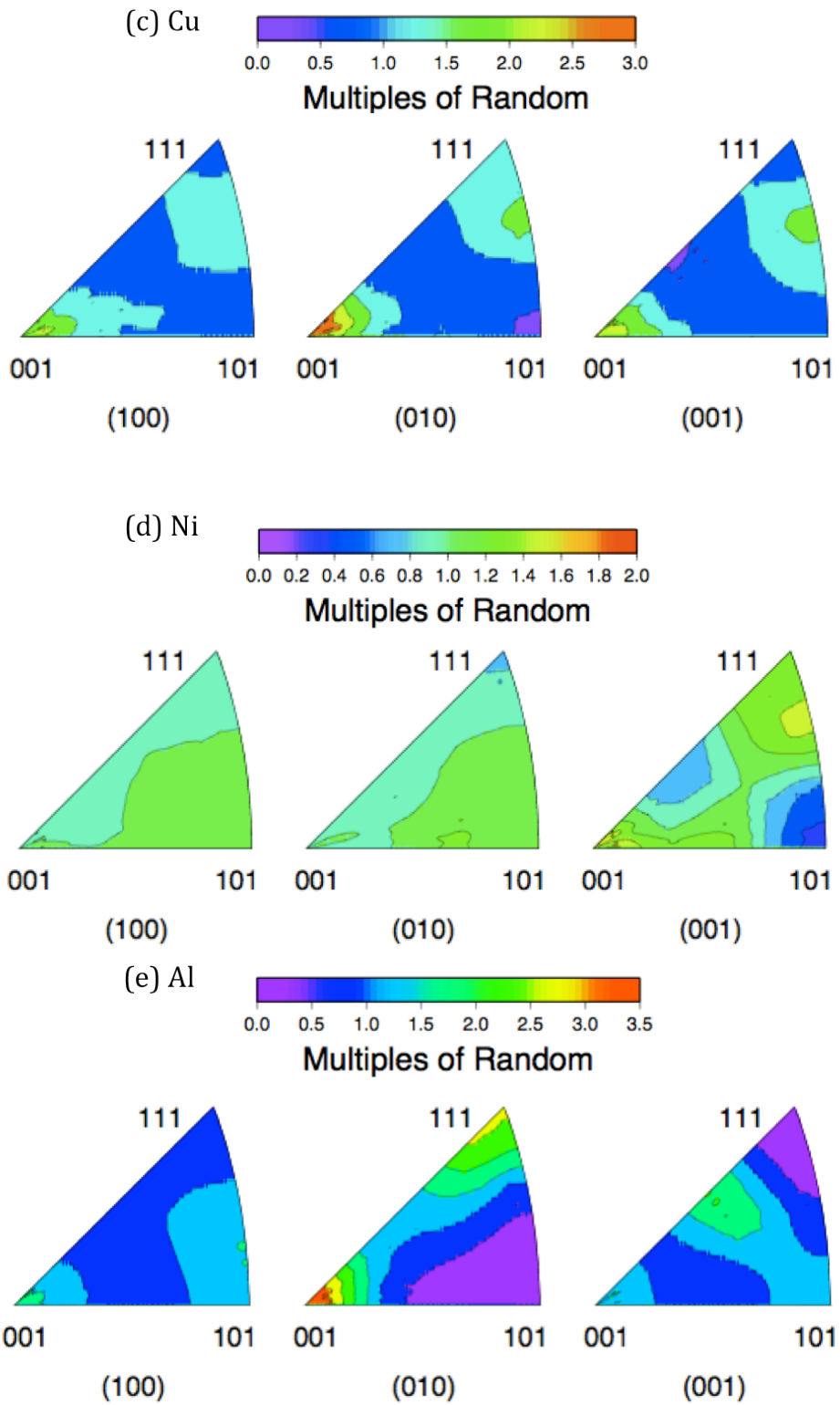

Figure 4.3, continued. Inverse pole figures for the specimens, (c) Cu, (d) Ni, and (e) Al.

4.3 Grain Boundary Character Distribution (GBCD)

The grain boundary character distribution (GBCD) is derived from the stereological analysis of grain boundary line segments. As discussed in §3.3.2, there are uncertainties from reconstructing grain boundary line segments. To reduce these uncertainties, we use a step size that is approximately one tenth of average grain sizes for EBSD measurements. As shown in **Figure 4.4** and **Table 3.2**, the reconstructed line segments have similar distributions as well as comparable values of the average number of steps per line.

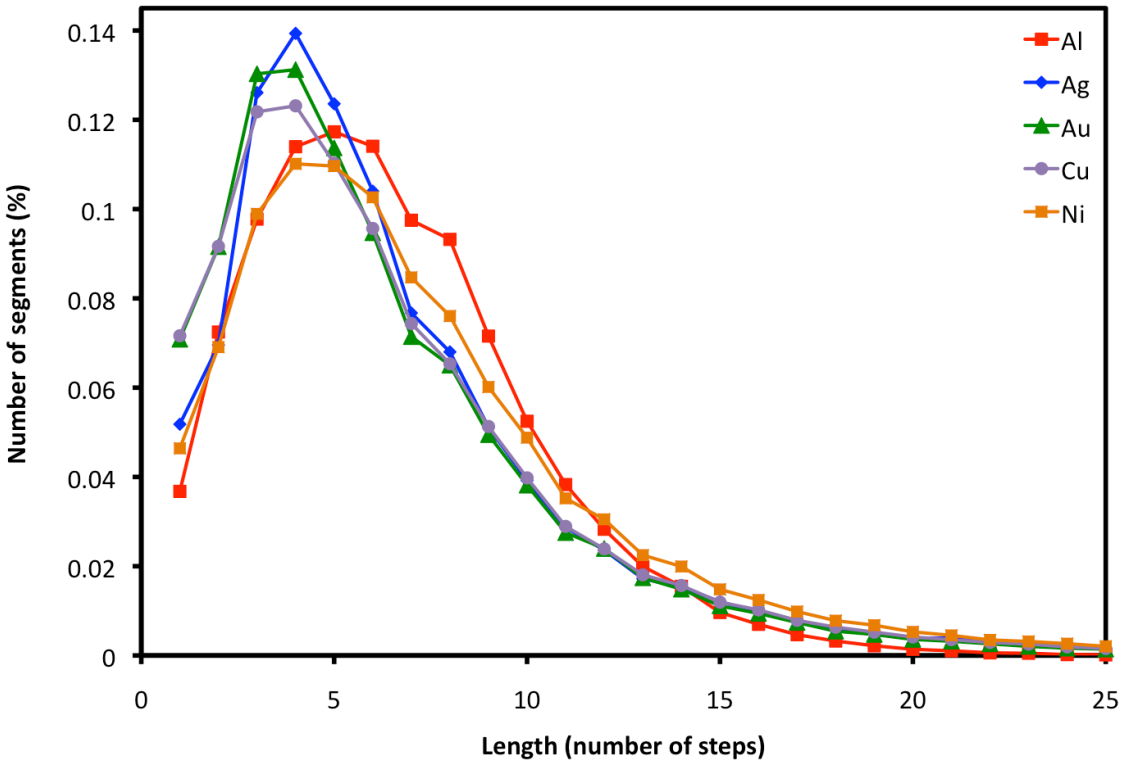

Figure 4.4. The distribution of the number of segments (%) with a given segment length, measured in multiple of the step size.

Using 76,707 line segments for Al and approximately 300,000 line segments for Ag, Au, Cu, and Ni specimen, we calculated grain boundary plane distributions (GBPD) with 10° bins. The GBPDs of Al, Ag, Au, Cu, and Ni are plotted in stereographic projection. Because the distribution of Al is much lower in intensity, it is plotted separately (see **Figure 4.5**). As shown in **Figure 4.5a** and **Figure 4.6a**, the (111) plane is clearly favored compared to the (101) and (001) planes for all FCC specimens. The anisotropies of these distributions are comparable to the GBPDs of FCC structure previously reported for Al [28], Ni [6][26], Cu[26][16], Pb [39], brass [31][13], CuZr alloy [22], and stainless steel [41]. The peak at the (111) plane is coincident with the lowest energy surface orientation in FCC metals (**Figure 4.5c**) [104]. The coherent twin boundary is a 60 ° misorientation about the [111] axis with (111) planes on either side of the boundary. This is the lowest energy grain boundary and the most populated grain boundary. As shown in the grain boundary plane distributions in **Figure 4.5b** and **Figure 4.6b**, the highest peaks are located at the position of the coherent twin boundary for all FCC specimens. Even though there is a significant population of incoherent boundaries in Ag that do not appear in Al, Au, Cu, and Ni, the distribution still reaches a maximum at the position of the coherent twin. It should be noted that the number of distinguishable grain boundaries depends on the resolution of binning. The observed GBCD is therefore expected to vary with the bin size. If a certain feature in the GBCD is narrower than the binning resolution, peaks in the distribution will increase as the size of the bins decreases (see **Figure 2.2**) [25]. However, the distribution of relative grain boundary areas may contain many peaks with different widths. As an example, we calculated GBCD in Au with binning resolutions of 10° and 8.2°.

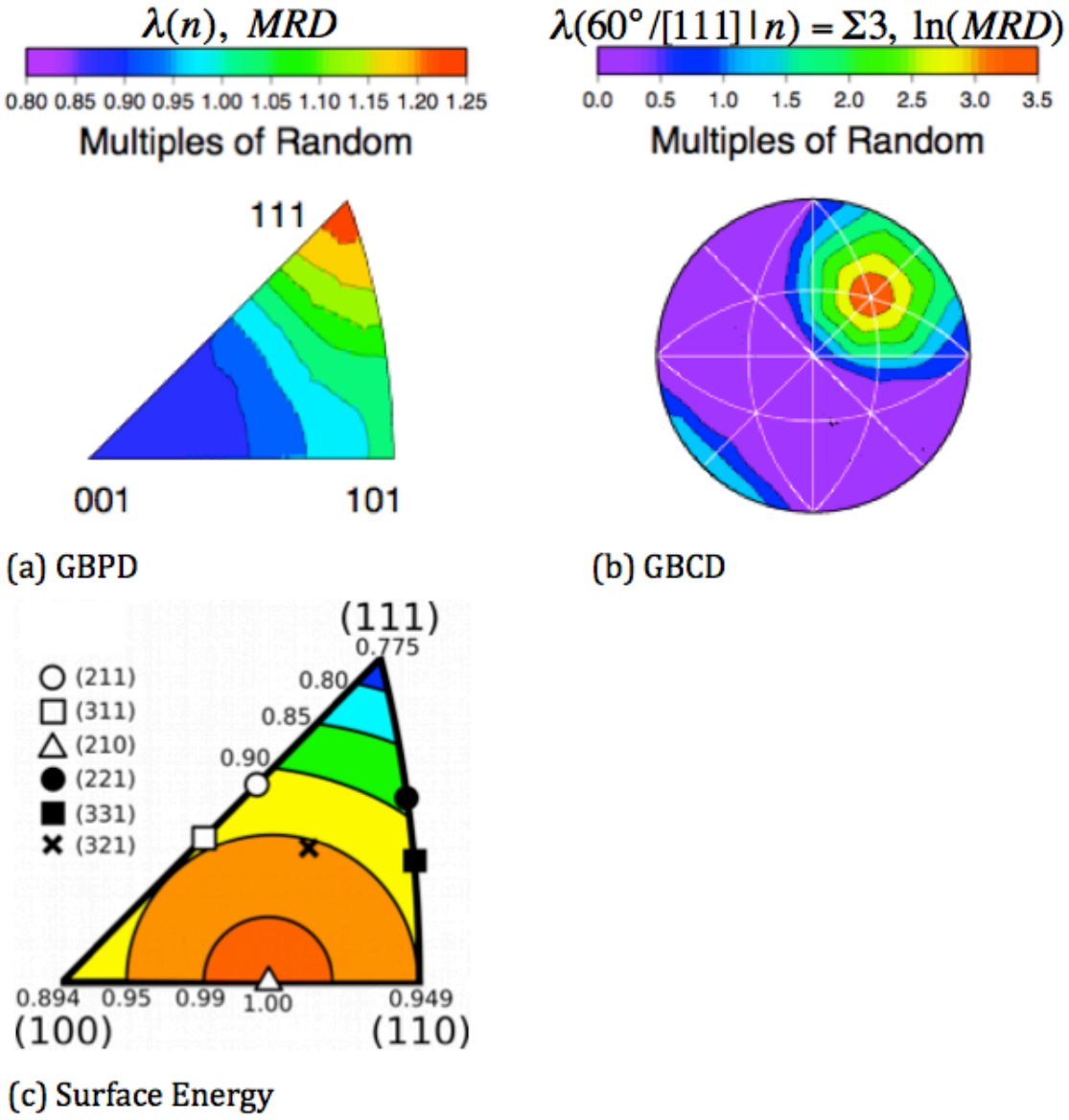

Figure 4.5. Grain boundary plane distributions of Al. (a) Grain boundary plane distributions (GBPD) calculated without considering the misorientation. (b) Grain boundary character distribution (GBCD) with a misorientation of 60° about [111]. (c) Surface energy calculated from the broken nearest neighbor bond in FCC metals. This figure was reproduced from reference [104]. Note that the energy unit in this figure is scaled with E (210) = 1.

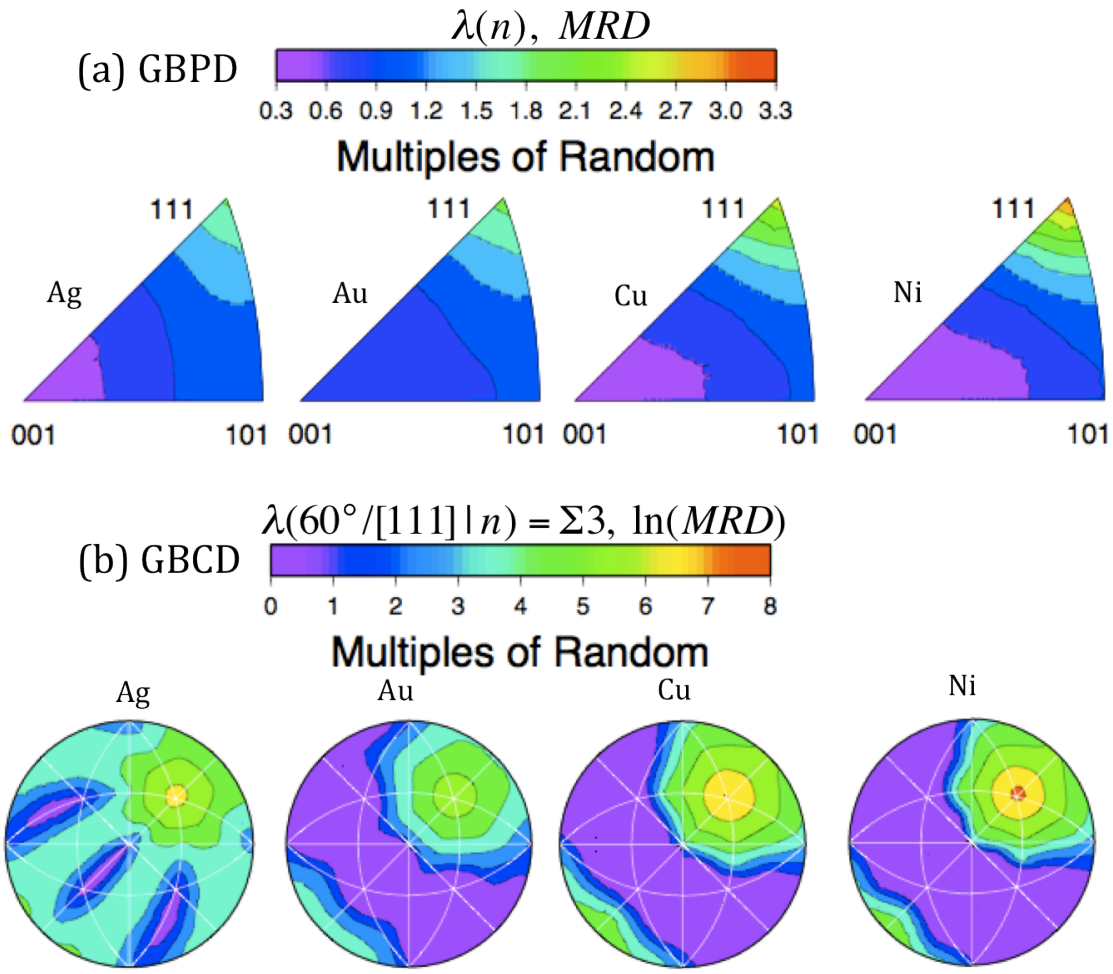

Figure 4.6. Grain boundary plane distributions of Ag, Au, Cu and Ni. (a) Grain boundary plane distributions (GBPD) calculated without considering the misorientation. (b) Grain boundary character distribution (GBCD) with a misorientation of 60° about [111].

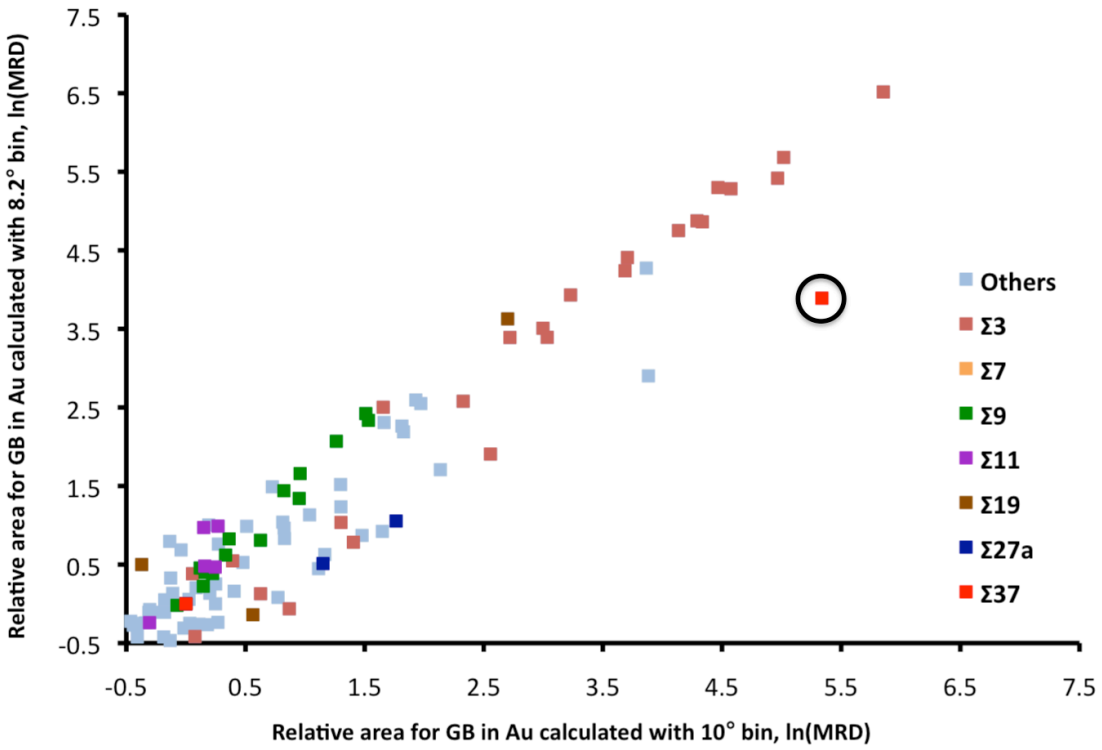

Figure 4.7. Comparison of GBCD in Au calculated with resolutions of 10° and 8.2°. Each point corresponds to the crystallographically identical grain boundary. The horizontal axis and vertical axis show the relative areas for grain boundary calculated with resolutions of 10° and 8.2°, respectively. Σ37 50.6° (111)[111] is highlighted by black circles.

The effects of the binning resolution and placement of the bin boundaries to the calculated GBCDs are illustrated in **Figure 4.7**. The apparent relative area of the coherent twin boundary is increased when the bin size is decreased. The relative areas of Σ9 boundaries with a 38.9° misorientation about the [110] axis also increase when the bin size is decreased. However the relative areas of the Σ27a boundaries with a 31.6° misorientation about the [110] axis decrease when the bin size is decreased. Because the misorientation angle of Σ9 (38.9°) is close to the Σ27a (31.6°) misorientation, the populations of Σ9 and Σ27a boundaries overlap and fall within the same bin when calculated with a binning resolution of 10°. When increasing the resolution to 8.2°, the populations of Σ9 boundaries increase and the populations of Σ27a decrease because the boundaries are classified in separate bins.

Furthermore, the placement of the bin also lowers the relative area of the Σ37 boundary. The Σ37 boundary has a 50.6° misorientation about the [111] axis. Because of the close proximity to the coherent twin, some of the coherent twins may be included when the resolution is 10°, but are excluded at 8.2°. As a result, the population of the Σ37 boundaries calculated with a 10° resolution is higher than when calculated with a resolution of 8.2°.

To compare the populations (P) of groups of grain boundaries with identical crystallographic parameters, we use the following procedure. The population range is discretized into bins of fixed width, Δ (in this case, Δ = 0.2 MRD). We then create a histogram by finding all of the boundaries in one data set that have populations between P and P+ Δ, and average these populations. In the next data set, we then find the average population of the set of boundaries that have the identical crystallographic parameters. Thus we have an ordered pair consisting of the average population of all of the boundaries in a fixed population range and the average population of the crystallographically identical boundaries in a second material. This procedure is repeated for each population range so that we can then examine correlations between the two data sets. The result of comparing the GBCD of Ni to the GBCDs of Al, Ag, Au, Cu is shown in **Figure 4.8**. In this case, the GBCD was discretized with 10° bins. The same comparison for the case of 8.2° bins is shown in **Figure 4.9**. Because the relative areas vary by more than three orders of magnitude, the natural logarithm of the relative area is plotted. As clearly shown in **Figure 4.8** and **Figure 4.9**, strong correlations among the FCC specimens are found for both resolutions. The correlations are quantified by the values in **Table 4.1**. These results provide evidence that the GBCDs of isostructural polycrystalline materials are correlated to each other regardless of the binning resolution.

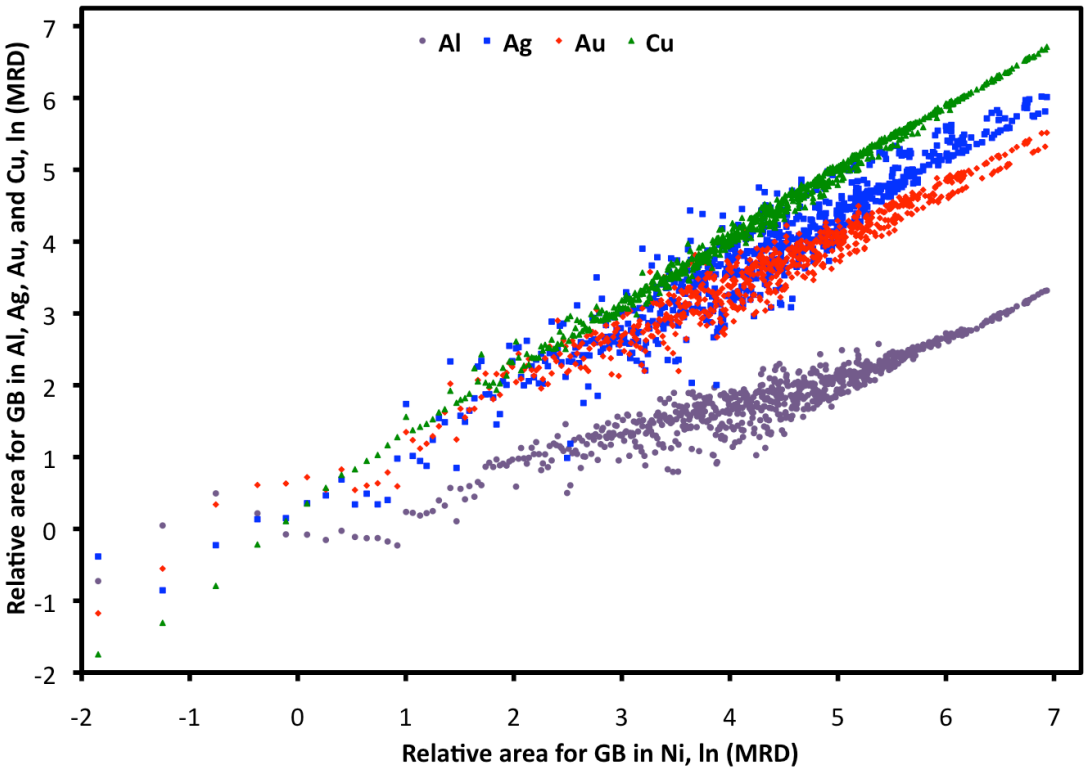

Figure 4.8. Comparison of GBCD calculated with a resolution of 10° in Al (violet), Ag (blue), Au (red), and Cu (green). The average grain boundary populations in Al, Ag, Au, and Cu are plotted with the average populations of the same boundaries in Ni.

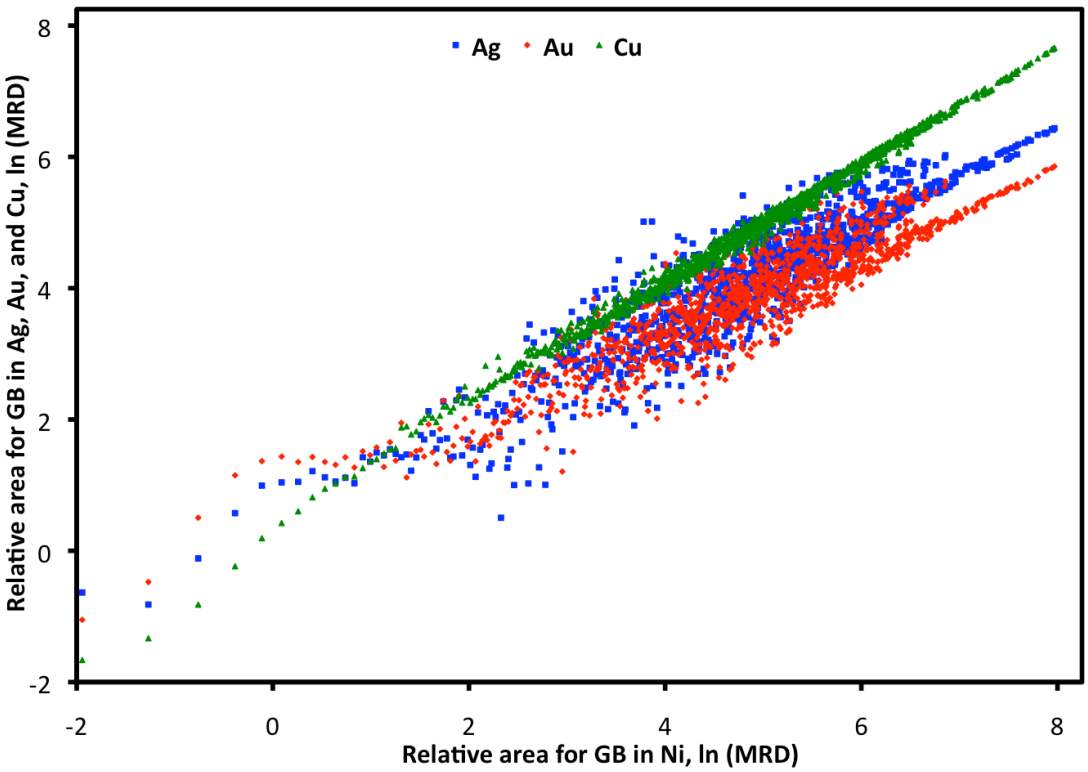

Figure 4.9. Comparison of GBCD calculated with a resolution of 8.2° in Ag (blue), Au (red), and Cu (green). The average grain boundary populations in Ag, Au, and Cu are plotted with the average populations of the same boundaries in Ni. Note that Al has been excluded from this comparison because the data set consists of only 76,707 line segments, which are not sufficient to calculate the GBCD with a resolution of 8.2°.

Table 4.1. The correlation coefficients for GBCD calculated with binning resolutions of 10° and 8.2°.

	Pearson 10°	Spearman 10°	Pearson 8.2°	Spearman 8.2°		Pearson 10°	Pearson 8.2°

Ni-Ag	0.96	0.95	0.90	0.91	ln(Ni)-ln(Ag)	0.96	0.92
Ni-Au	0.97	0.97	0.86	0.90	ln(Ni)-ln(Au)	0.97	0.92
Ni-Cu	1.00	1.00	1.00	1.00	ln(Ni)-ln(Cu)	1.00	1.00
Ni-Al	0.96	0.93	-	-	ln(Ni)-ln(Al)	0.94	-
Ag-Au	0.97	0.96	0.95	0.94	ln(Ag)-ln(Au)	0.97	0.95
Ag-Cu	0.97	0.95	0.92	0.92	ln(Ag)-ln(Cu)	0.96	0.93
Ag-Al	0.95	0.93	-	-	ln(Ag)-ln(Al)	0.94	-
Au-Cu	0.98	0.96	0.87	0.90	ln(Au)-ln(Cu)	0.97	0.92
Au-Al	0.98	0.96	-	-	ln(Au)-ln(Al)	0.96	-
Cu-Al	0.96	0.91	-	-	ln(Cu)-ln(Al)	0.93	-

Table 4.2. Population fractions of general boundaries, Σ3, Σ9, Σ27a, Σ27b, and coherent twin boundary of the FCC specimens. The fractions of the general boundaries are defined as the total fraction of the other boundaries, which are not Σ3, Σ9, Σ27a, and Σ27b boundaries.

Boundary Types	Al	Au	Cu	Ni	Ag
General Boundaries (%)	96.20	71.09	46.77	50.78	41.86
Σ3 (%)	3.54	27.31	48.33	44.53	54.59
Σ9 (%)	0.19	1.40	3.87	3.72	3.18
Σ27a (%)	0.03	0.13	0.65	0.58	0.26
Σ27b (%)	0.04	0.07	0.38	0.39	0.11
Coherent twin boundary (%)	0.90	8.79	18.69	20.81	16.77

Considering that we have about 300,000 line segments and 6,561 distinguishable bins of grain boundaries with resolution of 10°, 1 MRD is then equivalent to 46 line segments in a bin. For statistical comparisons, a reasonable threshold would be about 10 line segments per bin or 0.5 MRD for Ag, Cu, and Ni.

For Al and Au, which contain many fewer Σ3 boundaries, 0.5 MRD corresponds to approximately 6 and 17 line segments, respectively. In the analysis that follows, we used grain boundary populations calculated with a bin size of 10°.

Among all possible grain boundaries in Al, Ag, Au, Cu, and Ni, there were 1,497 different boundaries with populations greater than 0.5 MRD in both materials and these are the data on the plot in **Figure 4.10**. Note that while there is some averaging in the result shown in **Figure 4.8** and **Figure 4.9**, **Figure 4.10** shows a direct point-by-point correlation. The horizontal axis shows the relative area in Ni and the vertical axis shows the relative areas for the same boundary in Al, Ag, Au, and Cu. As shown in the plot, the grain boundary populations fall along straight lines, especially for high MRD. This indicates that there are strong correlations among the distributions in FCC metals. There is more scatter for the low population boundaries because these boundaries are observed less frequently and the populations might be not determined as accurately. This scatter is absent in the plots shown in **Figure 4.8** and **Figure 4.9** because of the averaging scheme that is used. As clearly shown in **Figure 4.10**, the correlation between Al and Ni has the most scatter, which is quantified by the relatively low value (0.38) of the Spearman correlation (see **Table 4.3**). The Spearman correlations are high for Ni-Au, Ni-Cu, and Au-Cu, but lower for Ni-Ag, Ag-Au, Ag-Cu, Ag-Al, Au-Al, and Cu-Al. The Al specimen was the least pure and was annealed at much higher homologous temperature (T_H = 0.72) than the other specimens (T_H = 0.4). It is expected that the purity and the annealing temperature could influence the GBCD and weaken the correlation with the other specimens.

It also should be noted that Ag has a very different microstructure and crystallographic texture compared with ones of Au, Cu, and Ni (see **Figure 4.1**, **Figure 4.2**, and **Figure 4.3**). While the microstructures of Ag, Au, Cu, and Ni are composed of parental grains with multiple twin lamellae, Ag has much larger parental grains and much finer twin lamellae. In addition there are many more

island grains in Ag than in Au, Cu, and Ni. The Ag specimen has a uniquely strong texture, which might be dominated by a few large grains (see **Figure 4.1a**). As a result, the GBCD correlation between Ag and the other FCC metals (Au, Cu, and Ni) are lower than those of Ni-Au, Ni-Cu, and Au-Cu.

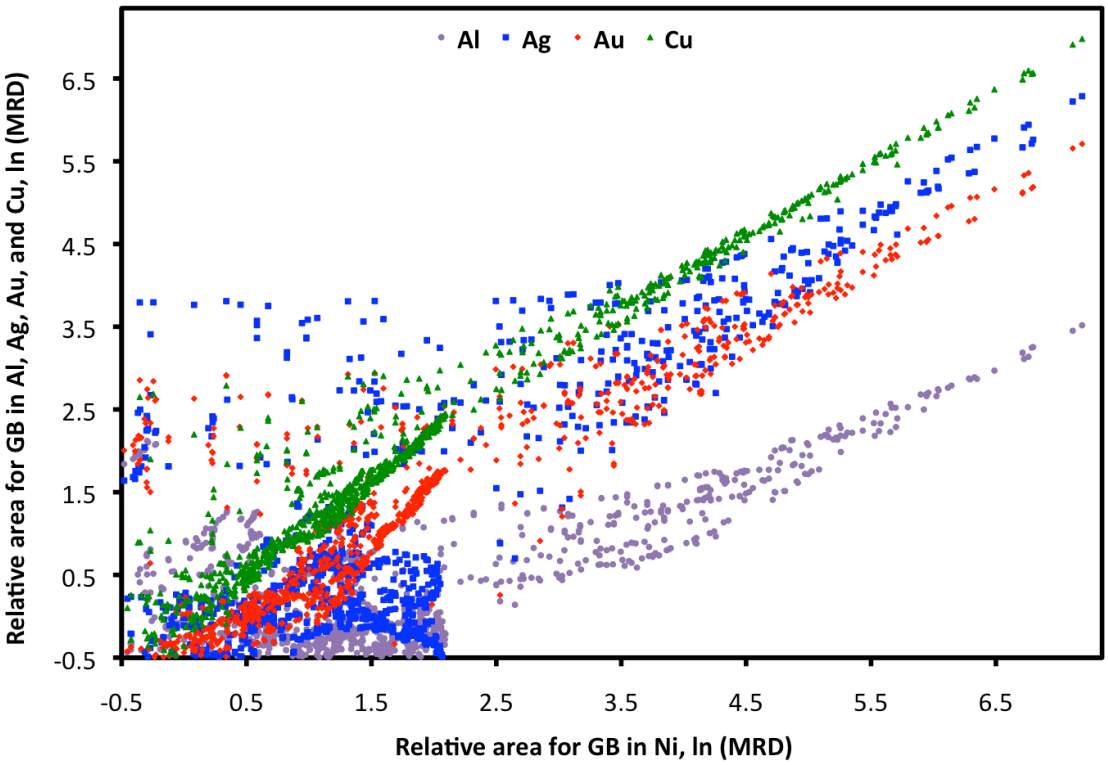

Figure 4.10. Comparison of GBCDs calculated with a resolution of 10° for Al (violet), Ag (blue), Au (red), and Cu (green) with relative area greater than 0.5 MRD. Each point corresponds to two identical grain boundary types in two materials. The horizontal axis shows the relative areas in Ni and the vertical axis shows the relative areas in Ag, Au, and Cu for the same boundary type.

Table 4.3. The correlation coefficients and slopes for GBCD of Al, Ag, Au, Cu, and Ni.

All GBs > 0.5 MRD	Pearson Correlation	Spearman Correlation		Pearson Correlation	Slope
Ni-Ag	0.97	0.55	ln(Ni)-ln(Ag)	0.80	0.77
Ni-Au	0.97	0.84	ln(Ni)-ln(Au)	0.90	1.05
Ni-Cu	0.99	0.96	ln(Ni)-ln(Cu)	0.98	0.99
Ni-Al	0.92	0.38	ln(Ni)-ln(Al)	0.64	1.17
Ag-Au	0.99	0.74	ln(Ag)-ln(Au)	0.90	1.10
Ag-Cu	0.98	0.65	ln(Ag)-ln(Cu)	0.84	0.89
Ag-Al	0.92	0.51	ln(Ag)-ln(Al)	0.76	1.43
Au-Cu	0.99	0.90	ln(Au)-ln(Cu)	0.93	0.81
Au-Al	0.93	0.56	ln(Au)-ln(Al)	0.74	1.15
Cu-Al	0.93	0.40	ln(Cu)-ln(Al)	0.62	1.12

4.4 Discussion

The central hypothesis that the GBCDs of isostructural materials with comparable microstructures are statistically correlated was tested. While we found a very high correlation among the high purity FCC metals with moderate stacking fault energy (Ni, Au, and Cu). Ag, with the lowest stacking fault energy among FCC specimens, has moderate correlation to the other FCC metals. The Ag microstructure

consists of a few large grains that contain many parallel twin lamellae, as shown in the EBSD map (**Figure 4.1a**). As a result, there are fewer non-Σ3 boundaries in the microstructure than was found in the other metals (see **Table 4.2**). Furthermore, the Σ3 boundaries in Ag are internal to the grains. Therefore, they do not impact the overall network in the same way as in the other metals. These characteristics are likely to contribute to the observed weak correlation between Ag and the other metals. In addition, the strong texture of Ag could also result in a different GBCD compared with ones of Au, Cu, and Ni. Because the misorientation angle distributions of the specimens are influenced by the texture and grain morphology, we will first calculate the misorientation angle distributions for all specimens. As shown in **Figure 4.11**, length fractions, which were normalized by the expected length from the random misorientation angle distribution, are plotted versus the misorientation angle in a unit of multiple of a random (MRD). The peak maxima in Ag, Au, Cu, and Ni (**Figure 4.11a**) are significantly higher than those of Al. The misorientation distribution of Cu and Ni have strong peak magnitudes at the 38° and 59°, which correspond to the highly populated boundaries of the Σ9 and Σ3 misorientations respectively. In contrast, the maxima in Ag and Au have weaker magnitudes and are broader than the ones in Cu and Ni. The misorientation angle distribution of Al has peak maxima around 45°, which is similar to the misorientation distribution of randomly oriented crystals known as the Mackenzie distribution (**Figure 4.11b**) [105].

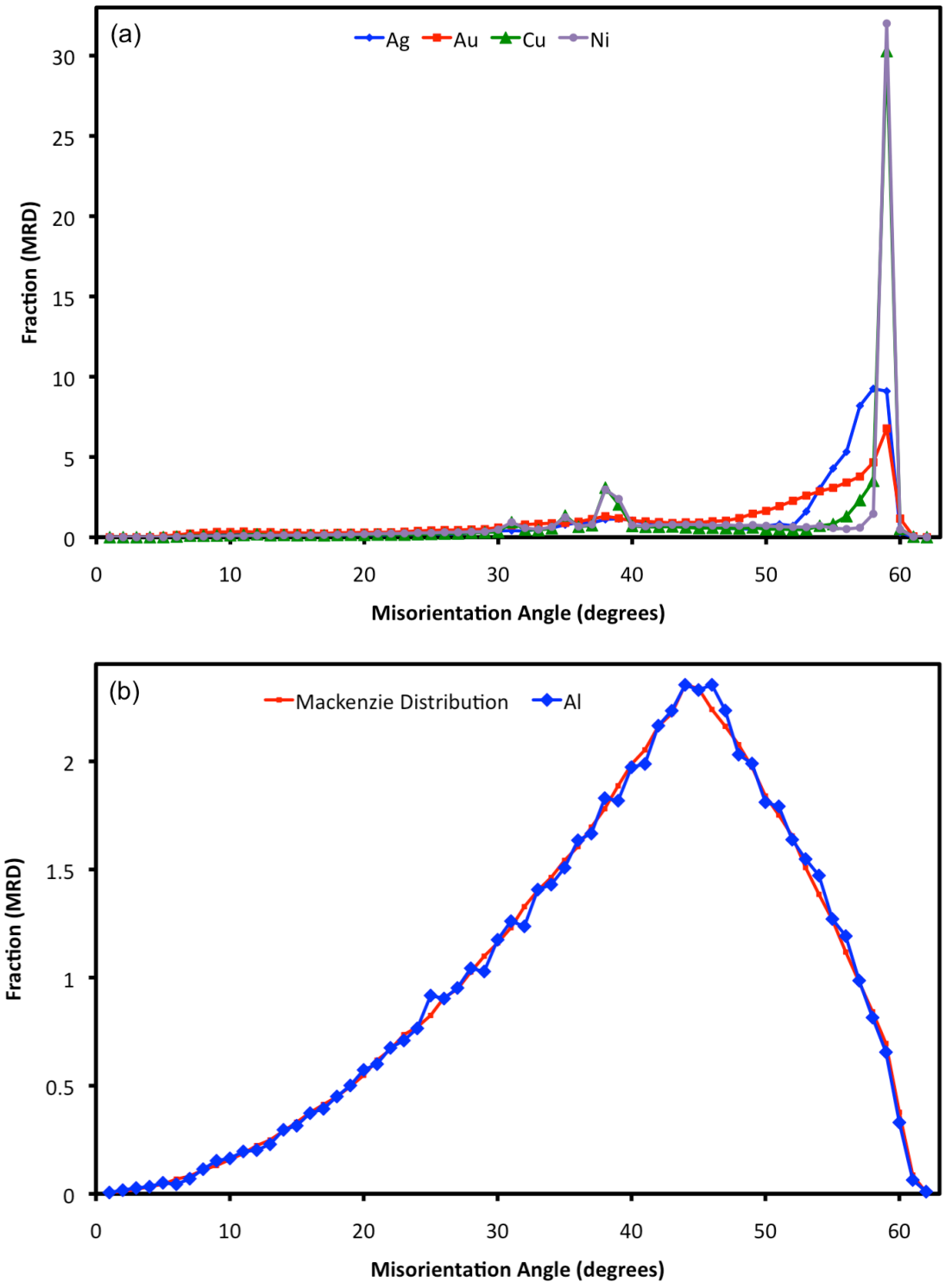

Figure 4.11. Misorientation angle distribution, (a) Ag (blue), Au (red), Cu (green), and Ni (violet), and (b) Al (blue) and the Mackenzie distribution (red).

Because the misorientation angle distribution is a one-dimensional projection of the five macroscopic parameters of grain boundary space, the similarity of the distributions in Cu and Ni is associated with the fact that the GBCDs of Cu and Ni were strongly correlated. However it is not clear why the misorientation distribution of Ag and Au are different from those of Cu and Ni. To clarify this, we will investigate the texture intensity and grain morphology of the specimens. To quantify the texture, we will calculate and compare the texture strength and the standard deviation of the crystallographic texture of the specimens. In addition, the number of the nearest neighbor (NNN) grains will be used to characterize the grain morphology. For the crystallographic texture analysis, we examined the inverse pole figures (**Figure 4.3**). Based on the inverse pole figure files (ipf1.gpf, ipf2.gpf, and ipf3.gpf), which were generated by the WTS2POP code, we calculated the minimum, maximum, and standard deviation of the values and listed them in **Table 4.4**. Interestingly, when one considers how the fraction of observations is distributed by texture strength, the texture strength in Al, Au, Cu and Ni (see **Figure 4.12**), which resemble normal distributions, have much lower texture strengths and standard deviations than Ag (see **Table 4.4**).

Table 4.4. The average, minimum, maximum, and the standard deviation of the crystallographic textures for all specimens. Note NNN is stand for the number of nearest neighbor grain. Ag2 is the Ag data when resolution was coarsened to the 8 times of the original step size.

Materials	Minimum (MRD)	Maximum (MRD)	Standard Deviation	Average NNN
Al	0.01	7.03	0.88	-
Ag	0.01	21.52	1.44	4.17
Au	0.16	3.39	0.64	5.38
Cu	0.29	7.89	0.87	5.03
Ni	0.25	3.70	0.29	5.52
Ag2	0.01	18.24	1.31	4.80

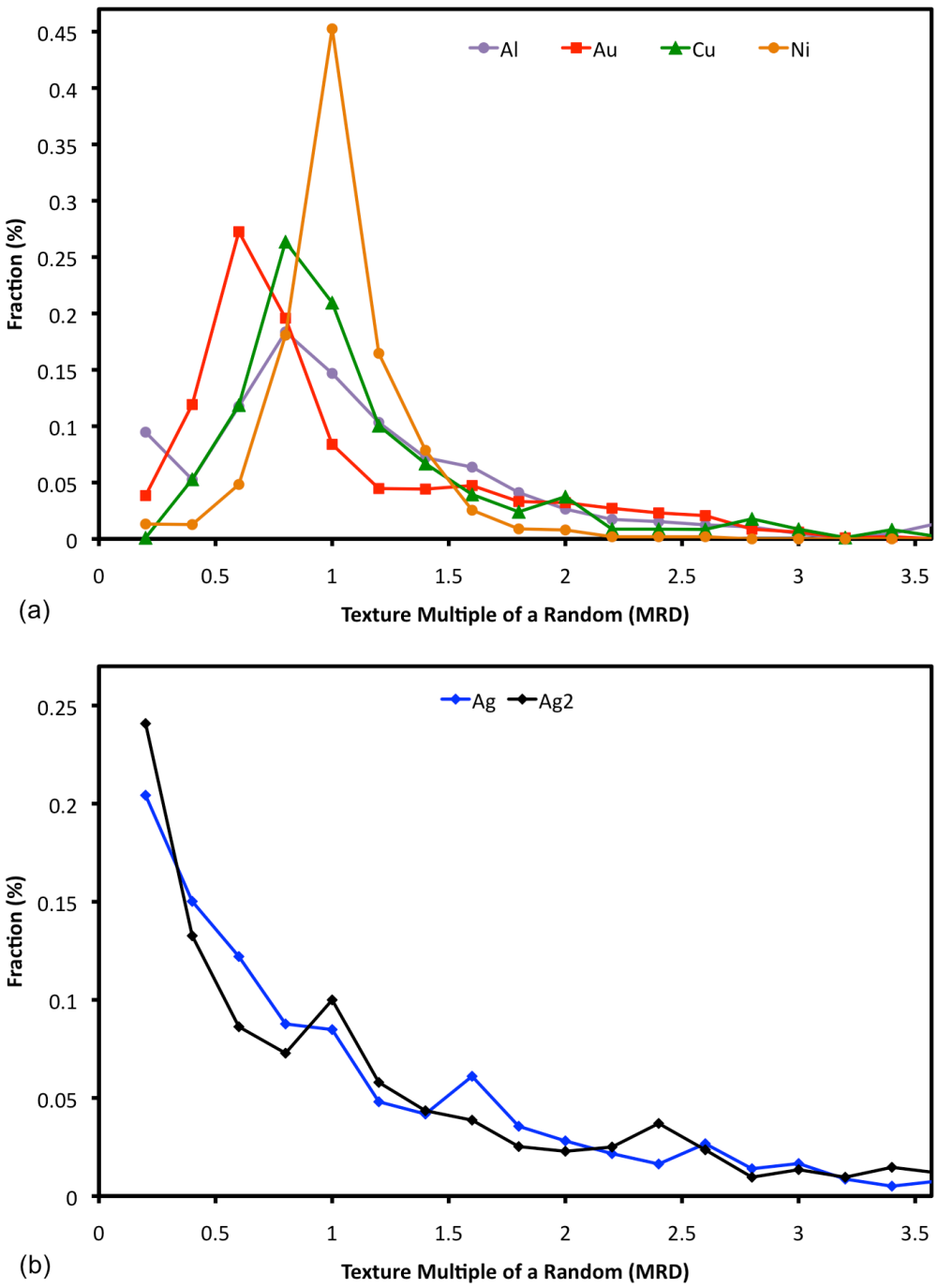

Figure 4.12. The fraction of bins in the IPF with different texture strengths for (a) Al, Au, Cu, and Ni, (b) Ag and Ag2. The horizontal axis represents the texture strength in units of multiples of a random (MRD), while the vertical axis indicates the fraction of bins with that strength, in percent.

Although the texture strength of Cu (7.89 MRD) is approximately twice of those in Au (3.39 MRD) and Ni (3.70 MRD), the Spearman correlation coefficient of Au-Cu and Ni-Cu are very strong (see **Table 4.3**). The GBCD of Ag, which has a distinct texture (21.52 MRD), is less correlated to the other high purity FCC specimens (**Table 4.3**). However, these maximal values may be outliers so it is more reliable to the use the width of distribution as measure of similarity. The standard deviation of the texture values for Ag (1.44 MRD) is significantly larger than those of the other metals, which range from 0.29 MRD to 0.88 MRD. These results suggest that the strong GBCD correlation of FCC specimens occurs if the standard deviations of the texture distributions are less than 1 MRD and the maximal values are less than 8 MRD. Note that the actual limit was not determined in this study and further study would be needed to establish a more well-defined limit. It should be noted that the average number of the nearest neighbor grains (NNN) in Ag is the lowest among the FCC materials (4.17, compared to more then 5 in the others), which indicated that the grain morphology in Ag is distinguishably different from the rest of the specimens. In addition, the plot in **Figure 4.13** indicates that Ag contains a higher fraction of island grains with the numbers of nearest neighbor grain equal to one, two, or three. An attempt was made to eliminate the island grains by artificially reducing the resolution of the EBSD maps. The resolution was coarsened by a factor of eight and the results from this coarser data set are referred to in this thesis as Ag2. The average NNN in Ag was increased from 4.17 to 4.80 by this coarsening procedure, but it is still lower than for the other materials, as shown in **Table 4.4**. The distribution of nearest neighbors in the Ag with the coarsened step size (Ag2) is more like Au and Cu than the original data, but still differs, as shown in **Figure 4.13**. Furthermore, we found that GBCDs of Σ3 boundaries for Ag and Ag2 calculated with a normal GBCD calculation are comparable, as in **Figure 4.14a** and **Figure 4.14b**. However, the distribution of texture strength for Ag2, shown in **Figure 4.12b**, differs insignificantly from the Ag data set. In other words, attempts to artificially make the grain shapes in the Ag data set comparable to those in the Au, Cu, and Ni were largely unsuccessful. The texture can affect the results in another way, and this is discussed below.

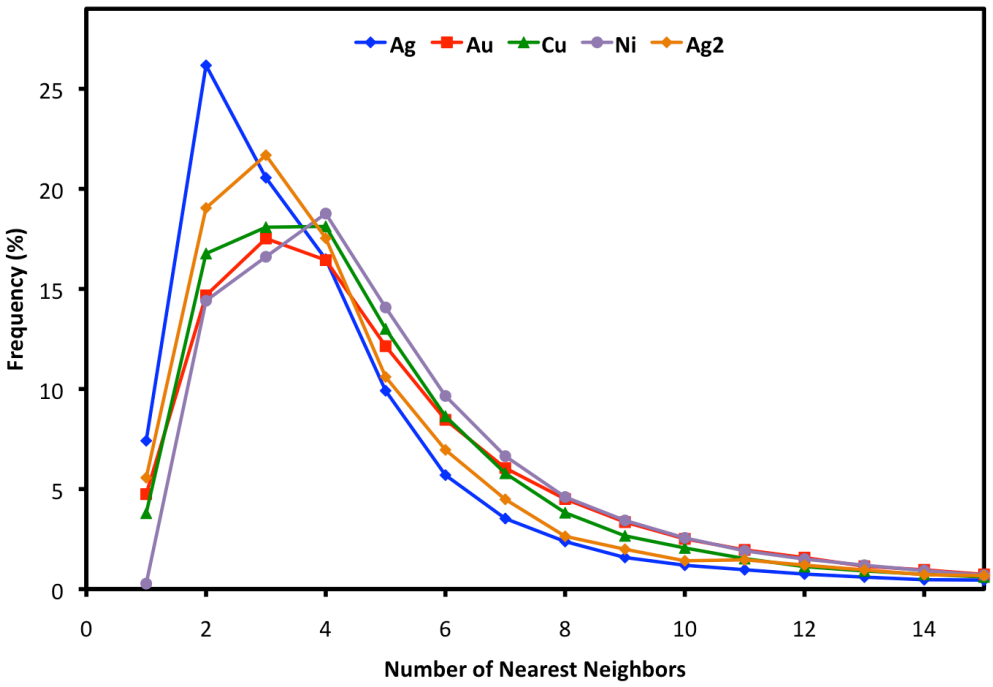

Figure 4.13. The frequency distributions of the number of nearest neighbor grain for all specimens. The horizontal axis represents the number of nearest neighbors while the vertical axis indicates the frequency. Note Ag2 is the Ag data when the resolution was coarsened to eight times of the original step size.

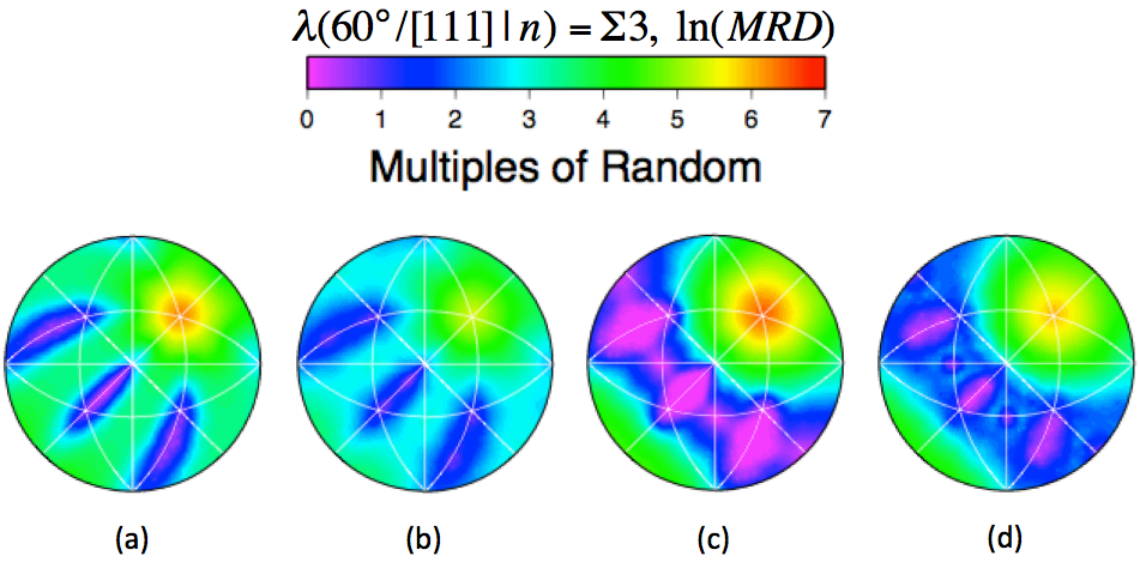

Figure 4.14. Grain boundary character distribution (GBCD) with a misorientation of 60° about [111]: (a) Ag and (b) Ag2 without texture correction, (c) Ag and (d) Ag2 with texture correction.

It should be pointed out that the Ag and Ag2 data sets have 16 fields of view. In Ag2 data set, there are only 4,253 grains, of which 31 grains have grain size greater than 20,000 μm^2 and contribute to 33% of the total area. Because most of the small grains were the twin lamellae, which were formed within a large grain, the unusual pole figure of Ag in **Figure 4.2** derives from a relatively small number of large grains. The stereological calculation of the GBCD assumes that the grain orientations are uniformly distributed at each misorientation. However, this is not the case for the textured materials. To minimize the influence of strong texture that could bias the stereological calculation, the programs calc_gbcd_stereo_cor_1 and orient_pref_1 (version 05/27/2011) were use to calculate GBCDs [95]. The details of the calculation are in Appendix A, but we also summarize the procedure here. First, the orient_pref_1 program calculates a texture correction factor in the following way. For each misorientation, the number of times each grain orientation occurred is recorded and tabulated. By repeating for every line segment, the distributions of grain orientation at each misorientation are obtained. Next, the distributions of grain orientations are normalized separately for each misorientation. The texture correction factor is then assigned to the inverse of the orientation distribution. While observations of grain boundaries are weighted only by line length in calc_gbcd_stereo, observations of grain boundaries in calc_gbcd_stereo_cor_1 are weighted by the multiplication of the line lengths and a correction factor that adjusts the length to account for non-uniform sampling.

The distributions of grain boundary planes for Σ3 boundaries in Ag and Ag2, were calculated with the texture correction, as depicted in **Figure 4.14c** and **Figure 4.14d**, reveal that the populations of the incoherent Σ3 twin boundaries in Ag and Ag2 are decreased. In addition, these distributions are similar to the ones of Cu and Ni (**Figure 4.15**). Note that the Ag2 data set has only 16,069 line segments, which is much lower than the minimum requirement of 50,000 lines for the GBCD calculation with a bin resolution of 10° [14][16]. Nevertheless, the comparison between the high populations for Σ3 misorientation in Ag and Ag2 is deemed to be reliable.

It should be pointed out that the texture strength in Ag2 (18.24 MRD) is still very high compared with the other FCC specimens (see **Table 4.4**), and the same is true for the standard deviation of the texture (1.31 MRD). Consider the fact that Ag2 has similar grain morphology to those of Au, Cu, and Ni (see **Figure 4.13**), the results in **Figure 4.14** suggest that the grain boundary morphology influences the GBCD less than the crystallographic texture (**Table 4.4**).

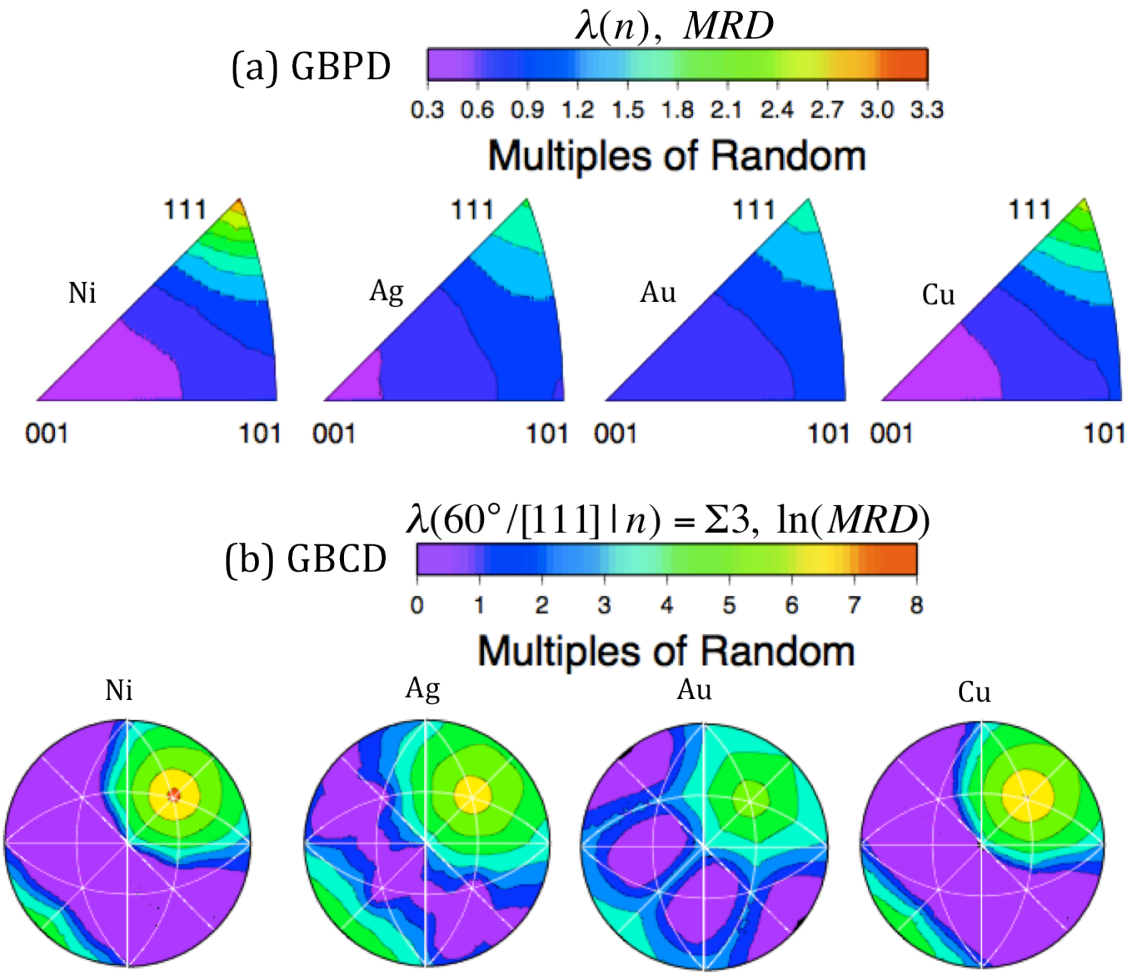

Figure 4.15. Grain boundary plane distributions with texture correction in Ag, Au, Cu and Ni. (a) Grain boundary plane distributions (GBPD) calculated without considering the misorientation. (b) Grain boundary character distribution (GBCD) with a misorientation of 60° about [111].

We calculated the GBPD with the texture correction code with 10° bins for all of the FCC materials. **Figure 4.15a** shows the stereographic projections of the GBPDs in Ni, Ag, Au, and Cu. The GBPDs are similar to the GBPDs calculated with the normal GBCD scheme (see **Figure 4.6a**). **Figure 4.15b** shows the grain boundary plane distributions for boundaries with a misorientation of 60° about [111] axis. The highest peaks are all located at the position of the coherent twin boundary for all FCC specimens, which are also similar to the GBCDs calculated with the normal GBCD code in **Figure 4.6b**. We observed that the populations of incoherent twin boundaries in Ag are decreased and the resultant distribution is similar to the ones of Ni and Cu. We also found that the distribution of incoherent twin boundaries in Au is slightly different from the ones calculated without the texture correction. This indicates that the brass texture could result in the non-uniform distribution of in-plane angle in the Au specimen. **Figure 4.16** shows the grain boundary plane distributions (GBPD) in Al. Both of the grain boundary plane distributions of Al in **Figure 4.16** are very similar to the ones calculated with the normal GBCD calculation (see **Figure 4.5a**).

To examine the difference between GBCD calculated with and without texture correction for all grain boundaries in the five-parameter grain boundary space, we extract the relative areas of grain boundaries with a binning resolution of 10°. Grain boundaries, which have GBCD greater than 0.5 MRD, are selected for statistical comparison. **Figure 4.17a** shows the comparisons of GBCDs in Ni calculated with and the without texture correction. The linear relationship in the plot suggests that the magnitude of correction factor is low for the weak texture of annealed Ni. We also observed the similar linear relationship in the weak texture of annealed Cu (see **Figure 4.17b**). For Ag with strong texture, GBCD calculated with texture correction shows significant large deviations from the linear relationship in **Figure 4.17c**. The large deviation corresponds to the low intensity of the incoherent twin boundaries in Ag (**Figure 4.15b**), and results in a low correlation coefficient (see **Table 4.5**).

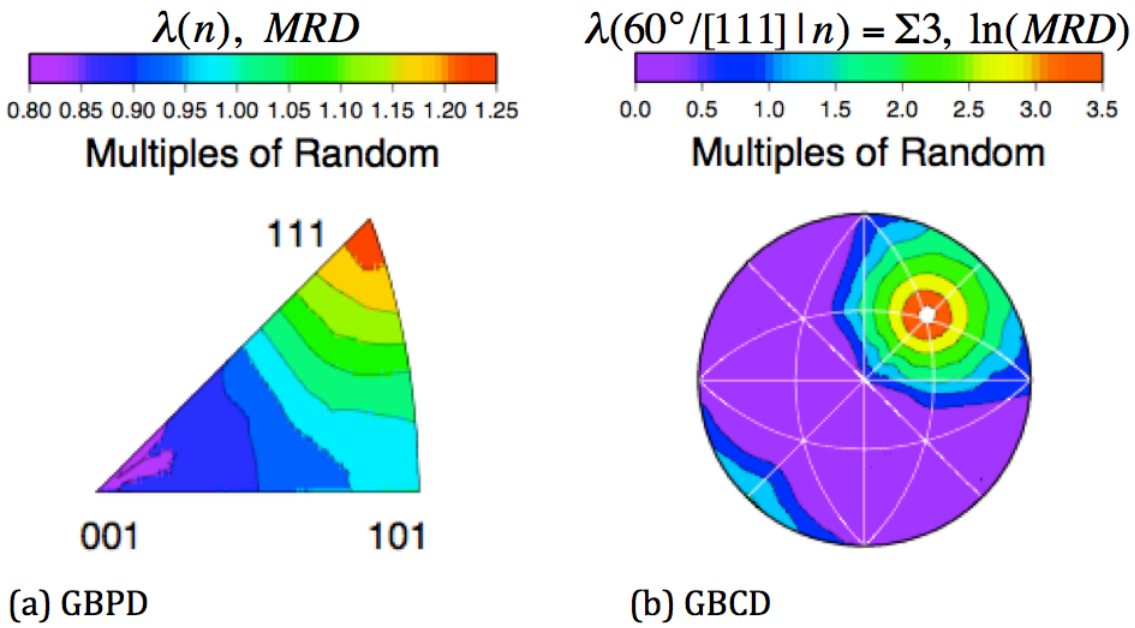

Figure 4.16. Grain boundary plane distributions of the texture correction for Al. (a) Grain boundary plane distributions (GBPD) calculated without considering the misorientation. (b) The distribution of grain boundary planes for boundaries with a misorientation of 60° about [111].

Table 4.5. The correlation coefficients for GBCDs calculated with and without texture correction in Ni, Ag, Au, Cu, and Al.

All GBs > 0.5 MRD	Pearson Correlation		Pearson Correlation	Spearman Correlation
Linear-Ni	1.00	Log-Ni	0.99	0.98
Linear-Ag	0.98	Log-Ag	0.85	0.70
Linear-Au	0.99	Log-Au	0.92	0.88
Linear-Cu	1.00	Log-Cu	1.00	0.99
Linear-Al	0.98	Log-Al	0.97	0.95

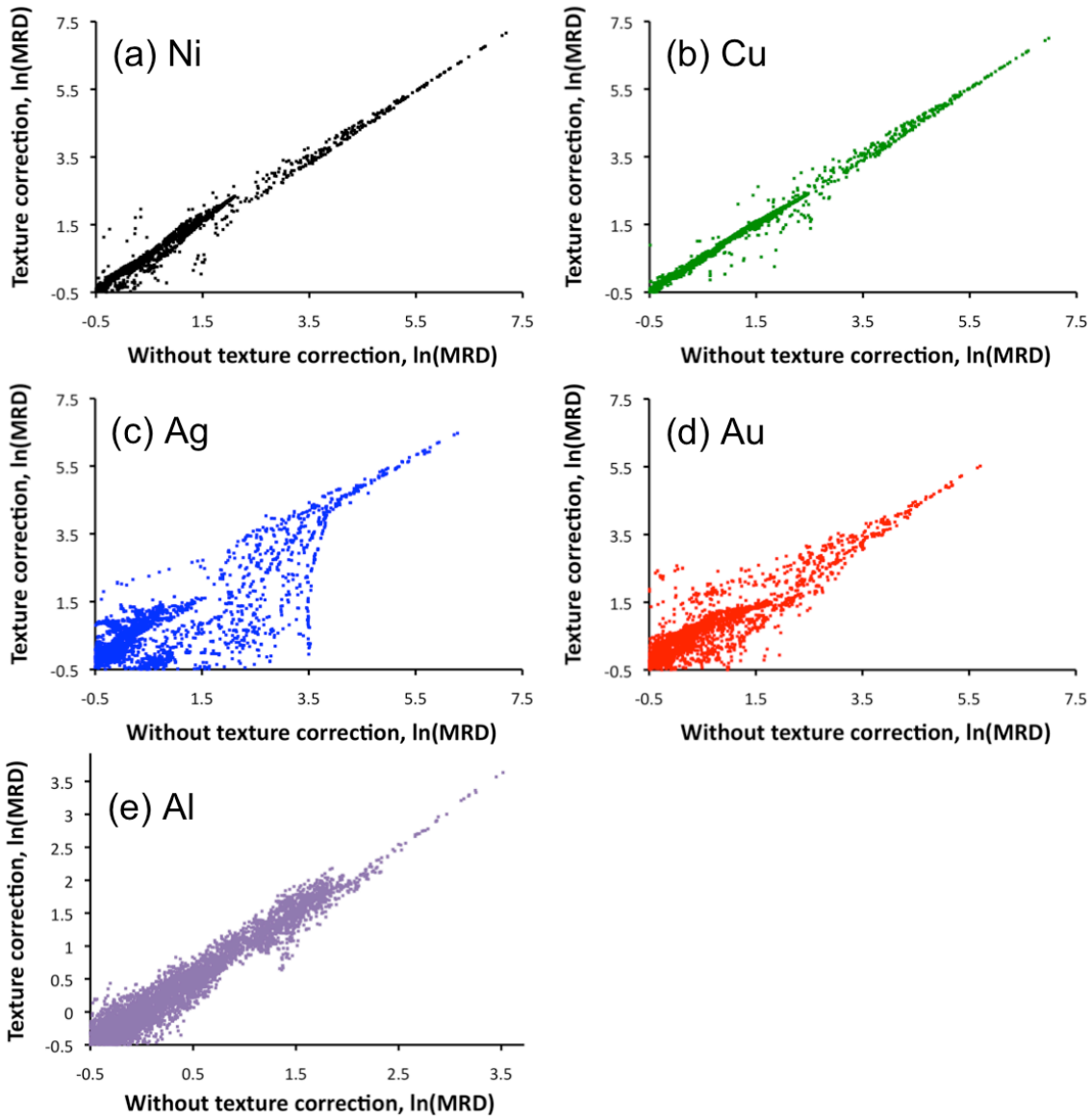

Figure 4.17. Comparison of the relative areas of grain boundaries calculated with and without the texture correction in (a) Ni, (b) Cu, (c) Ag, (d) Au, and (e) Al. Each point corresponds to the same grain boundary, for all boundaries with populations greater than 0.5 MRD. The horizontal axis shows the GBCD calculated without texture correction and the vertical axis shows the GBCD calculated with texture correction.

The comparison between the GBCDs of Au calculated with and without the texture correction is plotted in **Figure 4.17d**. Even though it is a linear relationship,

there is considerably more scatter than for Ni and Cu in **Figure 4.17a**, and **Figure 4.17b**, respectively. This indicates that the (110)[112] brass texture affects the stereological calculation and the true GBCD of Au. The comparison between GBCDs of Al calculated with and without texture correction is plotted in **Figure 4.17e**. There is a strong linear correlation, which is comparable with the one of Ni and Cu. For all of the FCC specimens, we have observed that the maxima are at the coherent twin boundary for both of the GBCDs calculated with and without texture correction. There are slight deviations of the correlation at the lower populations, which depend on the texture strengths in each specimen. The Spearman correlation coefficients of the weakly textured specimens (Ni, Cu, Au, and Al) are nearly perfect, while the correlation coefficient in Ag with stronger texture is 0.70 (see **Table 4.5**). This result revealed that those differences of the GBCDs calculated with and without the texture correction are correlated to degree of texture, as expected. The effect of texture on the GBCD calculation might be a factor that contributes to the weak correlation with the other FCC metals. However, even if the GBCD calculation were perfect, we would still expect textured and untextured FCC materials to have different GBCDs.

It should be noted that while the crystallographic texture affects the stereological GBCD calculation, it does not alter the conclusion that the GBCDs of FCC metals are correlated for specimens with similar microstructures, i.e. textures and grain shapes, as shown in **Figure 4.18**. The examples described here suggest that texture is more influential than grain shape and that the standard deviation of the texture strength must be less than 1.0. Because Al is not high purity (and the data set contains fewer observations) and Ag has a distinct microstructure and crystallographic texture, we will consider only Au, Cu, and Ni for the further analysis.

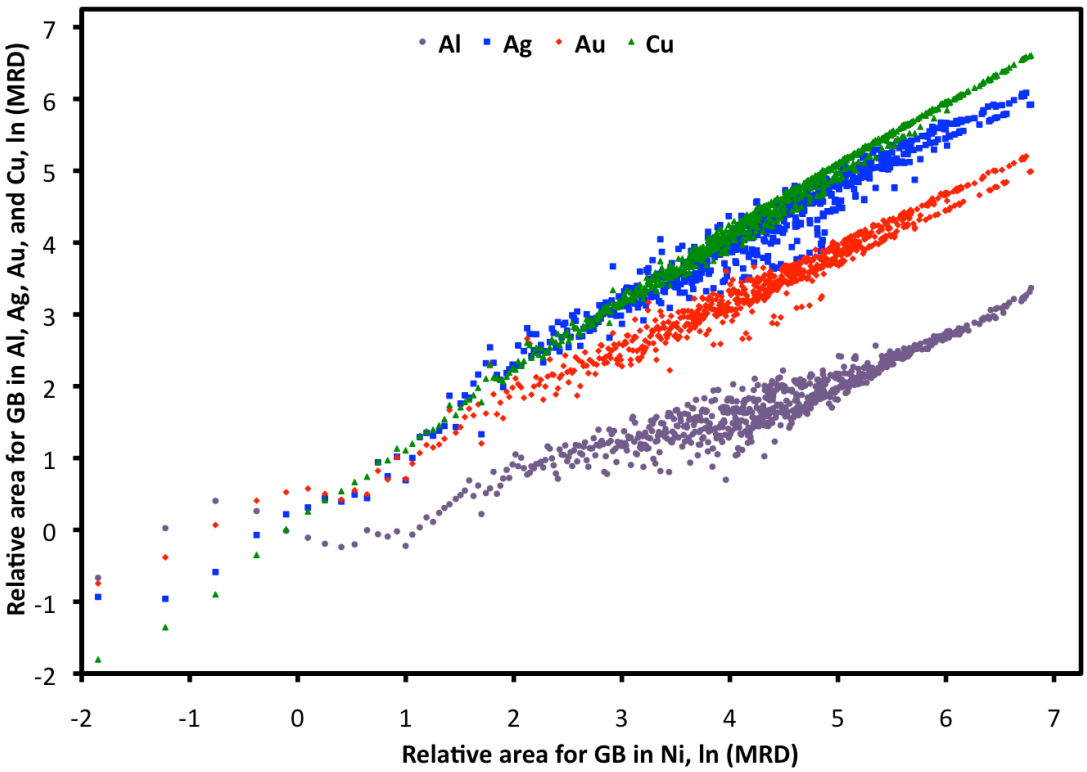

Figure 4.18. Comparison of the texture corrected GBCDs calculated with a resolution of 10° for Al (violet), Ag (blue), Au (red), and Cu (green). The average grain boundary populations in Al, Ag, Au, and Cu are plotted with the average populations of the same boundaries in Ni.

The relative areas for grain boundaries in Au, Cu, and Ni were derived from the normal GBCD calculation (calc_gbcd_stereo) with a binning size of 10° [95]. Among the 1,956 different boundaries with populations greater than 0.5 MRD, there are 159 Σ3 boundaries and 282 Σ9 boundaries. Those data are plotted in **Figure 4.19**. The horizontal axis shows the relative area in Ni and the vertical axis shows the relative areas for the same boundary in Au and Cu. As shown in the plot, the Σ3 boundaries in Au are more scattered than ones in Cu; nonetheless, the Σ3 boundaries in both Au and Cu monotonically increase with respect to the grain boundary population in Ni. The relative areas for incoherent twin boundaries in Au and Cu, which correspond to those observations with ln(MRD) between -0.5 and 1.5 in Ni, show more scatter around the linear relationship. The relative areas of Σ9 and Σ27 boundaries have lower populations than the Σ3 boundaries, but still show

strong correlations. The Spearman correlations of Ni-Au, Ni-Cu, and Au-Cu are nearly perfect for Σ3, Σ9, and Σ27 boundaries (see **Table 4.6**). Note that the Σ27 boundary classification includes both Σ27a, 31.6°/[110], and Σ27b, 35.4°/[210]. There are a lot of highly populated grain boundaries, which are classified as "Others", because those grain boundaries have relative populations comparable to the Σ3 boundary. In fact, these boundaries have high populations because they are crystallographically "close" to the Σ3 misorientation. To examine this assumption, we excluded Σ3 boundaries and repeated the GBCD calculation. **Figure 4.20** shows the GBCD comparison in Au, Cu, and Ni. The grain boundaries labeled "Others", which have relatively high populations in **Figure 4.19**, do not appear in **Figure 4.20**. This result validates the assumption that those labeled "Others" are related to the discretization of the calculation.

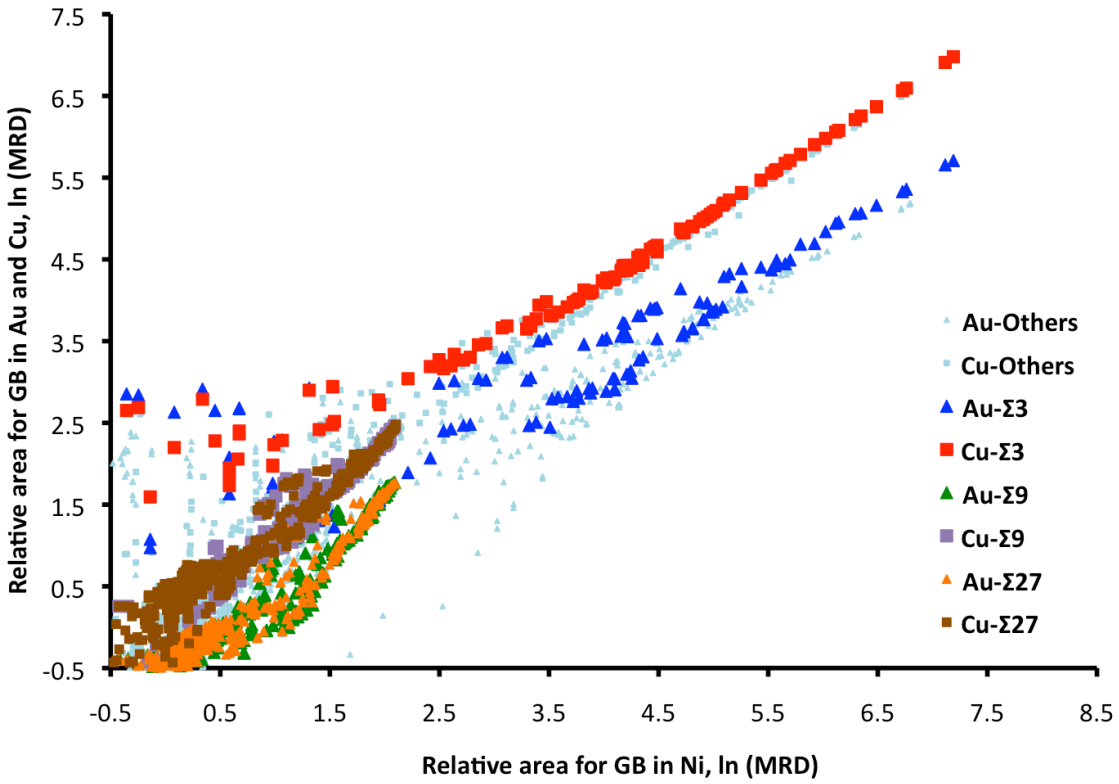

Figure 4.19. Comparison of GBCDs in Au, Cu, and Ni with populations greater than 0.5 MRD. Each point corresponds to two crystallographically identical grain boundaries in two different materials. The horizontal axis shows the relative area in Ni and the vertical axis shows the relative area in Au or Cu for the same boundary.

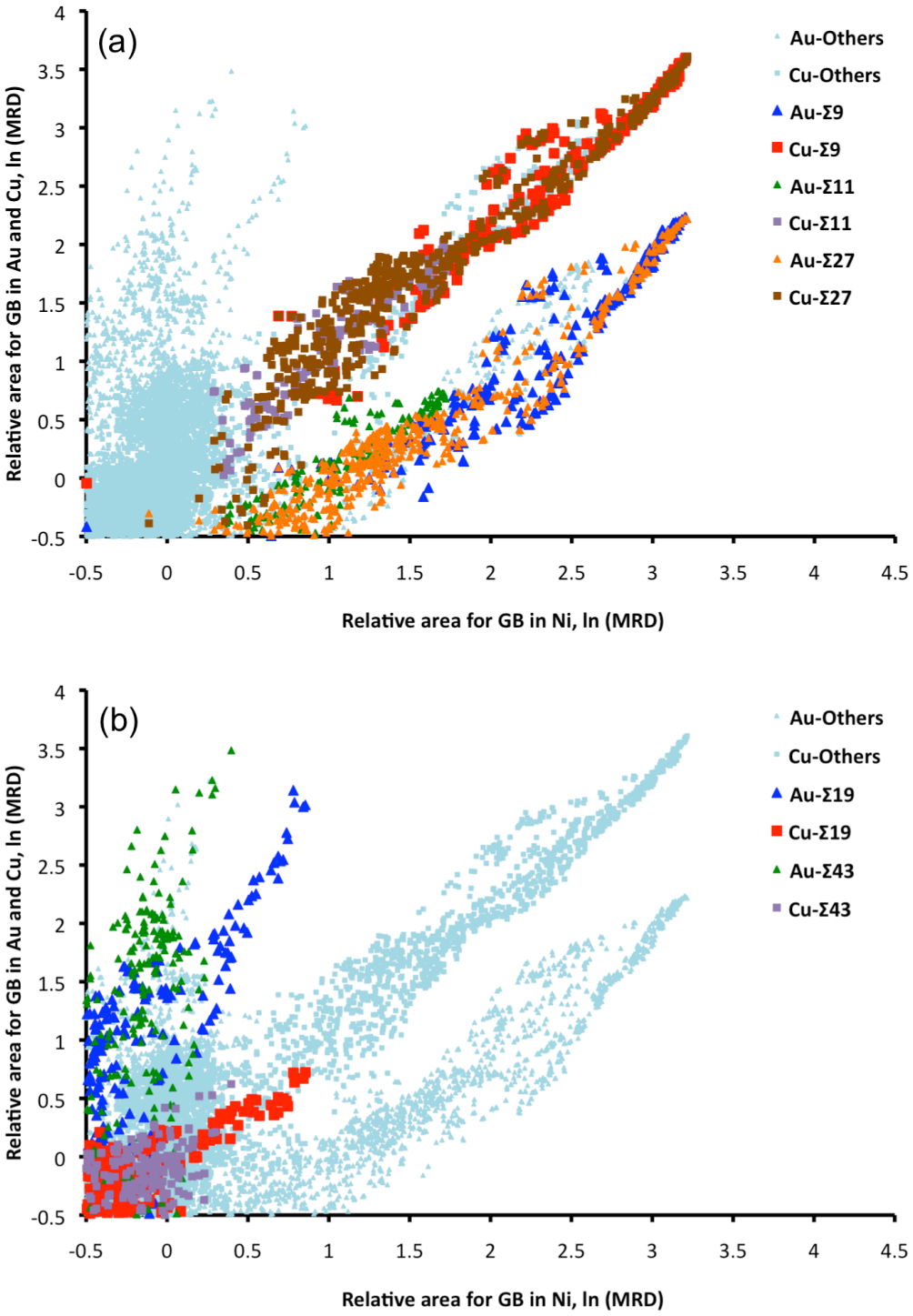

Figure 4.20. Comparison of GBCDs excluding Σ3 boundaries in Au, Cu, and Ni with populations greater than 0.5 MRD. (a) and (b) are plotted from the same data set. Each point corresponds to two crystallographically identical grain boundaries in two different materials. The horizontal axis shows the relative area in Ni and the vertical axis shows the relative area in Au or Cu for the same boundary.

Table 4.6. The correlation coefficients and slopes for the GBCDs of Ni, Au, and Cu.

All GBs > 0.5 MRD	Pearson Correlation	Spearman Correlation		Pearson Correlation	Slope
Au-Ni	0.97	0.85	ln(Ni)-ln(Au)	0.91	0.80
Cu-Ni	0.99	0.96	ln(Ni)-ln(Cu)	0.98	0.97
Cu-Au	0.99	0.91	ln(Au)-ln(Cu)	0.94	1.06
Σ3 only					
Au-Ni	0.98	0.94	ln(Ni)-ln(Au)	0.89	0.51
Cu-Ni	1.00	1.00	ln(Ni)-ln(Cu)	0.98	0.69
Cu-Au	0.99	0.96	ln(Au)-ln(Cu)	0.95	1.16
Σ9 only					
Au-Ni	0.94	0.93	ln(Ni)-ln(Au)	0.92	1.06
Cu-Ni	0.97	0.96	ln(Ni)-ln(Cu)	0.96	1.13
Cu-Au	0.98	0.98	ln(Au)-ln(Cu)	0.95	0.98
Σ27 only					
Au-Ni	0.96	0.94	ln(Ni)-ln(Au)	0.95	0.95
Cu-Ni	0.98	0.96	ln(Ni)-ln(Cu)	0.97	1.01
Cu-Au	0.99	0.96	ln(Au)-ln(Cu)	0.97	1.01

It should be noted that the data in **Figure 4.20a** and **Figure 4.20b** are plotted from the same data set but colored differently. In this analysis, we observed that Σ19b (46.8° misorientation about the [111]) and Σ43 (60.8° misorientation about the [332]) in Au have significantly higher populations than ones in Cu and Ni (see **Figure 4.20b**). The Σ19 boundaries in Au lead to the broadening of the peak maxima in the misorientation angle distribution (see **Figure 4.11a**). The slopes of the relative areas for Σ19 and Σ43 boundaries in Au versus ones in Ni clearly deviate from rest of the grain boundaries in Au. This deviation leads to the slight lowering of the Spearman correlation of Au-Ni in **Table 4.6**. These results indicate that the GBCDs in the isostructural FCC polycrystallines are more strongly correlated at specific misorientations than over the entire five macroscopic parameters. To generalize our finding that the GBCDs in isostructural materials are correlated, the relative areas of grain boundaries in BCC structure Fe and Mo are investigated in next Chapter.

Chapter 5

5. Grain Boundary Character Distributions in BCC Metals

5.1 Introduction

In the previous chapter, it was shown that the GBCDs of polycrystalline materials, which shared the same FCC crystal structure (isostructural), are strongly correlated [3]. It was reported that the GBCD is inversely correlated to the grain boundary energy [5][6][43][44][45][46][47][106]. Wolf previously reported that the energy anisotropies of BCC metals (Fe and Mo) were very similar for symmetrical tilt boundaries, symmetrical boundaries on (100) and (110) planes, and general grain boundaries [107][108][109]. These results implied that grain boundary energies in Fe and Mo were correlated. As a result, the GBCDs of Fe and Mo might be also correlated in a similar manner to that of FCC metals. We shall investigate the GBCDs of annealed Fe and Mo. To show that the correlations do not exist with metals of other structures, the Ni data set, which was recorded by Miller [25], was also included in this study.

5.2 Microstructure

The BCC polycrystalline specimens used in this study were annealed from the cold-rolled Fe 99.995% pure (Puratronic, Alfa Aesar, Ward Hill, MA) and the cold-rolled Mo 99.95% pure (Alfa Aesar, Ward Hill, MA). The cold-rolled specimens were

cut and annealed in the hydrogen flow furnace as summarized in **Table 3.2**. The samples were polished with SiC papers, diamond suspension, and polished with 0.04 μm colloidal silica, as described in **Table 3.3**. All EBSD measurements were carried out with the step size of 1 μm. EBSD raw data were processed with standard clean up functions in the TSL software described in §3.3.1. **Figure 5.1** shows the typical microstructure of the specimens. The EBSD maps of Fe annealed for 2 and 4 hours, which are shown in **Figure 5.1a** and **Figure 5.1b** respectively, indicate that these specimens are partially recrystallized. In other words, the deformed grains were not entirely consumed by the undeformed grains. The deformed grains, which can be identified by the color gradient inside the grain, are located at the bottom right in Figure 1a and at the top left in **Figure 5.1b**. The Fe specimens annealed for 8 (**Figure 5.1c**) and 16 hours (**Figure 5.1d**) are fully recrystallized. The EBSD map of Mo in **Figure 5.1e** reveals a very strong grain orientation texture with [100] along the normal direction of the specimen. Multiple grains in each scan had assigned orientations that were influenced by the so-called "pseudo-symmetry" problem, where the EBSD pattern recognition software could not distinguish between two similar orientations separated by particular rotations about symmetry axes. This causes many false grain boundaries, obvious in orientation maps such as the one shown in **Figure 5.2a**, that influence the misorientation distributions. Therefore, when line segments are extracted from this EBSD map, artificial boundaries are generated from these false grains (see **Figure 5.2b**). To eliminate these boundaries, the pseudosymmetry clean up was use to remove these 30° <111> false boundaries with a tolerance of 2°. This clean up procedure changes only 1.5% of all data in the EBSD map. Because these false grains have much smaller grain size than the rest of the polycrystalline grain, we also partition the EBSD data using a grain size criterion. **Figure 5.2c** shows the EBSD map of the partitioned data selected only grain with CI greater than 0.1 and grain size larger than 10μm. This partitioning removes approximately 1% of the EBSD data. As shown in the reconstructed grain boundary maps of the partitioned data in **Figure 5.2d**, there are no false boundaries, which previously observed in **Figure 5.2b**.

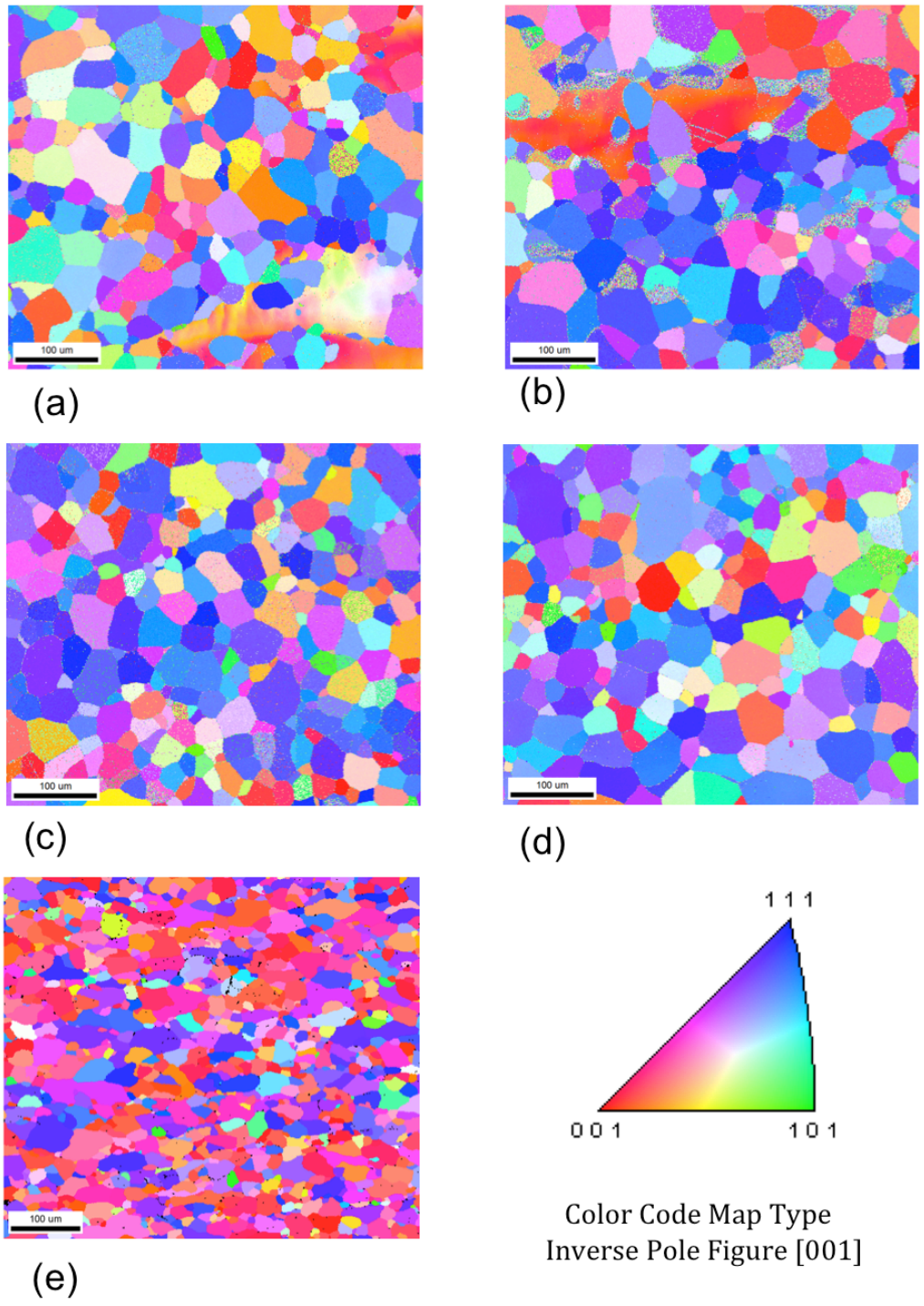

Figure 5.1. EBSD maps for Fe specimens annealed at four different annealing times: (a) 2 hours, (b) 4 hours, (c) 8 hours, (d) 16 hours, and (e) Mo specimen annealed for 2 hours. The crystallographic orientations are colored according to the standard stereographic triangle on the bottom right. Note that all EBSD maps were plotted from raw data.

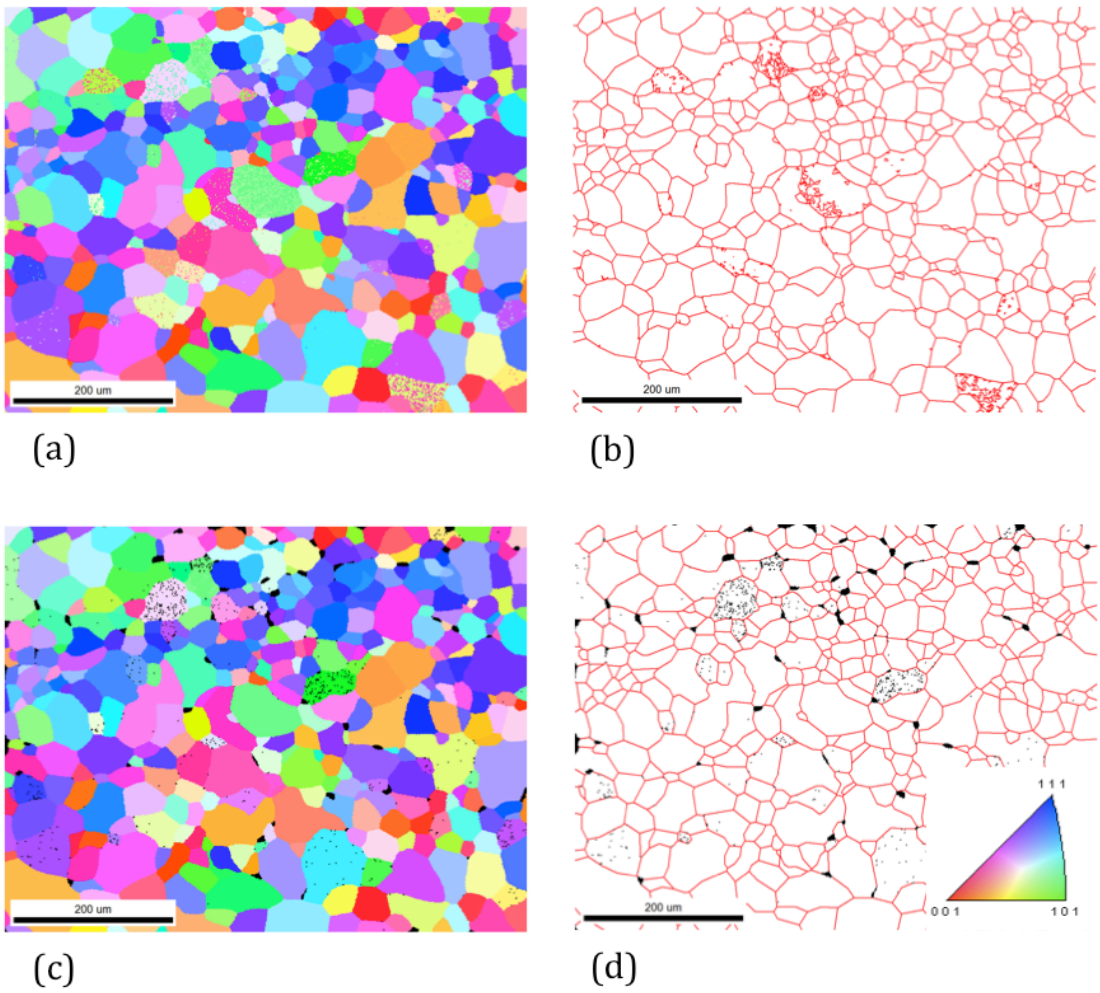

Figure 5.2. Inverse pole figure (IPF) maps for Fe specimen annealed for 16 hours, (a) EBSD map and (c) pseudosymmetry cleaned up and partitioned EBSD map. Reconstructed grain boundary maps from (a) and (c) are shown in (b) and (d) respectively. The crystallographic orientations are colored according to the standard stereographic triangle shown as inset in (d). Note that, reconstructed boundaries are marked by red lines and false grains are colored black.

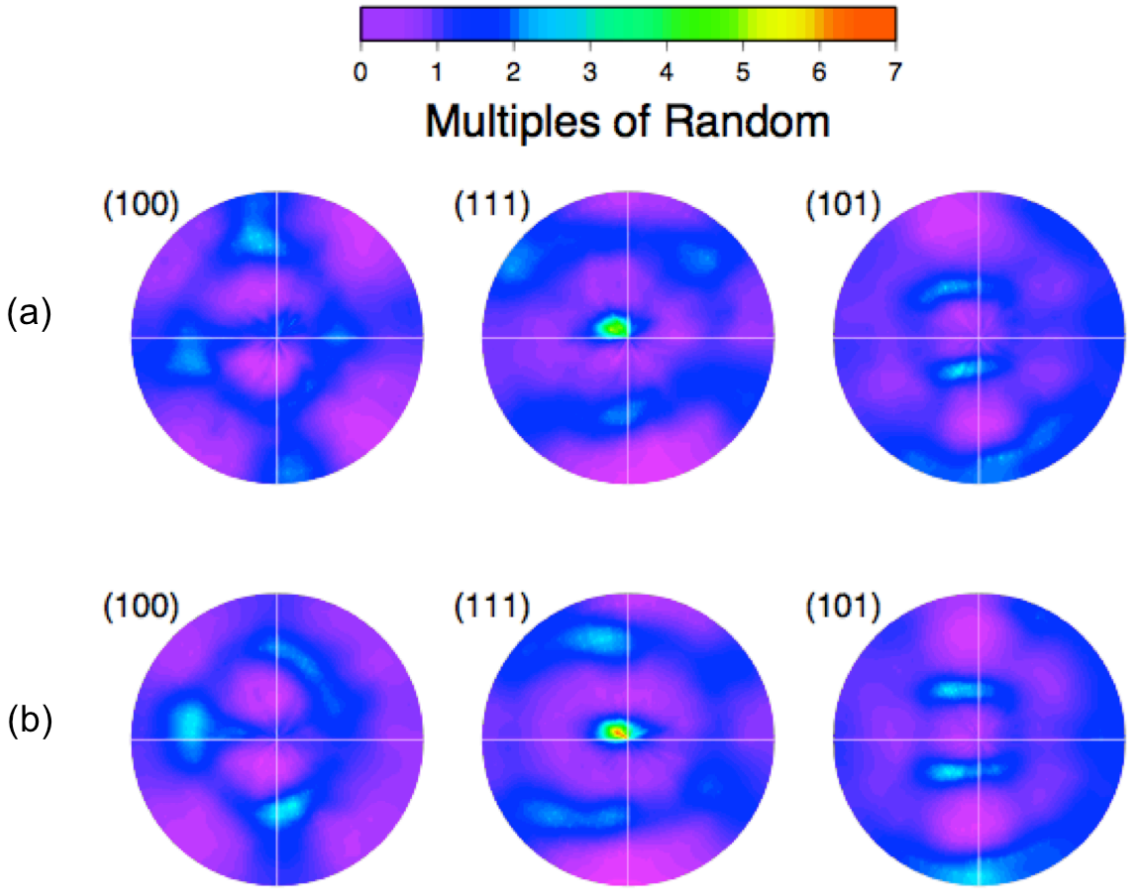

Figure 5.3. Pole figures for the specimens, (a) Fe 2 hours annealing, (b) Fe 4 hours annealing, (c) Fe 8 hours annealing, (d) Fe 16 hours annealing, and (e) Mo 2 hours annealing.

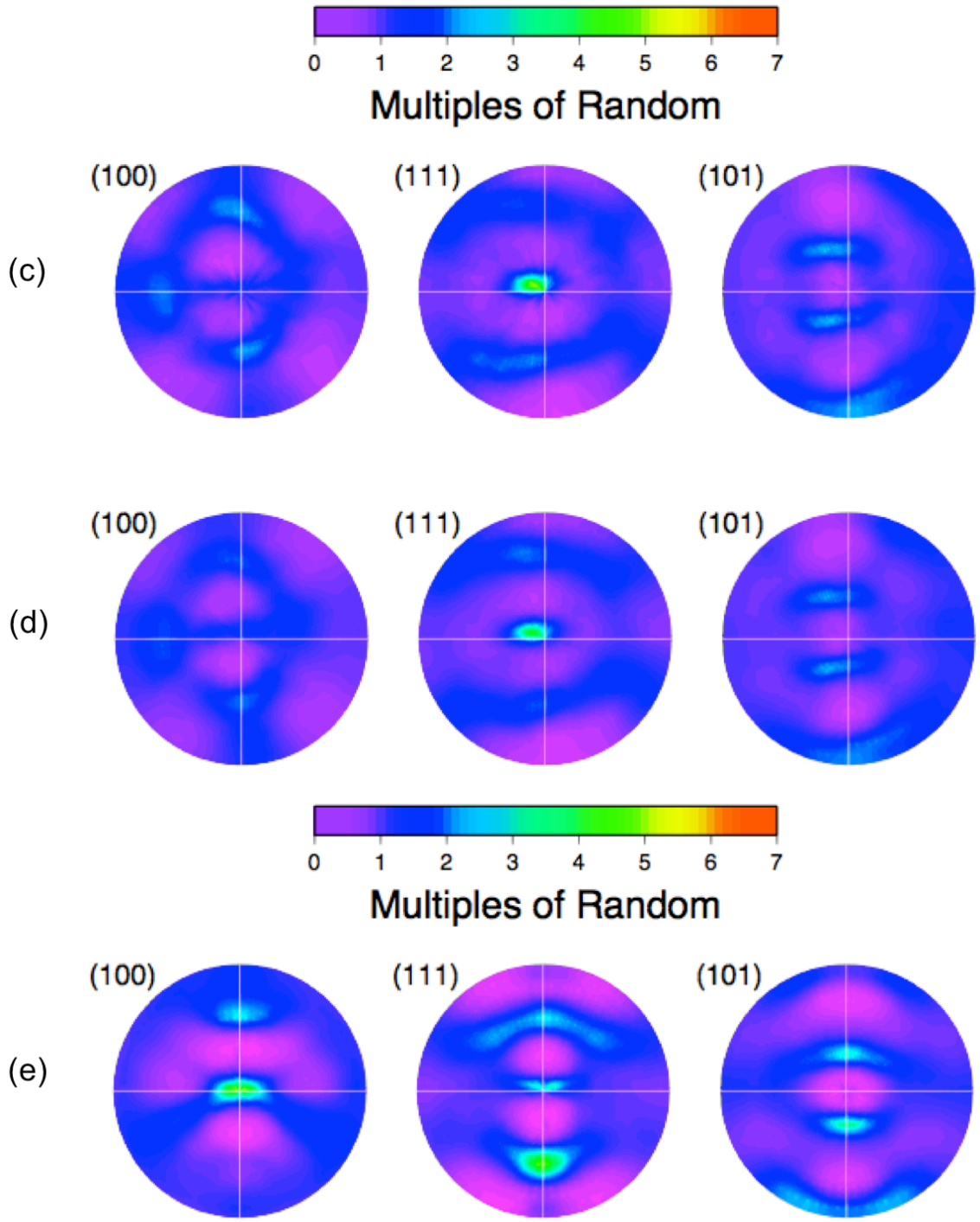

Figure 5.3, continued. Pole figures for the specimens, (c) Fe 8 hours annealing, (d) Fe 16 hours annealing, and (e) Mo 2 hours annealing. Note that the Mo has residual deformation texture from prior rolling, which results in the strong (001)[110] component.

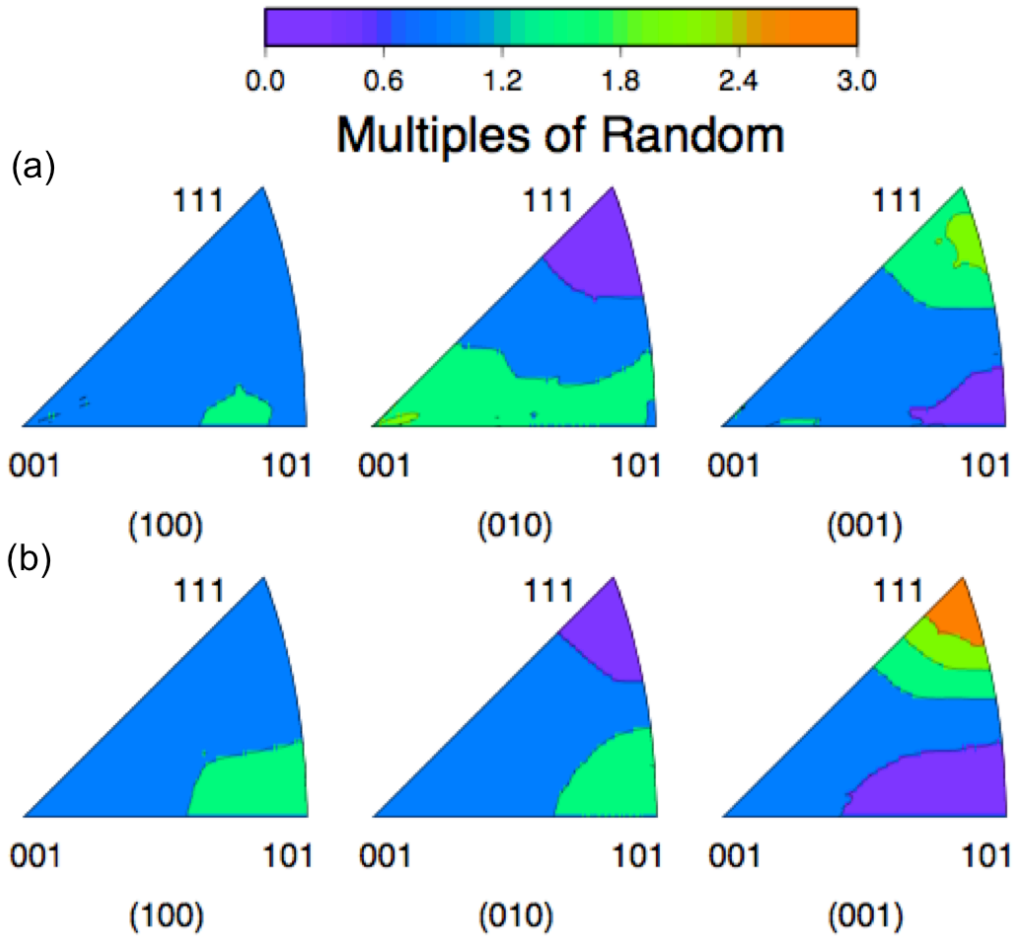

Figure 5.4. Inverse pole figures for the specimens, (a) Fe 2 hours annealing, (b) Fe 4 hours annealing, (c) Fe 8 hours annealing, (d) Fe 16 hours annealing, and (e) Mo 2 hours annealing.

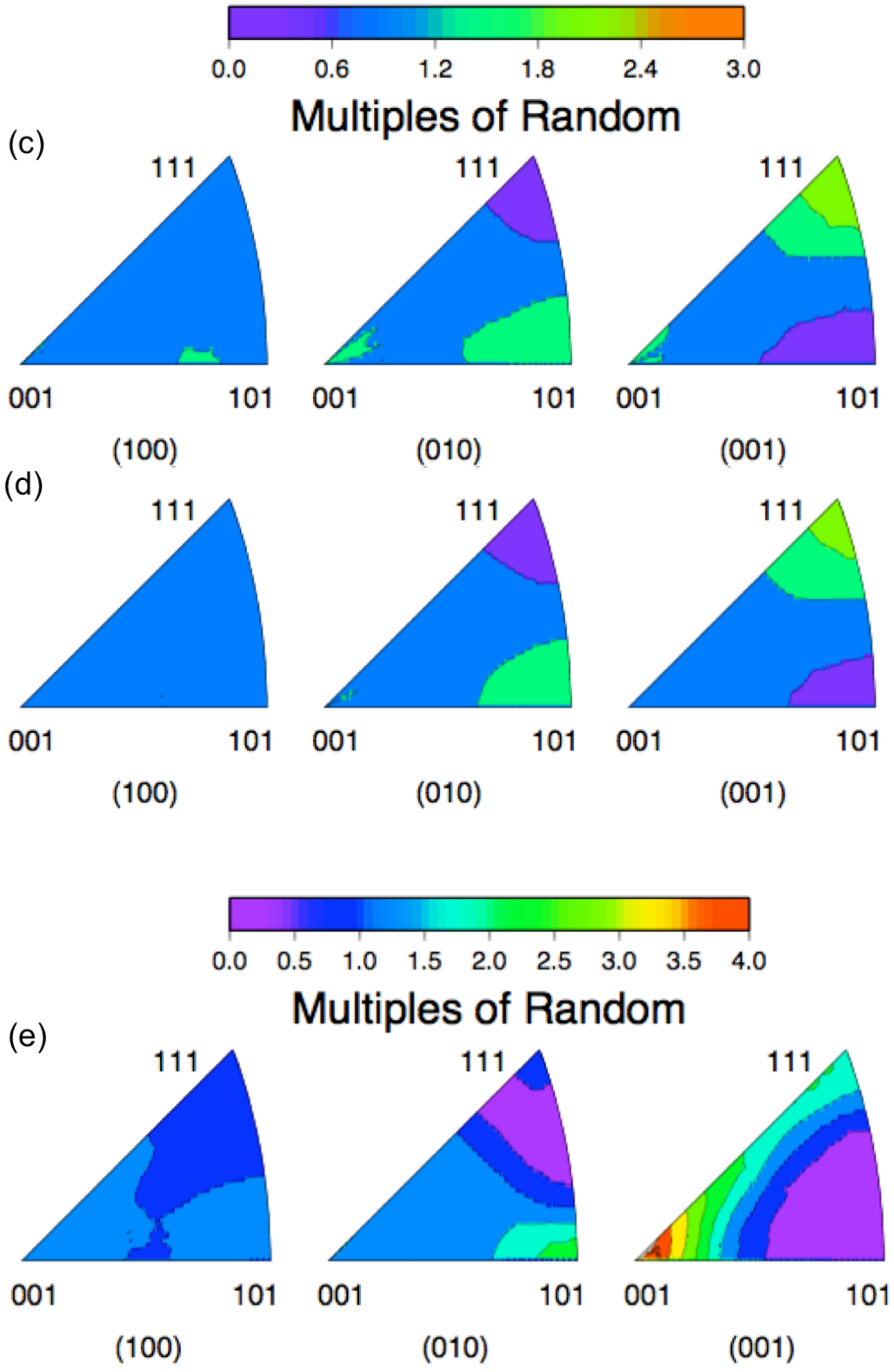

Figure 5.4, continued. Inverse pole figures for the specimens, (c) Fe 8 hours annealing, (d) Fe 16 hours annealing, and (e) Mo 2 hours annealing.

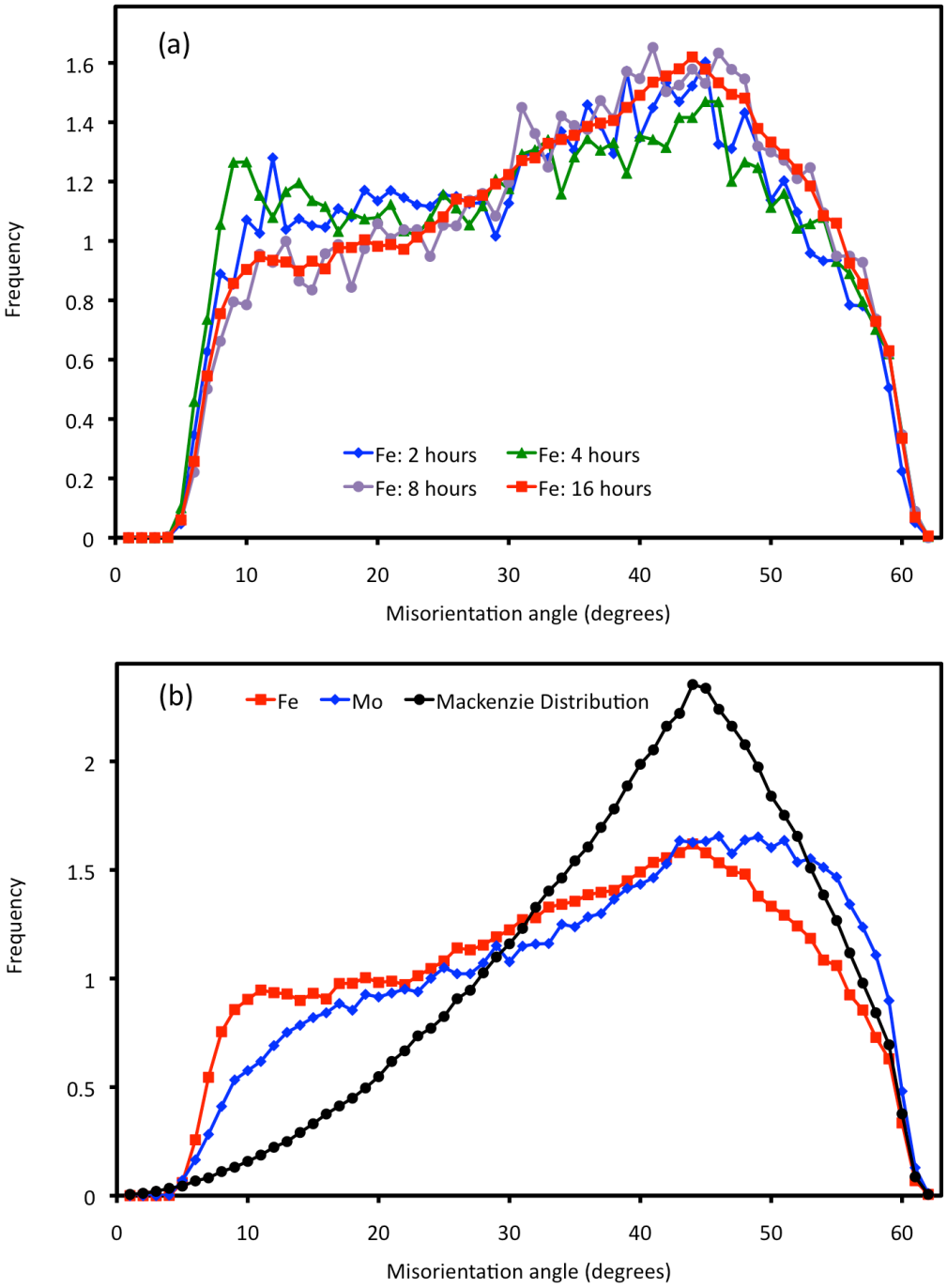

Figure 5.5. Misorientation angle distributions. (a) All Fe specimens and (b) Fe 16 hours annealing, Mo 2 hours annealing, and the Mackenzie distribution.

Figure 5.3 and **Figure 5.4** show the pole figures and inverse pole figures of the specimens, which clearly show grain orientation texture for all specimens. Annealed Fe specimens have a strong γ-texture, which is a typical texture for cold rolled and annealed BCC Fe [8][110]. Note that the sample frames of the EBSD measurements for Fe specimens are slightly different due to the tilts of polishing planes. Mo has a (001)[110] α-fiber texture, which is similar to the texture of annealing of cold-rolled Ta [111]. **Figure 5.5a** shows the misorientation distribution for all Fe specimens. As shown in the plot, the frequencies of the low angle grain boundaries with misorientation angles less than 15° in Fe annealed for 8 and 16 hours are lower than that of Fe annealed for 2 and 4 hours. **Figure 5.5b** shows the comparable plot for Fe annealed at 550 °C for 16 hours and Mo annealed at 1050 °C for 2 hours. The misorientation distributions of Fe and Mo are clearly different from the random misorientation angle distribution (Mackenzie distribution), which has its peak at about 45° [105]. These results also show that the occurrence of low angle grain boundaries in Fe is greater than in Mo. The misorientation distributions are also quite different from those of the FCC metals (Ag, Au, Cu, and Ni), which have the peak centered at 60° (**Figure 4.11a**).

5.3 Grain Boundary Character Distribution (GBCD)

The GBCDs of our specimens were calculated using the texture correction scheme described in detail in Appendix A. The line segments, which are the initial input for the GBCD calculation, were extracted from the EBSD maps using the TSL/OIM software. The numbers of line segments and the average length, measured in step size, for each data set are listed in the **Table 3.2**. **Figure 5.6** shows stereographic projections of the grain boundary plane distribution for all misorientations in units of multiple of a random distribution (MRD). Note that **Figure 5.6f** shows the surface energy of a BCC metal calculated from the broken nearest neighbor bond model [104]. These distributions reveal weak anisotropy for all specimens ranging from 0.85 MRD to 1.13 MRD. These low anisotropies are consistent with the previous studies of Fe-1%Si [112] and ferritic steels [8][110], but the peak maxima were located at different positions. The distributions of the Fe specimens have maxima at the (001) position, which is also the peak position for the Mo specimen (see **Figure 5.6e**). The peak maxima in the Fe-1%Si and ferritic steels were centered at (110) and (111) planes respectively [110][8][112]. It is possible that the alloying components in the Fe-1%Si and ferritic steels influenced the relative energies and the preferred grain boundary planes. To support this idea, note that the GBCD of the ferritic steels [112] had maxima that corresponded to the lowest surface energy (see **Figure 5.6f**). It should also be noted that previous studies showed that artifacts in the GBCD calculation could produce small anisotropies and suggested that anisotropies less than 10% should not be considered significant [9]. Therefore the (001) maxima in Fe (1.11 MRD) and Mo (1.13 MRD) are barely greater than the expected range of experimental uncertainty.

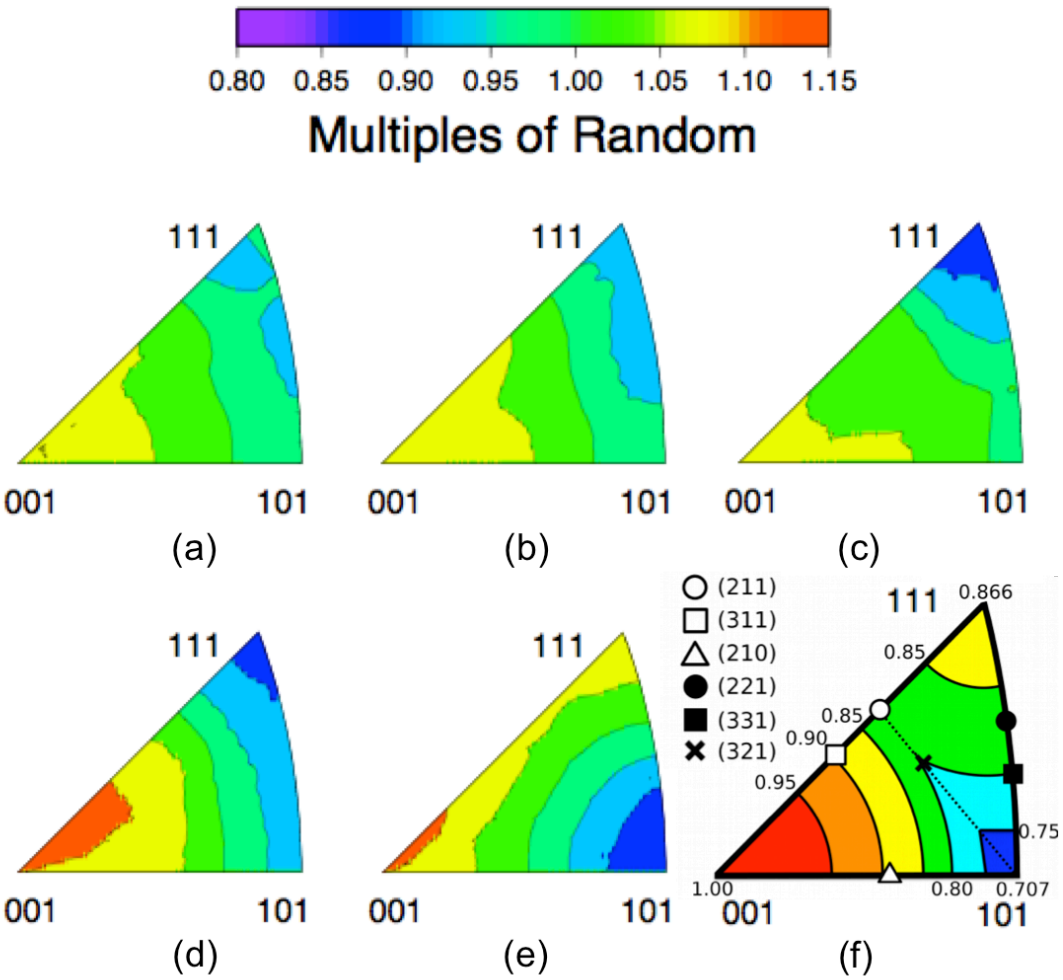

Figure 5.6. Grain boundary plane distributions (GBPDs) in (a) Fe annealed for 2 hours, (b) Fe annealed for 4 hours, (c) Fe annealed for 8 hours, (d) Fe 16 annealed for hours, (e) Mo annealed for 2 hours, and (f) the surface energy calculated from the broken nearest neighbor bond in BCC metals. This figure was reproduced from reference [104]. Note that the energy unit in this figure is scaled with E (100) = 1.

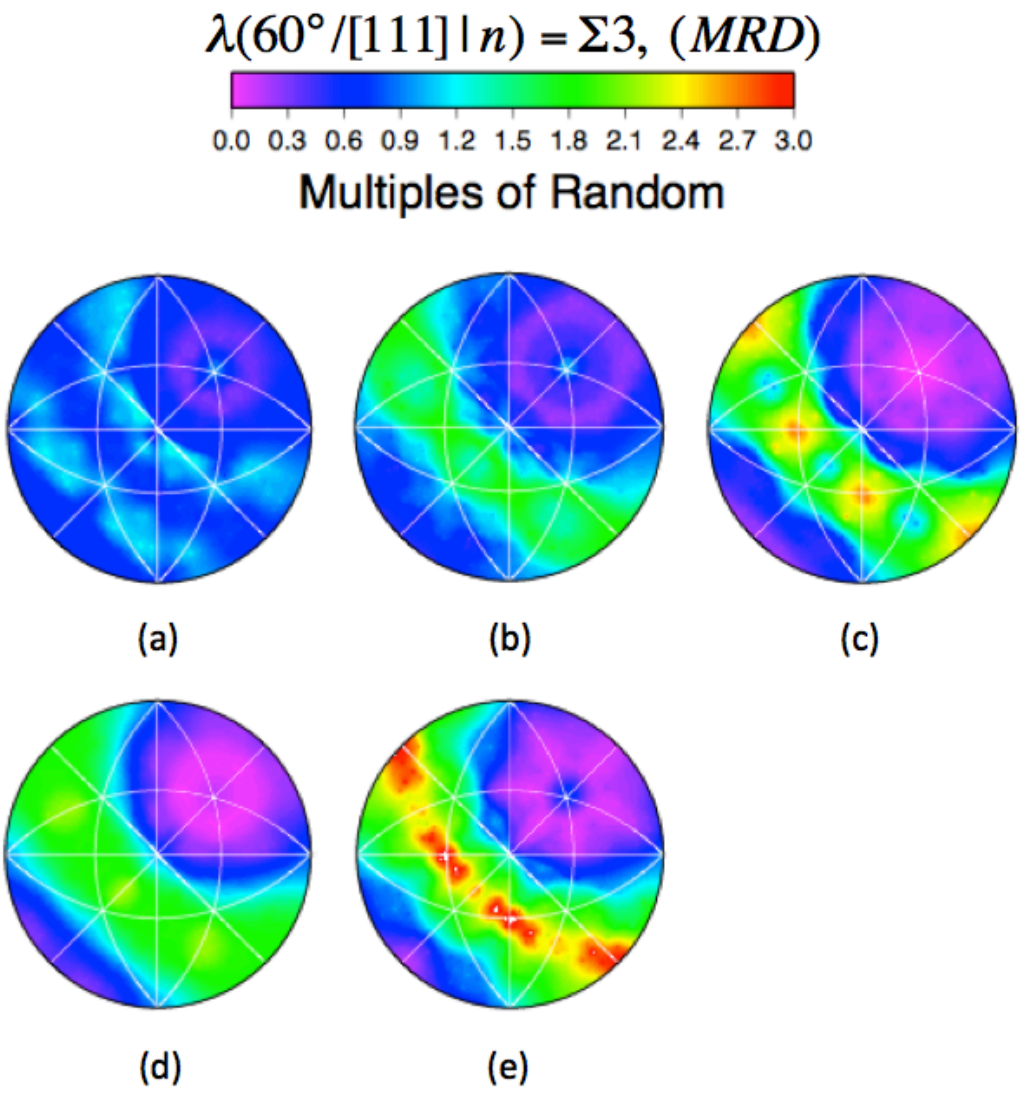

Figure 5.7. Observed distribution of grain boundary plane normal for boundary with 60° about [111] axes, (a) Fe annealed for 2 hours, (b) Fe annealed for 4 hours, (c) Fe annealed for 8 hours, (d) Fe annealed for 16 hours, and (e) Mo annealed for 2 hours. Note that the GBCDs were calculated with a binning resolution of 10°.

Figure 5.7 shows the GBCDs for all specimens with a misorientation of 60° about [111] axis. The Σ3 boundary populations in Fe specimens change continuously with the annealing times. Specifically, there is no clear peak after 2 hours annealing (see **Figure 5.7a**). The population intensities of the tilt grain boundaries in the (111) zone develop gradually at the symmetrical (110) tilt boundary and broaden in the Fe specimens annealed for 4 hours and 8 hours, as depicted in **Figure 5.7b** and **Figure 5.7c** respectively. Because the (110) plane is

expected to have the lowest energy in BCC materials, one might expect that the most highly populated grain boundaries to be comprised of these planes. In fact, this is the case for Mo (although the maxima are not significantly larger than any of the other tilt grain boundaries in the (111) zone). Interestingly, the peak for the Fe specimen annealed for 16 hours (**Figure 5.7d**) is centered at the symmetrical (112) tilt boundary, which is analogous to the coherent twin boundary in FCC metals. In addition, the symmetrical (111) twist boundary, which is the predominant boundary in FCC metals, is the minimum of this distribution with a population of ~ 0 MRD. The distribution of Σ3 boundaries in Fe annealed for 16 hours is comparable with the ones in ferritic steels [8][110]. However the population of the coherent boundaries in **Figure 5.7d** (2.3 MRD) is much lower than those of the ferritic steels, which were about 13 MRD [8] and 16 MRD [110]. The annealing temperatures (650°C to 1200 °C) during thermomechanical processing in the ferritic steels are much higher than the annealing temperature (550 °C) of our Fe specimens. Therefore, both the thermal processing and presence of alloying elements are factors that might lead to observation of more coherent twin boundaries in the ferritic steels. The distribution of Σ3 boundaries in Mo specimen annealed for 2 hours (see **Figure 5.7e**) has a peak at the symmetrical (110) tilt boundary, which is quite similar to the distributions of Fe annealed for 4 hours (**Figure 5.7b**) and 8 hours (**Figure 5.7c**). Because the Fe and Mo specimens were annealed at the same homologous temperature (T_H = 0.46), it is possible that the peak maximum in Mo might have changed from the (110) to the coherent twin with longer annealing as observed for the Fe specimens. If that were the case, it would also explain how the symmetrical (110) tilt boundary was predominant among Σ3 boundaries in Fe-1%Si, which was annealed at 787 °C for 1 hour [112]. However, as mentioned above, the actual populations at (112) and (110) are not significantly different.

In what follows, it is assumed that the Fe specimen annealed at 550 °C for 16

hours is the most ideal and nearest to an equilibrium state. Thus, we chose this Fe specimen and the Mo annealed at 1050°C for 2 hours for further investigation. The GBCD of Ni, which was calculated with the texture correction scheme, was also included in the comparison. We plot the average grain boundary populations using the same procedure that was used to create the plots in **Figure 4.8** and **Figure 4.9**. The comparison of the GBCD of Mo to the GBCDs of Fe is shown in **Figure 5.8**. The average grain boundary populations of Mo are strongly correlated to the ones of Fe for both 10° (**Figure 5.8a**) and 8.2° (**Figure 5.8b**) resolutions (see **Table 5.1**). As expected, the average grain boundary populations in Fe and Mo are not positively correlated with the ones of Ni (see **Figure 5.9**). It should be noted that the Pearson correlation coefficients of ln(Fe)-ln(Ni) is relatively high. As we mentioned before in §3.4, the Pearson correlation coefficients are dominated by the highly populated grain boundaries and not are robust to quantify correlations when the data varies over orders of magnitude. Because the Spearman rank-order correlation coefficients are weakly negative or moderately negative for the comparison of Fe and Mo to Ni, the results indicate that the GBCDs are positively correlated only for isostructural materials. **Figure 5.10** shows a direct point-by-point correlation. The horizontal axis shows the relative area in Fe and the vertical axis shows the relative areas for the same boundary in Mo. While there is considerable scatter, the relative areas for the $\Sigma 3$ boundaries between Mo and Fe are strongly correlated. This result implies that the GBCD might be more strongly correlated at each misorientation than over the entire grain boundary space. Also, in comparison to the GBCDs of the FCC materials, note that the dynamic range of the data is much smaller for the BCC materials, so that small deviations are more obvious on the correlation graphs.

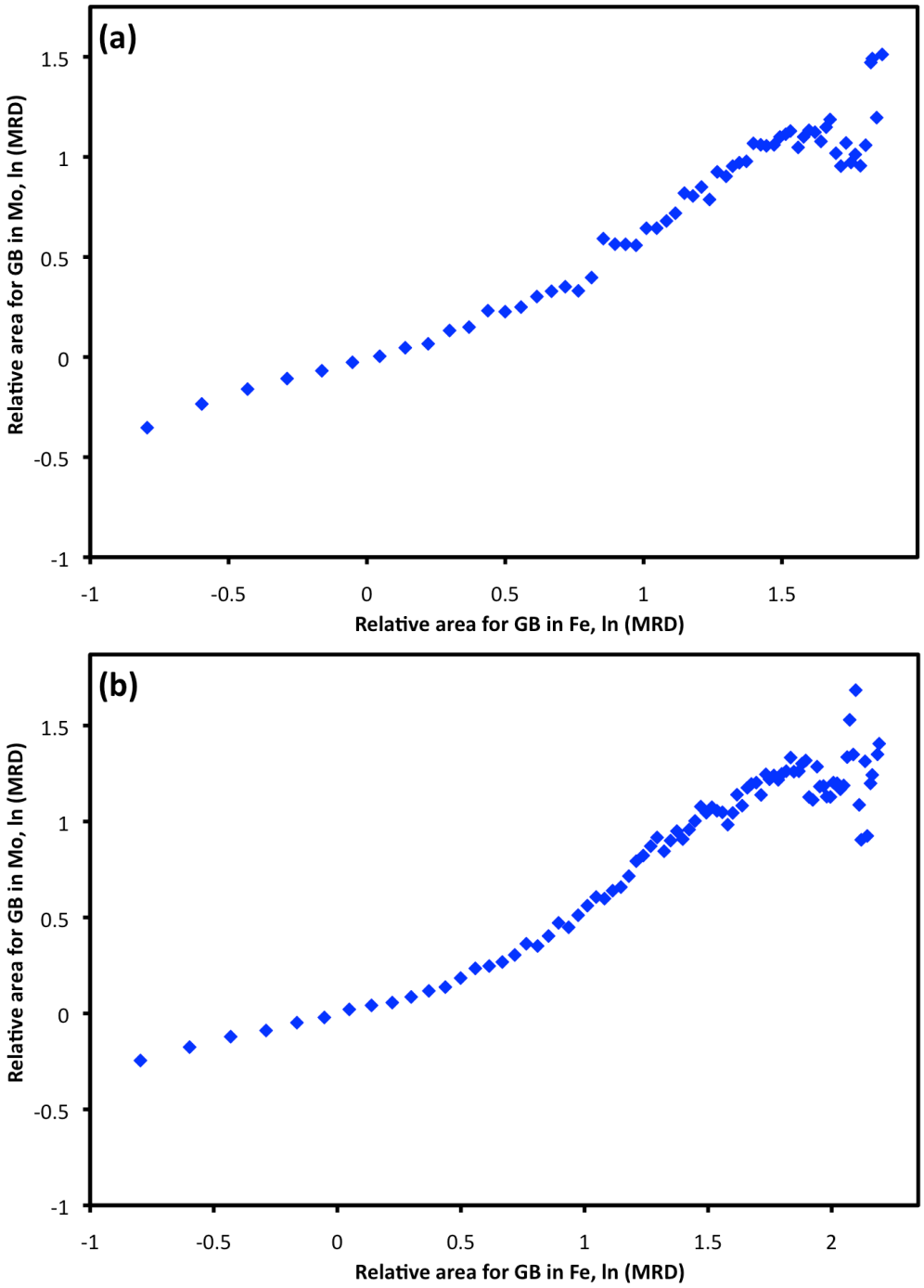

Figure 5.8. Comparison of GBCD calculated with resolutions of (a) 10° and (b) 8.2° in Mo and Fe. The average grain boundary populations in Mo are plotted with the average populations of the same boundaries in Fe. Both plots were discretized into bins of fixed width, $\Delta = 0.1$ MRD.

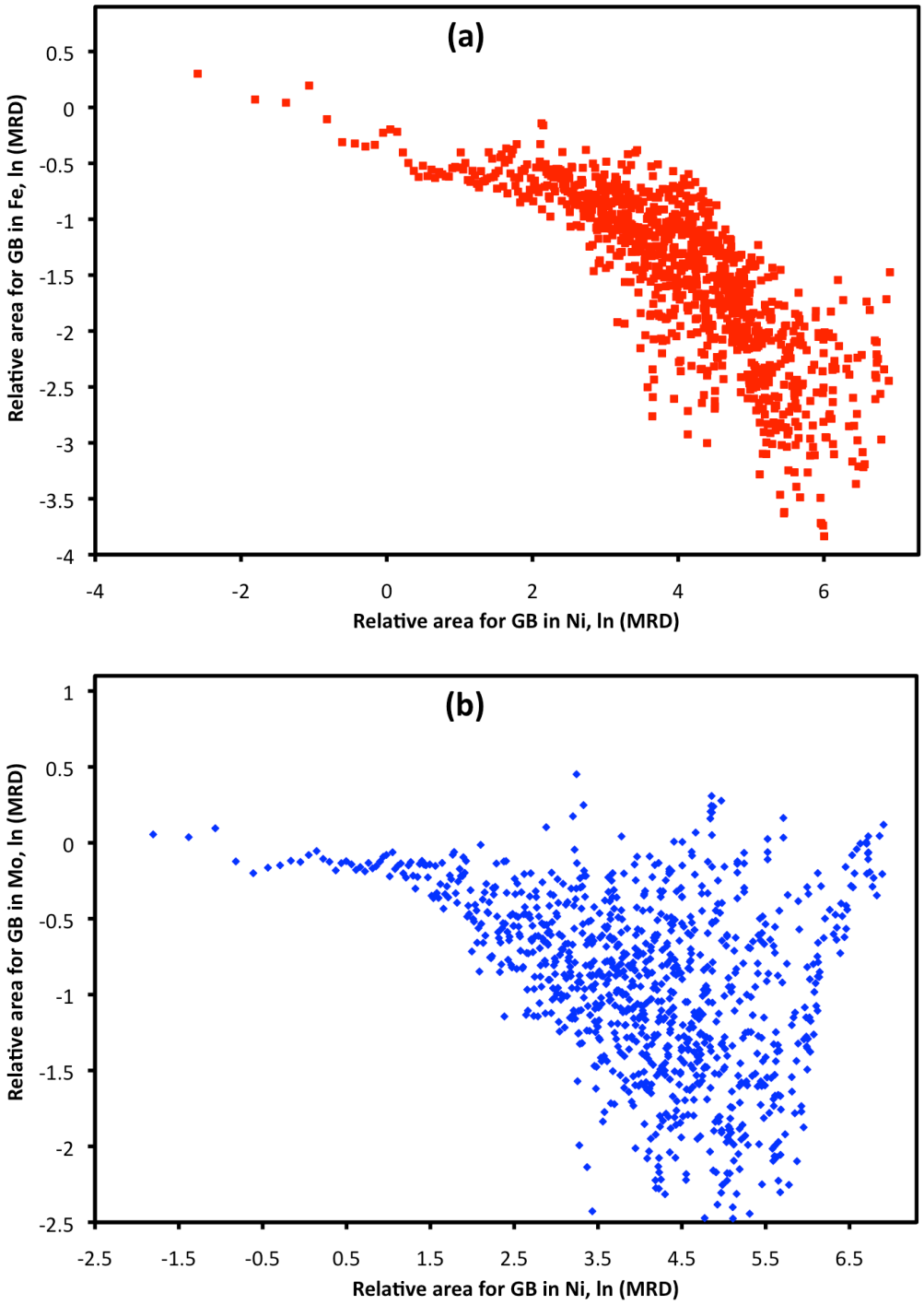

Figure 5.9. Comparison of GBCD of (a) Fe and (b) Mo. The average grain boundary populations in Fe and Mo are plotted with the average populations of the same boundaries in Ni. Both plots were calculated with resolutions of 10° and discretized into bins of fixed width, $\Delta = 0.1$ MRD.

Table 5.1. The correlation coefficients for the average grain boundary populations in Fe, Mo, and Ni. GBCD calculated with binning resolutions of 10° and 8.2° were both discretized into bins of fixed width, Δ = 0.1 MRD.

	Pearson 10°	Spearman 10°	Pearson 8.2°	Spearman 8.2°		Pearson 10°	Pearson 8.2°
Fe-Mo	0.95	0.87	0.92	0.85	ln(Fe)-ln(Mo)	0.95	0.94
Ni-Fe	-0.55	-0.20	-0.46	-0.05	ln(Ni)-ln(Fe)	-0.80	-0.62
Ni-Mo	0.02	-0.31	0.02	-0.22	ln(Ni)-ln(Mo)	-0.37	-0.31

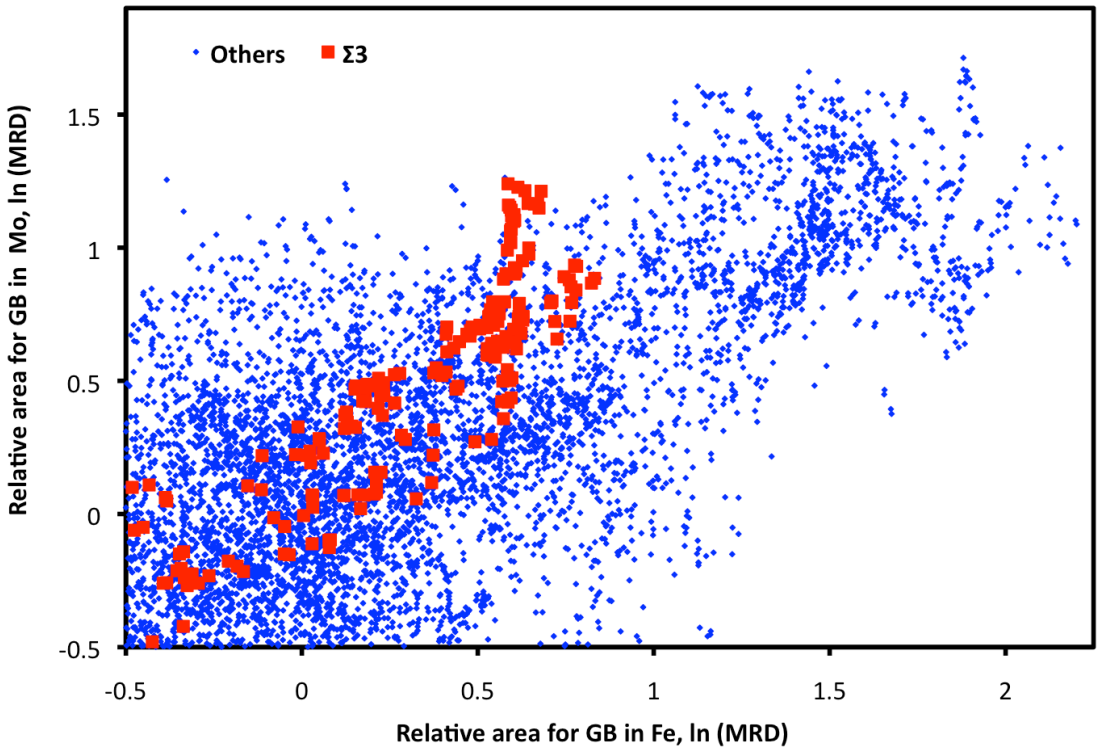

Figure 5.10. Comparison of GBCDs calculated with a resolution of 10°. Each point corresponds to two crystallographically identical grain boundary types in two materials with populations greater than 0.5 MRD. The horizontal axis shows the relative areas in Fe and the vertical axis shows the relative areas in Mo for the same boundary type. Note that the Σ3 boundaries and the other grain boundary types are marked red squares and blue diamonds respectively.

5.4 Discussion

The hypothesis that the GBCDs of isostructural BCC polycrystalline materials (Fe and Mo) are correlated has been verified. The comparisons between the GBCDs of the BCC metals (Fe and Mo) to the FCC metal (Ni) in **Figure 5.9** indicate, as expected, that GBCDs are positively correlated only for materials that share the same crystal structure (see **Table 5.1**). Furthermore, the result in **Figure 5.10** reveals that the GBCD might be more strongly correlated at each misorientation. To investigate this, we deliberately extracted the relative areas for 408 distinct grain boundaries. The particular set was selected because the energies of the grain boundaries were calculated using atomistic simulations with EAM potentials, as described in the next chapter. These 408 boundaries, which are comprised of 127 tilt, 24 twist, and 257 mixed boundaries, span 49 different misorientations. A comparison between grain boundary populations in Fe and the Mo for 229 boundaries, which have relative grain boundary populations greater than 0.5 MRD, is shown in **Figure 5.11**. The points are marked according to the Σ misorientations as in **Figure 5.11a**. Note that Σ3, Σ33, Σ41 were colored red, blue, and black respectively. Because Σ9, 38.9°/[110] has a misorientation angle close to Σ27, 31.6°/[110], Σ9 and Σ27 boundaries were colored brown. The misorientations of Σ13, 27.8°/[111] and Σ39, 32.2°/[111] are also close, therefore we colored both Σ13 and Σ39 green. Σ17, 28.1°/[100], Σ53, 31.9°/[100], and Σ65, 30.5°/[100] have similar misorientations about the same [100] axis, therefore we colored these boundaries orange. We also compared the relative areas of grain boundary in Fe and Mo according to the types of grain boundary structures as in **Figure 5.11b**. The grain boundaries are separated into three categories: tilt (diamonds), twist (squares), and mixed (circles). Asymmetrical boundaries, symmetrical boundaries, (110) symmetrical boundaries, and (112) symmetrical boundaries, were colored blue, red, green, and black respectively. The GBCDs of Fe and Mo for these 229 boundaries are moderately correlated with a correlation coefficient of 0.56.

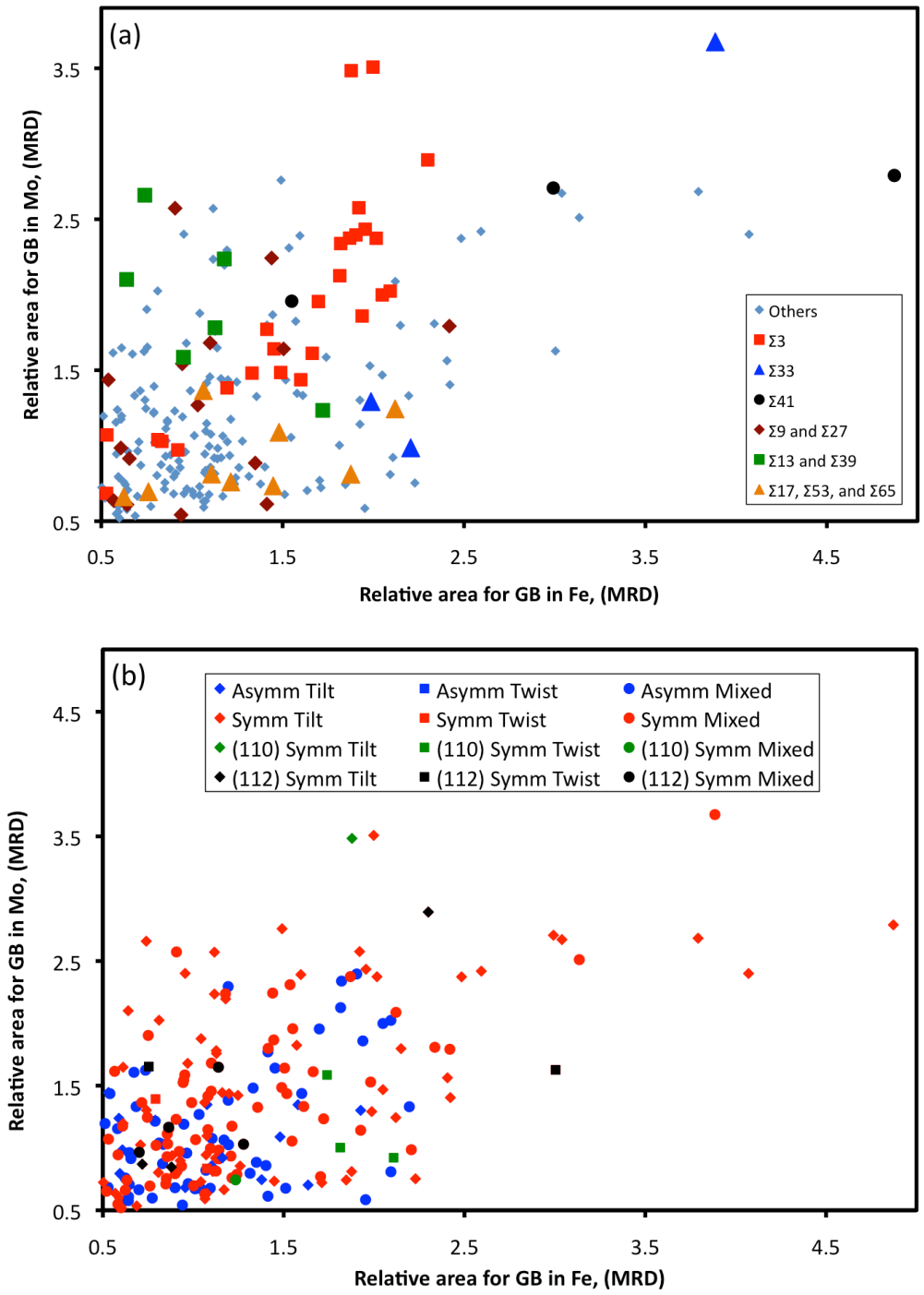

Figure 5.11. Comparison between the relative areas of grain boundaries in Fe annealed for 16 hours and Mo annealed for 2 hours, (a) Grain boundaries were colored according to the Σ misorientations. (b) Grain boundaries were colored according to the types of boundary structures. Each point corresponds to two crystallographically identical grain boundaries in two different materials. The horizontal axis shows the relative areas in Fe and the vertical axis shows the relative area in Mo for the same boundary.

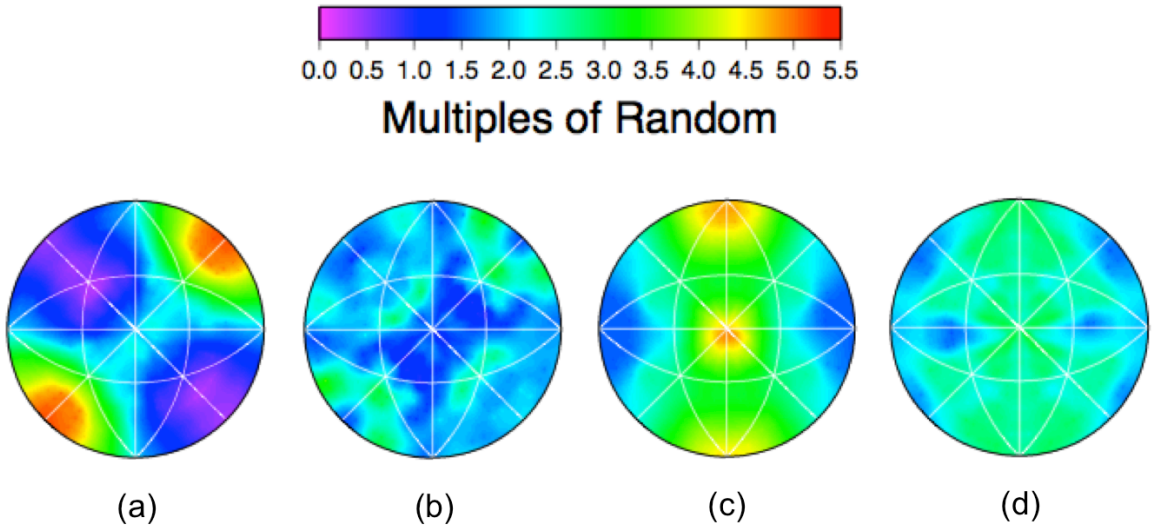

Figure 5.12. The distributions of grain boundary planes for Σ33, 20.1°/[110] and Σ41, 12.7°/[100] in Fe annealed for 16 hours and Mo annealed for 2 hours: (a) Σ33 Fe, (b) Σ33 Mo, (c) Σ41Fe, and (d) Σ41 Mo.

The correlation coefficient increased from 0.56 (for all of the boundaries) to 0.82 when only Σ3 boundaries were considered. While the GBCDs of Fe and Mo are correlated when separated by Σ misorientations (**Figure 5.11a**), there is no correlation between GBCD in Fe and Mo when they are separated by the structure type of the grain boundary (**Figure 5.11b**). Among the select set of 229 high symmetry grain boundaries, the most populated boundaries in Fe and Mo are the Σ41, 12.7°/[100] with the symmetrical (9,1,0) planes and the Σ33, 20.1°/[110] with the symmetrical (6,5,4) planes respectively. Because the most populated grain boundaries in Fe and Mo are different, the relationship between the average grain boundary populations in Fe and Mo shows more scatter at the highly grain boundaries (**Figure 5.8**) It should be noted that there are limited numbers of Σ33 and Σ41 in the set used to construct **Figure 5.11a,** the global maxima may actually occur at other positions. As an example, the grain boundary plane area distributions for Σ33, 20.1°/[110] and Σ41, 12.7°/[100], are plotted in **Figure 5.12**. As shown in **Figure 5.12**, there are significant differences of the peak intensities and the grain boundary distribution in the Fe and Mo specimens. While there were no noticeable peak maxima in Mo, the peak maxima in Fe are clearly observed at the orientations

of the low index planes of (110) and (100) in Σ33 and Σ41 respectively. Because we calculated the GBCD with 10° bins, the populations of the low angle grain boundaries fall into the bin of Σ41, 12.7°/[100], and leads to the high fraction of the Σ41 boundaries in Fe. Although there was no clear peak in the plots in Mo, the average population of Σ33 (1.9 MRD) and Σ41 (2.6 MRD) boundaries are higher than that of Σ3 (1.3 MRD) boundaries. The average populations in Fe are followed a similar trend, in which the Σ33, Σ41, and Σ3 have average populations of 2.0 MRD, 3.5 MRD, and 1.1 MRD respectively. These results indicate that the low angle grain boundaries in Fe and Mo are highly populated grain boundaries, which is in fact consistent with the misorientation angle distribution in **Figure 5.5b**.

Based on the results in this chapter, we conclude that the GBCDs of BCC polycrystals are more likely correlated at each misorientation than over the entire grain boundary space (see **Figure 5.10**), which is consistent with the results of the FCC metals in Chapter 4. Because the relative areas for grain boundary in polycrystalline materials are controlled by the boundary energy [5][6] [43][44][45][46][47][106], it is of interested to examine the relationship between grain boundary population and energy in the BCC metals. In the next Chapter, we shall describe how the energies of 408 grain boundaries in Fe and Mo were determined using atomistic simulations.

Chapter 6

6. Atomistic Simulation of the Grain Boundary Energies in Fe and Mo

6.1 Introduction

In this chapter, we shall describe the atomistic simulations of 408 distinct grain boundaries in Fe and Mo. Holm et al. recently showed that boundary energies in the Al, Au, Cu, and Ni, which shared the same face-centered cubic (FCC) crystal structure (isostructural), are correlated and scaled with the shear modulus [10][69]. These significant results implied that the variation of the grain boundary energy in the body-centered cubic (BCC) metals might also be correlated in a similar manner to that of the FCC metals. There have been a number of atomistic simulations that surveyed grain boundaries energy in BCC metals [107][108][109][113][114]. Wolf previously showed that the energy anisotropies of Fe and Mo were similar for symmetrical tilt boundaries, symmetrical boundaries on (100) and (110) planes, and certain general grain boundaries [107][108][109]. In addition, Tschopp and colleagues recently examined a large data set of grain boundary energies of Fe by using molecular statics [113]. However, much of this work focused on symmetrical boundaries with a limited number of general grain boundaries.

Kim et al. developed a systematic scheme to construct a grain boundary energy database, which covered the entire five macroscopic degrees of freedom [114]. In this scheme, grain boundary energies of Fe were calculated from an atomistic model using molecular statics. A large number of grain boundaries were

constructed using misorientation and grain boundary plane as the parameters, similar to the parameterization of the (GBCD). However, the discretization of grain boundary planes is relatively coarse. Olmsted et al. demonstrated that the minimized energies of the same macroscopic grain boundaries varied with the starting configurations [69]. Although some of the starting configurations minimized to the same lowest energy, it is no guarantee that the global minimum is the minimized energy when only one starting configuration is considered. To have quantitatively corrected boundary energy, it is important to consider alternative grain boundary structures, which have different relative translations between the adjacent crystals (microscopic configurations).

Hence the atomistic simulations, that considers a wide range of grain boundary types and a large number of grain boundary structures for each grain boundary type, are needed to provide insight into how the energy of the grain boundary varies over all five macroscopic parameters. We chose Fe and Mo as model materials because these polycrystalline materials were widely used and well studied by the atomistic simulation. A large number of grain boundaries (408) will be investigated. In the following, we examine the correlation between grain boundary energy in Fe and Mo associated with the material properties in **Table 6.1**. We also compare the simulated boundary energy of Fe to the experimental measured boundary energy of Fe [8].

Table 6.1. Materials properties and the ratios of selected materials properties calculated from the EAM potentials. The ratios are scaled with the lattice constant (a_0) to obtain the unit of grain boundary energy (energy per area).

Materials properties	Mendelev Fe EAM2 [a]	Finnis-Sinclair Mo EAM [b]
Lattice constant a_0 (Å)	2.8553	3.1472
Melting point T_m (K)	1773	3062.6 ± 7.6
Cohesive energy E_{coh} (eV)	4.122	6.82
Coherent twin energy (mJ m^{-2})	26.2	38.9
Bulk modulus B (GPa)	177.8	262.6
Voigt average shear modulus μ_{voigt} (GPa)	89.28	125.98
C' (GPa)	49.2	151.6
C_{11} (GPa)	243.4	464.7
C_{12} (GPa)	145.0	161.5
C_{44} (GPa)	116.0	108.9
E_{coh}/ a_0^2 (ratio)		1.4
Coherent twin energy (ratio)		1.5
a_0B (ratio)		2.5
a_0C' (ratio)		3.4
a_0C_{44} (ratio)		1.0
$a_0\mu_{voigt}$ (ratio)		1.6

[a] Material properties of Fe are from Ref [115][116]

[b] Materials properties of Mo are from Ref [89] except for T_m from Ref [117]

6.2 Computational Approach

We constructed 408 distinct grain boundaries in a periodic cell size of $20a_0/2$, where a_0 is the lattice spacing. The 408 boundaries, selected based on the periodic cell size, include 49 different misorientations. Based on the grain boundary planes, 127 are tilt-type grain boundaries, 24 are twist-type, and 257 mixed boundaries. It should be noted that the 408 boundaries do not provide comprehensive coverage of the grain boundary space. Because the grain boundaries were selected based only upon the size of the periodic repeat unit, it is unlikely that these 408 will represent the most frequently observed boundaries in the real materials. Grain boundary energies were computed using atomistic simulations based on the embedded-atom method (EAM) potential. The computational scheme is similar to prior studies of the grain boundary energy for FCC metals, which have been described in details in Ref. [10] and [69]. The Mendelev potential 2 was used for Fe [115] and Finnis-Sinclair potentials was used for Mo [89]. These potentials have appropriately reproduced the lattice constants, the elastic constants, and have been successfully used to simulate the grain boundary energies in Fe and Mo [107][108][109][113]. For each macroscopic grain boundary structure, large sets of initial configurations, roughly from 10^2 to 10^4, were minimized using the conjugate-gradient method in the LAMMPS code [70]. The initial configurations in Fe and Mo were generated using a similar method, which was already established by Olmsted et al. [69]. The only difference was that the atoms near the grain boundary were randomly perturbed before we removed the atoms that are very close to one another. Therefore, we will have more initial configurations and this should improve the chances of finding the actual energy minimum. The grain boundary energy, which is the global energy minimum for each macroscopic grain boundary, was chosen from the lowest energy from the large initial configurations.

6.3 Results and Discussion

The calculated boundary energy of Fe is shown as a function of disorientation angle in **Figure 6.1a**. The equivalent plot for Mo is shown in **Figure 6.1b**. The energies of 408 boundaries were separated into three categories: tilt (diamonds), twist (squares), and mixed boundary (circles) that have both twist and tilt components. Note that asymmetrical boundaries, symmetrical boundaries, symmetrical boundaries with (110) planes, and symmetrical boundaries with (112) planes, were colored blue, red, green, and black respectively. As shown in **Figure 6.1**, it clearly demonstrates that the (110) symmetrical boundaries are the low boundary energy regardless of the grain boundary types and the disorientation angle. These results are consistent with the previous results [109] and in fact emphasize that grain boundary energy could be thought of as the total energy of adjoining surfaces minus the bonding energy [1][2]. The (110) surface has the lowest energy, so, symmetric grain boundaries composed of two (110) planes have much lower boundary energies than the asymmetrical grain boundaries with boundary planes composed of planes with higher energy orientations.

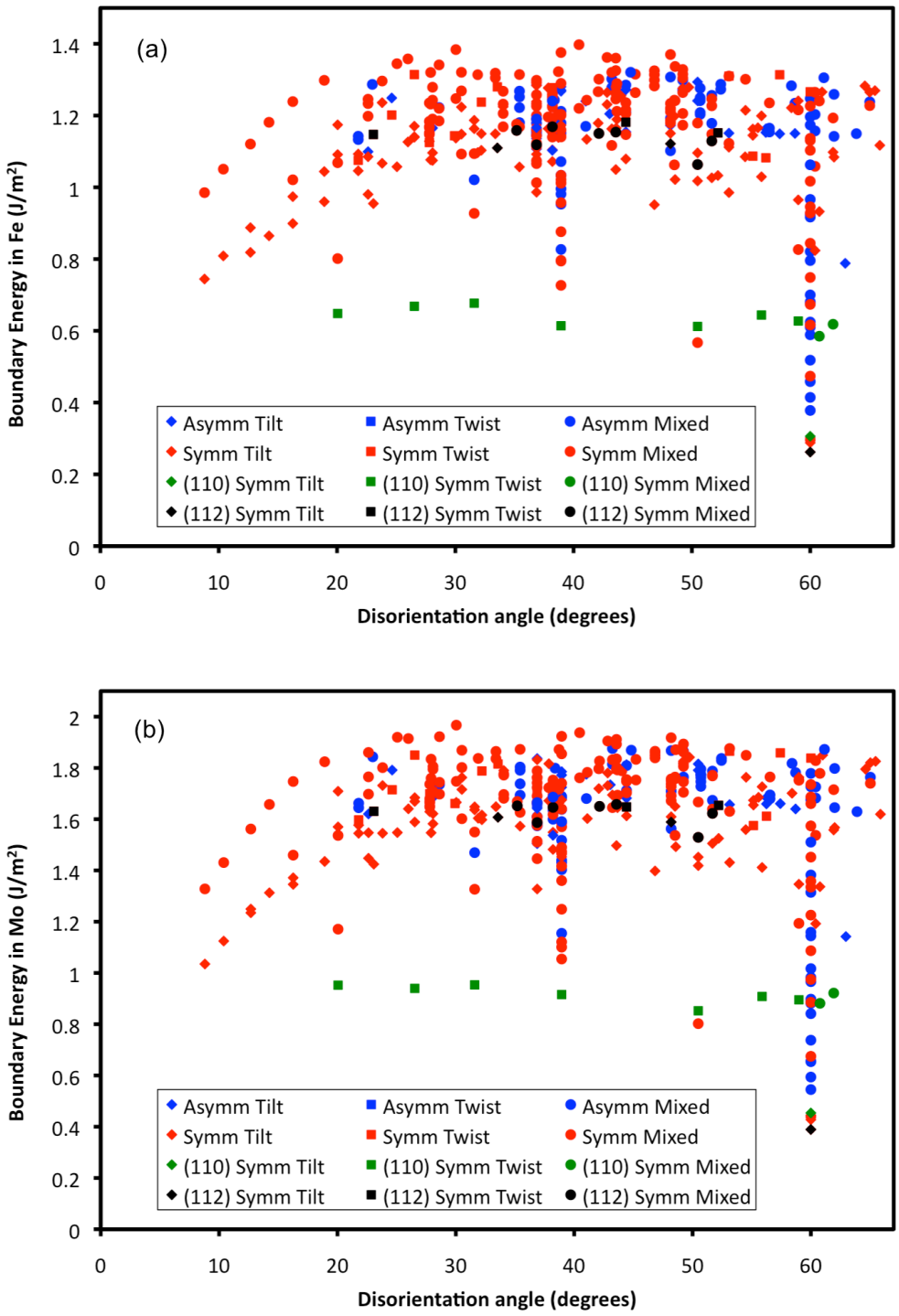

Figure 6.1. The calculated boundary energies of Fe (a) and Mo (b) plotted versus a disorientation angle. The grain boundaries are separated into three categories: tilt boundaries (diamonds), twist boundaries (squares), and mixed boundaries (circles). Asymmetrical boundaries, symmetrical boundaries, (110) symmetrical boundaries, and (112) symmetrical boundaries, are colored blue, red, green, and black respectively.

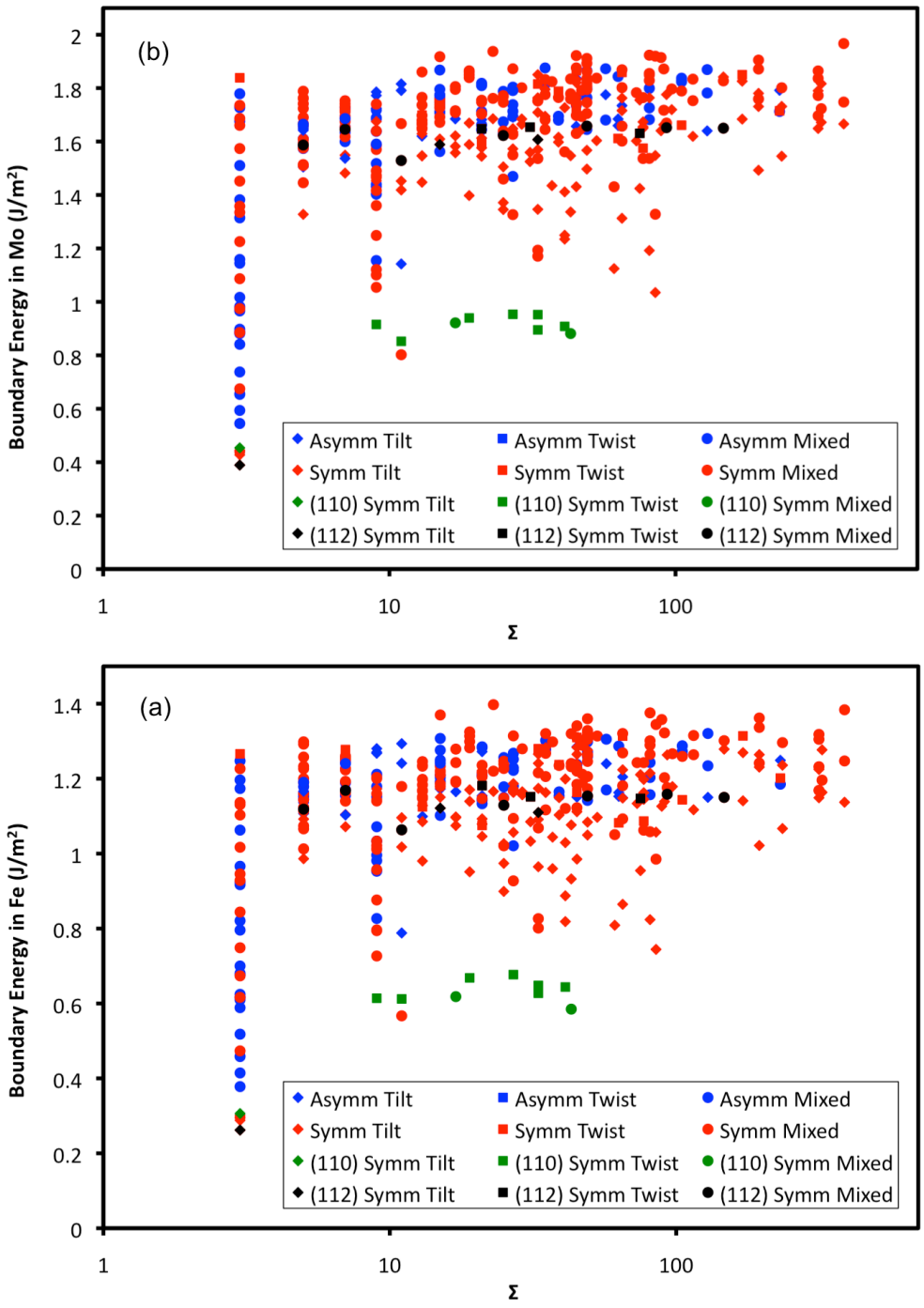

Figure 6.2. Calculated boundary energies for Fe (a) and Mo (b) plotted versus Σ, the inverse density of coincident lattice sites. The grain boundary types are colored the same as in Figure 6.1.

It important to mention that the symmetrical mixed boundary with (741) planes at the disorientation angle of 50.48° has a uniquely low energy, which is even lower than the (110) symmetric twist boundary at this disorientation angle. It is possible that the long-range interaction between atoms across the grain boundary plane could enhance the bonding energy and lead to a reduction in the grain boundary energy. To investigate this, we plotted the computed energies for Fe and Mo as a function of Σ value, which is the inverse of the density of coincident lattice sites. **Figure 6.2** shows the relationship between the calculated boundary energies in Fe and Mo plotted versus Σ with the color marks the same as in the **Figure 6.1**, and clearly demonstrates that the value of Σ is a poor predictor of grain boundary energy. The (741) symmetrical mixed boundary is at Σ11 with the boundary energy of 0.57 J/m^2 (Fe) and 0.80 J/m^2 (Mo). We also observed that the (751) symmetrical mixed boundary at Σ3 also has low energies of 0.47 J/m^2 (Fe) and 0.68 J/m^2 (Mo). However, at this Σ3, three asymmetrical mixed boundaries with boundary planes of (11,7,1)(3,3,1), (8,3,2)(6,5,4), and (13,11,5)(5,3,1), have lower energy than the (751) boundary in both Fe and Mo data set, as in **Figure 6.2a**, and **Figure 6.2b** respectively.

There are 40 Σ3 boundaries in the set of 408 grain boundaries. The energy of these Σ3 boundaries ranges from 0.26 J/m^2 and 1.27 J/m^2 in Fe and from 0.39 J/m^2 and 1.84 J/m^2 in Mo. This energy range indicates that the energies of Σ3 boundaries are strongly influenced by the boundary plane orientation, which is consistent with the measurement and simulation results for Fe and Mo [8][107][109][113]. If surface energy were the only factor that determined grain boundary energies, then one would expect the energy of the symmetrical (112) boundary to be greater than that of the symmetrical (110) boundary [118]. However at the Σ3 misorientation, the energy of the (110) symmetrical tilt grain boundary, 0.31 J/m^2 in Fe and 0.45 J/m^2 in Mo, is slightly higher than that of the (112) symmetrical tilt grain boundary (the coherent twin boundary), 0.26 J/m^2 in Fe and 0.39 J/m^2 in Mo. The relatively low energy of the coherent twin boundary is consistent to the measured boundary energy in Fe [8] and Mo [119].

In addition, the energy of the (110) symmetric grain boundary at Σ3 is much lower than the other (110) symmetric boundaries. Therefore, it is possible that bonds within the interface at this boundary are responsible for the lower energy. Note that there are other Σ3 grain boundaries in Fe and Mo whose energies are near the maximum of each data set, showing that it is not the misorientation that confers low energy to a grain boundary, but the details of the interface structure. Because the grain boundary energy is determined from the sum of the two surface energies minus the bonding energy, we can approximately determine the boundary energy if we know the surface and the bonding energies. As a simple approximation, the bonding energies can be assumed to be constant. However, there are expected to be significant variations for special, high symmetry boundaries where the bonding energy will be a sensitive function of interface structure. This sensitivity is probably the reason that the (112) symmetric Σ3 boundary has a lower energy than the (110) symmetric Σ3 boundary.

Nevertheless, the distribution of grain boundary energies for Fe and Mo in **Figure 6.1** and **Figure 6.2** are very similar. To investigate the correlation between grain boundary energies in Fe and Mo, a comparison of the 408 calculated boundary energies is shown in **Figure 6.3**. The data are colored according to the grain boundary type: (110) symmetrical boundaries (green circles), Σ3 boundaries (red squares), the coherent twin boundary (black square), and the other type of boundaries (blue diamonds). The scaling factors associated with the ratios of $a_0\mu_{voigt}$, the coherent twin energy, and a_0C_{44} are shown as lines in the **Figure 6.3**. There is a nearly perfect correlation; the correlation coefficient is equal to 0.99. The lowest boundary energy is the coherent twin boundary with energies of 0.26 J/m^2 and 0.39 J/m^2 in Fe and Mo, respectively. However the highest boundary energy in Fe (1.40 J/m^2) and Mo (1.97 J/m^2) is not the same grain boundary. However, in this part of the distribution, there are more boundaries with nearly degenerate energies than at lower energies.

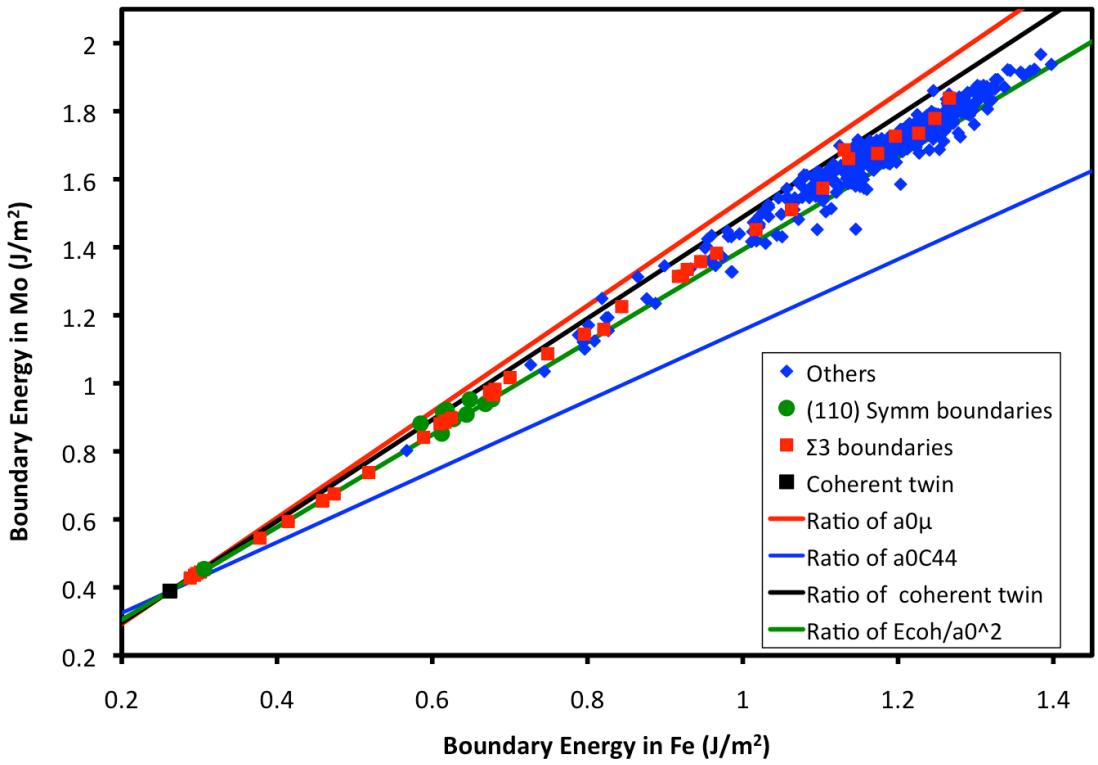

Figure 6.3. The relationship between the calculated boundary energies for Fe and Mo. Each point corresponds to two crystallographically identical grain boundaries in two different materials. The horizontal and vertical axes show the boundary energy in Fe and Mo respectively. Note that the data are colored according to the grain boundary types: (110) symmetrical boundaries (green circles), Σ3 boundaries (red squares), the coherent twin boundary (black square), and the other type of boundaries (blue diamonds). Lines show scaling factors predicted by the various materials parameters.

The EAM potential, which was used to determine the boundary energy, could play a major role in the scatter. It should also be noted that for each macroscopic grain boundary, the microscopic configurations, which specify the arrangements of atoms at the grain boundary, might be not the same for all boundaries in Fe and Mo. Nonetheless, the results in **Figure 6.3** reveal that all types of grain boundaries ranging from low to high boundary energy follow the same trend. It is possible that the ratio of grain boundary energies in Fe and Mo are similar because these quantities scaled with the ratio of the bond strength (cohesive energy). Because the dimension of the grain boundary energy is energy per length squared, it is required

to divide the cohesive energy by the square of the lattice constant (E_{coh}/a_0^2). Interestingly the ratio of the E_{coh}/a_0^2 (1.4) is equal to the actual scaling factor (see **Figure 6.3**). It should be noted that while the grain boundary energies between these two BCC metals are scaled with E_{coh}/a_0^2, the boundary energies in FCC metals are not scaled with E_{coh}/a_0^2 but strongly scaled with the ratio of a lattice constant multiplied by shear modulus (a_0C_{44}) and a lattice constant multiplied by Voigt average shear modulus ($a_0\mu_{voigt}$) [10][69]. Our results show that the ratio of shear modulus (a_0C_{44}) predicts a ratio of 1.0, which is clearly inconsistent with the actual scaling factor (1.4). The ratio of $a_0\mu_{voigt}$ (1.6), which is the average elastic modulus of an aggregate of crystals with all possible lattice orientations [120], is also in poor agreement with the actual scaling factor. At this point, it is not clear how the grain boundary energy in Fe and Mo with BCC structure is scaled with the ratio of the E_{coh}/a_0^2. It is possible that the grain boundary energy in Fe and Mo are correlated with E_{coh}/a_0^2 might be coincidental; more boundary energies of different BCC metals are needed to confirm these findings.

Recently, a large data set of grain boundary energies of BCC Fe was experimentally measured. The measured boundary energies of BCC Fe were extracted from a ferritic steel, which has an average grain size of $\sim$ 6μm and a number of alloying elements that were not accounted for in the simulation [8]. The 3D microstructure was characterized using focused ion beam serial sectioning combined with an electron backscatter diffraction (EBSD) system. The measured grain boundary energies were then calculated using Morawiec's procedure described in §2.3 [8][79].

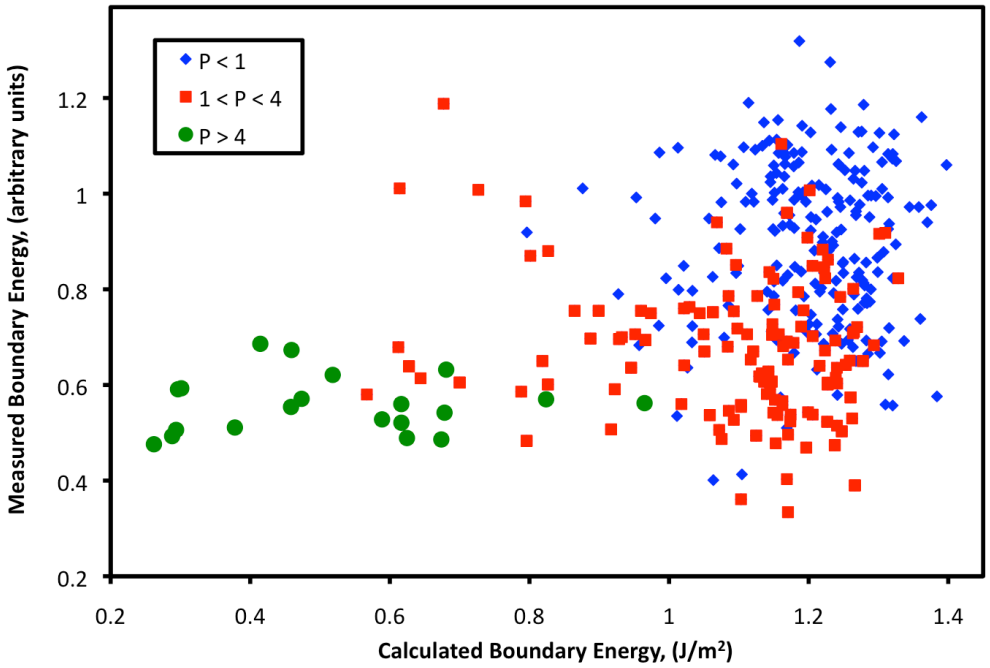

Figure 6.4. The relationship between measured and calculated grain boundary energy in Fe. Note that the data fall into three distinct population groups: P < 1 (blue diamonds), 1 < P < 4 (red squares), and P > 4 (green circles).

We compare our simulated boundary energies in Fe to the experimental grain boundary energies (see **Figure 6.4**). The data are colored according to the observed grain boundary population (P) [8]. Note that there is a weak correlation between measured and calculated boundary energies. Nonetheless the results show that the data on the plot are clustered corresponding to the three distinct population ranges. Specifically, grain boundaries with fewer observations (P < 1 MRD) mostly have higher boundary energies as determined from both measurement and computation, whereas more frequently observed boundary grain boundaries (P > 4 MRD) are relatively low in both measured and calculated boundary energies. It should be pointed out that both energy data sets have sources of error and uncertainty, which could result in a broad scatter and a weak Pearson correlation coefficient (R= +0.32).

The experimental measurement of grain boundary energy presumed that all

grain boundary triple junctions were in thermodynamic equilibrium and grain boundary energies were close for grain boundaries that are close in crystallographic space [79]. Therefore a large data set of triple junctions, which cover the full five crystallographic dimensions, was required. However, the grain boundary character distribution (GBCD) of this specimen is an anisotropic distribution. The most common boundary in the system was the {112} symmetric tilt with the Σ3 misorientation (the coherent twin boundary) [8]. It should be noted that the grain boundary energies were derived from the GBED in the same way as we obtained the grain boundary population for a specific type of grain boundary. As a result, poor statistics of non-uniform sampling of grain boundary might lead to an error of measured boundary energies [4]. For example, the experimental grain boundary energy distribution (GBED) of Fe contains many zero values (where there were no observations), which are not physically meaningful description of the grain boundary energy.

It should be noted that grain boundary energies are the average values of the grain boundary energies that have the same bi-crystal symmetry in the discretized system. Therefore for a specified grain boundary, zero values in certain categories of the experimental data can lead to an underestimation in the energy. To ameliorate this problem, only grain boundary energies that contained less than 5% of zero points are included in the comparison in **Figure 6.4**. On the other hand, the calculated boundary energies could also have errors from the grain boundary construction, minimization procedures, and EAM interatomic potential function. Even though a large number of initial configurations are minimized, the global minimum might not be a true global minimum [4]. Furthermore, the framework of the grain boundary energy calculation minimized the excess enthalpy at 0 K, rather than the free energy. Computational studies recently showed that grain boundary energies decrease with temperature [121][85]. However, it is possible that not all of the boundary energies vary with temperature in a similar manner [1]. In addition, it should be noted that the measured boundary energies were derived from a ferritic steel. Previous studies of the effect of solute atoms on the grain boundary energies

suggested that impurities could both increase or decrease boundary energies, depending on the change in grain boundary structure [11][122][123]. However, we currently don't have measured boundary energies of high purity BCC Fe to compare with this measured boundary energies [8]. Even though the point-by-point comparison does not obviously show the linear relationship, the average relationship between measured and calculated boundary energies, as illustrated in **Figure 6.5**, represents a strong linear relationship. In the plot, measured and calculated boundary energies were classified into equally spaced bins with a width of 0.05 arbitrary units and 0.05 J/m^2 respectively. The average result clearly reveals a strong linear correlation (+0.91). This high correlation coefficient suggests that the measured boundary energy validates the calculated boundary energy.

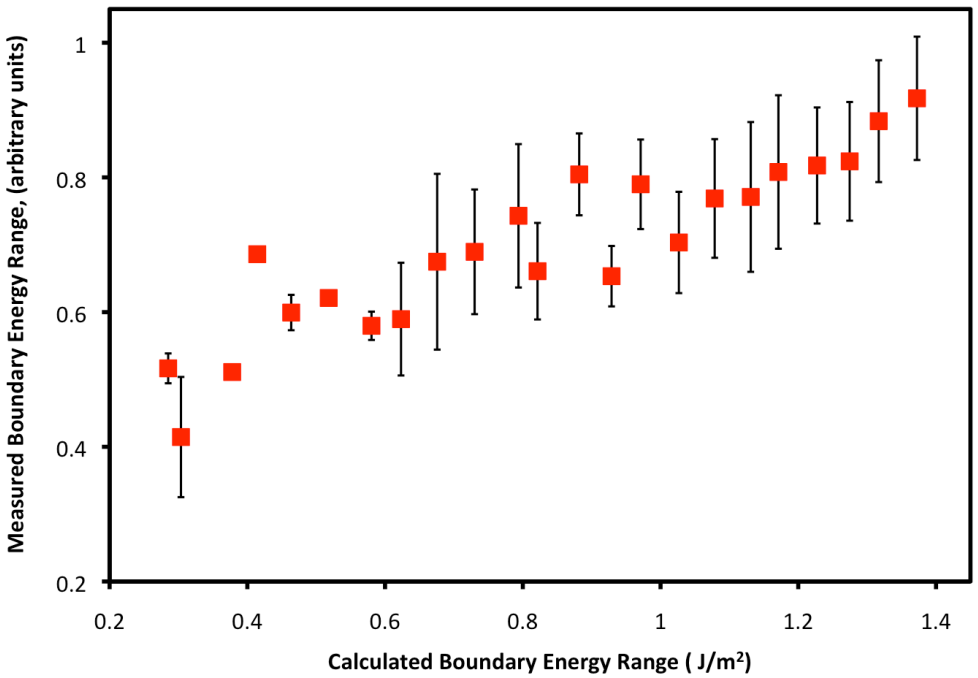

Figure 6.5. The average relationship between measured and calculated boundary energies. Error bars were plotted with 0.5 standard deviation of the measured boundary energies. Note, the variances of the calculated boundary energies are smaller than the width of the markers.

In conclusion, we found that the calculated boundary energies of Fe and Mo

were strongly correlated with a correlation coefficient of 0.99. The slope of the linear relationship between the calculated boundary energies of Fe and Mo scaled with the ratio of E_{coh}/a_0^2. The calculated boundary energies are weakly correlated to the experimentally measured boundary energies. However on average, the comparison between computational and experimental boundary energies reveals a strong linear correlation, which validates the calculated boundary energy data set.

Theoretical studies suggested that the anisotropy of experimental GBCDs are strongly affected by the energy anisotropy rather than by the mobility anisotropy [45][46][47][106]. The anisotropy of the GBCD is inversely correlated to the anisotropy of grain boundary energy [5][6][43][44][45][46][47][106]. Recall that the critical event model (see **Figure 2.4**) [47] demonstrated that the anisotropy of the GBCD depends on the energy anisotropy (the difference between maximum and minimum boundary energies). Even though this model can predict the GBCD with low energy anisotropy, it might not be representative of the energy anisotropy of FCC metals (Al, Au, Cu, and Ni) and BCC metals (Fe and Mo). If the grain boundary populations obey a fixed relationship between the grain boundary energies and the grain boundary populations, the GBCD correlation in FCC metals (**Table 4.1**) and in BCC metals (**Table 5.1**), could provide insight into the correlation of the calculated boundary energies in FCC and BCC metals [3][4][10][69]. To verify this hypothesis, we shall investigate the relationship between the experimental GBCDs and grain boundary energies.

Chapter 7

7. The Relationship between Grain Boundary Populations and Energies

7.1 Introduction

In this chapter, we shall investigate the relationship between the experimental GBCDs and the calculated grain boundary energies. For FCC metals, the GBCDs of Au and Cu are compared with the boundary energies calculated by Olmsted et al. [69]. We also use the previous GBCDs of Al and Ni, which were measured by Miller [25]. For BCC metals, we compare the GBCDs of Fe and Mo to our calculated boundary energies described in Chapter 6. The GBCD of BCC Fe derived from a 3D-EBSD measurement of a ferritic steel [8] is also included in the comparison between the grain boundary population and the calculated boundary. Throughout this chapter, when we refer to calculated grain boundary energies, this means the energies calculated at T= 0 K (enthalpy) using EAM simulations.

7.2 FCC metals

7.2.1 Results FCC metals

In the Chapter 4, we showed that the degree of correlation among the GBCDs of FCC metals is related to the microstructure and the crystallographic texture. Ag, which has the distinct microstructure, has the relatively weak correlation to the

other FCC specimens. While the GBCD of Ag is not as strongly correlated as the other FCC metals, chapter 5 showed that BCC metals had negative correlations with FCC structured Ni. These results imply that the grain boundary energy is the factor that controls the correlation amongst the GBCDs of the FCC materials. As mentioned earlier, atomistic simulations showed that the energies of crystallographically identical grain boundaries in Al, Au, Cu, and Ni are correlated to one other [10]. Because recent studies have reported the correlations among the GBEDs and GBCDs in Al and Ni [3][4], these results are included here for comparison.

The experimental GBCDs of Al, Au, Cu, and Ni in **Figure 7.1** show moderately negative correlations to the 388 calculated grain boundary energies, as listed in **Table 7.1**. It should be noted that the 388 calculated GB energies were selected based on their symmetry, and not their population. In fact, most of these boundaries have minority populations in the experimental data sets. The inverse correlations in Au and Cu are consistent with the previous results, which indicate that the anisotropic distributions of grain boundary populations are related to anisotropic distributions of grain boundary energy [5][6][7][21][46][47]. If we use the experimental population as an indication of the reliability of the observation, it is reasonable to consider only grain boundaries with populations greater than 0.5 MRD (the rational for this cutoff was previously addressed in §4.3).

Table 7.1. The correlation coefficients and slopes between experimental GBCDs and 388 calculate grain boundary energies.

Population-Energy	Pearson Correlation	Spearman Correlation		Pearson Correlation	Slope
Al: MRD-Energy	-0.61	-0.49	Al: ln(MRD)-Energy	-0.57	-8.66
Au: MRD-Energy	-0.49	-0.55	Au: ln(MRD)-Energy	-0.65	-11.74
Cu: MRD-Energy	-0.45	-0.41	Cu: ln(MRD)-Energy	-0.62	-5.94
Ni: MRD-Energy	-0.44	-0.40	Ni: ln(MRD)-Energy	-0.61	-8.66

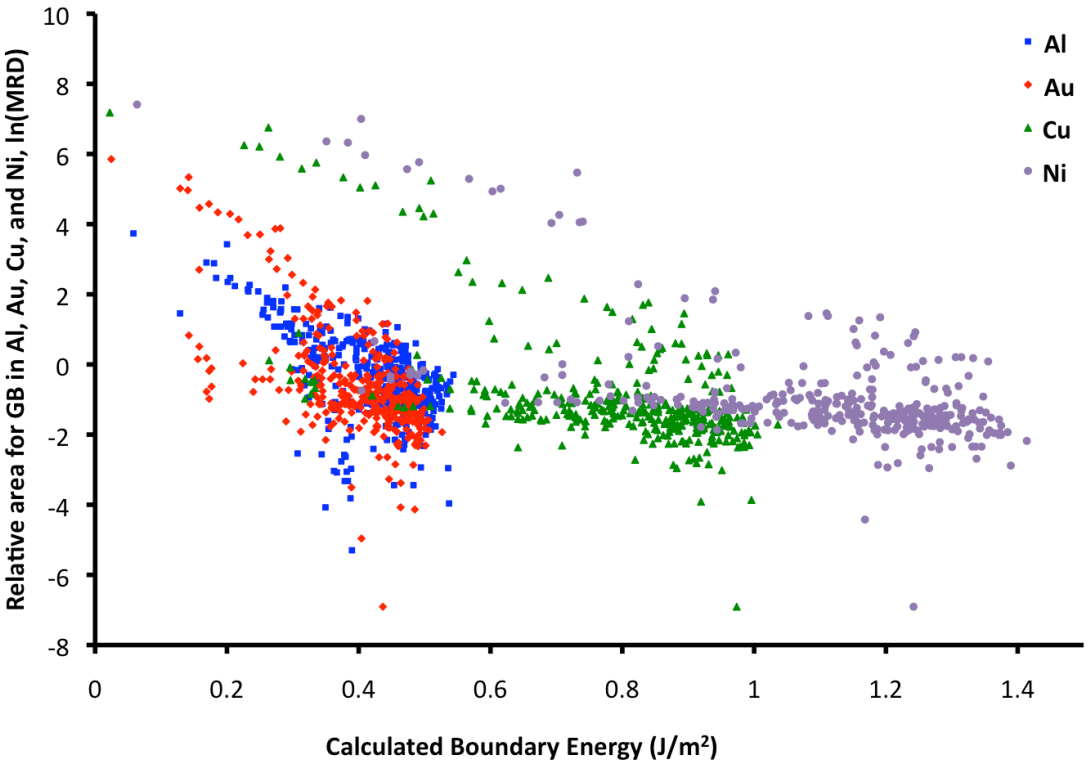

Figure 7.1. The relationship between experimental GBCDs and 388 calculated boundary energies. Each point corresponds to the same grain boundary type. The horizontal axis shows the calculated boundary energies, while the vertical axis shows the relative grain boundary areas in Al (blue), Au (red), Cu (green), and Ni (violet).

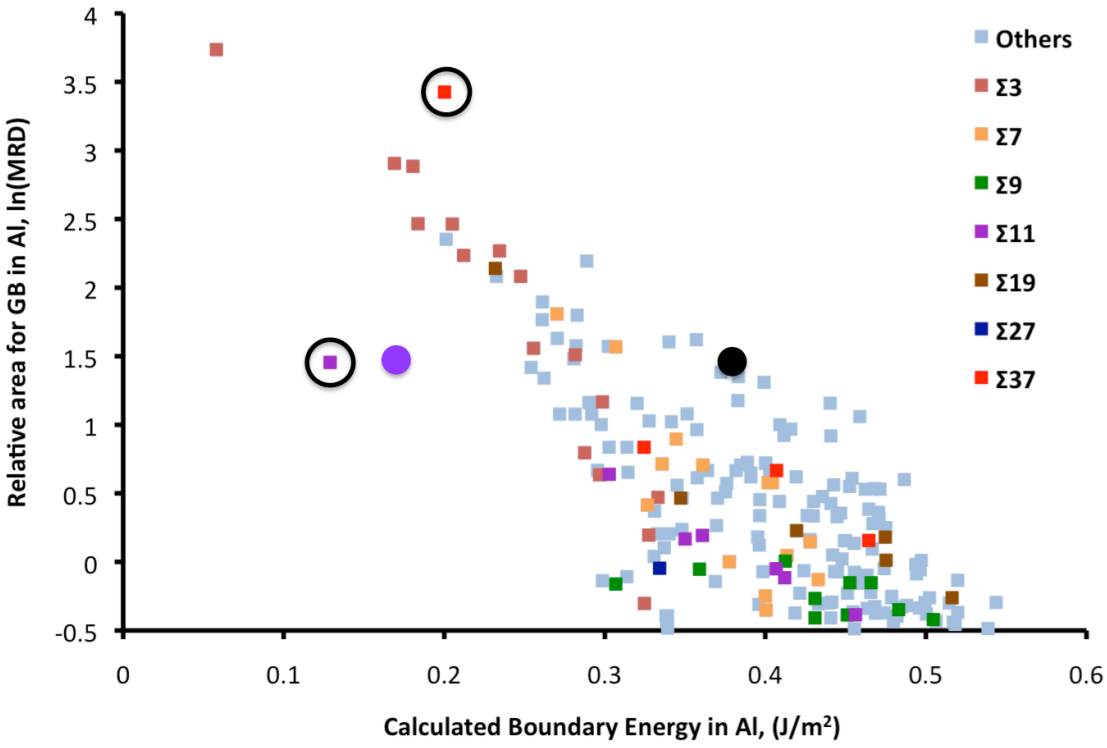

Figure 7.2. The relationship between grain boundary populations and calculated grain boundary energies in Al. Each point represents a grain boundary type, only boundaries with populations greater than 0.5 MRD are plotted. The horizontal axis shows the calculated boundary energies, while the vertical axis shows the relative grain boundary areas. Outliers are marked by black circles. The relative energies of the Σ11 (110)[311] boundary calculated by DFT (purple) and measured experimentally (black) are shown with the large solid circles.

In **Figure 7.2** we apply this cutoff (0.5 MRD) and plot experimental grain boundary populations of Al versus the calculated grain boundary energies and label the grain boundaries by type. Σ3 boundaries, the most populated boundaries, show a strong inverse correlation to the calculated grain boundary energies. The second most populated boundaries, Σ9, show the same trend but with a broad scatter, especially at high energies. The experimental GBCDs for low population boundaries have broad scatter, because these boundaries are observed less frequently and the populations are not determined accurately. The outlier of Σ37 50.6° (111)[111], circled in **Figure 7.2**, has a higher population because of its proximity to the coherent Σ3 twin boundary 60° (111)[111]. When the population of this boundary is

calculated, the bin containing the Σ3 twin boundaries may occasionally be sampled and this leads to an overestimation of the Σ37 grain boundary population [3]. The other outlier is the Σ11 50.5° (110)[311] symmetric tilt boundary. The population of the Σ11 boundary is significantly lower than the other boundaries with similar boundary energies. The Σ11 is one of energy cusps in **Figure 2.9b** and it is therefore possible that the underestimate is a result of its finite width compared to the discretization. If it were a narrow cusp, then the experimental GBCD calculated with a resolution of 10° will underestimate the population of this boundary, as previously observed for the coherent twin boundary in **Figure 4.7**. However, the population of this Σ11 boundary calculated with a resolution of 10° (4.3 MRD) is comparable to the one calculated with resolution of 8.2° (4.8 MRD), so we do not think this underestimate is a result of the discretization. We can also consider possible errors from the atomistic calculation of the grain boundary energy, which could yield an especially low energy for this Σ11. Even though several hundred to several thousand configurations are optimized via a molecular statics method using the EAM inter-atomic potentials, there is no guarantee that the lowest optimized energy for each grain boundary is the global energy minimum. However, this error would result in higher boundary energy rather than one that is too low. The Σ11 (110)[311] boundary energy in Al calculated by the *Ab initio* Density functional theory (DFT), 166.0 mJ/m^2 [124], appears to be higher than the one calculated by the EAM inter-atomic potentials, 128.9 mJ/m^2. Both the EAM and DFT calculated boundary energy of Σ11 (110)[311] are in poor agreement with the experimental value of 174-580 mJ/m^2, computed from the relative energy between the Σ11 and the coherent twin boundary (see **Figure 2.9b**) [73][74]. Even though the experimental value has a wide range, if the true value were in the center of the range (marked as a black solid sphere), it would not be an outlier in **Figure 7.2**. Therefore, the experimental population is in better agreement with the experimental energy than either of the simulated energies. It should be noted that the calculated grain boundary energies are simulated based on free energy minimization at 0 K (i.e. enthalpy). If all grain boundary energies scale with temperature in a similar manner, the calculated

enthalpies could then be interpreted as the relative boundary free energies. Recent computational studies suggested that the free energies of grain boundaries decrease with temperature from 0 K to near the melting point [85][86]. In addition, the experimental grain boundary energy of the Σ11 (113) boundary in Cu decreases with temperature in **Figure 2.9b** [53][73][74][76]. However, the same figure also suggests that not all grain boundary energies decrease at the same rate when increasing temperature. If the boundary energies of FCC metals annealed at temperatures listed in **Table 3.2** do not linearly decrease with temperature, the calculated boundary energies would not represent the actual relative grain boundary energies. In this case, the comparisons between grain boundary populations and calculated grain boundary energies in Al, Au, Cu, and Ni, would contain uncertainties. At this point, we do not have a way to determine these uncertainties.

The Σ37 50.6° (111)[111] and Σ11 50.5° (110)[311] also appeared as outliers when the experimental grain boundary populations and calculated grain boundary energies were compared for Au, Cu, and Ni. Both of the outliers have characteristics similar to those described in Al. In addition to these boundaries, the Σ19 46.8° (111)[111] in Au, Cu, and Ni (see **Figure 7.3**, **Figure 7.4**, and **Figure 7.5**), has a lower population than would be predicted by the calculated energy. The population of this boundary in Au (see **Figure 7.3**) is ln(MRD)=2.7, which is lower than suggested by its energy (ln(MRD) ~4.5). Although this boundary showed some sensitivity to the discretization, it was not strong enough to account for the large difference. While it is possible that the calculated boundary energy for this boundary is incorrect, there is no convincing argument for why the calculation would provide an energy that is anomalously low. One possibility is that the specific atomic configuration in the simulation that minimizes the energy is rare or even unique and, therefore, difficult to achieve in a real polycrystal where configurations of adjoining boundaries might constrain the local microscopic degrees of freedom. Investigating this possibility is beyond the scope of the current project.

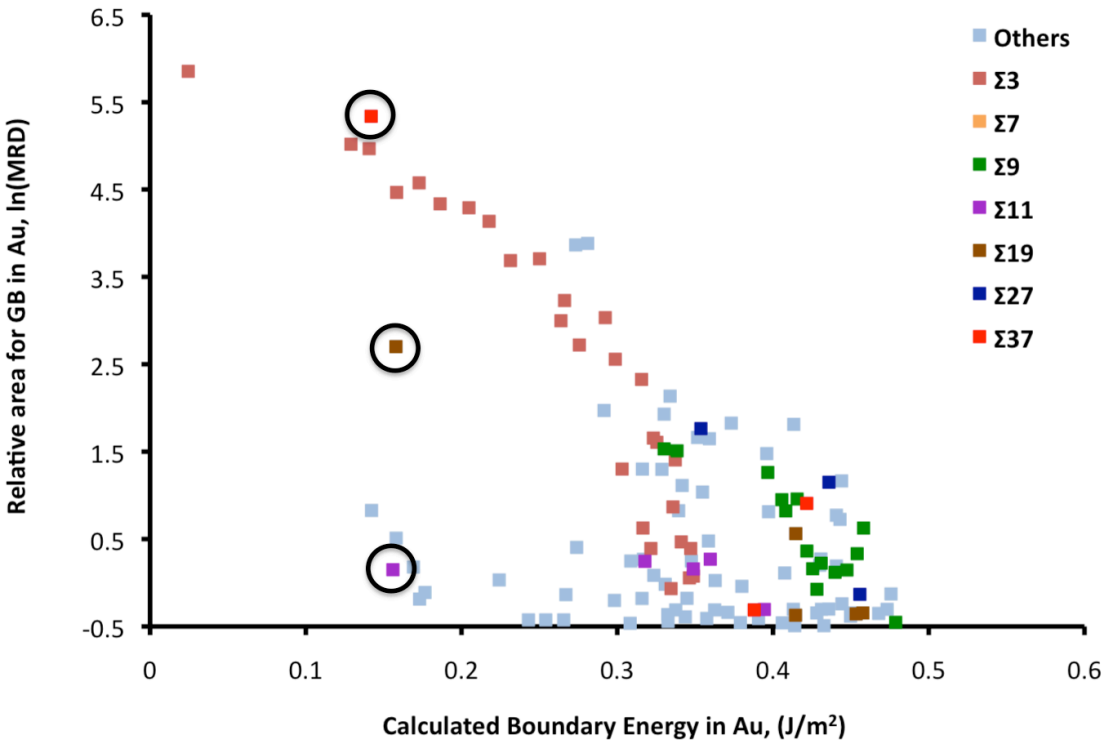

Figure 7.3. The relationship between grain boundary populations and calculated grain boundary energies in Au. Each point represents a grain boundary type, only boundaries with populations greater than 0.5 MRD are plotted. The horizontal axis shows the calculated boundary energies, while the vertical axis shows the relative grain boundary areas. Outliers are marked by black circles.

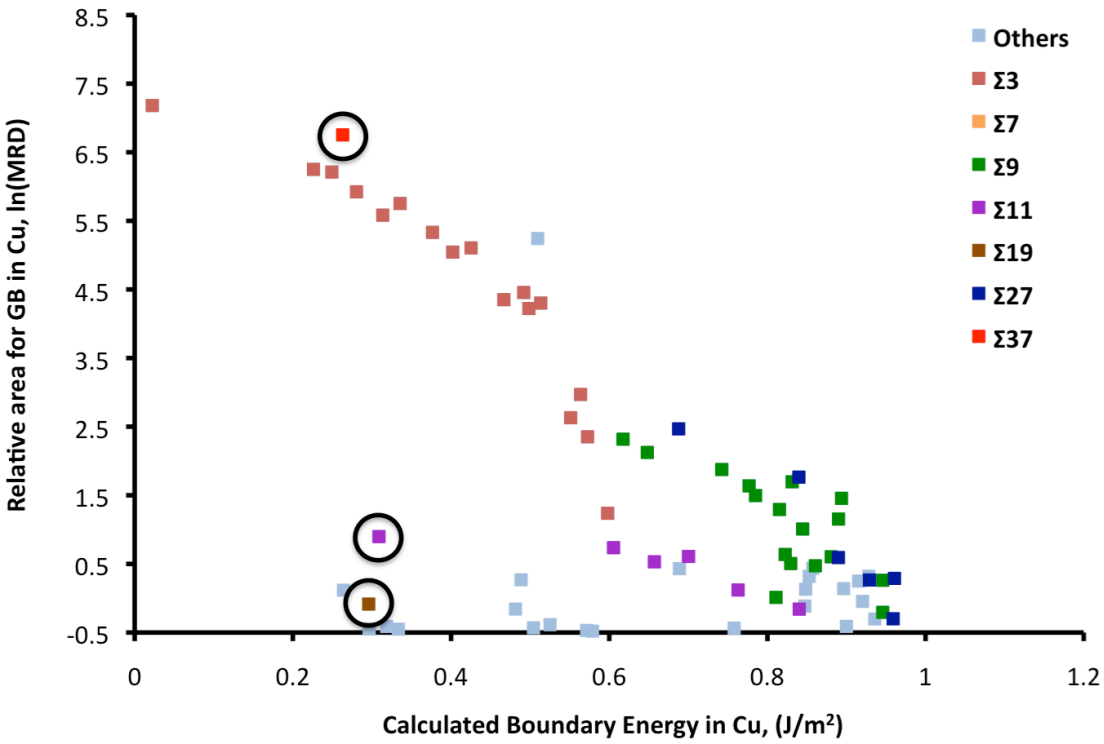

Figure 7.4. The relationship between grain boundary populations and calculated grain boundary energies in Cu. Each point represents a grain boundary type, only boundaries with populations greater than 0.5 MRD are plotted. The horizontal axis shows the calculated boundary energies, while the vertical axis shows the relative grain boundary areas. Outliers are marked by black circles.

We observed that the relative areas for twin-related grain boundaries (Σ3, Σ9, and Σ27) in Ni all linearly decrease as the grain boundary energies increase. However the large number of Σ3 boundaries in Ni makes the relative areas for all other grain boundaries so low that it is difficult to make a reliable comparison to the energies. Therefore, we repeated the normal GBCD calculation after excluding Σ3 boundaries. The list of reconstructed line segments, which are not the Σ3 misorientation, was obtained by using the twin_filter program version 01/25/2009 written by Rohrer [95]. There are 162,865 line segments, which is sufficient for the GBCD calculation with a bin resolution of 10° [14][16]. The relative areas for Σ7, Σ9, Σ11, and Σ27 in Ni are higher when the GBCD is calculated without the Σ3 boundaries (see **Figure 7.6**) than when it is calculated with all boundaries (see **Figure 7.5**). The increase in relative population is simply scaled with a factor,

magnifying the relatively more rare boundaries. While the relative areas of Σ7, Σ9, Σ11, and Σ27 grain boundaries are all inversely correlated with the calculated boundary energies, there is a different slope for each misorientation.

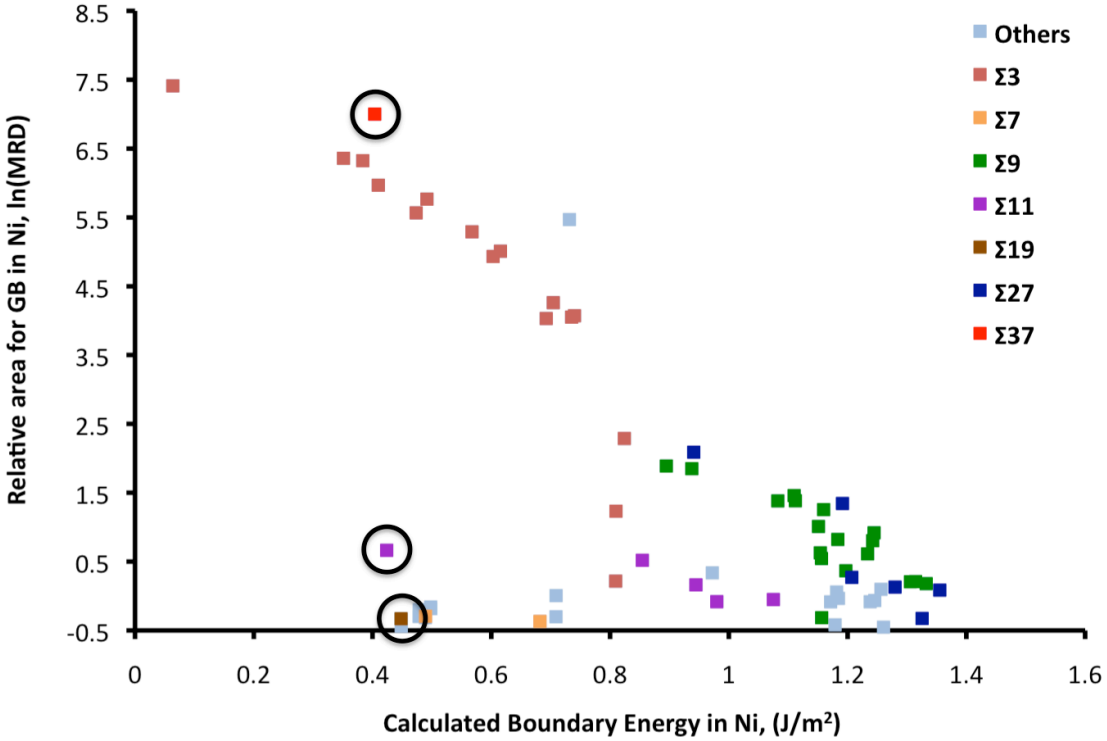

Figure 7.5. The relationship between grain boundary populations and calculated grain boundary energies in Ni. Each point represents a grain boundary type, only boundaries with populations greater than 0.5 MRD are plotted. The horizontal axis shows the calculated boundary energies, while the vertical axis shows the relative grain boundary areas. Outliers are marked by black circles.

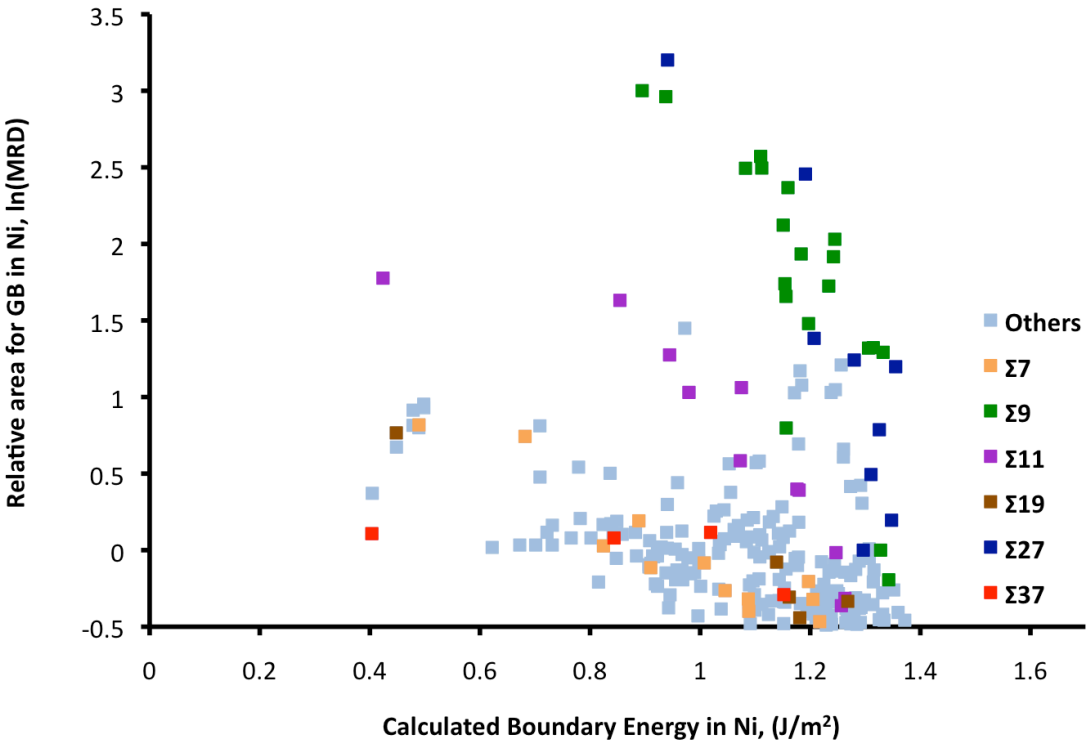

Figure 7.6. The relationship between grain boundary populations and calculated grain boundary energies in Ni after excluding Σ3 boundaries. Each point represents a grain boundary type, only grain boundaries with populations greater than 0.5 MRD are plotted. The horizontal axis shows the calculated boundary energies, while the vertical axis shows the relative grain boundary areas.

The relative populations of the coherent twin boundaries in Au, Cu, and Ni are significantly different, even though they are all annealed at about the same homologous temperature, T_H = 0.4. Therefore it is sensible to ask how the grain boundary network of FCC metals evolves during grain growth. Previous simulations of grain growth showed that the anisotropic distribution of grain boundaries is related to the energy anisotropy (see **Figure 2.4**). Even though the simulation was based on a simple model of grain boundary energy, which does not represent the actually energy distribution in FCC metals, it clearly showed that the anisotropies in the populations increase with the anisotropy in the energy [2][47][125]. Assuming that the 388 calculated boundary energies span the full five-dimensional grain boundary space [10], the energy anisotropy is therefore the difference between the

maximum and minimum energy, a parameter we will call the energy range. The results in **Table 7.2** reveal that the populations of coherent twin boundaries in Al, Au, Cu, and Ni are not correlated with the boundary energy but actually correlated to the energy range. We note that Al was annealed at much higher homologous temperature, T_H = 0.72 and this might lead to lower populations of coherent twin boundaries in Al. It should also be noted that the population standard deviation (P_σ) is also correlated to the energy standard deviation (E_σ) for Au, Cu, and Ni. The higher population of coherent twin boundary might enhance the populations of the twin-related boundaries. As a result, a higher population of the twin-related boundaries might also affect the relative areas of grain boundaries of other types, which are not twin-related boundaries. Even though extensive twinning might enhance the grain boundary populations of Σ9 and Σ27, the relative grain boundary populations for the twin-related grain boundaries follow the inverse correlation for these misorientations. Interestingly the relative areas for the twin-related grain boundaries (Σ3, Σ9, and Σ27) follow approximately the same scale in Al, Au, Cu, and Ni (see **Figure 7.7**). Those boundaries have nearly perfect correlations between grain boundary populations and calculated boundary energies as listed in **Table 7.3.**

Table 7.2. The homologous temperatures (T_H) of the annealed FCC specimens are listed with, the coherent twin energy, and the relative area for a coherent twin boundary (MRD). The energy range (mJ/m^2), which is defined by the difference between the maximum and minimum energy among 388 calculated grain boundary energies[10], is listed with the energy standard deviation (E_σ) and the population standard deviation (P_σ).

	T_H	Coherent Twin (mJ/m^2)	Coherent Twin (MRD)	Maximum (mJ/m^2)	Energy Range	E_σ (mJ/m^2)	P_σ (MRD)
Al	0.72	58.11	42	543.70	485.59	0.08	3
Au	0.43	24.48	349	526.40	501.92	0.08	25
Cu	0.43	22.25	1314	1035.99	1013.74	0.17	93
Ni	0.40	63.61	1654	1413.87	1350.26	0.23	113

Table 7.3. The correlation coefficients and slopes between experimental GBCDs and calculated grain boundaries energies for twin-related grain boundaries (Σ3, Σ9, and Σ27) in Al, Au, Cu, and Ni.

	Pearson Correlation	Spearman Correlation	Slope	k_BT (10^{-21} J)	α (10^{-20} m^2)
Al: ln(MRD)-Energy	-0.94	-0.95	-10.56	9.29	9.80
Au: ln(MRD)-Energy	-0.99	-0.99	-15.72	7.91	12.43
Cu: ln(MRD)-Energy	-0.99	-0.99	-8.92	7.91	7.06
Ni: ln(MRD)-Energy	-0.99	-0.99	-6.82	9.51	6.48

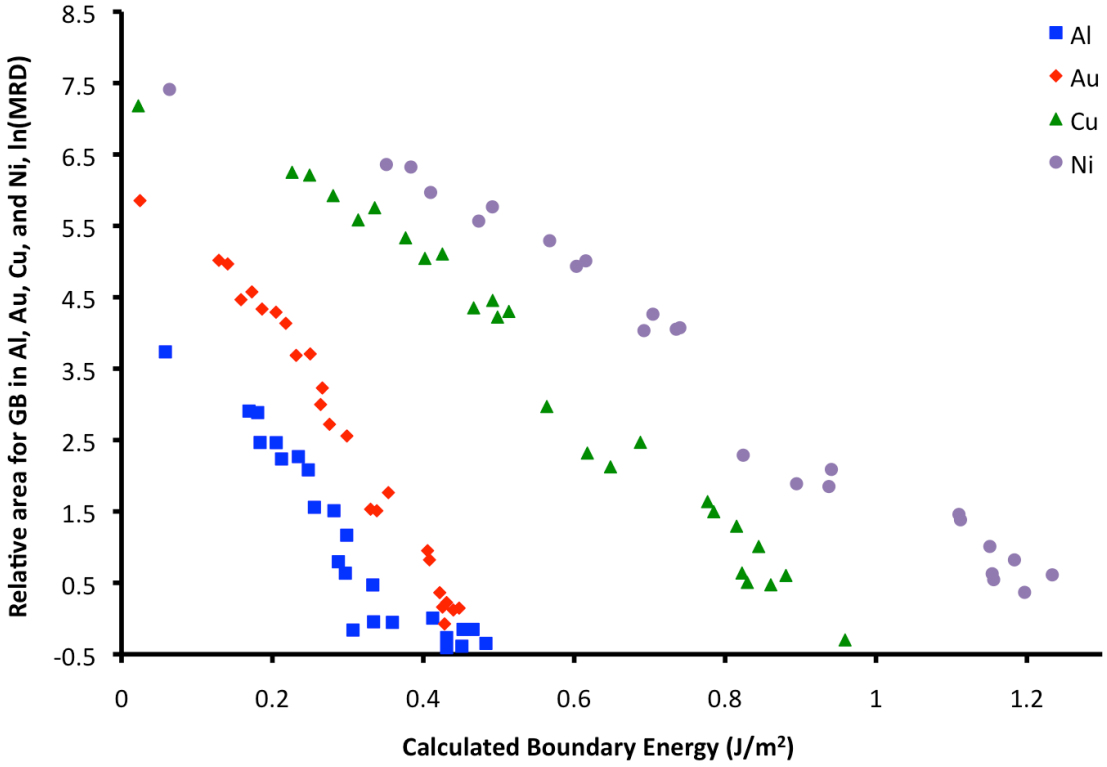

Figure 7.7. The relationship between grain boundary populations and calculated grain boundary energies for Σ3, Σ9, and Σ27 boundaries. The horizontal axis shows the calculated boundary energies, while the vertical axis shows the relative grain boundary areas in Al (blue), Au (red), Cu (green), and Ni (violet).

The inverse relationship between grain boundary populations and energies in **Figure 7.7** is consistent with the Boltzmann distribution. From Equation 2.17 in §2.4, it must be true that

$$N_{\Sigma 3} = N \times \frac{e^{\frac{-E_{\Sigma 3}\alpha_{\Sigma 3}}{k_B T}}}{Z(T)} \qquad \text{Equation 7.1}$$

Dividing Equation 2.17 by Equation 7.1, we obtain

$$\frac{N_i}{N_{\Sigma 3}} = \exp\left(\frac{E_{\Sigma 3}\alpha_{\Sigma 3} - E_i\alpha_i}{k_B T}\right) \qquad \text{Equation 7.2}$$

By assuming that $\alpha_i = \alpha_{\Sigma 3} = \alpha$ for those twin-related grain boundaries (Σ3, Σ9, and Σ27), Equation 7.2 is then described by

$$\ln(N_i) = \frac{-E_i\alpha}{k_B T} + \left(\frac{E_{\Sigma 3}\alpha}{k_B T} + \ln(N_{\Sigma 3})\right) \qquad \text{Equation 7.3}$$

The unknown constant $\left(\frac{\alpha}{k_B T}\right)$ could be derived from the slope of the data plotted in **Figure 7.7** and listed in **Table 7.3**. The slopes are temperature dependent and related to the strength of energy anisotropy. By assuming that the grain boundary energy is related to the grain boundary population by the Boltzmann distribution, we could construct GBEDs based on measurements of the GBCD. According to Equation 7.3, the grain boundary energy (E_i) could be determined by

$$E_i = E_{\Sigma 3} - \frac{k_B T}{\alpha}\ln\left(\frac{N_i}{N_{\Sigma 3}}\right) \qquad \text{Equation 7.4}$$

Where the values of $\ln(N_i/N_{\Sigma 3})$ are determined from the experimental GBCDs and α is a material constant listed in **Table 7.3**. If this process is valid, it would enormously simplify the process of deriving grain boundary energies from experimental GBCDs. It should be noted that α is derived from the GBCDs of twin-related grain boundaries (Σ3, Σ9, and Σ27). Strictly speaking, therefore, this extrapolation scheme is limited to only these grain boundary types.

7.2.2 Discussion FCC metals

We have shown that the experimental GBCDs in Au and Cu are inversely correlated to the calculated boundary energies, which is consistent with the previous studies of Al and Ni [3][4]. While we observed that the relative areas of Σ3, Σ9, Σ11, and Σ27 grain boundaries in Al, Au, Cu, and Ni, are all inversely correlated with calculated boundary energies, the slopes of those twin-related grain boundaries (Σ3, Σ9, and Σ27) are comparable and higher than the slope for Σ11 boundaries. The relative populations of these twin-related grain boundaries could be influenced by the geometrical constraint of the triple junction between grains A, B, and C, described as the following [126].

$$\Sigma_{CA} = \Sigma_{AB}\Sigma_{BC}/d^2 \qquad \text{Equation 7.5}$$

Where Σ_{AB}, Σ_{BC}, and Σ_{CA} are the CSL values of the three boundaries that meet at the triple junction, d is an integer common divisor of Σ_{AB}, Σ_{BC}. To investigate the influence of geometric constraints to the grain boundary population distribution, we examine different types of triple junctions by using the following procedures. The list of triple junctions was obtained by sorting the reconstructed line segments by using the find_tjs program, version 02/03/2008. The tj_sort_wcoherency program (version 11/05/2008) was then used to indentify types of triple junctions. We plot the number fraction of different types of triple junctions in Al, Au, Cu, and Ni in **Figure 7.8**. The probabilities of forming a certain type of triple junction can be calculated using the assumption that the boundaries are randomly mixed at the triple junctions. While the probability of forming R-R-R is the third power of a random grain boundary fraction (R^3), the probability of forming Σ3-Σ3-Σ9 is second power of Σ3 grain boundary fraction $(\Sigma3)^2$ because the probability of forming the Σ9 boundary is not independent but constrained by the geometry at the triple junction. Because Σ3, Σ9, and Σ27 boundaries have significantly larger populations than any other misorientations in Al, Au, Cu, and Ni, we could assume that the random grain boundary (R) fraction is equal to one minus

the total fractions of the Σ3, Σ9, Σ27a, and Σ27b grain boundaries (see **Table 4.2**). Based on these criteria, the probabilities of forming the R-R-R junctions in Al (89.0%), Au (35.9%), Cu (10.2%), Ni (13.1%) are comparable with the measured ones (Al = 85.8%, Au = 35.5%, Cu = 9.2%, and Ni = 12.3%) as shown in **Figure 7.8**. It should be pointed out that the probabilities of forming the Σ3-Σ3-Σ9 junction in Al (0.13%) and Au (7.5%) are higher than the measured values (Al=0.03% and Au=4.9%). Interestingly, the probabilities of forming the Σ3-Σ3-Σ9 junction in Cu (23.4%) and Ni (19.8%) are comparable with the measured values (Cu = 25.0% and Ni = 20.8%). These results indicate that the R-R-R junction for Al, Au, Cu, and Ni are random mixing. It is important to note that the Σ3-Σ3-Σ9 junctions in Cu and Ni are random mixing and, therefore, enhanced by the geometrical constraint at triple junction.

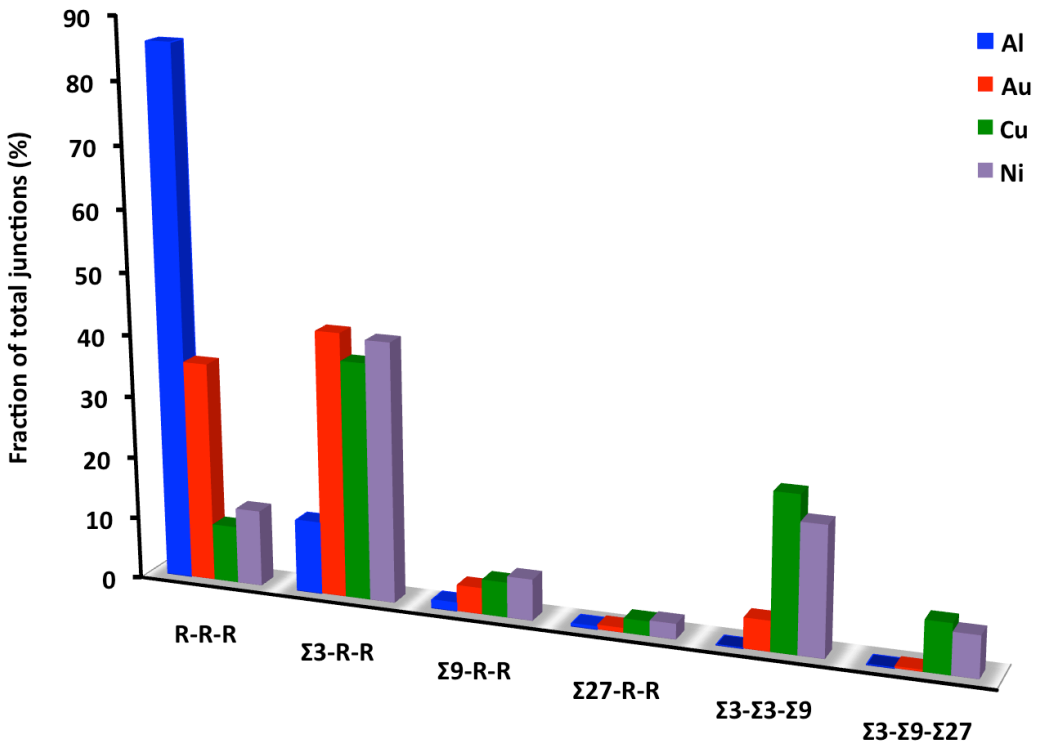

Figure 7.8. The schematic diagram shows the number fractions of different types of triple junctions in Al, Au, Cu, and Ni. Where R is referred to a random grain boundary other than Σ3, Σ9, or Σ27.

While we observed that in Al the numbers of Σ9-R-R junctions is slightly larger than that of the Σ3-Σ3-Σ9 junctions, the numbers of Σ9-R-R junctions in Au, Cu, and Ni are much smaller than those of the Σ3-Σ3-Σ9 junctions. In addition, the numbers of Σ3-Σ9-Σ27 junctions in Cu (8.1%) and Ni (6.8%) are higher than those of the Σ27-R-R junctions (Cu = 2.3%, Ni = 2.5%). These results demonstrate the number fractions of twin variant grain boundaries (Σ9 and Σ27) in Cu and Ni clearly arise as a geometrical consequence of Σ3 boundaries meeting at triple junctions [127][128]. This experimental evidence is consistent with previous studies of brass [13] and Ni [42]. The abundance of Σ3 boundaries means that they are more likely to intersect at triple junctions and enhance the formations of the twin-related boundaries (Σ9 and Σ27 boundaries). For that reason Al and Au specimens, which have fewer Σ3 boundaries, are less influenced by twinning than Cu and Ni. The results in **Figure 7.8** confirm that the number fractions of triple junctions in Au, Cu, and Ni are influenced by the crystallographic constraint. Because the triple junction distribution strongly influences the misorientation angle distribution and the GBCD, we could investigate the influence of the crystallographic constraint by comparing the GBCD to the misorientation angle distribution. To examine this possibility, we compare the misorientation angle distribution to the plots between grain boundary populations and calculated grain boundary energies in Al, Au, and Cu. Note that the data in the misorientation angle distributions, which are colored according to a grain boundary type, also include other misorienations that share the same misorientation angle.

The grain boundary populations of Al, which have a random misorientation angle distribution (**Figure 7.9a**), are overall linearly correlated to the calculated boundary energies (**Figure 7.9b**). While the fraction at the Σ9 misorientation angle in the Al is as expected in a random distribution, (**Figure 7.9a**), the observed fractions of the Σ9 boundaries are relatively high in Au (**Figure 7.9c**) and significantly higher than random in Cu (**Figure 7.9e**).

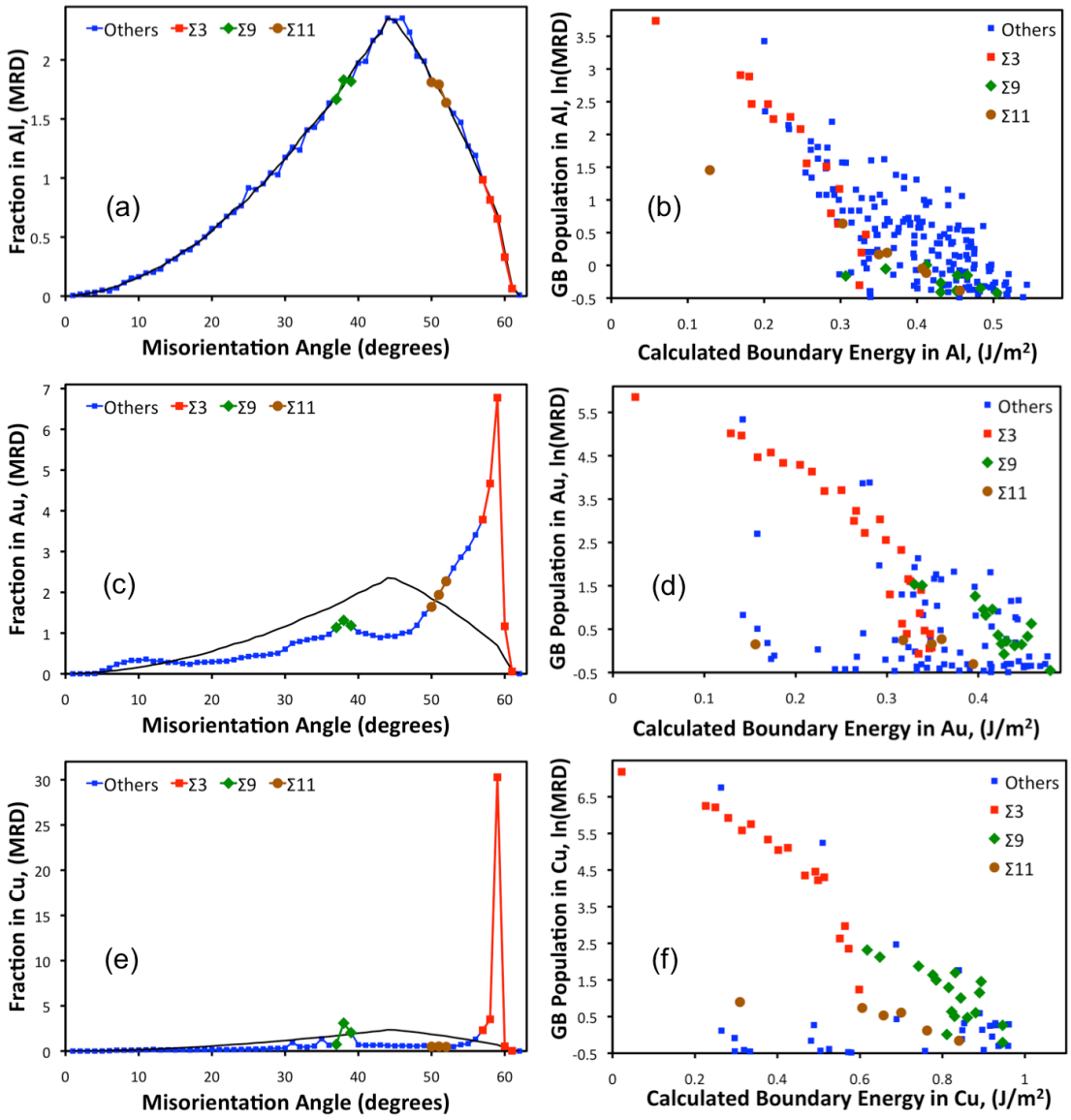

Figure 7.9. Misorientation angle distributions in, (a) Al, (c) Au, and (e) Cu. Black lines show the Mackenzie distribution. The relationship between grain boundary populations and calculated grain boundary energies in Al, Au, and Cu are plotted in (b), (d), and (f) respectively. Each point represents a grain boundary type, only boundaries with populations greater than 0.5 MRD are plotted. The horizontal axis shows the calculated boundary energies, while the vertical axis shows the relative grain boundary areas. The data are colored according to a grain boundary type: Σ3 (red squares), Σ9 (green diamonds), and Σ11 (brown circles), and the others boundaries (blue squares). Note that results of the Ni specimen are similar to the results for the Cu specimen.

These results indicate that Σ9 boundaries are frequently observed in Cu and Ni not only because they are low in energy, but also as a consequence of the Σ3 boundaries which can meet to form Σ9 boundaries. On the other hand, the fractions of boundaries with the Σ11 misorientation are less than what is expected in a random distribution for Cu and Ni. Because the grain boundary populations are defined from the relative area for grain boundary, the enhancement of twin related boundaries results in a decrease in the grain boundary populations for the Σ11 boundaries. In other words, having an anisotropic misorientation distribution with strong maxima for certain boundaries biases the inverse correlation between grain boundary population and energy for other boundaries and causes different slopes at each misorientation.

It was reported that the misorientation angle spread of Σ3 is lower than 3° in multiplely twined polycrystalline materials (silicon ingots, Cu thin films, nickel superalloys, and Ni-Bi alloys) [129][130]. Because the misorientation of Σ3 is not exact, the misorientation angle spreads of grain boundaries generated from the twining process are higher for Σ9 than Σ27 misorientations [129][130] (see **Figure 4.11a**). It should be pointed out that these results contradict Brandon's criterion for the maximum deviation ($\Delta\theta_{\max}$) of a special boundary misorientation from the CSL configuration (Σ), $\Delta\theta_{\max} = 15°/\sqrt{\Sigma}$. Because the misorientation angle spread of Σ3 for Cu and Ni have sharp peaks, this suggests that the multiple twining process is active during recrystallization in Cu and Ni specimens and Σ9, and Σ27 are generated as a result of the multiple twining. Therefore the misorientation angle distribution is influenced by the twinning process, which leads to the inverse relationship with different slopes at each misorientation.

In §2.4 we have made an analogy between the interaction at the triple junction and the transfer of energy that occurs when particles collide in Boltzmann statistics. The interaction at the triple junction must be weak so that the grain boundaries can act independently. Nevertheless this analogy is only valid for Al specimen, which has the fewest Σ3 boundaries. For Cu and Ni, which have

significantly large fractions of Σ3 boundaries, the interaction at the triple junction is so strong such that we cannot treat the grain boundaries independently due to the abundance of the Σ3 at triple junctions. Previous studies reported that twin-related grain boundaries (Σ3, Σ9, and Σ27) occurred in the form of separated clusters within the grain boundary network of the polycrystalline Cu and Ni [129][131][132][133]. This implies that interactions occur only between the clusters of twin-related grain boundaries. As a result, these twin-related grain boundaries can be considered as a separate system obeying Boltzmann statistics. Therefore, the slope of the relationship between grain boundary population and energy for these boundaries is clearly different from that of Σ11 boundaries. One could argue that the Σ11 and Σ3 could be meet at the triple junction with Σ33 boundary [134][135]. However, the actual relative areas for Σ33a, Σ33b, and Σ33c are relatively low in both Cu and Ni. Therefore, it is reasonable to believe that the Σ11 and these twin-related grain boundaries belong to two independent grain boundary networks. Considering that the inverse relationships between grain boundary population and energy for these twin-related grain boundaries (Σ3, Σ9, and Σ27) and Σ11 have different slopes (**Figure 7.9**), one might assume that the slope of the population-energy relationship is different at each misorientation. If so, it would be possible to predict the relative boundary energy (E_i) at misorientation Σn_i from the GBCD according to the relationship similar to Equation 7.4, $E_i = E_{\Sigma n_i} - C_{\Sigma n_i} \ln\left(\frac{N_i}{N_{\Sigma n_i}}\right)$. In this case, we assumed that the maximum observed boundary ($N_{\Sigma n_i}$) has the lowest boundary energy $E_{\Sigma n_i}$ and the slope of the relationship $\frac{k_B T}{\alpha_{\Sigma n_i}}$ is equal to $C_{\Sigma n_i}$. Because the slope of the relationship $C_{\Sigma n_i}$ is different at each misorientation, the predicted boundary energies are the relative boundary energy at each misorientation not the absolute values.

The relative areas for the twin-related grain boundaries in Al, Au, Cu, and Ni in **Figure 7.7** are nearly perfectly correlated with the calculated boundary energies. This suggests that we can predict the grain boundary energies of those twin-related grain boundaries from the experimental GBCDs using the energy-population relationship described by Equation 7.4. Based on this Equation, we could extend this relationship to correlate the anisotropy of grain boundary populations and annealing temperatures. From Equation 7.2, grain boundary population, N_i, with boundary energy, E_i, at T_1 and T_0 are given by:

$$\frac{N_i^1}{N_{\Sigma 3}^1} = \exp\left(\frac{E_{\Sigma 3}\alpha - E_i\alpha}{k_B T_1}\right) \qquad \text{Equation 7.6}$$

$$\frac{N_i^0}{N_{\Sigma 3}^0} = \exp\left(\frac{E_{\Sigma 3}\alpha - E_i\alpha}{k_B T_0}\right) \qquad \text{Equation 7.7}$$

Dividing Equation 7.6 by Equation 7.7, we obtain:

$$\frac{N_i^1}{N_{\Sigma 3}^1} \Big/ \frac{N_i^0}{N_{\Sigma 3}^0} = \exp\left(\frac{E_{\Sigma 3}\alpha - E_i\alpha}{k_B T_1} - \frac{E_{\Sigma 3}\alpha - E_i\alpha}{k_B T_0}\right)$$

$$\ln\left(\frac{N_i^1}{N_{\Sigma 3}^1}\right) - \ln\left(\frac{N_i^0}{N_{\Sigma 3}^0}\right) = \frac{\alpha(E_{\Sigma 3} - E_i)}{k_B}\left(\frac{1}{T_1} - \frac{1}{T_0}\right) \qquad \text{Equation 7.8}$$

For example, we extrapolate the normalized relative areas for twin-related grain boundaries in Cu from experimental data (T_0 = 300 °C) to T_1 equals to 150 °C, 500 °C, and 900 °C. In this case, the unit area variables ($\alpha_i = \alpha_{\Sigma 3} = \alpha$), which was derived from the slope of the plot for Σ3, Σ9, and Σ27 grain boundaries in **Figure 7.7** and listed in **Table 7.3**, is assumed to be independent of temperature. Grain boundary energy (E_i) is obtained from reference [10]. **Figure 7.10** shows the relationships between the normalized relative areas of grain boundaries ($N_i/N_{\Sigma 3}$), and calculated boundary energies in Cu. The slopes of the relationships decrease with temperature. This reveals that the anisotropy of the grain boundary distributions decrease with increasing temperature.

It could also be interpreted that the relative area of the coherent twin boundary ($N_{\Sigma 3}$) decreases with temperature. Because the anisotropy of the grain boundary population is correlated to the energy anisotropy [47], this result implies that the anisotropy of the boundary energy decreases with temperature. Foiles reported that the grain boundary free energy of a symmetric Σ79 tilt boundary in Ni calculated using the EAM method decreases from 1,200 mJ/m^2 at 0 °K to about 400 mJ/m^2 at the melting temperature [86]. Because the boundary energy of 1,200 mJ/m^2 is considered high and comparable with the maximum calculated boundary energy with EAM method in Ni, we could expect that the maximum boundary energy will decrease with temperature.

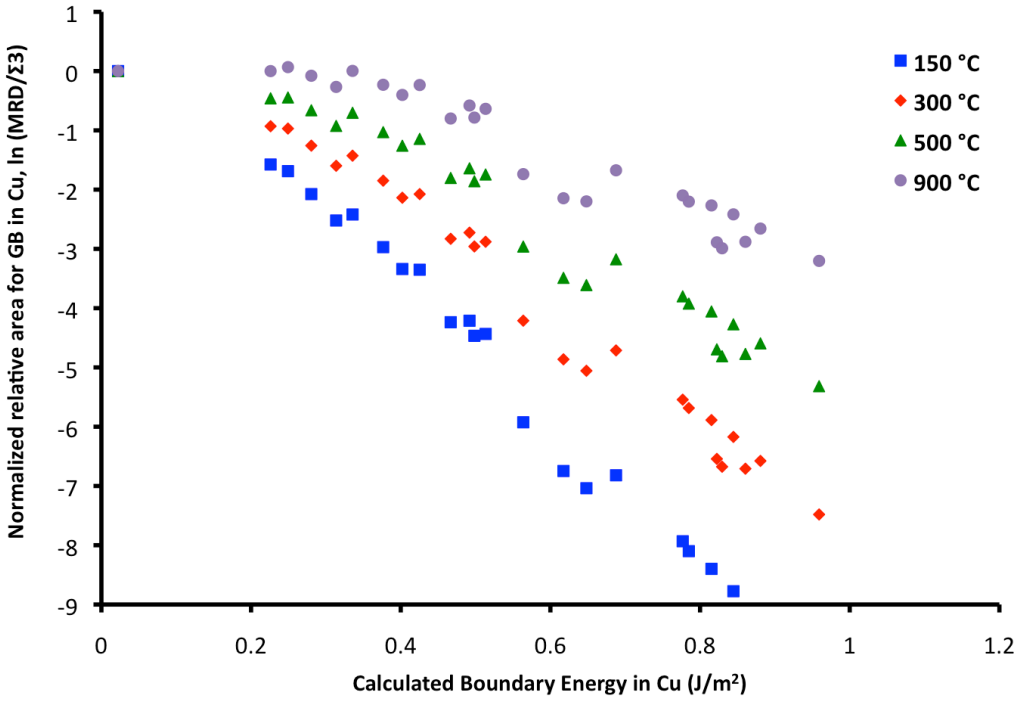

Figure 7.10. Comparison of relative grain boundary areas normalized to the population of the Σ3 coherent twin boundary in Cu. The horizontal axis shows the calculated boundary energies, while the vertical axis shows the relative grain boundary areas at 150 °C, 300 °C (Experiment), 500 °C, and 900 °C.

The energy anisotropy, which is the difference between the maximum and minimum boundary energy (coherent twin boundary), therefore decreases with temperature. This could results in the reduced anisotropy of the grain boundary population distribution as shown in **Figure 7.10**. However there is no experimental evidence to confirm this result. Therefore it would be of interest to explore this by measuring GBCDs of polycrystalline Cu annealed at various temperatures. Unfortunately, at low temperatures it may not be possible to get complete recrystallization and, at higher temperatures, the grain size will be very large and it may not be possible to collect statistically significant data.

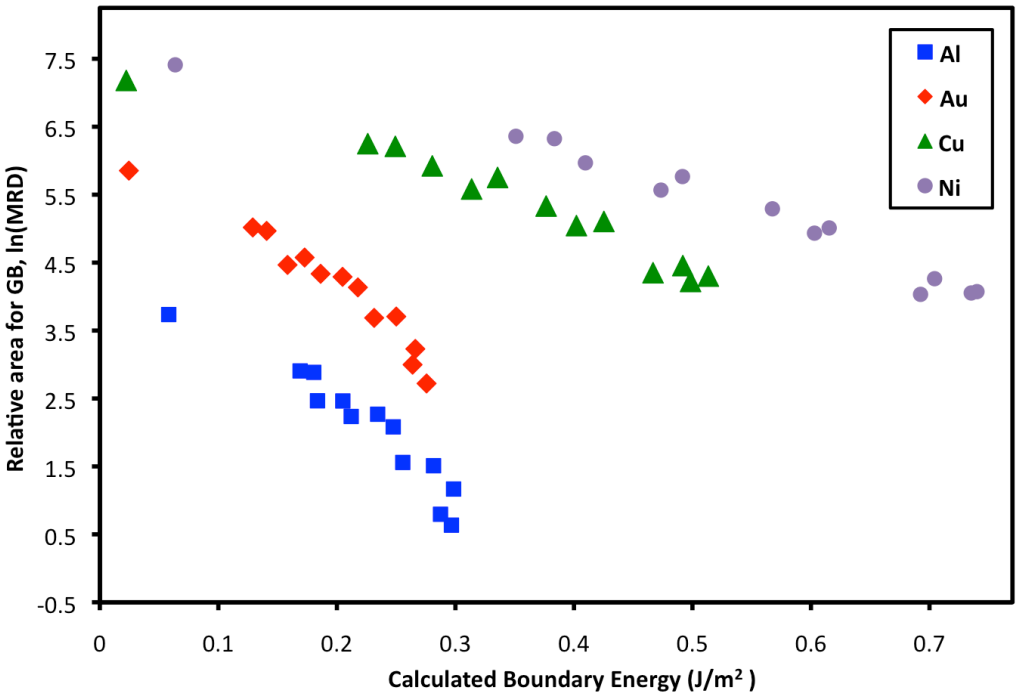

Figure 7.11. The relationship between experimental GBCD and the atomistic calculated grain boundary energy for the Σ3 grain boundaries. The horizontal axis shows the calculated boundary energies, while the vertical axis shows the relative grain boundary areas in Al (blue), Au (red), Cu (green), and Ni (violet).

Table 7.4. The minimum, maximum, and ranges of population and energy for the Σ3 grain boundaries in Al, Au, Cu, and Ni

	Annealing (TH)	Maximum (mJ/m^2)	Minimum (mJ/m^2)	Energy Range	Maximum (MRD)	Minimum (MRD)	Population Range
Al	0.72	298.46	58.11	240.35	41.90	1.89	40.01
Au	0.43	275.66	24.48	251.18	348.51	15.19	333.32
Cu	0.43	513.39	22.25	491.14	1314.35	68.19	1246.16
Ni	0.40	740.05	63.61	676.44	1654.31	56.41	1597.9

Because we have a limited number of the calculated boundary energies, it is not possible to compare the grain boundary population to the calculated boundary energy for every misorientation. Therefore we will focus our investigation on only the Σ3 misorientation. **Figure 7.11** shows the comparison between the populations of Σ3 boundaries in Al, Au, Cu, and Ni versus the calculated boundary energies. As shown in the plot, it is clear that the ranges of the energy distributions in Au, Cu, and Ni are correlated to the boundary population of the Σ3 boundaries, as shown in **Table 7.4**. **Figure 7.12** shows the relationship between the energy range and the population range. The grain boundary population ranges vary by more than three orders of magnitude; therefore the logarithms of the distributions are plotted. Note that the Al specimen was annealed at T_H = 0.72 and this higher temperature could potentially reduce the anisotropy. In addition, the comparison between the calculated boundary energies of the Al and the other FCC metals showed more scatter [10]. This previous result suggested that the structures of a specified macroscopic grain boundary in Al are different from the other FCC metals. In other words, the atoms at the grain boundary do not act as identical hard spheres. Therefore the characteristic differences in the electronic structure of the bonding in Al might also lead to the significantly lower population range in Al, as shown in **Figure 7.12**. The empirical evidence in **Figure 7.12** shows that the population ranges of the Σ3 boundaries in FCC metals (Ag, Au, Cu, and Ni) are strongly

correlated to the energy ranges. Therefore the population ranges could be predicted from this relationship. It should be noted that this empirical relationship between population and energy range, which was derived from only four points on a log-linear plot, contains uncertainty. More accurate relationship could be obtained by included more FCC metals in the comparison. Nevertheless, the results in **Figure 7.12** clearly demonstrate that the population range is proportional to the energy range. It was reported that the simulated boundary energies in FCC metals are linearly scaled with the lattice constant (a_0) multiplied by the shear modulus; the Voigt average shear modulus (μ) and C_{44} modulus [10][69]. Although the a_0C_{44} is slightly better than the $a_0\mu$ in scaling the energies of 388 boundary energies, the differences between the energies of Σ3 boundaries generated from a_0C_{44} and $a_0\mu$ are negligible.

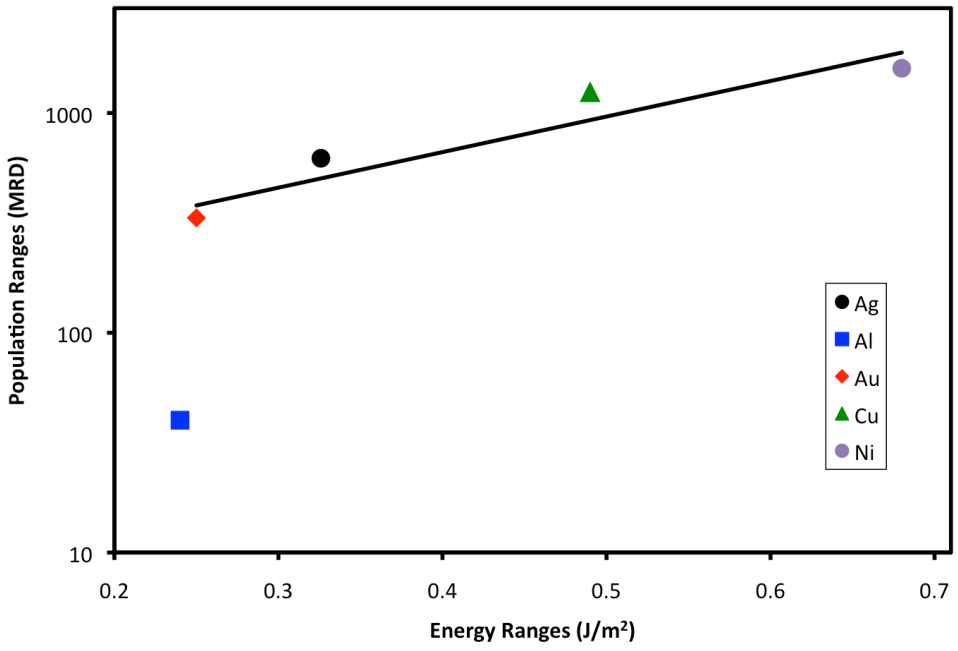

Figure 7.12. The relationship between the grain boundary population ranges and the boundary energy range for Σ3 grain boundaries. The horizontal axis shows the boundary energy ranges, while the vertical axis shows the grain boundary population ranges in Ag (black), Al (blue), Al (red), Cu (green), and Ni (violet). Note the energy range of Ag is extrapolated from the $a_0\mu$ ratio between Ag and Ni.

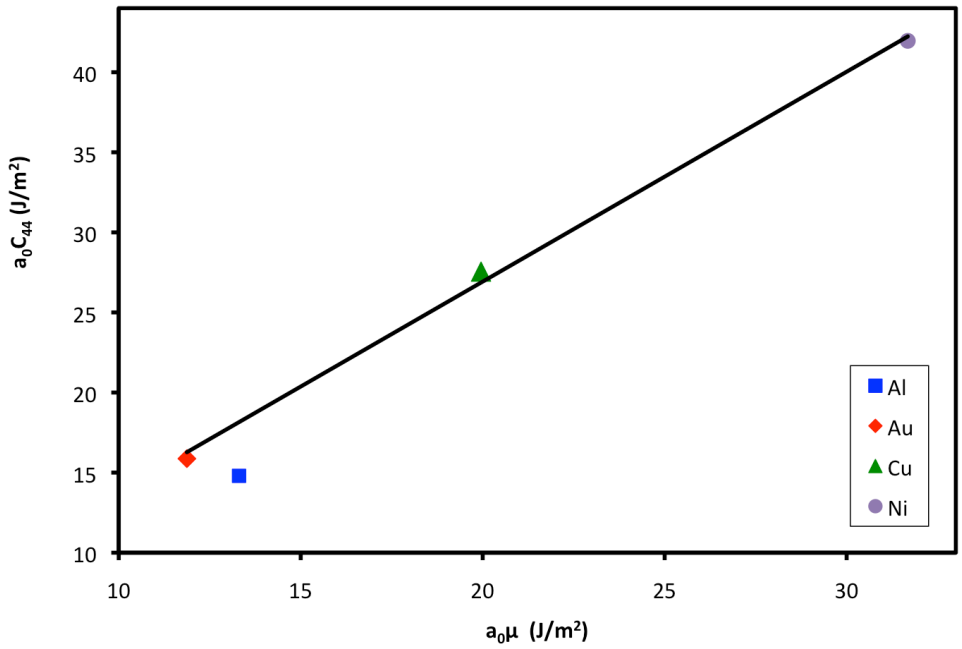

Figure 7.13. The relationship between $a_0\mu$ and a_0C_{44} in FCC metals. The horizontal axis shows $a_0\mu$, while the vertical axis shows the a_0C_{44} in Al (blue), Al (red), Cu (green), and Ni (violet).

The relationship between $a_0\mu$ and a_0C_{44} in Al, Au, Cu, and Ni, shown in **Figure 7.13**, is linear. The ratio of a_0C_{44} and $a_0\mu$ for Al is much lower than expected. This deviation could be reasonably explained the unique EAM potential of Al, which has different functional form compared with the other FCC metals. As a result, the boundary energies of Al, which were simulated from the EAM potentials, showed the most scatter among the boundary energies in FCC metals [10]. Nevertheless, the comparisons between the calculated boundary energies of Σ3 in Al, Au, Cu, and Ni, in **Figure 7.14**, reveal a very strong correlation. The predicted energies, which were derived from the ratio of $a_0\mu$ between two metals, are also very close to the simulated energies. These results in **Figure 7.12** and **Figure 7.14** indicate that the grain boundary population ranges of the Σ3 misorientation could be predicted from a single grain boundary energy data set.

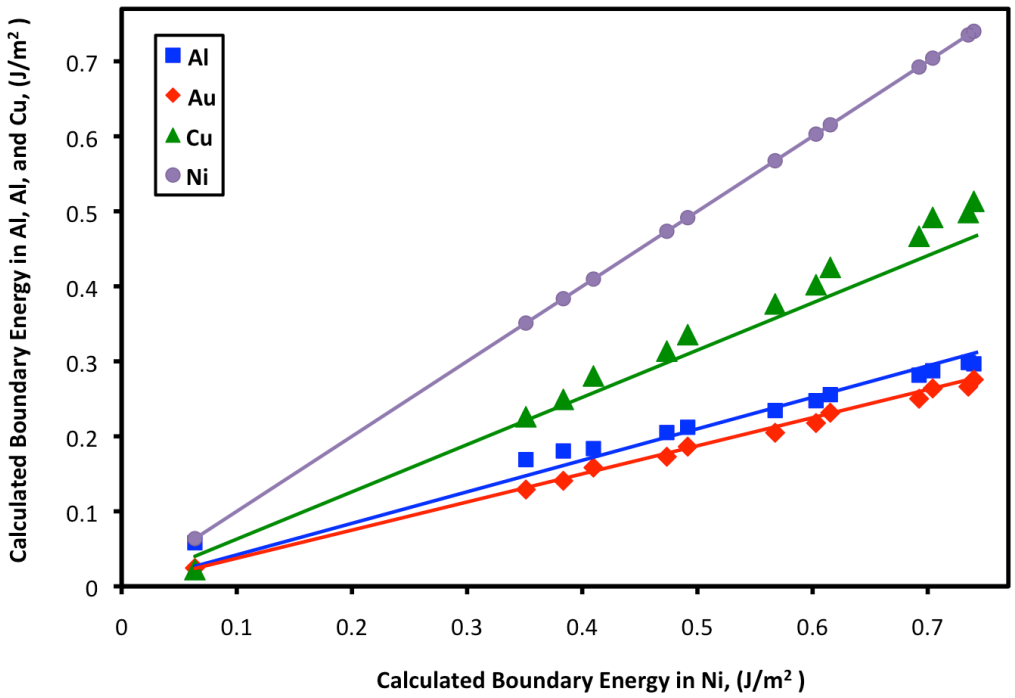

Figure 7.14. The relationship between the atomistic calculated boundary energy for the Σ3 boundaries. The horizontal axis shows the calculated boundary energies in Ni while the vertical axis shows the calculated boundary energies in Al (blue), Au (red), Cu (green), and Ni (violet). Note lines show the scaling predicted by the ratio between the $a_0\mu$ of FCC metals and the $a_0\mu$ of Ni. This figure was reproduced from reference [10].

The grain boundary energies can be obtained by the linear relationship, which are scaled by the ratio of $a_0\mu$ as shown in **Figure 7.14**. The boundary energy ranges of the Σ3 misorientation are then calculated from the difference between the maximum and minimum boundary energies. The boundary energy ranges are then used to estimate the boundary population ranges (see **Figure 7.12**). It should be noted that the least populated Σ3 boundaries are ≤ 5% of the populations of the coherent twin boundaries (**Table 7.4**). It was reported that a 10% variation of GBCD could be derived from the experimental uncertainties [9]. We could therefore assume that the populations of the coherent twin boundaries are approximately equal to the grain boundary population ranges.

7.3 BCC metals

7.3.1 Results BCC metals

It was reported that the steady state GBCD is strongly affected by the energy anisotropy and weakly influenced by the mobility anisotropy [45][46]. A steady state GBCD that is inversely correlated to the energy distribution is reached with sufficient annealing time [9][6][5] [43][44]. To investigate the GBCD evolution in BCC Fe, we compare the relative areas of Σ3 boundaries of the Fe specimens annealed at four different annealing times with the calculated boundary energies. As shown in **Figure 7.15**, the correlations coefficients between the Σ3 boundary populations and the calculated energies in Fe specimens annealed for 2, 4, 8, and 16 hours are 0.04, -0.71, -0.65, and -0.88 respectively, suggesting that with annealing, the distribution is approaching the expected inverse correlation with the energies. While the correlation coefficients for Fe annealed for 4 and 8 hours were relatively high, the coherent twin, the lowest boundary energy among Σ3 boundaries, is not the most populated boundary. However, after the Fe was annealed for 16 hours, it was the most populated Σ3 boundary orientation. It should be noted that the average populations of Σ3 boundaries in Fe annealed for 2 hours (0.79 MRD), 4 hours (0.99 MRD), 8 hours (1.04 MRD) and 16 hours (1.08 MRD), increased with the annealing time. The increase in the average populations of Σ3 boundaries is predicted to occur as grains grow during annealing by simulations and models for the development of anisotropic GBCDs [43][45].

To investigate the inverse correlation between the grain boundary population and the calculated boundary energy, we compare the grain boundary populations in the Fe annealed for 16 hours to the 408 calculated energies in Fe. As shown in **Figure 7.16**, the highest population is the Σ41, 12.7°/[100]. In addition, Σ33, Σ9, Σ27, Σ13, Σ39, Σ17, Σ53, and Σ65 are also relatively highly populated boundaries. The correlation coefficient for all grain boundaries with population greater than 0.5 MRD is -0.45, which is much lower than the correlation coefficient

of Σ3 boundaries (-0.91). While the inverse correlation between grain boundary population and energy is very strong for the Σ3 boundaries (see **Figure 7.16a**), it is very difficult to determine the slope of the correlation at the other misorientations due to the limited number of the calculated boundary energies at each misorientation. Nevertheless, it is very clear that the inverse correlation between grain boundary population and energy follows different scaling at each misorientation. **Figure 7.16b** shows the similar plot, in which the data are colored according to their tilt or twist character. The inverse correlation between grain boundary population and energy is not apparent for any particular type of grain boundary structure (see **Figure 7.16b**).

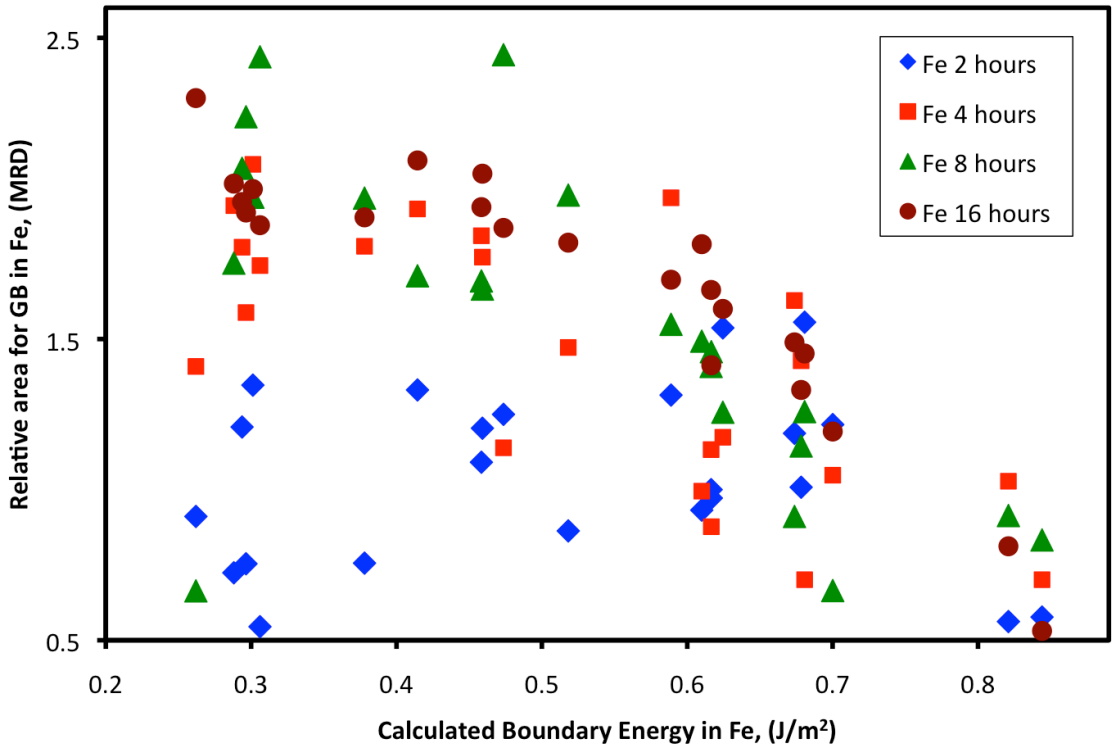

Figure 7.15. The relationship between the calculated grain boundary energies in Fe and the relative areas of Σ3 boundaries in Fe specimens annealed at four different annealing times: 2 hours (blue diamonds), 4 hours (red squares), 8 hours (green triangles), and 16 hours (brown circles). The horizontal axis shows the calculated boundary energy in Fe and the vertical axis shows the relative area of Σ3 boundaries in Fe for the same boundary.

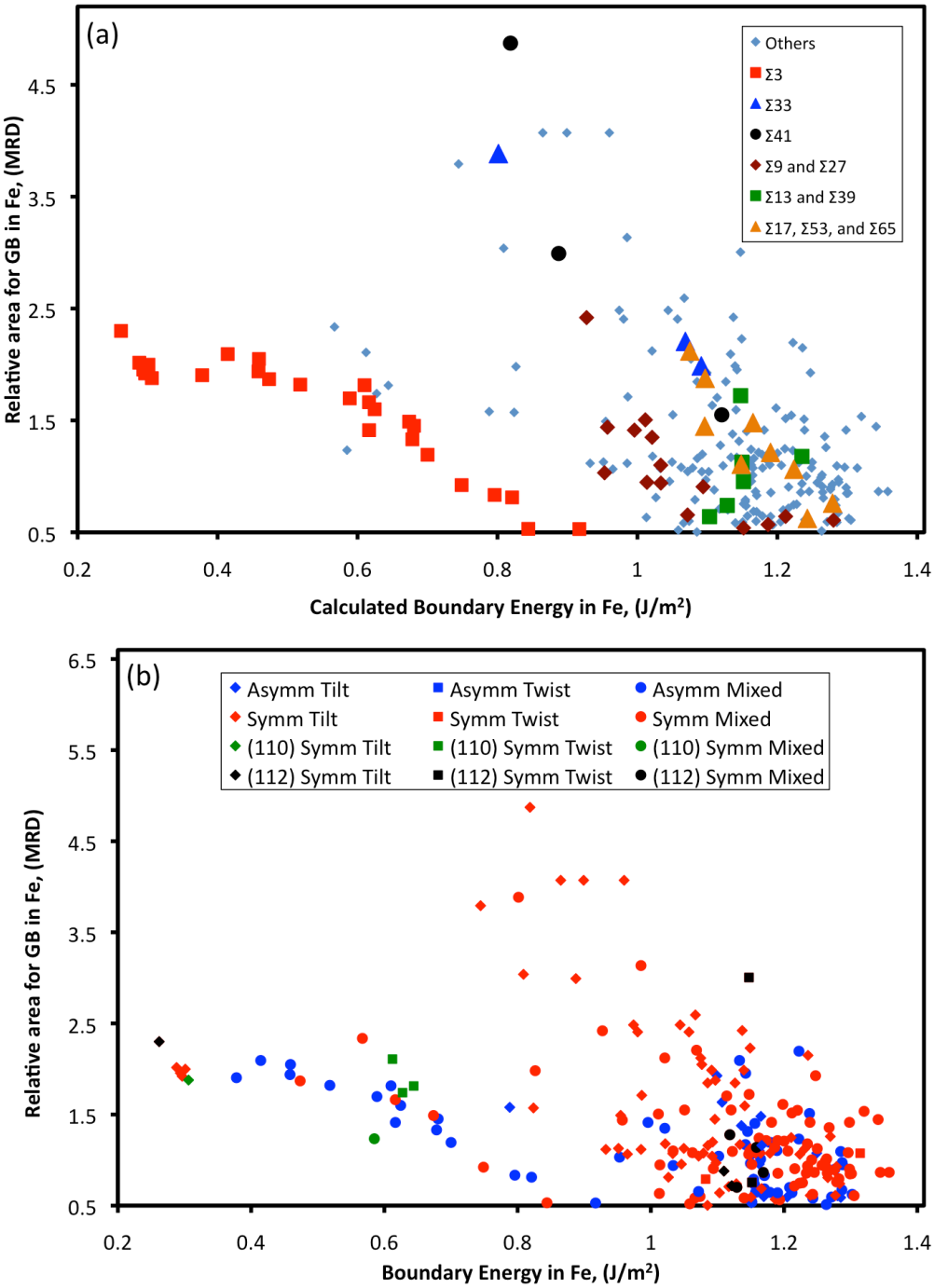

Figure 7.16. The relationship between the experimental GBCD and the calculated grain boundary energies in Fe annealed for 16 hours. (a) Grain boundaries were colored according to the Σ misorientations. (b) Grain boundaries were colored according to the types of boundary structures. The horizontal axis shows the calculated boundary energy in Fe and the vertical axis shows the relative area in Fe for the same boundary.

It should be noted that the relationship between grain boundary population and energy is not a one to one function, but constrained by the misorientation of the boundary. **Figure 7.17** shows comparisons between the grain boundary population in Mo and the calculated boundary energy in Mo. The results in this plot show a similar trend as in the Fe specimen (See **Figure 7.16**). The correlation coefficient between all grain boundaries with population greater than 0.5 MRD and the calculated boundary energies is increase from -0.52 to -0.91 when only the Σ3 boundaries are considered. It should be noted that the most observed boundary in Mo at the Σ3 misorientation is not located at the coherent twin boundary. However, the coherent twin boundary is the third most populous at the Σ3 misorientation (**Figure 7.17**). It is possible that a longer annealing time could enhance the populations of the coherent twin boundary as observed for the Fe specimens as shown in **Figure 7.15**. It was reported that a polycrystalline material with random texture could evolve to a steady state misorientation distribution, while a textured polycrystalline sample could not reach a steady state misorientation distribution [136]. The texture in the Mo sample will alter the grain boundary distribution. The preference for [100] orientations perpendicular to the observation plane will enhance the population boundary planes in this zone (for example, {011}) while lowering the probability of boundaries that do not belong to this zone, such as {112}. Therefore the texture makes comparison between the boundary population and the calculated boundary energy in Mo less reliable than in the Fe specimen.

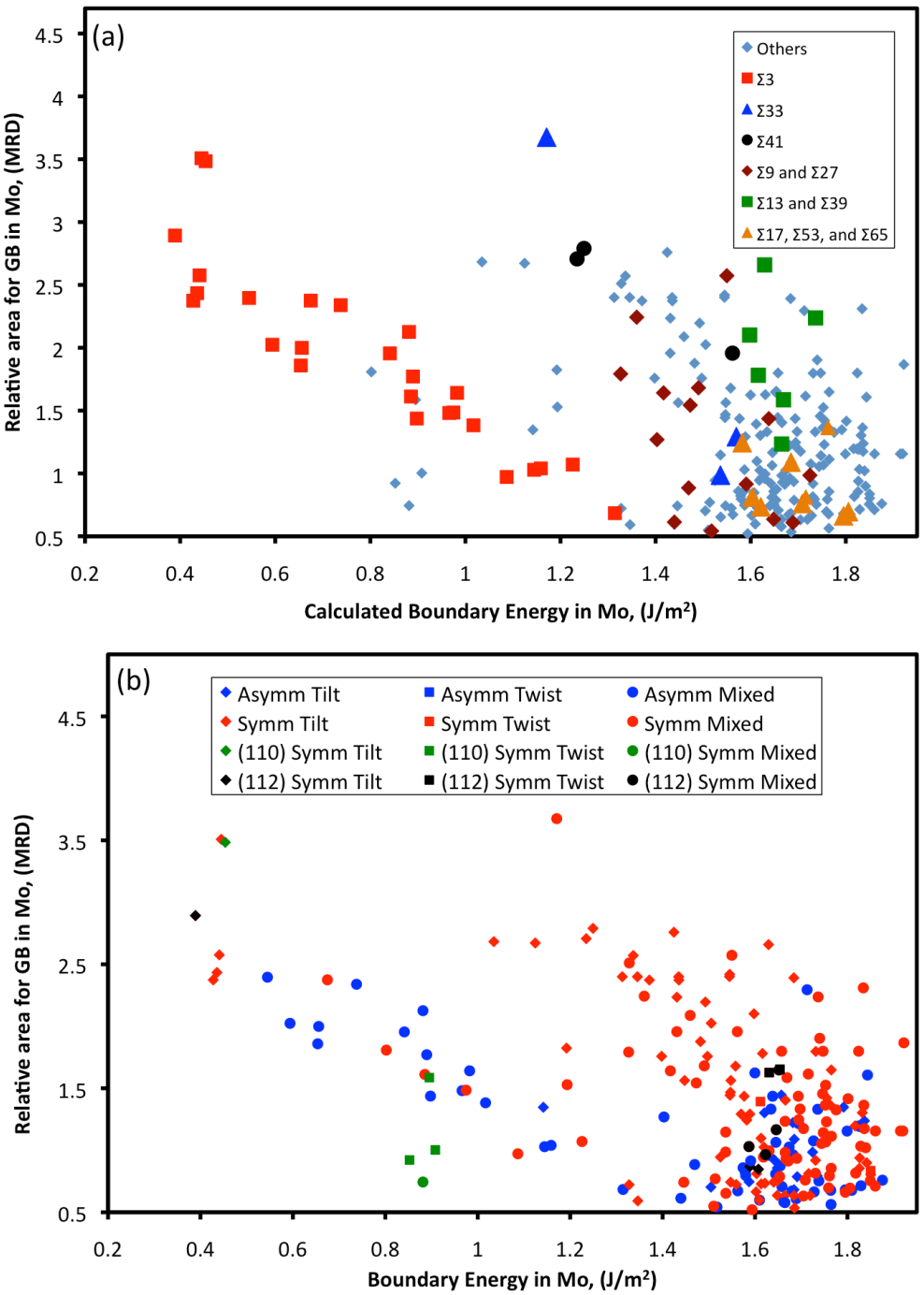

Figure 7.17. The relationship between experimental GBCD and calculated grain boundary energies in Mo. (a) Grain boundaries were colored according to the Σ misorientations. (b) Grain boundaries were colored according to the types of boundary structures. The horizontal axis shows the calculated boundary energy in Mo and the vertical axis shows the relative area in Mo for the same boundary.

7.3.2 Discussion of results for BCC metals

We have shown that the GBCDs of Fe evolved during isothermal annealing. While the Fe specimen annealed for 16 hours (2D-EBSD) has the highest correlation coefficient between the populations and energy at the Σ3 boundaries, it is not guaranteed that this Fe specimen is actually in a steady state (or that such a state could ever be achieved). As another check of the computed grain boundary energies, we include the GBCD of BCC Fe derived from a 3D-EBSD measurement of a ferritic steel [8] with 10° resolution. The relative areas for the 408 grain boundaries were extracted and compared to the calculated boundary energy. **Figure 7.18a** shows a logarithmic plot of the grain boundary populations (P > 0.5 MRD) versus the calculated grain boundary energies. Even though grain boundary energies could be altered by the alloying elements, the correlation coefficient is relatively high (-0.69). This strong inverse correlation between measured populations and calculated boundary energies is in agreement with the inverse relationship between the experimental grain boundary populations and the atomistic calculated energies in Al [3][4] (see **Figure 7.9b**). As depicted in **Figure 7.18b**, **Figure 7.18c**, and **Figure 7.18d**, the correlation coefficient between grain populations and energies for Σ3 boundaries has a nearly perfect correlation coefficient (-0.95), which is significantly higher than the correlation coefficients of Σ9 (-0.51) and Σ13 (-0.40). While there are uncertainties in the calculations of the boundary energy and also in the measurements of the grain boundary population, our results indicate that the slopes of the inverse relationship are different at each misorientation: Σ3 (-1.42), Σ9 (-0.69), and Σ13 (-3.17). The misorientation angle distributions of Fe measured from 3D-EBSD [8] and 2D-EBSD measurements are shown in **Figure 7.19**. Both misorientation distributions are different from the distribution of misorientation angles for a randomly texture (Mackenzie distribution). It should be noted that the misorientation angle distribution of the 3D-EBSD has the maximum peak around 60°, which is the misorientation angle for the Σ3 boundaries.

It is worth noting that the anisotropy of the GBCD of BCC Fe is significantly smaller than in the FCC metals. While the energy anisotropy of Ni (1.35 J/m^2) is slightly larger than that of the BCC Fe (1.14 J/m^2), the lowest boundary energy in BCC Fe (0.26 J/m^2), the symmetric tilt twin boundary with (211) plane, is much larger than the lowest boundary energy in Ni (0.06 J/m^2), the twist twin boundary with (111) plane [10]. The depth of the energy cusp at the twin boundary might be a major factor that determines the resultant GBCD.

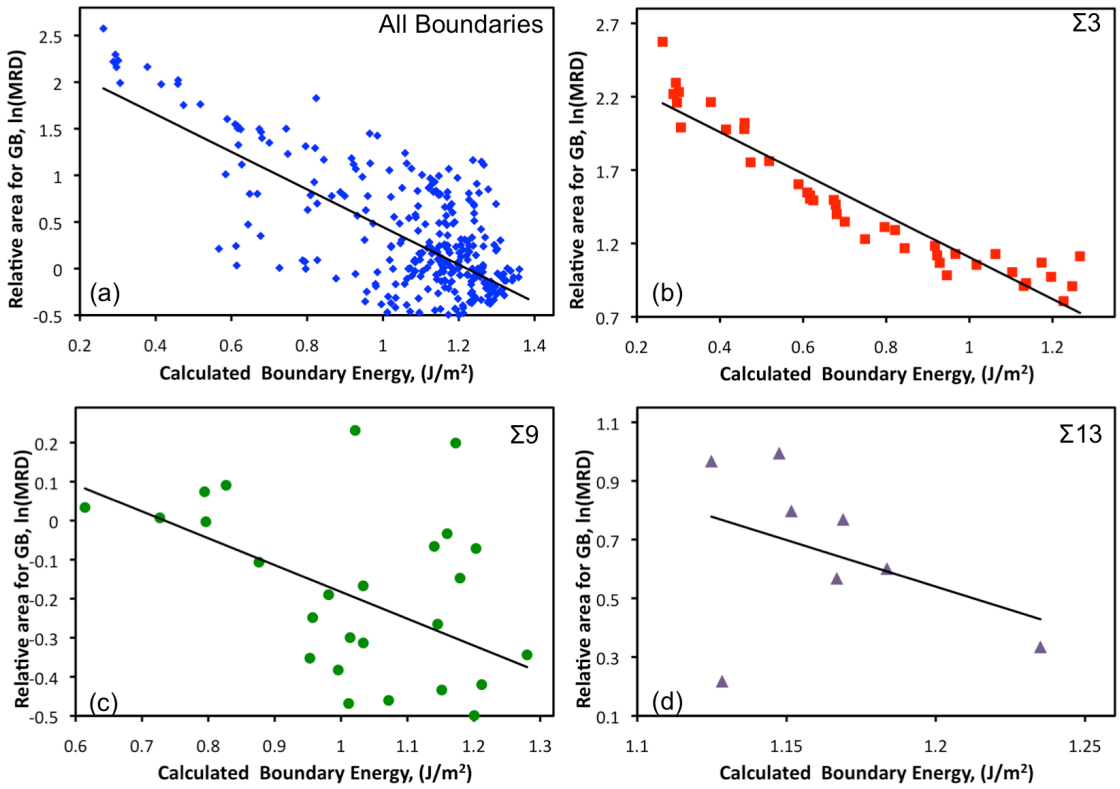

Figure 7.18. The relationship between the experimental GBCD calculated from the Fe 3D-EBSD [8] and the calculated grain boundary energies. The linear relationships between population and energy are shown as solid lines. (a) All boundaries with populations > 0.5 MRD show an inverse correlation between the GBCD and energy. (b) Σ3 boundaries show a strong inverse correlation over the boundary energy and population ranges. (c) Σ9 boundaries show a moderate inverse correlation with the slope lower than that of the Σ3 boundaries. (d) Σ13 boundaries show a weak correlation at the high-energy range.

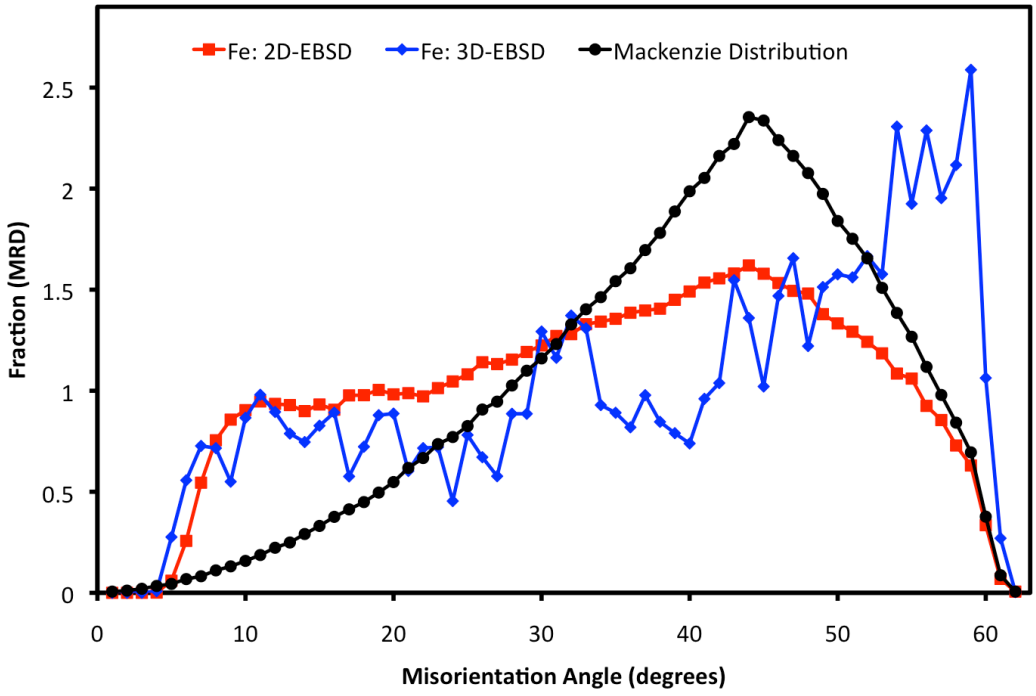

Figure 7.19. Misorientation angle distributions of from Fe 2D-EBSD (red), Fe 3D-EBSD (blue), and Mackenzie distribution (black).

7.4 Conclusions

We have shown that in FCC metals the grain boundary population has a weak inverse correlation when all of the 388 calculated boundary energies are considered. Nevertheless, the relative areas for the twin-related grain boundaries (Σ3, Σ9, and Σ27) are nearly perfectly correlated with the calculated boundary energies, which are consistent with the Boltzmann distribution. The abundance of the Σ3 boundaries enhances the occurrences of the twin variant grain boundaries (Σ9 and Σ27). Because of the large number of twin related boundaries, the inverse correlations between the grain boundary population and the calculated boundary energy have different slopes at each misorientation. Therefore it is not only the grain boundary energy but also the crystallographic constraint at triple junction that determine the GBCD.

In BCC metals, the inverse relationship between boundary population and energy has different slopes at each misorientation. It should be pointed out that the relative areas for the Σ3 boundaries in the Fe specimens evolved from weaker to stronger anisotropy when the annealing time was increased from 2 to 8 hours. Interestingly, the most populated boundary for the Σ3 misorientation changed from the symmetrical (110) tilt boundary to the coherent twin boundary, the lowest boundary energy at this misorientation, when the annealing time was increased from 8 to 16 hours. Even though the Fe specimen was annealed at about the same homologous temperature as those of the FCC metals, it required a much longer annealing time for the boundaries to develop a strong inverse correlation with the calculated grain boundary energies. Because the energy cusps at the twin in the FCC metals are much deeper than the one in Fe, there is a stronger driving force for boundaries to adopt the twin configuration.

Chapter 8

8. Modeling the Grain Boundary Character Distribution (GBCD) in Ac

Based on our finding that the GBCDs of isostructural polycrystalline materials are correlated at each misorientation more so than over the entire grain boundary space, in this Chapter we will use this principle to model the GBCD of a metal that has not yet been studied. We derived the GBCD of Actinium (Ac) based on the GBCD of Cu and the misorientation distribution of Au. The population of the coherent twin boundary in Au was derived from empirical data as described in §7.2.2. Finally, qualitative and quantitative analyses of the Ac GBCD will be presented. Our findings indicated that the GBCDs of isostructural FCC metals are strongly correlated at each misorientation, rather than over the entire grain boundary space (see **Figure 4.19** and **Figure 4.20**). We found that the inverse correlation between the grain boundary population and the calculated boundary energy has a different slope at each misorientation because of the large number of Σ3 and twin related boundaries. Nevertheless we found that at a specific misorientation the grain boundary population is inversely correlated to the boundary energy, which is characterized by the Boltzmann distribution. The correlation is strongest for the Σ3 misorientation where we have the most data.

Because the boundary energies in FCC metals were scaled with the ratio of $a_0\mu$ in two materials [10][69], we could use this relationship in determining the

boundary energy range at the Σ3 misorientation. Furthermore, the grain boundary population ranges would be predicted from the empirical relationship in **Figure 7.12**. Because the least observed boundary populations at the Σ3 misorientation are very small compared with the populations of the coherent twin boundary (see **Table 7.4**), the grain boundary population ranges are approximately equal to that for the coherent twin boundary. Ideally, we would like to investigate the inverse correlation between boundary energy for every misorientation, in that case the unit area variables for every misorientation (α_i) could be defined, and the GBCD could be simply predicted from the grain boundary energy distribution (GBED) using Equation 2.17. However it is currently not possible to simulate enough boundary energies to fully cover the entire grain boundary space. The grain boundary populations at each misorientation are mainly controlled by the crystallographic texture and the consequences of the Σ3 boundaries at triple junctions. It should be noted that information about the crystallographic texture and the triple junction distribution are embedded in the misorientation angle distribution. As a result, we could use the misorientation angle distribution to specify the crystallographic texture and the grain boundary connectivity (triple junction distribution). The misorientation angle distribution could be obtained by experiment or reasonable speculation. To show that it is possible to predict the GBCDs and GBEDs of isostructural FCC polycrystallines, we can model the GBCDs and GBCDs of Rh, Pd, Pt, Ir, and Ac (see **Figure 8.1**). As example, we chose Ac, a FCC structured material with lattice parameter of 5.47 (A°) [137], as a model material. Ac is a radioactive element, which is usually found with uranium ores. Because it occurs in low concentration and has properties that are similar to lanthanum, it is not practicable to obtain high purity Ac using physical and chemical separation from the actinium ores, usually containing large amount of lanthanum. High purity Ac is only artificially made from neutron irradiation of Ra in a nuclear reactor [138]. Because of its highly radioactivity and scarcity, little has known about the physical properties.

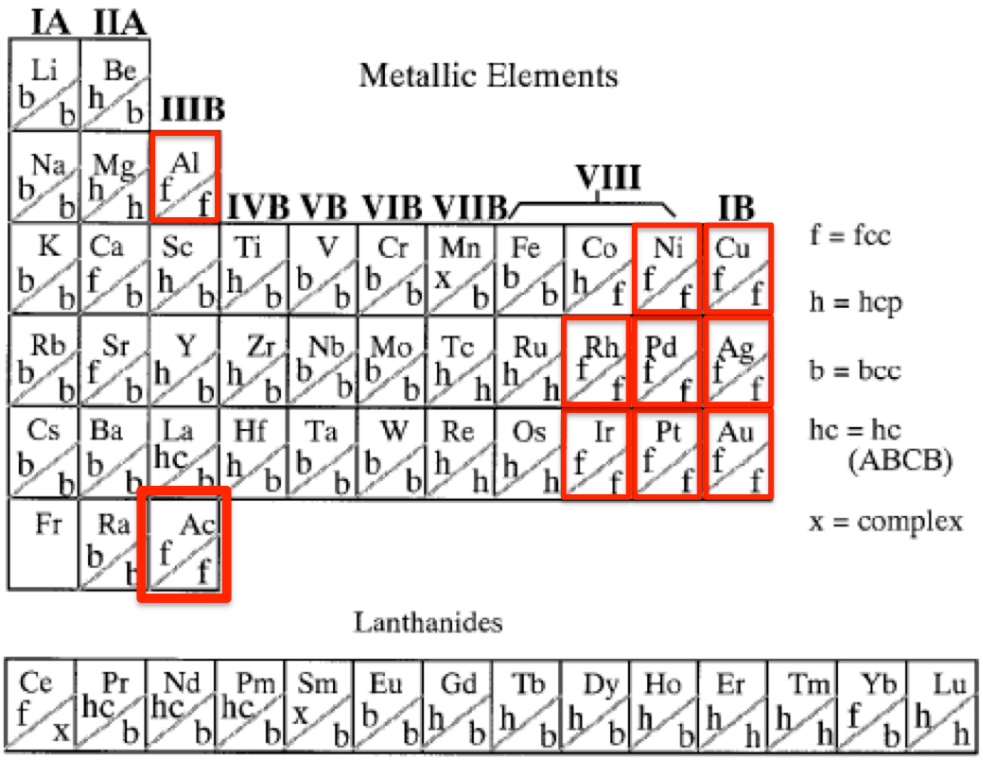

Figure 8.1. The crystal structures of the metallic elements. The symbol in the upper left and the lower right refer to the crystal structure at the room temperature and at temperature before it melts. Note f = face-centered cubic, h= hexagonal close packed, b = body-centered cubic, hc = ABCB stacking, and x = complex structures. Elements with FCC stable at both temperatures are labeled by red rectangular. This figure was reproduced from reference [139].

In this study, the Voigt average shear modulus (μ) was obtained from the Naval Research Lab Tight Binding Program (NRTL-TB) [138]. While there is no current engineering application, Ac has a potential application as an active element in radioisotope thermoelectric generators for spacecraft [140]. If the active element were Ac bulk metal, radiation damage at the grain boundaries would be critical for the device integrity. Therefore, modeling the GBCD of Ac would possibly benefit future investigations and computational simulations of thermoelectric generators with Ac metal radiation source. The predicted GBCD of Ac was derived from the

GBCD of Cu, which has the least crystallographic texture. Because the lattice constant multiplied by the Voigt average shear modulus $a_0\mu$ in Ac (9.96 J/m^2) is comparable to that of Au (11.87 J/m^2), we assumed that the misorientation angle distribution of Ac would be similar to that of Au. The boundary energies of Ac were extrapolated from the boundary energy data set of Cu [10] by scaling with the ratio of $a_0\mu$ between Cu and Au. The boundary energy range for the Σ3 misorientation in Ac (0.21 J/m^2) was then determined by the difference between the maximum and minimum boundary energy at this misorientation. The population of the coherent twin boundary in Ac (330 MRD) was then determined from the empirical result in **Figure 7.12**. The lengths of grain boundary line segments in Cu were changed to account for the target misorientation angle distribution of Au. Specifically, we first calculate the misorientation angle distributions for Au and Cu. The ratios of the line length fraction in Au and in Cu at each misorientation angle were then used to modify the length of the line segments in Cu. The initial GBCD of Ac was then calculated based on the modified grain boundary line segments of Cu. At this step, the coherent twin boundary of the initial Ac GBCD has population of 705 MRD, which is significantly greater than the expected population of the coherent twin boundary (330 MRD). To account for the expected coherent twin population, all bins in the GBCD with values grater than 0.5 MRD were renormalized so that the population of the coherent twin boundary was 330 MRD. The bins with values less than 0.5 MRD will be all renormalized with a constant factor of 2.19. These procedures ensure that the average population across the entire GBCD is 1. The grain boundary plane distribution of Ac in **Figure 8.2** has a peak maximum centered at the (111) position, which is similar to the ones of Au and Ni. **Figure 8.3** shows the comparison between the grain boundary populations in Ac and Au. Interestingly, the relative areas for grain Σ3, Σ9, Σ11, and Σ27 boundaries in Ac are almost followed the same scaling with the ones in Au. In addition the grain boundary population of Ac also shows inverse correlation to the extrapolated boundary energy in Ac (see **Figure 8.4**).

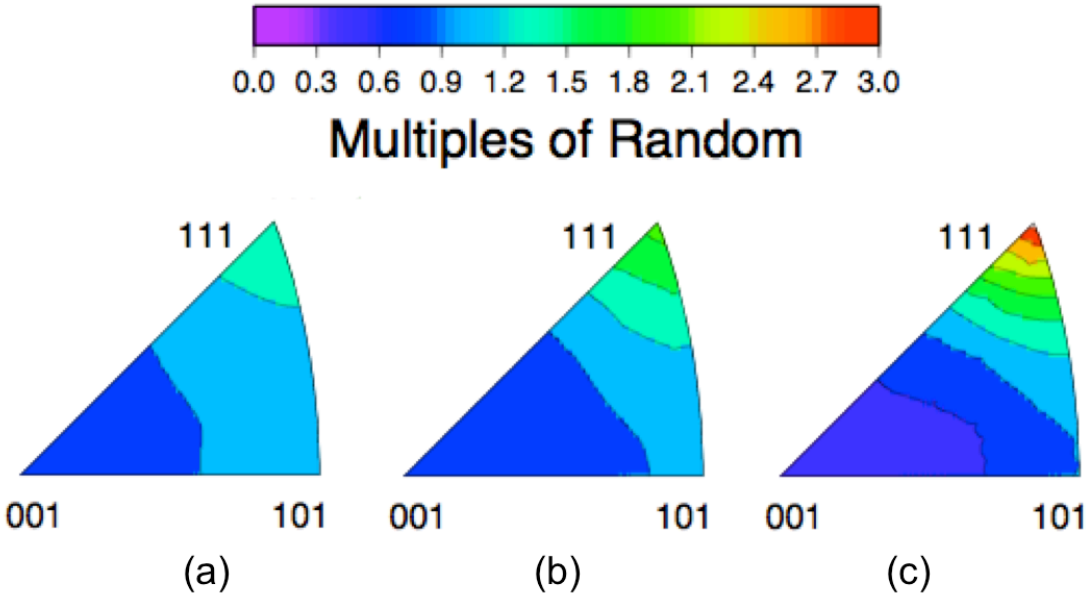

Figure 8.2. Grain boundary plane distributions in (a) Ac, (b) Au, and (c) Ni.

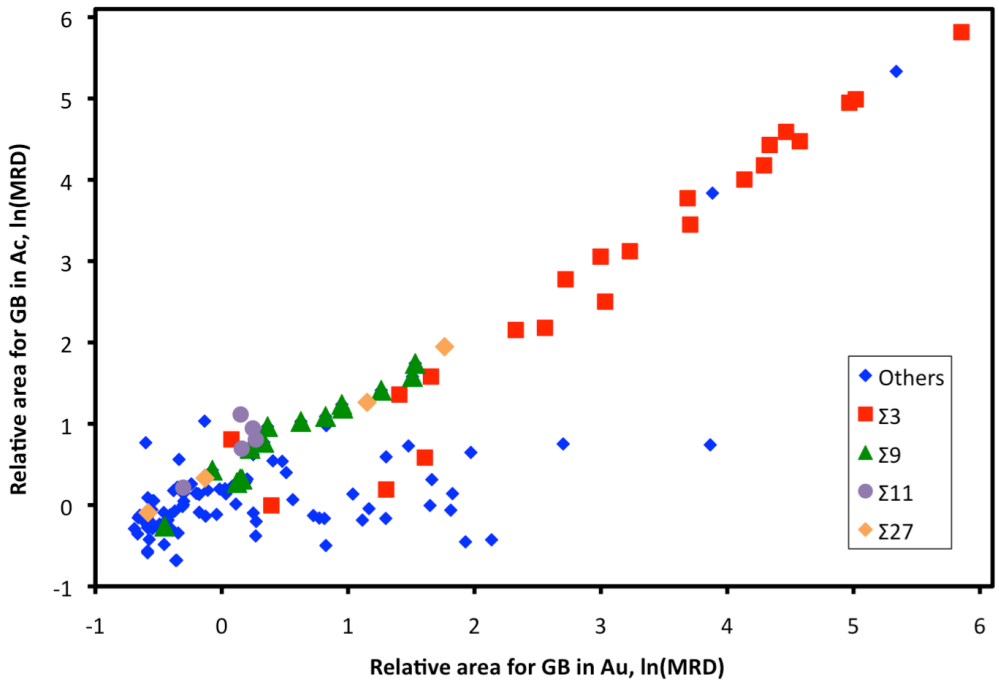

Figure 8.3. Comparison between the relative areas for grain boundaries in Ac and Au.

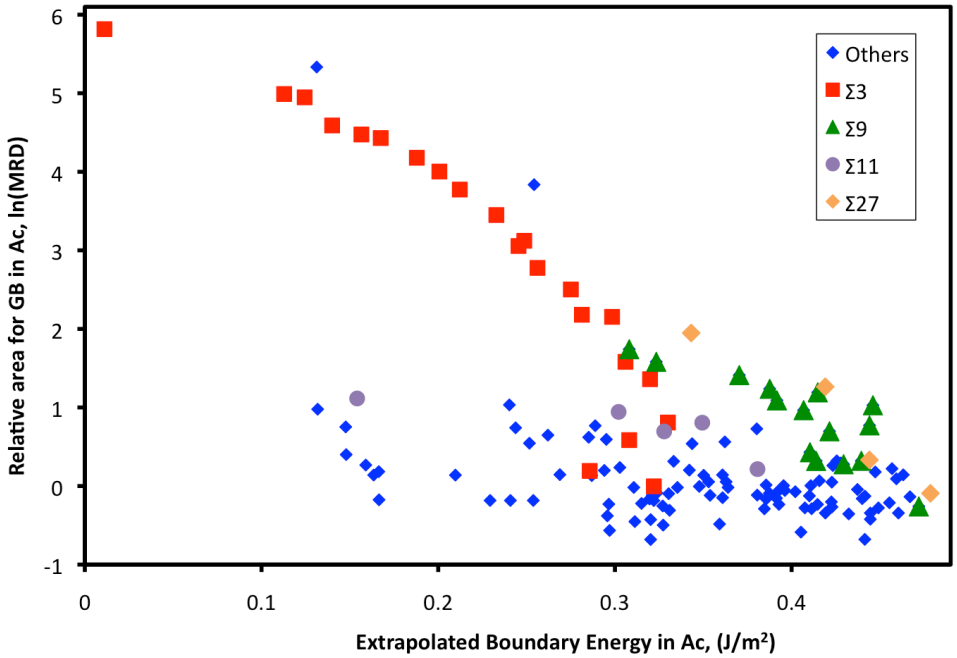

Figure 8.4. Comparison between the relative areas for grain boundaries in Ac and the extrapolated boundary energy of Ac.

As we mentioned before in §2.2, the resolution of the GBCD calculation could influence to the magnitude of the peak maxima. Therefore the predicted population of the coherent twin boundary estimated by this relationship (see **Figure 7.12**.) could contain errors. It should be noted that the relationship was derived for FCC metals, which were annealed at about the same homologous temperature (T_H~0.4). The boundary population ranges or the relative area for the coherent twin boundary were expected to decrease with annealing temperature, as described in **Figure 7.10**. However, we currently don't know the actual relationship between the grain boundary populations and the annealing temperature. In this study, we assumed that Ac metal was annealed at T_H~0.4. Even though the modeling is very likely to contain errors and not accurately represent the actual GBCD of Ac, it is intended to demonstrate the possibility of predicting the GBCD of a material that has not yet been studied. It should also be noted that the same principle could also be used to model the GBCDs of Pt, Pd, or Ir, which have not yet received much attention and could be studied in the future.

Chapter 9

9. Conclusions

The experimental GBCDs of FCC metals, derived from stereological interpretations of EBSD maps, support the hypothesis that the GBCDs of well annealed isostructural materials with similar microstructures (Au, Cu, and Ni) are strongly correlated. As we expected, the FCC distributions are not correlated to GBCDs of BCC metals (Mo and Fe). Ag was also correlated to Au, Cu, and Ni, but it was a relatively weaker correlation. This is explained by the fact that it has a very different microstructure and crystallographic texture. Therefore, significant differences in grain shape and texture can also influence the GBCD. As a result, the strong correlations observed for Au, Cu, and Ni can only be expected to persist in other FCC metals with comparable microstructures and limited texture.

We have found that grain boundary populations are inversely correlated to calculated boundary energies with a different slope at each misorientation. Crystallographic constraints due to extensive twinning in FCC metals affect the misorientation distribution. When the misorientation distribution is not random, the slope of the correlation between the logarithms of the population can be different at each misorientation. Nevertheless, it is possible to predict GBCDs and GBEDs in isostructural polycrystalline material by using a single GBCD and GBED. As an example, we modeled the GBCD of Actinium (Ac) based on the GBCD of Cu and the misorientation angle distribution of Au.

Our atomistic simulations suggested that grain boundary energies in Fe and Mo are strongly correlated and scaled with the ratio of the cohesive energy divided by the square of the lattice constant (E_{coh}/a_0^2). The comparison between the relative areas of grain boundary in Fe and Mo showed a moderate correlation. Interestingly, the anisotropies of the grain boundary populations in Fe and Mo are significantly weaker than those of FCC metals, even though the boundary energy anisotropies are slightly different. The results indicate that grain boundary population has a negative exponential correlation to the grain boundary energy, which has a functional form similar to the Boltzmann distribution. Specifically, FCC metals with a deeper energy cusp will have a wider range of grain boundary populations than those with a shallower energy cusp.

To conclude, the GBEDs and GBCDs in isostructural materials are correlated. While GBEDs in isostructural materials are nearly perfectly correlated, the degree of correlation among the isostructural materials is strongly influenced by the microstructure and crystallographic texture of the specimens. The inverse correlation between grain boundary population and energy, which has different slopes at each misorientation when the misorientation distribution is non-random, leads to GBCDs of isostructural materials that are also strongly correlated at each misorientation.

Chapter 10

10. Future Work

We demonstrated that the inverse relationship between the grain boundary population and energy for those twin-related grain boundaries in Al, Au, Cu, and Ni are consistent with the Boltzmann distribution. It was realized that if the Boltzmann distribution governs these grain boundary populations, then the anisotropies of these grain boundary population distributions would be expected to decrease as the annealing temperature increases. To verify this, we would measure the experimental GBCDs of Cu annealed at various temperatures. Although, there might be many complicating factors that could influence the resultant GBCDs, it is very interesting to investigate the effect of the annealing temperature to the GBCDs.

Throughout our study, the calculated boundary energies are the simulated boundary energies at T= 0 K (enthalpy). We assumed that all grain boundary energies scale with temperature in a similar manner and the relative grain boundary free energies at specified temperatures are proportional to the calculated enthalpies. However there is no guarantee that this would be the case. As we mentioned before in §7.2.1, the populations of Σ11 (110)[311] in Al specimen are very small and obviously deviate from rest of the boundaries despite its low calculated boundary energy. It is possible that the simulated boundary structure of the lowest optimized energy at 0 K might be different from the actual structure at the experimental temperature. This might be the reason that the comparison between the experimental grain boundary population and the computational grain boundary energy for this Σ11 boundary is unreliable. Therefore it is important to

clarify this uncertainty. To investigate the influence of the temperature on the boundary free energy of this Σ11 boundary, we shall use the atomistic model to simulate the boundary energy in Al at five different temperatures.

We demonstrated that the simulated boundary energies of Fe and Mo are strongly correlated and scaled with the ratio of the cohesive energy divided by the square of the lattice constant (E_{coh}/a_0^2). Nonetheless, it is very probable that these results might be a coincidence that might not occur in other BCC metals. To verify this, we would like to simulate the boundary energy in BCC tungsten (W). Only a few boundary types that span the full range of grain boundary energy in Fe and Mo will be selected for this computational study.

Appendix A

Measurement of the Grain Boundary Character Distribution in Textured Polycrystals from Planar Sections with Texture Correction

Abstract

The calculation that corrects the grain boundary character distribution (GBCD) for the effect of texture is described. The texture correction factor, which is the inverse occurrence of the grain orientations at each misorientation, was derived from the planar electron backscatter diffraction (EBSD) maps. A stereological method was used to estimate the GBCD from the line lengths weighted by the correction factor. The method has been tested on polycrystalline copper specimens with weak and strong textures. The results show that the texture correction scheme can alleviate the non-uniform sampling of highly textured specimens. Furthermore the GBCDs of the copper specimens, which have substantially different textures, are strongly correlated after the texture correction. These results clearly indicate that the texture correction procedure provides a reasonable estimate of the GBCD in a highly textured polycrystalline material.

Introduction

A grain boundary, which is a transition region between adjacent grains of two different crystal orientations, can be parameterized by five macroscopic degrees of freedom $(\varphi_1,\Phi,\varphi_2,\theta,\phi)$. The grain boundary character distribution

(GBCD), $\lambda(\Delta g,n)$, is defined as the relative frequency of occurrence of a grain boundary with a misorientation, $\Delta g(\varphi_1,\Phi,\varphi_2)$, and a boundary plane normal, $n(\theta,\phi)$. The domain of grain boundary parameters $(\varphi_1,\Phi,\varphi_2,\theta,\phi)$, as described in **Figure 1**, ranges from 0 to 2π, π, 2π, π and 2π, respectively [14][16][15]. The number of distinguishable boundary types, N, in the domain is given by: $N = \frac{8\pi^5}{4 \times 24 \times 24 \times \Delta^5}$ [14]. Note that these distinguishable bins, which were parameterized by φ_1, $\cos\Phi$, φ_2, $\cos\theta$, and ϕ, have the same volume when an angular resolution (Δ) are equally partitioned. We could directly obtain the GBCD from three-dimensional techniques such as x-ray diffraction, transmission electron microscopy, and electron backscatter diffraction (EBSD) [5][6][7][21][22][23][141]. However, these techniques remain slow and difficult.

An EBSD map provides four of the five parameters, $(\varphi_1,\Phi,\varphi_2,\theta)$. The only unknown parameter is the angle (ϕ) between the observation plane and the grain boundary plane. The probability of a specific boundary plane occurring can be estimated using the stereological technique [14][16]. The stereological GBCD calculation has been validated and tested with simulated data as well as 3D-EBSD data [16]. The method has successfully characterized anisotropic distributions in a variety of polycrystalline materials [6][11][12][13][16][22][26][27][28][29] [30][31][32][33][34][35][36][37][38][39][40][41]. However, the stereological calculation presumes random sampling of the line segments at each misorientation. Specifically, the occurrences of grain orientation are assumed to be uniformly distributed at each misorientation, which is not the case for the highly textured polycrystallines. To improve the uniformity of random sampling, we corrected for the texture in the GBCD calculation. This new GBCD calculation is validated on polycrystalline copper, using samples with weak and strong texture.

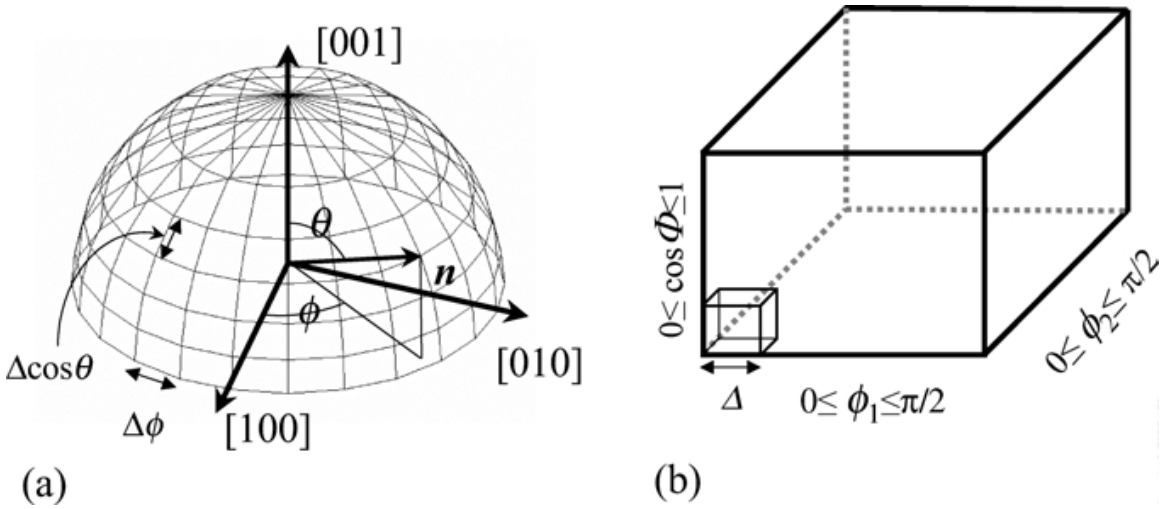

Figure 1. The schematic diagram shows the parameterization of the five macroscopic degrees of freedom, $\lambda(\Delta g,n)$, (a) two boundary plane orientation parameters and (b) three lattice misorientation parameters. This figure was reproduced from reference [14][16].

Method

The GBCD calculation with the texture correction factor is similar to the normal GBCD calculation [14][16][15]. **Figure 2** shows how the grain boundary traces are treated in the typical calculation. For a grain boundary trace (l'_{ij}), a set of grain boundary plane normals (n'_{ijk}), which obey the condition $l'_{ij} \cdot n'_{ijk} = 0$, were plotted on the great circle of the stereographic projection. While we don't know the true boundary plane, it is certain that the true boundary is in the set of boundary normal (n'_{ijk}). For each line segments, the boundary plane normal (n'_{ijk}) is weighted by the line length and added to the discrete data array according to the misorientation, $\Delta g(\varphi_1,\cos\Phi,\varphi_2)$, and the boundary plane normal, $n(\cos\theta,\phi)$. Note that for each line segments, the symmetry operations generate 36 equivalent representations in the discrete data array.

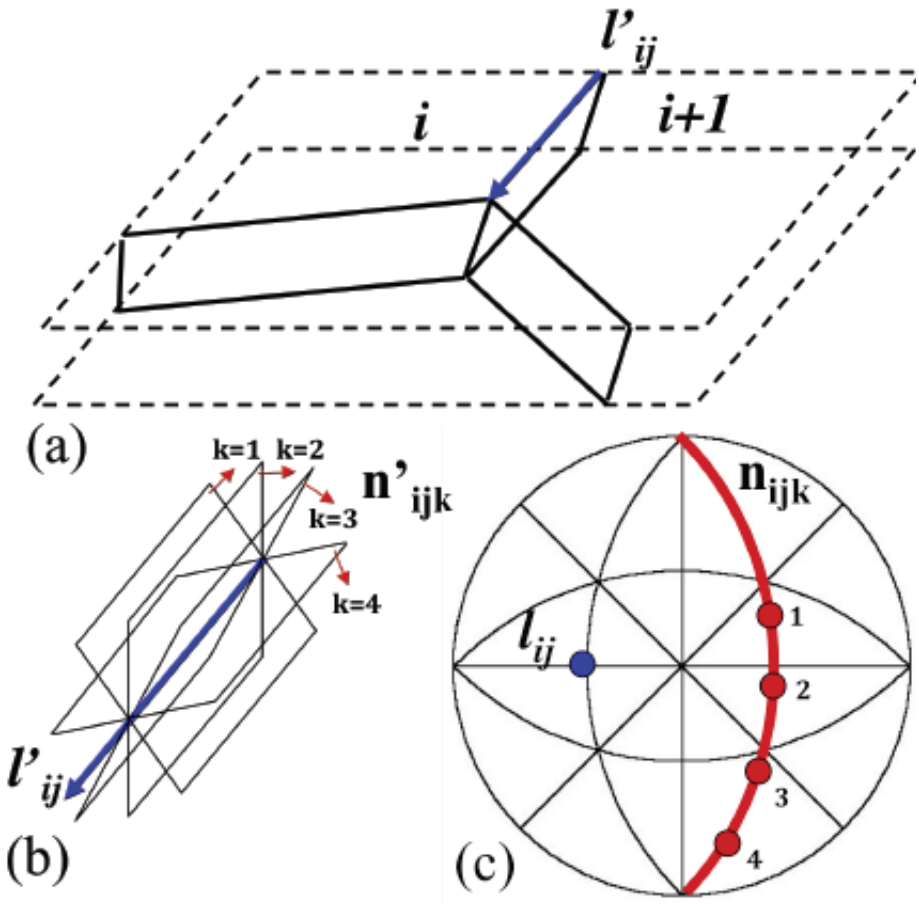

Figure 2. The schematic diagram shows the grain boundary traces process. (a) The identifications of a trace between crystals in the sample reference frame. (b) The set of grain boundary plane normal n'_{ijk}. (c) A stereographic projection represents the boundary trace, l'_{ij}, and the set of possible plane, n'_{ijk}, on the great circle in the grain boundary reference frame. This figure was reproduced from reference [16].

After sufficient observations, the true boundary will occur more frequently than the incorrectly assigned planes. The observed length (l_i^o) at cell i could be realized as the sum of the correct line length (l_i^c) and the length (l_j^c) from some other cell j that has cell i in the zone of observed traces. The total observed length (l_i^o) is

$$l_i^o = l_i^c + \sum_{j=1, j\neq i}^{D^2} \omega_{ij} l_j^c \qquad \text{Equation 1}$$

Where D is the number of divisions of the accumulation chosen to be 18 in this study. ω_{ij} is a weighting factor, which is largest when i and j are the neighboring cell and constant in the case that i and j are not the neighboring cells. Because the relative area of grain boundary is equal to the fractional length of the line segment, it is required to remove the incorrect assignments from the discrete data arrays. To do this, it was presumed that the boundary planes are randomly distributed. With this consideration, the correct length (l_i^c) for a particular misorientation and ith boundary plane cell is described as

$$l_i^c = \frac{l_i^o + (Z-1)\frac{(D-1)}{D} < l^o >}{1 + Z(D-1)} \qquad \text{Equation 2}$$

Where Z=2/D and $< l^o >$ is the average value of l^o, which is the total observed length at this particular misorientation. The details of this procedure have been described in [14][16][15]. As mentioned before, the grain orientations are not randomly distributed in a highly textured polycrystalline material. Therefore the normal GBCD calculation yields a biased result texture polycrystals. To alleviate this issue, we derive a texture correction factor, which is the inverse frequency of the grain orientations at each misorientation.

Results and Discussion

The highly texture polycrystalline specimens used in this study is a high purity copper film. The sample was made by sputtering copper and subsequently annealed in the vacuum at 900 °C to achieve the strong [111] texture parallel to the normal direction of the film, **Figure 3a** For a comparison, we use a polycrystalline copper, which has a weaker texture, **Figure 3b.** This specimen was made by annealed copper foil (99.9999% pure, Puratronic, Alfa Aesar, Ward Hill, MA) at 300 °C for 2 hours in the hydrogen flow furnace.

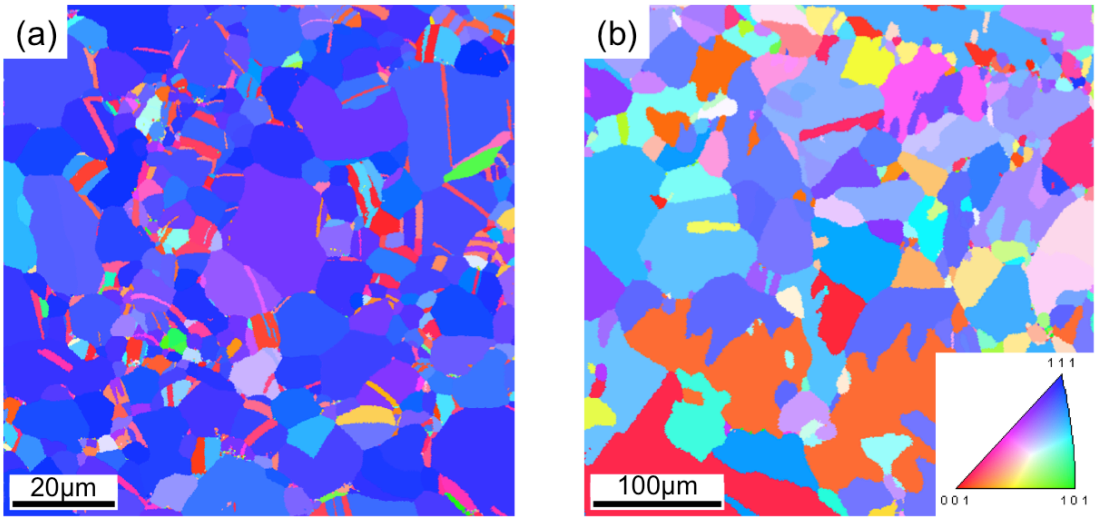

Figure 3. EBSD inverse pole figure maps of (a) Copper thin film, (b) Copper bulk. The crystallographic orientations are colored according to the standard stereographic triangle shown as an inset in (b).

The bulk specimen was ground with SiC paper and polished with diamond suspensions. The samples were fine polished with colloidal silica (40 nm). The local crystal orientations of the specimens were characterized by the EBSD technique. Note that the as-received copper thin film is flat and smooth enough for the EBSD measurement. We use a field-emission gun SEM (Quanta 200, FEI Company) equipped with an EBSD detector. EBSD patterns are collected and analyzed by TSL/OIM software. The step sizes of the measurements were deliberately selected to be greater than one tenth of the average grain size. The reconstructed grain boundary line segments were extracted from the EBSD maps. The numbers of line segments for each specimen are listed in **Table 1**. It should be noted that the population of Σ3 boundaries in the copper thin film is much lower than that of the copper bulk. At the same time, the coherent twin boundary population of the copper thin film (29%) is slightly greater than that of the copper bulk (27%). In other words, the distribution of the coherent twin boundary in the copper film has a shaper peak than that of the copper bulk. While it was found that the strong [111] texture of the copper film was generated from the strain energy minimization

during thermal annealing [142][143][144], it is possible that the shaper peak of the coherent twin boundary in the copper film could be also created by the strain energy. Nonetheless the analysis of the shape distribution of the coherent twin boundary is beyond the scope of the present study. The textures were calculated from the line segments using the WTS2POP code written by A.D. Rollett. **Figure 4** and **Figure 5** show the pole figures and the inverse pole figures of the specimens. The copper thin film has a significantly stronger [111] texture, see **Figure 4a** and **Figure 5a** This strong texture with [111] parallel to the normal direction of the annealed copper film is in agreement with the previous studies [143][144]. The copper bulk has much weaker texture as in **Figure 4b** and **Figure 5b**, which is similar to the (001)[100] cube texture of annealing texture of cold rolled Cu [98][99].

Table 1. Characteristics of samples and accumulated grain boundary data.

Polycrystalline copper	Annealed (°C)	Step size (μm)	Steps per segment	Number of segments	Non Σ3 (%)	Σ3 (%)	Coherent twin (%)
Film	900	0.2	8.2	68,102	62	38	29
Bulk	300	1.0	6.7	51,767	40	60	27

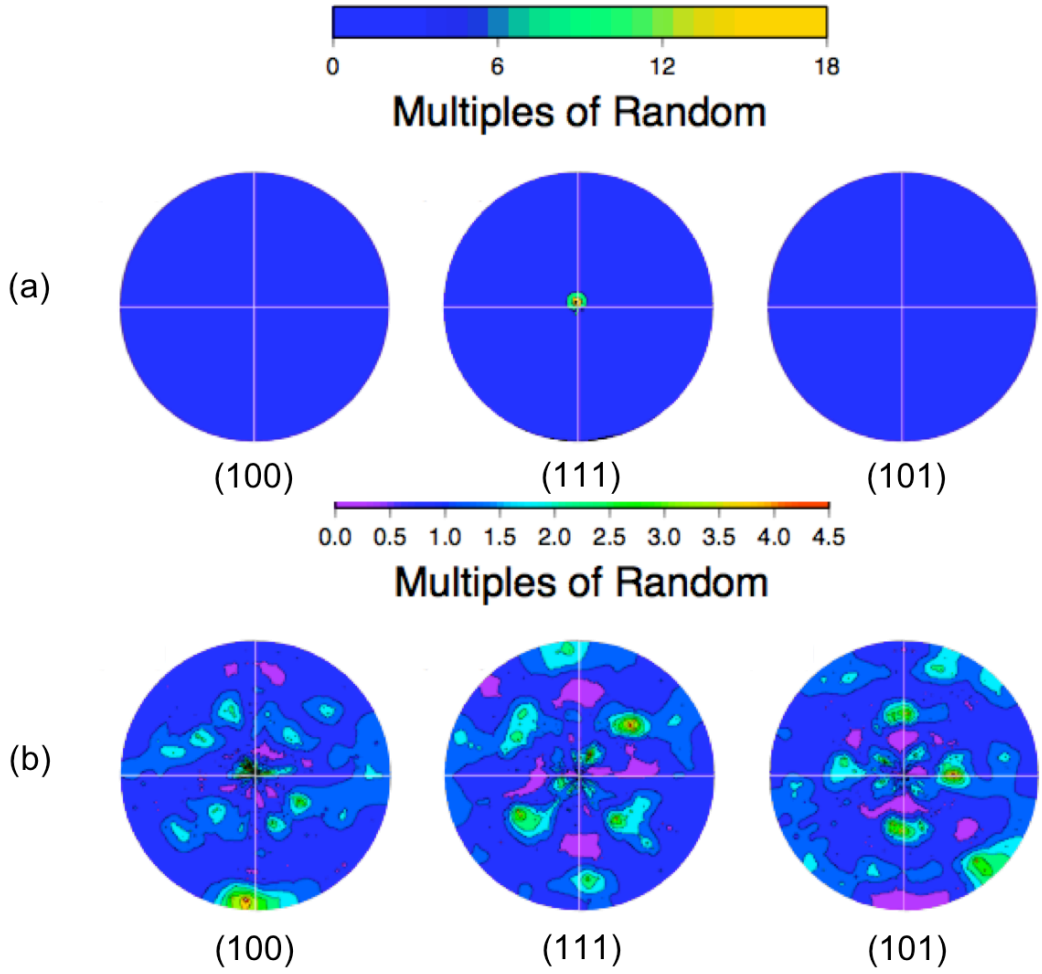

Figure 4. Pole figures for the specimens, (a) Copper film and (b) Copper bulk.

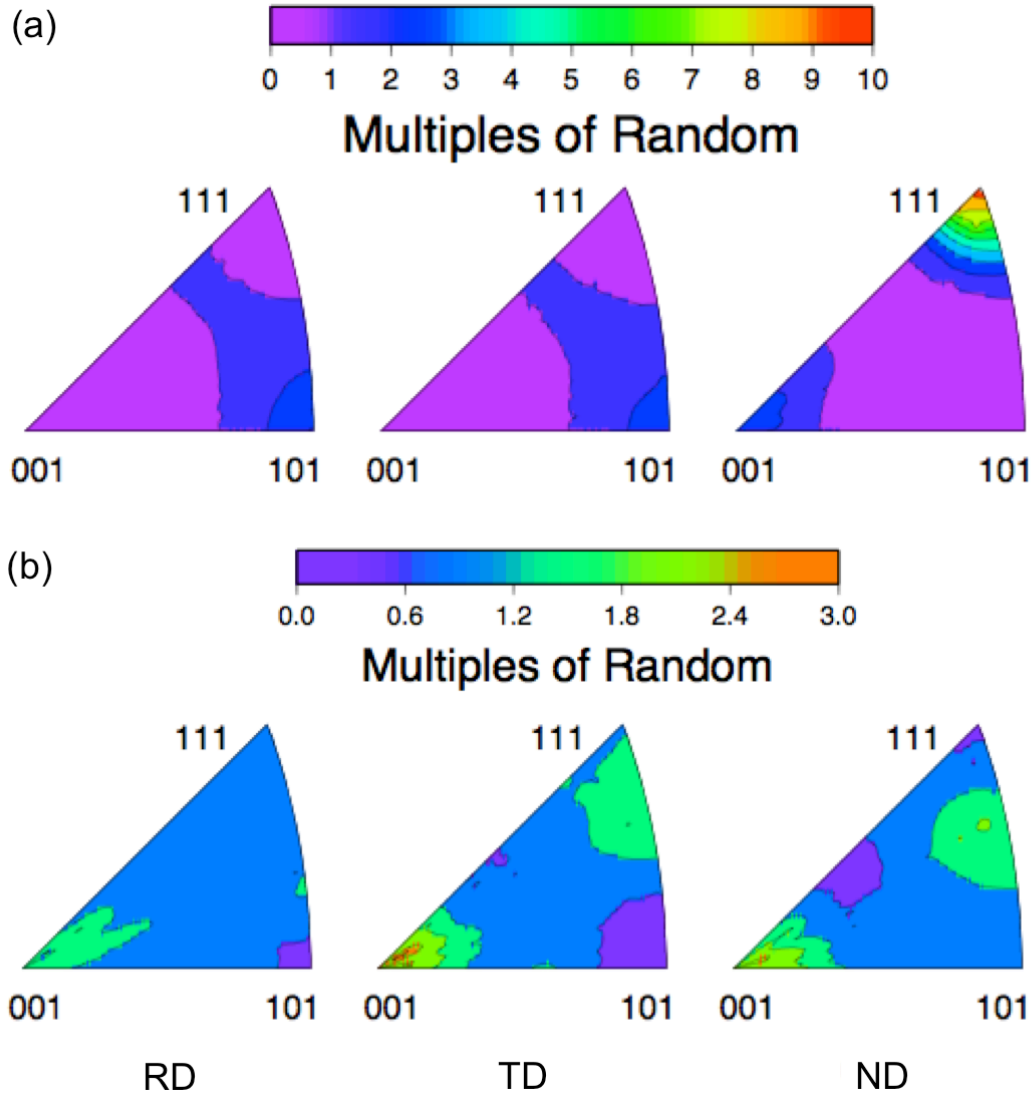

Figure 5. Inverse pole figures for the specimens, (a) Copper film and (b) Copper bulk. Note the sample reference frames were rolling direction RD, transverse direction TD, and normal direction ND.

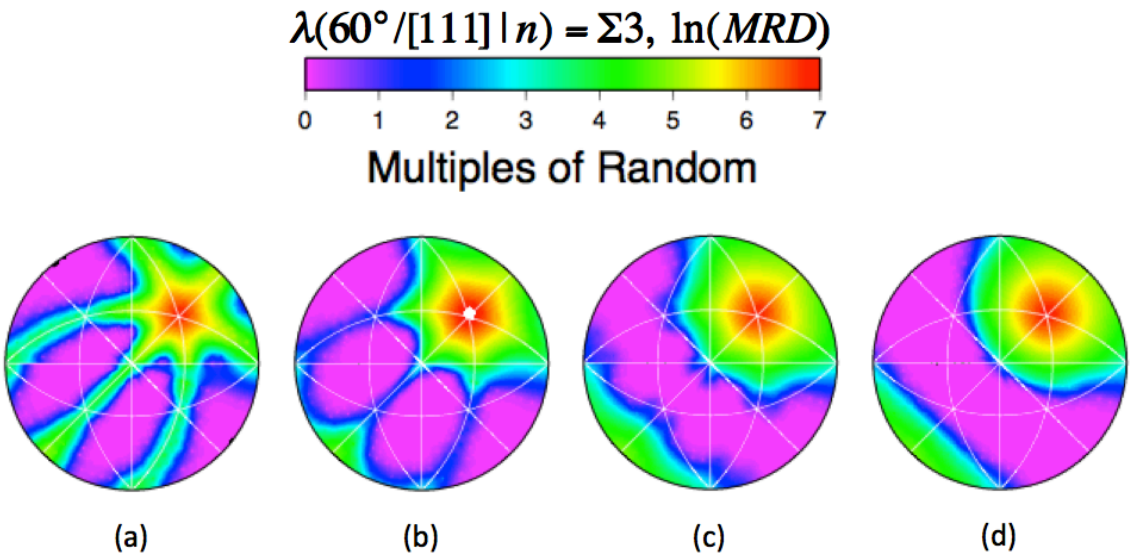

Figure 6. Grain boundary character distribution (GBCD) with a misorientation of 60° about [111] axis, (a) Copper thin film without texture correction, (b) Copper thin film with texture correction, (c) Copper bulk without texture correction, and (d) Copper bulk with texture correction.

Figure 6 shows the grain boundary plane distribution with a misorientation of 60° about the [111] axis. For the strongly textured specimen, the populations of the incoherent twin boundaries, which do not appear in the weak texture, are higher in the distribution calculated with the normal GBCD calculation (**Figure 6a**) than the one calculated using the texture correction scheme (**Figure 6b**). On the other hand, there are negligible differences between the grain boundary population distributions in the weakly textured specimen calculated using the normal scheme (**Figure 6c**) and the texture correction scheme (**Figure 6d**).

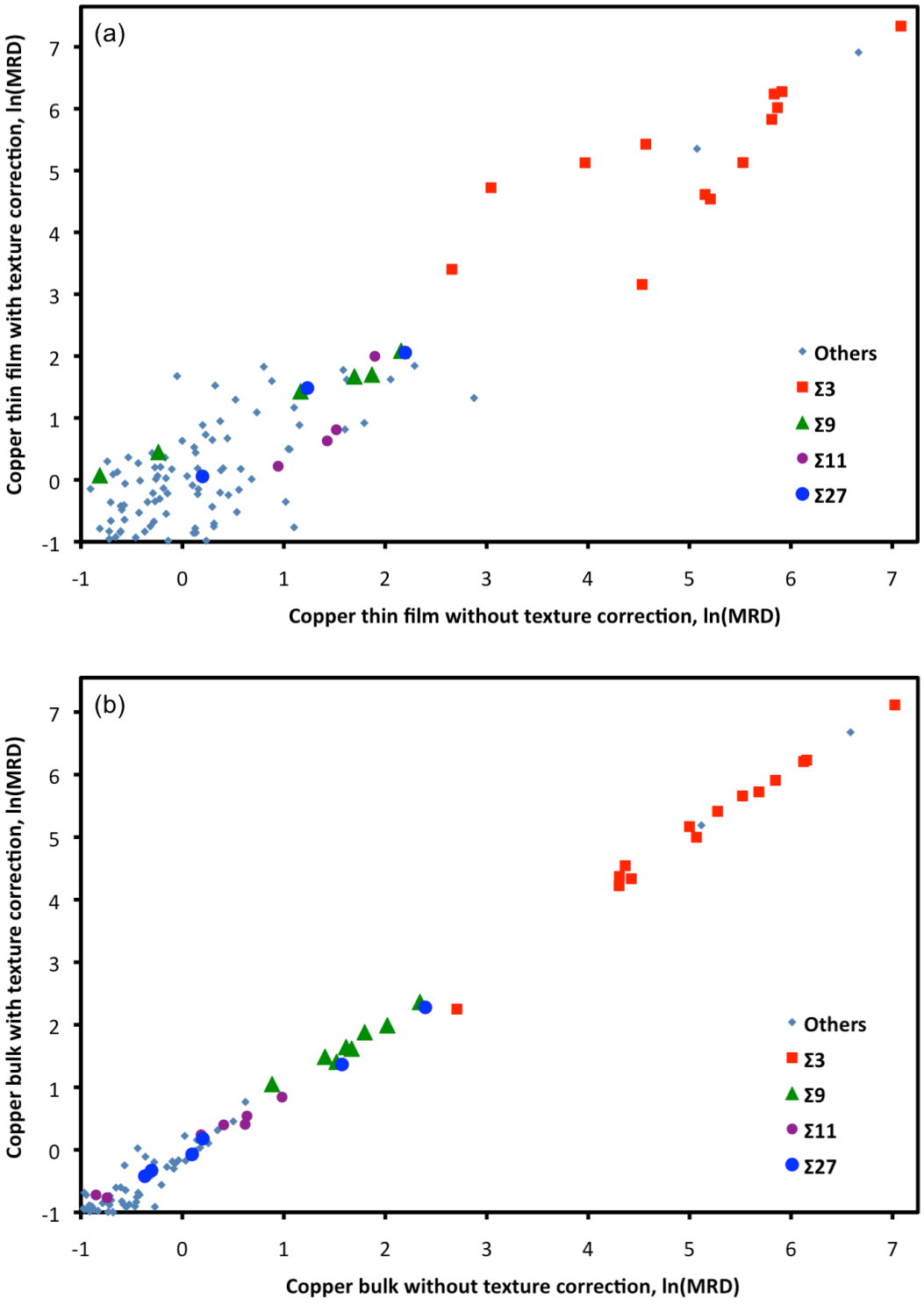

Figure 7. The relationship between GBCD of copper specimens calculated with and without texture correction, (a) Copper thin film and (b) Copper bulk. The grain boundaries separated into five categories: Σ3 boundaries (red squares), Σ9 boundaries (green triangles), Σ11 boundaries (violet circles), Σ27 boundaries (blue circles), and other types of boundaries (blue diamonds).

Figure 7a and **Figure 7b** show a comparison of the relative areas for grain boundary calculated with and without the texture correction in the strongly textured and the weakly textured specimens, respectively. The vertical axis and horizontal axis show the relative areas for grain boundary calculated with and without the texture correction, respectively. As clearly seen in **Figure 7a**, there is broader scatter for the grain boundary population in the strongly textured specimen when compared to the weakly textured sample (**Figure 7b**), especially for the Σ3 boundaries. The correlation coefficient of the relative area for grain boundary in the strongly textured specimen (0.89) is lower than that of the weakly textured specimen (0.98). This indicates that in the strongly textured specimen the grain boundary populations, which are determined by using the texture correction scheme, are significantly changed with respect to the boundary populations determined from the normal GBCD calculation.

Figure 8 shows a comparison between the relative areas for grain boundaries in the strong textured sample versus the weakly textured specimen. The correlation coefficient is improved from 0.68 to 0.75 when using the texture correction scheme in the GBCD calculation. It has been reported that the grain boundary population is inversely correlated to the boundary energy [6][5][9][43][44][9][2][3][4]. It is therefore reasonable to believe that the relative areas for grain boundaries in those two copper specimens are correlated. For this reason, the correlation coefficient could be used as an indicator that characterizes an improvement of the GBCD calculation with the texture correction. It should be noted that our specimens were annealed at different temperatures, see **Table 1**. Because the grain boundary energies vary with the temperature [85][53] [73][74][76], we would expect the annealing temperature to influence the GBCDs. Nevertheless, if the overall grain boundary energies scale with temperature in a similar manner, the influence of temperature on the relative boundary energies should be negligible.

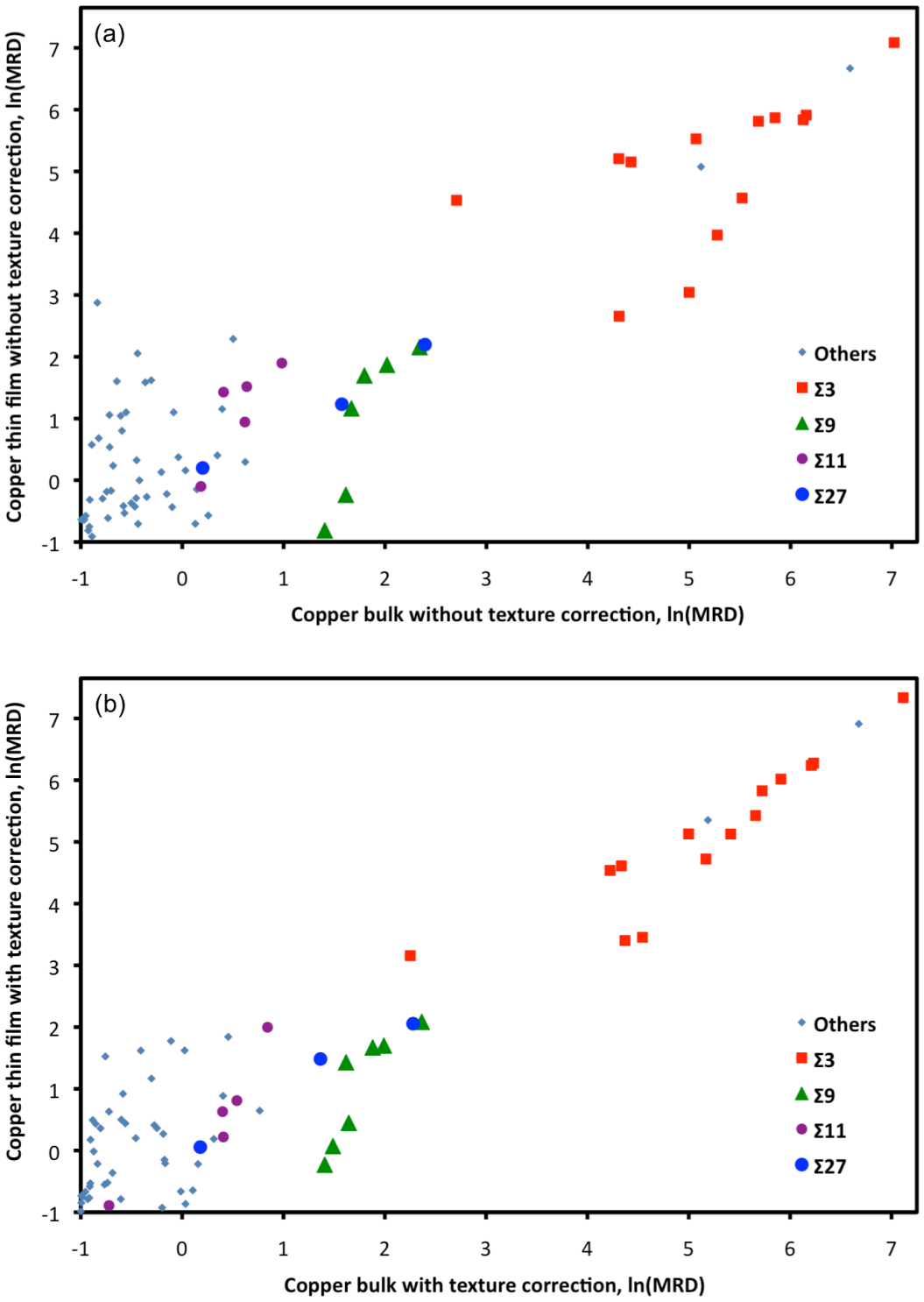

Figure 8. The relationship between GBCDs of copper thin film and copper bulk, (a) GBCD calculated without texture correction and (b) GBCDs calculated with texture correction. The grain boundaries were colored the same as in **Figure 7**.

The GBCD calculation could be improved by directly determining the weight factor ω_{ij}, which was estimated for the nearest neighbor cells and for non-neighboring cells. This assumption could lead to the errors in the estimation of the grain boundary population, in which the actual weight factor ω_{ij} is different for each cell. These weight factors, ω_{ij}, could be determined directly from the Equation 1. This will be part of future work.

Conclusion

In conclusion, we have developed a texture correction scheme to derive the GBCD in polycrystalline materials from planar EBSD maps. The method has been tested on strongly and weakly textured polycrystalline copper. We found that the GBCD correlation between those two copper specimens improves when the texture correction scheme is used. We conclude that the GBCD calculation with the texture correction is a reasonable method to estimate the relative areas for grain boundaries in highly textured polycrystals.

Appendix B

Grain Boundary Character Distribution of Perovskite $BaTiO_3$ and $SrTiO_3$

Abstract

The relative grain boundary areas of polycrystalline perovskite ($BaTiO_3$ and $SrTiO_3$) ceramics were measured. While the most populous boundaries in $BaTiO_3$ and $SrTiO_3$ sintered for 3 hours are centered at the coherent twin boundary, the population of the coherent twin boundary in $SrTiO_3$ is significantly lower than that of $BaTiO_3$ and decreased when the sintering time increased from 3 to 6 hours. The comparisons between the populations of the $\Sigma 3$ boundaries and the average populations of the other boundaries excluding $\Sigma 3$ boundaries in the $BaTiO_3$ and the $SrTiO_3$ specimens indicate that the perovskite ceramics have similar grain boundary character distributions.

Introduction

Polycrystalline perovskites with a simple cubic unit cell have a wide range of applications, such as electroceramic, colossal magnetoresistance, and high-temperature superconductivity [145]. The relative areas of grain boundaries, which is quantified by the grain boundary character distribution (GBCD) [14][16], plays a role in determining the overall macroscopic properties of the polycrystalline ceramics. A prior study of the GBCD in polycrystalline $SrTiO_3$ showed that the anisotropy of the GBCD is inversely correlated to the grain boundary energy, which is the free energy that is required to create this grain boundary [21]. In other words, the grain boundary energy could be simply defined as the sum of the adjacent

surface energies minus a binding energy that results from the bond formation when the two surfaces are brought together [65]. Because the binding energy is approximately constant and less significant for a general boundary [21], the boundaries that composed of the lowest surface energy (100) plane are hypothetical low energy boundaries and frequently observed in the polycrystalline $SrTiO_3$ [21][146]. Recent studies showed that the GBCDs of materials, which have FCC crystal structure (isostructural), are strongly correlated [3]. Because grain boundary energies of FCC materials are correlated [10], this clearly shows that the inverse correlation between grain boundary population and energy is the controlling mechanism leading to the strong correlation of the GBCDs in the FCC metals. $BaTiO_3$ and $SrTiO_3$, which are perovskite ceramics, have surface energy characteristics that are similar [147]. Grain boundary energy, which is dominated by the adjoining surface energies, would be expected to share this similarity; as a result, the GBCDs of $BaTiO_3$ and $SrTiO_3$ might be also correlated in a manner similar to what was reported for the FCC metals [3] and BCC metals [148]. If it were the case, this would be an enormous simplifying principle to obtain the GBCD of perovskite ceramic materials. Therefore the goal of this study is to investigate the GBCDs of isostructural perovskite polycrystalline ceramics. We chose $BaTiO_3$ and $SrTiO_3$ as model materials to represent a wide range of cubic perovskite materials because both materials have been well studied in our group and could be obtained from commercial sources with known purities. It was reported that $\Sigma 3$ boundaries in high purity $SrTiO_3$ have lower populations than (100) terminated boundaries, which dominated an entire grain boundary space [21]. A more recent study reported that the populations of $\Sigma 3$ boundaries in the polycrystalline $SrTiO_3$ decreased with the sintering time in the air [149]. However, this study focused only on the coincidence site lattice (CSL) distribution. To investigate the GBCD correlation between $BaTiO_3$ and $SrTiO_3$, we shall investigate the influence of annealing time on the GBCD of the polycrystalline $SrTiO_3$.

Experimental Methods

The polycrystalline samples were fabricated from 99.7 % pure $BaTiO_3$ and 99.7% pure $SrTiO_3$ (Alfa Aesar, Ward Hill, MA). The powders were ground and compressed at 220 MPa to form a pellet with diameter of 1 cm. The samples were placed in an alumina with excess powder to reduce the loss of volatile elements during sintering in the air. The temperatures for burn-off, densification, and sintering for each specimen are summarized in **Table 1**. The samples were lapped with 9 μm and 3 μm alumina slurries, and finally polished with 0.01 μm colloidal silica. The $SrTiO_3$ specimens were annealed at 1100 °C for 3 hours to repair polishing damage, and sputter coated with 1 nm Pt to avoid charging during electron backscatter (EBSD) measurements. A field-emission gun scanning electron microscope (Quanta 200, FEI Company) equipped with an EBSD detector was used to map the crystal orientations of the specimens. The EBSD patterns are collected from the sample, which is tilted to about 70° with respect to the electron beam. To reduce this source of uncertainty [14][16], we deliberately use a step size that is approximately one tenth of average grain size for the EBSD measurements; $BaTiO_3$ (2 μm) and $SrTiO_3$ (0.2 μm and 0.5 μm for 3 and 6 hours sintering respectively).

Table 1. The materials and materials' preparations of $BaTiO_3$ and $SrTiO_3$.

Steps	Temperature °C ($BaTiO_3$ / $SrTiO_3$)	Dwelling time hours ($BaTiO_3$ / $SrTiO_3$)
Burn-Off	900 / 900	10 / 10
Densification	1230 / 1340	10 / 10
Sintering	1360 / 1470	3 / 3(6)

The raw EBSD data were processed with standard cleaned up functions in the TSL software. To correct the misindexing in $SrTiO_3$, the pseudosymmetry clean up was used to remove 45° <001> false boundaries with a tolerance of 2°. This clean up procedure changes less than 1% of all data. The relative areas for grain boundaries were obtained from a stereological interpretation of the EBSD maps [14][15][16]. To reconstruct grain boundary line segments for the GBCD calculation, we used TSL/OIM software to extract line segments from the EBSD maps. The software first indentifies triple junctions and then estimates the in plane grain boundary geometry [94]. Straight lines are first used to connect all of the triple points. If these segments deviate from the boundary position more than two pixels, the segments will be divided to better match the curvatures of grain boundaries. About 50,000 line segments for each data set were used in the calculation GBCD with a binning resolution of 10°.

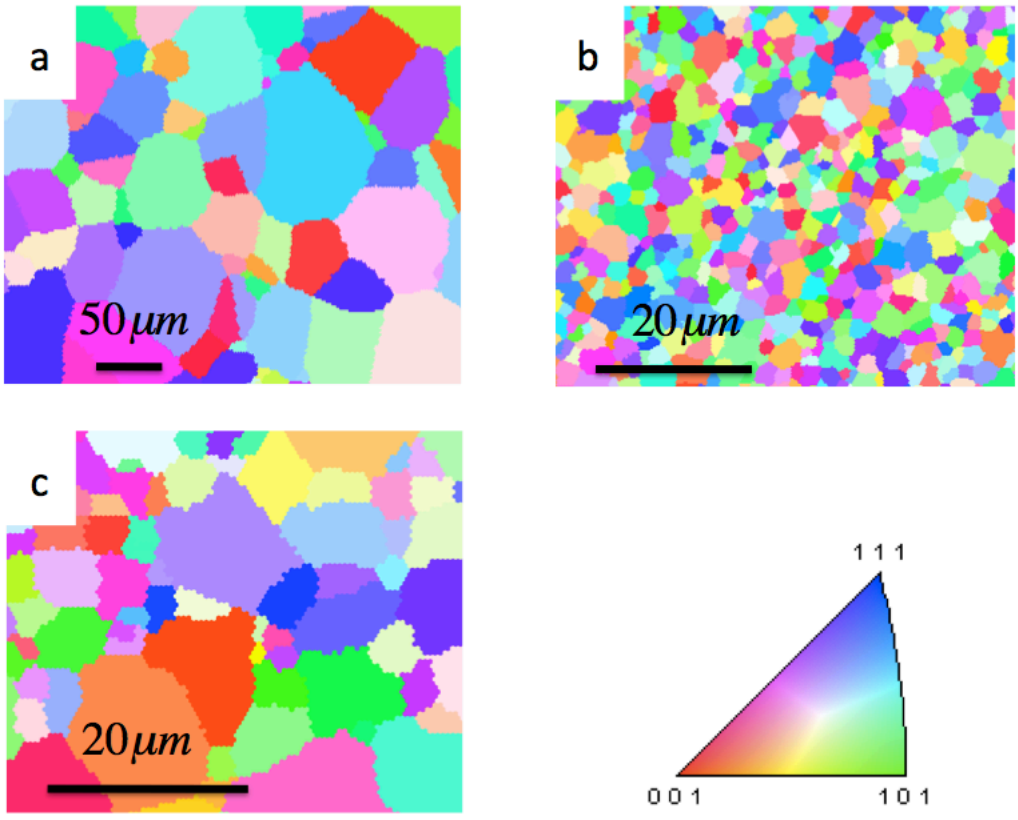

Figure 1. EBSD inverse pole figure maps of (a) $BaTiO_3$, (b) $SrTiO_3$ sintered for 3 hours, and (c) $SrTiO_3$ sintered for 6 hours. The crystallographic orientations are colored according to the standard stereographic triangle on the bottom right.

Results and Discussion

Figure 1 shows the nominal microstructure of the polycrystalline perovskite oxides, which clearly reveals no grain orientation texture for all specimens. **Figure 2** shows the misorientation angle distribution for all specimens. While $BaTiO_3$ has its peak maximum at about 60°, the frequencies of the other misorientation angles are clearly similar to the random misorientation angle distribution (Mackenzie distribution), which has its peak at about 45° [105]. The frequency of the misorientation angle at about 60° in the $SrTiO_3$ specimen sintered for 3 hours is slightly larger than the $SrTiO_3$ specimen sintered for 6 hours. Nevertheless, the misorientation angle distributions of both $SrTiO_3$ specimens are very similar to the randomly oriented polycrystalline (Mackenzie distribution) and consistent with the previous studies [25][150].

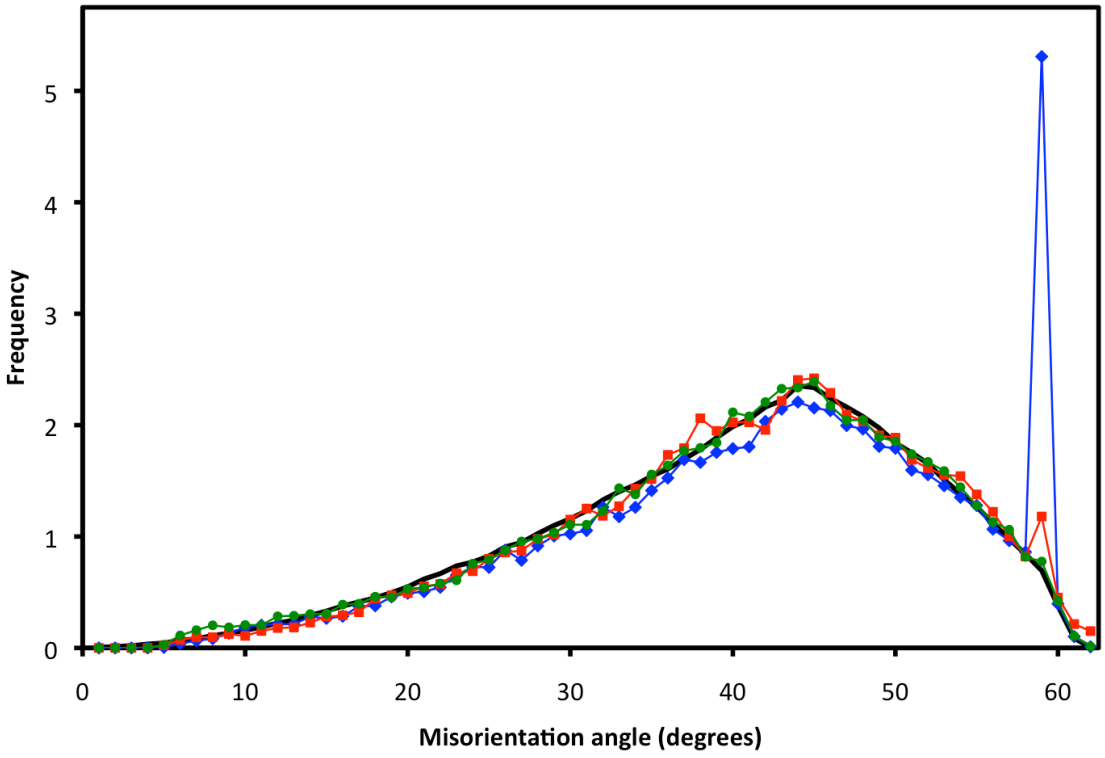

Figure 2. Misorientation angle distributions of $BaTiO_3$ (blue diamonds), $SrTiO_3$ sintered for 3 hours (red squares), and $SrTiO_3$ sintered for 6 hours (green circles). Black line shows randomly oriented crystals (Mackenzie distribution).

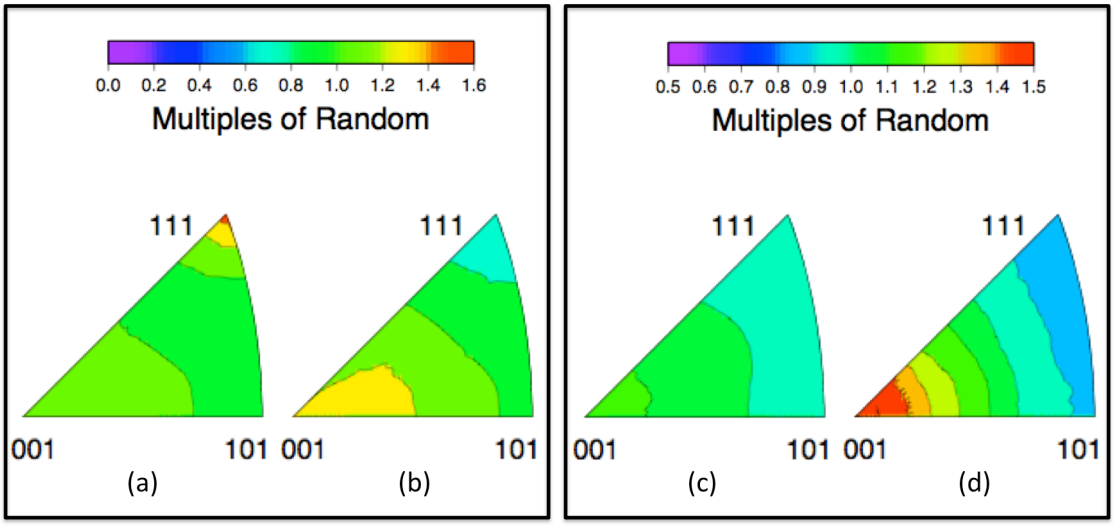

Figure 3. Grain boundary plane distributions in (a) $BaTiO_3$, (b) $BaTiO_3$ excluding the Σ3 boundaries, (c) $SrTiO_3$ with 3 hours sintering, and (d) $SrTiO_3$ with 6 hours sintering.

Figure 3 shows the grain boundary plane distributions (GBPDs) of the specimens plotted on a stereographic projection in units of multiple of a random distribution (MRD). These distributions have relatively weak anisotropy. The only prominent feature was the peak at the (111) orientation in $BaTiO_3$ (see **Figure 3a**). Interestingly, when excluding the Σ3 boundaries in the GBCD calculation of $BaTiO_3$, the peak was relocated from (111) to (100) planes (see **Figure 3b**). This observation indicates that the enhancement of (111) planes in $BaTiO_3$ originates from the high frequency of the Σ3 boundaries. In addition, the peak maxima of the (100) plane in $SrTiO_3$, as shown in **Figure 3c** and **Figure 3d**, increased from 1.1 MRD to 1.5 MRD when increasing the sintering times from 3 to 6 hours. The GBPDs of $BaTiO_3$ in **Figure 3b** and $SrTiO_3$ specimens (**Figure 3c** and **Figure 3d**) are consistent with the previous results of $SrTiO_3$ [21][25][150]. **Figure 4** shows the distribution of grain boundary plane normal with 60° misorientations about [111] axes. Both $BaTiO_3$ (**Figure 4a**) and $SrTiO_3$ specimen sintered for 3 hours (**Figure 4b**) have the same peak maxima at the coherent twin boundary with (111) plane on either side of the boundary.

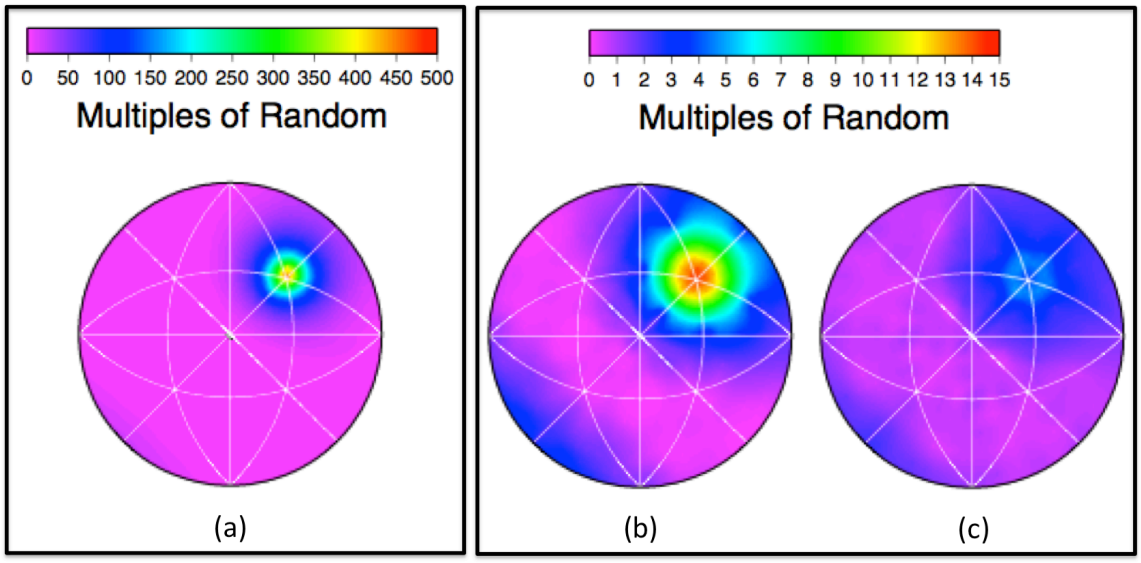

Figure 4. Observed distribution of grain boundary plane normals for boundaries with a 60° misorientation about the [111] axes, (a) $BaTiO_3$, (b) $SrTiO_3$ with 3 hours sintering, and (c) $SrTiO_3$ with 6 hours sintering.

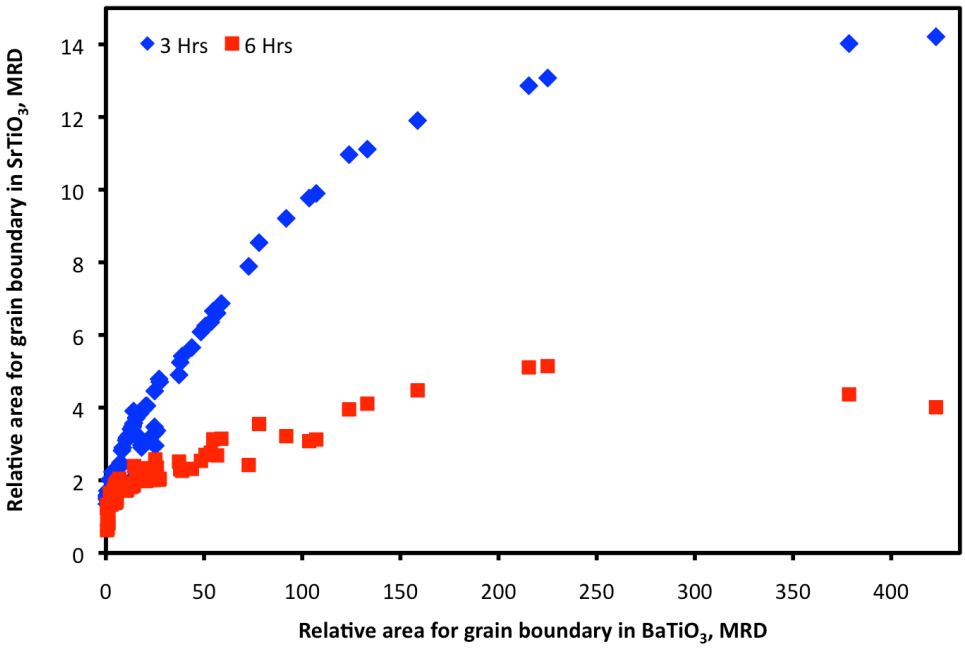

Figure 5. Comparison between the relative areas for Σ3 boundaries in $SrTiO_3$ and $BaTiO_3$. The horizontal axis shows the relative area in $BaTiO_3$ and the vertical axis shows the relative area in $SrTiO_3$ specimen sintered for 3 hours (blue diamonds) and 6 hours (red squares). Each point corresponds to two crystallographically identical grain boundaries in two different materials.

The peak magnitude in $BaTiO_3$ (576 MRD) is considerably larger than in $SrTiO_3$. Because of this large peak in the $BaTiO_3$ specimen, the GBPD of the $BaTiO_3$ in **Figure 3a** has its peak maximum centered at the (111). It should be noted that the peak maximum in the $SrTiO_3$ specimens disappears when increasing the sintering times from 3 to 6 hours (see **Figure 5**). As we mentioned before, the anisotropy of the grain boundary energy is dominated by the total energy of the adjoining surfaces. In this case, the (100) symmetric twist boundary would be the lowest boundary energy in perovskites. Because the coherent twin represents one of the lowest boundary energy in the cubic perovskites, therefore the coherent twin boundary could also be considered as a special grain boundary [151]. In this case, we would expect that the relative areas of the (100) symmetric twist boundary and the coherent twin boundary would be increased with the sintering time and reach a constant value in a steady state GBCD. However the fraction of the coherent twin boundary in the $SrTiO_3$ sintered for 6 hours (2.7 MRD) is less than that in the $SrTiO_3$ sintered for 3 hours (15.3 MRD) as shown in **Figure 4**.

It should be pointed out that the decreasing of the coherent twin boundary in the $SrTiO_3$ specimen is consistent with the previous report that the fraction of the $\Sigma 3$ boundaries in the high purity polycrystalline $SrTiO_3$ decreased with the sintering time [149]. Because the coherent twin boundary is composed of two highest surface energies with the (111) planes [146], the bonding energy for the coherent twin has to be relatively large compared with a general grain boundary. A high planar coincidence of the coherent twin boundary might be sensitive to shear stress originated from the sintering processes and the defect concentration in the polycrystalline oxide perovskites [152]. Prior experimental results suggested that the sintering atmosphere could influence to the grain growth behavior in $BaTiO_3$ [153] and $SrTiO_3$ [154]. The coherent twin-assisted abnormal grain growths are inhibited when decreasing the oxygen partial pressure to 4×10^{-18} atm [153][154][155]. These results indicated that the observation frequency of the coherent twin boundary was related to the oxygen vacancy concentration, which is in fact directly related to the oxygen partial pressure during sintering. Significant

studies of oxide perovskites by using a high-resolution transmission electron microscopy provide evidence for the presence of oxygen vacancies at the coherent twin boundary in $BaTiO_3$ [156] and $SrTiO_3$ [157]. A first principle calculation showed that the energy of the coherent twin boundary in $SrTiO_3$ significantly increased with the number of dangling bonds, which is defined as the number of missing coordination atoms (vacancy defect) in the grain boundary structure [151]. The coherent twin boundary energy changed from 0.48 to 2.05 J/m^2 when the number of normalized value of dangling bond changed from 0 to 0.85. In this case the five macroscopic degree of freedom does not necessary specify a single microscopic grain boundary structure and there are multiple atomic arrangements with different boundary energies for the coherent twin boundary. These vacancy defects at the grain boundary might be similar to the idea of the segregation at the grain boundary, known as the complexion [37][158]. Because an overall vacancy formation energy in $SrTiO_3$ is lower than the formation energy in $BaTiO_3$ [159], we would expect that the vacancy concentration in a polycrystalline $SrTiO_3$ sintered in the air might be much greater than in $BaTiO_3$. If the grain boundary energy is the key factor in controlling GBCD, the grain boundary energy associated with the vacancy defect could influence the population of the coherent twin boundary in $SrTiO_3$.

Figure 6 shows the grain boundary population of $BaTiO_3$ and $SrTiO_3$ at four misorientations about [100] axes. For all misorientations, the population peaks are located at the (100) plane. This indicates that the pure twist grain boundaries, in which both terminated boundaries are the lowest energy {100} plane, are the most prevalent grain boundaries, regardless of the boundary misorientations. There are also dominant tilt boundaries, in which one plane is terminated by {100}, and the other is terminated by the crystal plane that are tilted away from the {100} [21], as clearly depicted in **Figure 6l**. The distributions of $BaTiO_3$ are similar to those of $SrTiO_3$.

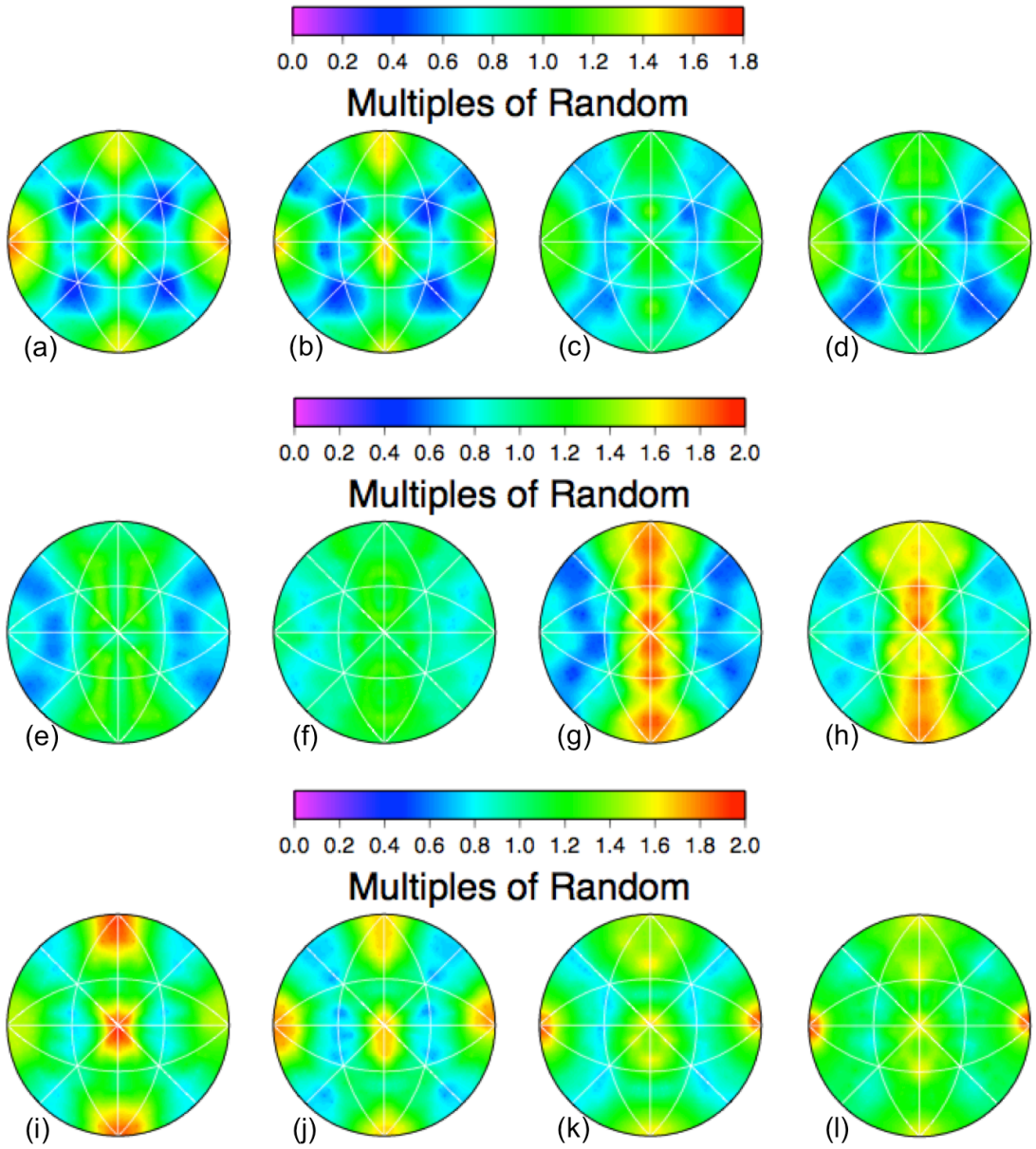

Figure 6. Observed distribution of grain boundary plane normal for boundary with (a) 10°, (b) 20°, (c) 30°, and (d) 40° about [100] axes in the $BaTiO_3$ specimen. (e)-(h) and (i)-(l) show the similar plots for the $SrTiO_3$ specimens sintered for 3 hours and 6 hours respectively.

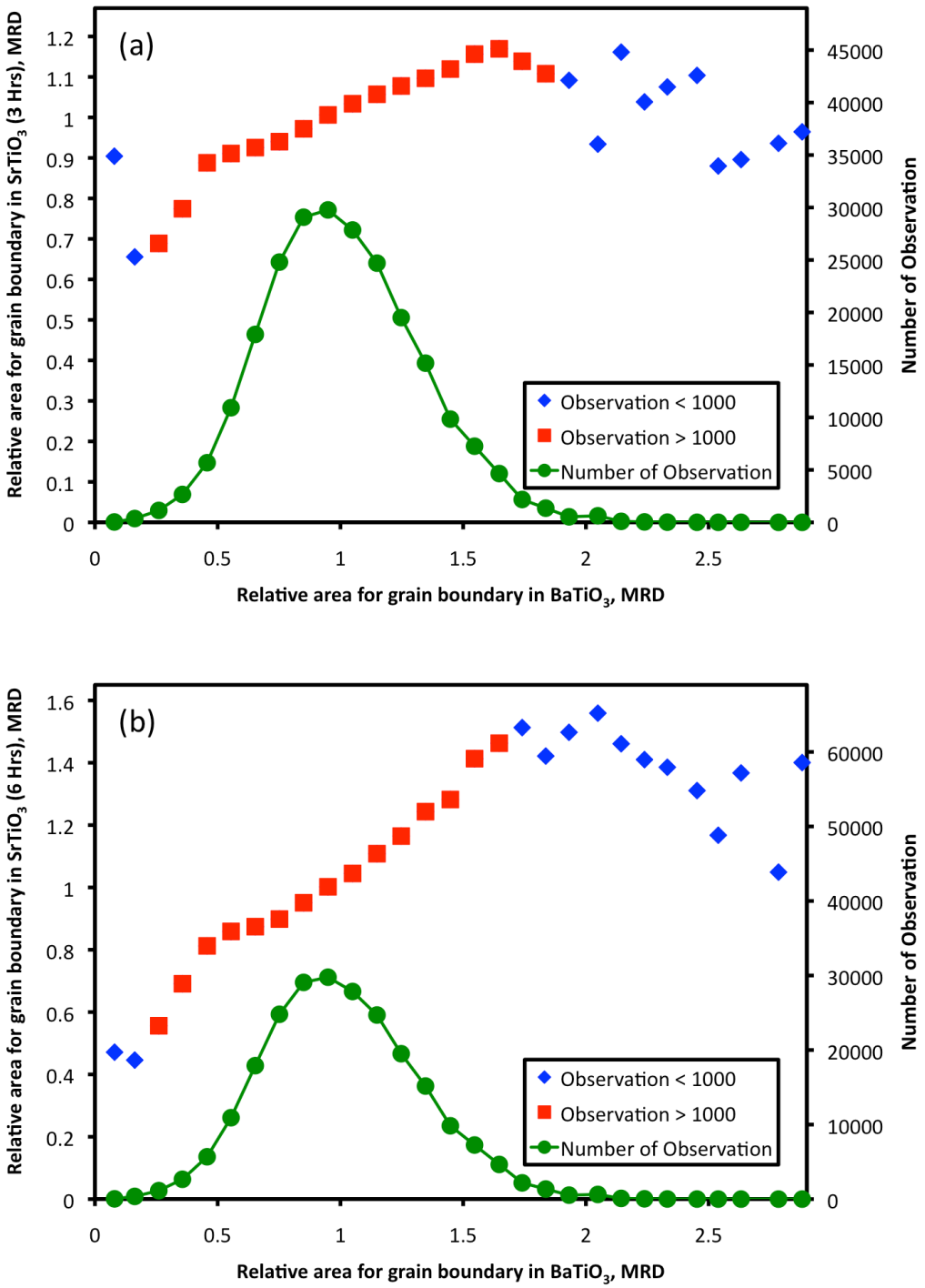

Figure 7. Comparison of GBCD calculated with excluding Σ3 boundaries in $SrTiO_3$ and $BaTiO_3$ specimens. The average grain boundary populations in $SrTiO_3$ sintered for 3 hours (a) and 6 hours (b) are plotted with the average populations of the same boundaries in $BaTiO_3$. Note that the average populations with observation less than 1000 and greater than 1000 are labeled by blue diamonds and red squares respectively. The number of observation is marked by green circles.

To quantitatively compare the grain boundary populations between $BaTiO_3$ and $SrTiO_3$, we use an averaging scheme. The population range (P) is discretized into bins of fixed width (Δ= 0.1 MRD). The averaged values of all of the boundaries in $BaTiO_3$ that have populations between P and P+ Δ, are determined. In the $SrTiO_3$ data sets, we then find the average populations of the set of boundaries that have the identical crystallographic parameters. It should be pointed out that there are 236,196 bins for the GBCD calculated with a resolution of 10° [14][15][16]. The averaged grain boundary populations in each population range of $BaTiO_3$ and $SrTiO_3$ and the number of bins that were included are shown in **Figure 7**. As shown in the plot, the maximum populations in the $SrTiO_3$ specimen sintered for 3 hours (**Figure 7a**) and 6 hours (**Figure 7b**), which include data from fewer bins, clearly deviate from the rest of the data. Nevertheless, the average populations in the $SrTiO_3$ specimens, which are based on more than 1000 bins, are strongly correlated with the average populations of the same boundaries in $BaTiO_3$. These results indicate that while the peak maxima in $BaTiO_3$ and $SrTiO_3$ are not the same boundary types, the characteristic distributions of grain boundary in $BaTiO_3$ and $SrTiO_3$ are strongly correlated on average.

Conclusion

The populations of the Σ3 boundaries in $SrTiO_3$, which decrease with the sintering time, are considerably smaller than in $BaTiO_3$. When the Σ3 boundaries and the other boundary types are considered separately, the relative grain boundary populations in the $BaTiO_3$ and the $SrTiO_3$ specimens are positively correlated. These observations indicate that the GBCDs of isostructural perovskite ceramics are positively correlated.

Reference

[1] G.S. Rohrer, “Grain boundary energy anisotropy: a review,” J. Mater Sci, vol. 46, pp. 5881–5895, 2011.

[2] G. S. Rohrer, “Measuring and Interpreting the Structure of Grain-Boundary Networks,” Journal of the American Ceramic Society, vol. 94, no. 3, pp. 633–646, 2011.

[3] E.A. Holm, G.S. Rohrer, S. M. Foiles, A.D. Rollett, H.M. Miller, and D.L. Olmsted, “Validating computed grain boundary energies in FCC metals using the grain boundary character distribution,” Acta Materialia,, vol. 59, pp. 5250–5256, 2011.

[4] G. S. Rohrer, E. A. Holm, A. D. Rollett, S. M. Foiles, J. Li, and D. L. Olmsted, “Comparing calculated and measured grain boundary energies in nickel,” Acta Materialia, vol. 58, no. 15, pp. 5063–5069, 2010.

[5] David M. Saylor, Adam Morawiec, and Gregory S. Rohrer, “The relative free energies of grain boundaries in magnesia as a function of five macroscopic parameters,” Acta Materialia, vol. 51, no. 13, pp. 3675–3686, 2003.

[6] J. Li, S. J. Dillon, and G. S. Rohrer, “Relative grain boundary area and energy distributions in nickel,” Acta Materialia, vol. 57, no. 14, pp. 4304–4311, 2009.

[7] S. J. Dillon and G. S. Rohrer, “Characterization of the Grain-Boundary Character and Energy Distributions of Yttria Using Automated Serial Sectioning and EBSD in the FIB,” Journal of the American Ceramic Society, vol. 92, no. 7, pp. 1580–1585, 2009.

[8] H. Beladi and G.S. Rohrer, “The relative grain boundary area and energy distributions in a ferritic steel determined from three-dimensional electron backscatter diffraction maps,” Acta Materialia, vol. 61, no. 4, pp. 1404–1412, 2013.

[9] H.M. Miller and G.S. Rohrer, “Evolution of the Grain Boundary Character Distribution in Strontium Titanate during Grain Growth,” Ceram. Trans., 201, J. Wiley & Sons, Hoboken, NJ, 2009, pp. 335–342, 2009.

[10] Elizabeth A. Holm, David L. Olmsted, and Stephen M. Foiles, “Comparing grain boundary energies in face-centered cubic metals: Al, Au, Cu and Ni,” Scripta Materialia, vol. 63, no. 9, pp. 905–908, 2010.

[11] F. Papillon, G. S. Rohrer, and P. Wynblatt, “Effect of Segregating Impurities on the Grain-Boundary Character Distribution of Magnesium Oxide,” Journal of the American Ceramic Society, vol. 92, no. 12, pp. 3044–3051, 2009.

[12] S. J. Dillon, M. P. Harmer, and G. S. Rohrer, “Influence of interface energies on solute partitioning mechanisms in doped aluminas,” Acta Materialia, vol. 58, no. 15, pp. 5097–5108, 2010.

[13] G. Rohrer, V. Randle, C. Kim, and Y. Hu, “Changes in the five-parameter grain boundary character distribution in α-brass brought about by iterative thermomechanical processing,” Acta Materialia, vol. 54, no. 17, pp. 4489–4502, 2006.

[14] Rohrer GS, Saylor DM, El Dasher B, Adams BL, Rollett AD, and Wynblatt P, “The distribution of internal interfaces in polycrystals,” Z. Metallk., vol. 95, no. 4, pp. 197–214, 2004.

[15] David M Saylor, Bassem S El-Dasher, Brent L Adams, and Gregory S Rohrer, “Measuring the Five-Parameter Grain-Boundary Distribution from Observations of Planar Sections,” Metall. Mater. Trans. A—Phys. Metall. Mater. Sci., 35A [7] 1981–9 (2004)., vol. 35A, no. 7, pp. 1981–9, 2004.

[16] G.S. Rohrer and V. Randle, “Measurement of the five-parameter grain boundary distribution from planar sections,” Electron Backscatter Diffraction in Materials Science, Springer, New York, vol. edited by A.J. Schwartz, M. Kumar, B.L. Adams, and D.P. Field, pp. 215–229, 2009.

[17] S. Schmidt, S. F. Nielsen, C. Gundlach, L. Margulies, X. Huang, and D. Juul Jensen, “Watching the Growth of Bulk Grains During Recrystallization of Deformed Metals,” Science, vol. 305, pp. 229–232, 2004.

[18] Christopher M. Hefferan, Jonathan Lind, Shiu Fai Li, Ulrich Lienert, Anthony D. Rollett, Robert M. Suter, “Observation of recovery and recrystallization in high-purity aluminum measured with forward modeling analysis of high-energy diffraction microscopy,” Acta Materialia, vol. 60, pp. 4311–4318, 2012.

[19] Hefferan, Christopher M, “Measurement of Annealing Phenomena in High Purity Metals with Near-field High Energy X-ray Diffraction Microscopy,” PhD thesis, Department of Physics, Carnegie Mellon University, 2012.

[20] H. H. Liu, S. Schmidt, H. F. Poulsen, A. Godfrey, Z. Q. Liu, J. A. Sharon, and X. Huang, “Three-Dimensional Orientation Mapping in the Transmission Electron Microscope,” Science, vol. 332, pp. 833–834, 2011.

[21] D. M. Saylor, B. Dasher, T. Sano, and G. S. Rohrer, “Distribution of Grain Boundaries in SrTiO3 as a Function of Five Macroscopic Parameters,” Journal of the American Ceramic Society, vol. 87, no. 4, pp. 670–676, 2004.

[22] A. Khorashadizadeh, D. Raabe, S. Zaefferer, G. S. Rohrer, A. D. Rollett, and M. Winning, “Five-Parameter Grain Boundary Analysis by 3D EBSD of an Ultra Fine Grained CuZr Alloy Processed by Equal Channel Angular Pressing,” Adv. Eng. Mater., vol. 13, no. 4, pp. 237–244, 2011.

[23] A. D. Rollett, S.-B. Lee, R. Campman, and G. S. Rohrer, “Three-Dimensional Characterization of Microstructure by Electron Back-Scatter Diffraction,” Annu. Rev. Mater. Res., vol. 37, no. 1, pp. 627–658, 2007.

[24] I.M. Robertson, C.A. Schuh, J.S. Vetrano, N.D. Browning, D.P. Field, D. Juul Jensen, M.K. Miller, I. Baker, D.C. Dunand, R. Dunin-Borkowski, B. Kabius, T.Kelly, S. Lozano-Perez, A. Misra, G.S. Rohrer, A.D. Rollett, M.L. Taheri, G.B. Thompson, M. Uchic, X.-L. Wang and G. Was, “Towards an integrated materials characterization toolbox,” Journal of Materials Research, vol. 26, pp. 1341–1383, 2011.

[25] Herbert M. Miller III, “Influences of Processing and Composition on the Grain Boundary Character Distribution,” PhD thesis, Department of Materials Science and Engineering, Carnegie Mellon University, 2008.

[26] V. Randle, G. Rohrer, H. Miller, M. Coleman, and G. Owen, “Five-parameter grain boundary distribution of commercially grain boundary engineered nickel and copper,” Acta Materialia, vol. 56, no. 10, pp. 2363–2373, 2008.

[27] D. M. Saylor, B. Dasher, Y. Pang, H. M. Miller, P. Wynblatt, A. D. Rollett, and G. S. Rohrer, “Habits of Grains in Dense Polycrystalline Solids,” Journal of the American Ceramic Society, vol. 87, no. 4, pp. 724–726, 2004.

[28] David M Saylor, Bassem S El Dasher, Anthony D Rollett, and Gregory S Rohrer, “Distribution of grain boundaries in aluminum as a function of five macroscopic parameters,” Acta Materialia, vol. 52, no. 12, pp. 3649–3655, 2004.

[29] C.-S. Kim, T. R. Massa, and G. S. Rohrer, “Interface Character Distributions in WC–Co Composites,” Journal of the American Ceramic Society, vol. 91, no. 3, pp. 996–1001, 2008.

[30] Edward P. Gorzkowski, Helen M. Chan, and Martin P. Harmer, “Changes in the distribution of interfaces in PMN-35 mol% PT as a function of time,” Zeitschrift fur Metallkunde, vol. 96, no. 2, pp. 207–210, 2005.

[31] C. S. Kim, Y. Hu, G. S. Rohrer, and V. Randle, “Five-Parameter Grain Boundary Distribution in Grain Boundary Engineered Brass,” Scripta Materialia, vol. 52, no. 7, pp. 633–637, 2005.

[32] V. Randle, Y. Hu, G. S. Rohrer, and C. S. Kim, “Distribution of Misorientations and Grain Boundary Planes in Grain Boundary Engineered Brass,” Materials Science and Technology, vol. 21, no. 11, pp. 1287–1292, 2005.

[33] V. Randle, Y. Hu, G.S. Rohrer, C.-S. Kim, “The Distribution of Misorientations and Grain Boundary Planes in Grain Boundary Engineered Brass,” Materials Science and Technology, vol. 21, pp. 1275–1281, 2005.

[34] S. T. Downey, N. Bembridge, P. N. Kalu, H. M. Miller, G. S. Rohrer, and K. Han, “Grain Boundary Plane Distributions in Modified 316 LN Steel Exposed at Elevated and Cryogenic Temperatures,” J Mater Sci, vol. 42, no. 23, pp. 9543–9547, 2007.

[35] V. Randle, G. S. Rohrer, and Y. Hu, “Five-Parameter Grain Boundary Analysis of a Titanium Alloy Before and After Low-Temperature Annealing,” Scripta Materialia, vol. 58, no. 3, pp. 183–186, 2008.

[36] V. Randle and R. Jones, “Grain Boundary Plane Distributions and Single-Step versus Multiple-Step Grain Boundary Engineering,” Mater. Sci. Eng. A—Struct. Mater. Prop. Microstruct. Process., vol. 524, no. 1–2, pp. 134–142, 2009.

[37] S. J. Dillon, M. P. Harmer, and G. S. Rohrer, “The Relative Energies of Normally and Abnormally Growing Grain Boundaries in Alumina Displaying Different Complexions,” Journal of the American Ceramic Society, 2010.

[38] Gregory S. Rohrer, “The Distribution of Grain Boundary Planes in Polycrystals,” JOM Journal of the Minerals, Metals and Materials Society, vol. 59, no. 9, pp. 38–42, 2007.

[39] W. Wang, B. Zhou, G. S. Rohrer, H. Guo, and Z. Cai, “Textures and grain boundary character distributions in a cold rolled and annealed Pb–Ca based alloy,” Materials Science and Engineering: A, vol. 527, no. 16–17, pp. 3695–3706, 2010.

[40] R. Jones, V. Randle, and G. Owen, “Carbide Precipitation and Grain Boundary Plane Selection in Overaged Type 316 Austenitic Stainless Steel,” Mater. Sci. Eng. A—Struct. Mater. Prop. Microstruct. Process., vol. 496, no. 1–2, pp. 256–261, 2008.

[41] R. Jones, V. Randle, D. Engelberg, and T. J. Marrow, “Five-parameter grain boundary analysis of a grain boundary-engineered austenitic stainless steel,” Journal of Microscopy, vol. 233, no. 3, pp. 417–422, 2009.

[42] C.B. Thomson and V. Randle, “‘Fine tuning’ at Σ3n boundaries in nickel,” Acta Materialia, vol. 45, no. 12, pp. 4909–4916, 1997.

[43] S. Dillon and G. Rohrer, “Mechanism for the development of anisotropic grain boundary character distributions during normal grain growth,” Acta Materialia, vol. 57, no. 1, pp. 1–7, 2009.

[44] G. Rohrer S., J. Li, S. Lee, A. Rollett D., M. Groeber, and M. Uchic D., “Deriving grain boundary character distributions and relative grain boundary energies from three-dimensional EBSD data,” Mats. Sci. Tech., 2009.

[45] J. Gruber, D. George, A. Kuprat, G. Rohrer, and A. Rollett, “Effect of anisotropic grain boundary properties on grain boundary plane distributions during grain growth,” Scripta Materialia, 2005.

[46] M. Upmanyu, G.N. Hassold, A. Kazaryan, E.A. Holm, Y. Wang, B. Patton and D.J. Srolovitz, “Boundary Mobility and Energy Anisotropy Effects on Microstructural Evolution During Grain Growth,” Interface Sci., vol. 10, no. 2–3, pp. 201–216, 2002.

[47] Gregory S. Rohrer, Jason Gruber, and Anthony D. Rollett., "A Model for the Origin of Anisotropic Grain Boundary Character Distributions in Polycrystalline Materials," Application of Texture Analysis Vol 201 Ceramic Transactions Edited by A.D. Rollett, pp. 343–354, 2009.

[48] Gregory S. Rohrer, "Influence of Interface Anisotropy on Grain Growth and Coarsening," Annual Review of Materials Research, vol. 35, no. 1, pp. 99–126, 2005.

[49] Koenraad G. F. Janssens, David Olmsted, Elizabeth A. Holm, Stephen M. Foiles, Steven J. Plimpton, and Peter M. Derlet, "Computing themobility of grain boundaries," Nature Materials, vol. 5, pp. 124–127, 2006.

[50] Elizabeth A. Holm and Stephen M. Foiles, "How Grain Growth Stops: A Mechanism for Grain-Growth Stagnation in Pure Materials," Science, vol. 328, pp. 1138–1141, 2010.

[51] H. Gleiter, "On the structure of grain boundaries in metals," Materials Science and Engineering, vol. 52, no. 2, pp. 91–131, 1982.

[52] W. T. Read and W. Shockley, "Dislocation Models of Crystal Grain Boundaries," Phys. Rev. B, vol. 78, pp. 275–289, 1950.

[53] N.A Gjostein, and F.N Rhines, "Absolute interfacial energies of [001] tilt and twist grain boundaries in copper," Acta Metallurgica, vol. 7, no. 5, pp. 319–330, 1959.

[54] D.G. Brandon, "The Structure of High-angle Grain Boundaries," Acta Metallurgica, vol. 14, pp. 1479–1484, 1966.

[55] D.G. Brandon, B. Ralph, S. Ranganathan, and M.S. Wald, "A field ion microscope study of atomic configuration at grain boundaries," Acta Metallurgica, vol. 12, pp. 813–821, 1964.

[56] V.Y. Gertsman, and S.M. Bruemmer, "Study of grain boundary character along intergranular stress corrosion crack paths in austenitic alloys," Acta Mater., vol. 49, p. 1589, 2001.

[57] Valerie Randle, "Special boundaries and grain boundary plane engineering," Scripta Materialia, vol. 54, pp. 1011–1015, 2006.

[58] K. Matsunaga, H. Nishimura, S. Hanyu, H. Muto, T. Yamamoto, and Y. Ikuhara, "HRTEM Study on Grain Boundary Atomic Structures Related to the Sliding Behavior in Alumina Bicrystals," Applied Surface Science, vol. 241, no. 1–2, pp. 75–79, 2005.

[59] A.P Sutton and R.W Balluffi, "Overview no. 61 On geometric criteria for low interfacial energy," Acta Metallurgica, vol. 35, no. 9, pp. 2177–2201, 1987.

[60] D. Wolf, “Structure-energy correlation for grain boundaries in F.C.C. metals—I. Boundaries on the (111) and (100) planes,” Acta Metallurgica, vol. 37, no. 7, pp. 1983–1993, 1989.

[61] D. Wolf, “Structure-energy correlation for grain boundaries in F.C.C. metals—II. Boundaries on the (110) and (113) planes,” Acta Metallurgica, vol. 37, no. 10, pp. 2823–2833, 1989.

[62] D. Wolf, “Structure-energy correlation for grain boundaries in F.C.C. metals—III. Symmetrical tilt boundaries,” Acta Metallurgica et Materialia, vol. 38, no. 5, pp. 781–790, 1990.

[63] D. Wolf, “Structure-energy correlation for grain boundaries in F.C.C. metals—IV. Asymmetrical twist (general) boundaries,” Acta Metallurgica et Materialia, vol. 38, no. 5, pp. 791–798, 1990.

[64] D. Wolf and S. Phillpot, “Role of the densest lattice planes in the stability of crystalline interfaces: A computer simulation study,” Materials Science and Engineering: A, vol. 107, pp. 3–14, 1989.

[65] D. Wolf, “Correlation between structure, energy, and ideal cleavage fracture for symmetrical grain boundaries in fcc metals,” Journal of Materials Research, vol. 5, no. 8, pp. 1708–1730, 1990.

[66] D. Wolf, “A broken-bond model for grain boundaries in face-centered cubic metals,” Journal of Applied Physics, vol. 68, pp. 3221–3236, 1990.

[67] Murray S. Daw and M. I. Baskes, “Semiempirical, Quantum Mechanical Calculation of Hydrogen Embrittlement in Metals,” Physical Review Letters, vol. 50, no. 17, pp. 1285–1288, 1983.

[68] M. Daw, “The embedded-atom method: a review of theory and applications,” Materials Science Reports, vol. 9, no. 7–8, pp. 251–310, 1993.

[69] D. L. Olmsted, S. M. Foiles, and E. A. Holm, “Survey of computed grain boundary properties in face-centered cubic metals: I. Grain boundary energy,” Acta Materialia, vol. 57, no. 13, pp. 3694–3703, 2009.

[70] S.J. Plimpton, “Large-scale atomic/molecular massively parallel simulator,” Sandia National Laboratories, 2007.

[71] D. Wolf, “A Read-Shockley Model for High-angle Grain Boundaries,” Scripta Metallurgica, vol. 23, pp. 1713–1718, 1989.

[72] Herring E. Kingston WE, “The physics of powder metallurgy,” McGraw-Hill, New York, 1951.

[73] G. Hasson, J.-Y. Boos, I. Herbeuval, M. Biscondi, and C. Goux, “Theoretical and experimental determinations of grain boundary structures and energies: Correlation with various experimental results,” Surface Science, vol. 31, pp. 115–137, 1972.

[74] G.C. Hasson and C. Goux, “Interfacial energies of tilt boundaries in aluminium. Experimental and theoretical determination,” Scripta Metallurgica, vol. 5, no. 10, pp. 889–894, 1971.

[75] W. W. Mullins, “Theory of Thermal Grooving,” J. Appl. Phys., vol. 28, no. 3, p. 333, 1957.

[76] H. Miura, “Temperature dependence of the energy of Cu [1 1 O] symmetrical tilt grain boundaries,” Journal of Materials Science Letters, vol. 13, pp. 46–48, 1994.

[77] D. M. Saylor, A. Morawiec, and G. S. Rohrer, “Distribution and Energies of Grain Boundaries in Magnesia as a Function of Five Degrees of Freedom,” Journal of the American Ceramic Society, vol. 85, no. 12, pp. 3081–3083, 2004.

[78] D. Saylor, “Distribution of grain boundaries in magnesia as a function of five macroscopic parameters,” Acta Materialia, vol. 51, no. 13, pp. 3663–3674, 2003.

[79] A. Morawiec, “Method to calculate the grain boundary energy distribution over the space of macroscopic boundary parameters from the geometry of triple junctions,” Acta Materialia, vol. 48, no. 13, pp. 3525–3532, 2000.

[80] K. Barmak, E. Eggeling, M. Emelianenko, Y. Epshteyn, D. Kinderlehrer, R. Sharp, and S. Ta’asan, “An entropy based theory of the grain boundary character distribution,” Discrete Cont. Dyn. Sys. A, vol. 30, no. 2, pp. 427–454, 2011.

[81] K. Barmak, E. Eggeling, M. Emelianenko, Y. Epshteyn, D. Kinderlehrer, R. Sharp, and S. Ta’asan, “Critical events, entropy, and the grain boundary character distribution,” Physical Review B, vol. 83, no. 13, p. 134117, 2011.

[82] L.K. Nash, “Elements of Statistical Thermodynamics,” Second Edition, Addison-Wesley Publishing Company, Inc, 2006.

[83] Terrell L. Hill, “An Introduction to Statistical Thermodynamics,” Dover Publications, Inc., 1987.

[84] WR Tyson and WA Miller, “Surface free energies of solid metals: Estimation from liquid surface tension measurements,” Surface Science, vol. 62, pp. 267–276, 1977.

[85] Stephen M. Foiles, “Evaluation of harmonic methods for calculating the free energy of defects in solids,” Phys. Rev. B, vol. 49, no. 21, pp. 14930–14938, 1994.

[86] Stephen M. Foiles, “Temperature dependence of grain boundary free energy and elastic constants,” Scripta Materialia, vol. 62, pp. 231–234, 2010.

[87] Byeong-Joo Lee, Jae-Hyeok Shim,and M. I. Baskes, “Semiempirical atomic potentials for the fcc metals Cu, Ag, Au, Ni, Pd, Pt, Al, and Pb based on first and second nearest-neighbor modified embedded atom method,” Physical Review B, vol. 68, p. 144112, 2003.

[88] Jian-Min Zhang, Dou-Dou Wang, and Ke-Wei Xu, “Calculation of the surface energy of bcc transition metals by using the second nearest–neighbor modified embedded atom method,” Applied Surface Science, vol. 252, pp. 8217–8222, 2006.

[89] M. W. Finnis and J. E. Sinclair, “A simple empirical N-body potential for transition metals,” Philosophical Magazine A, vol. 50, no. 1, pp. 45–55, 1984.

[90] Brent L. Adams, Stuart I. Wright and Karsten Kunze, “Orientation Imaging: The Emergence of a New Microscopy,” Metallurgical and Materials Transactions A, vol. 24A, no. 4, pp. 819–831, 1993.

[91] F. J. Humphreys, “Review Grain and subgrain characterisation by electron backscatter diffraction,” Journal of Materials Science, vol. 36, pp. 3833–3854, 2001.

[92] S. Zaefferer, “On the formation mechanisms, spatial resolution and intensity of backscatter Kikuchi patterns,” Ultramicroscopy, vol. 107, pp. 254–266, 2007.

[93] David M. Saylor, “The Character Dependence of Interfacial Energies in Magnesia,” PhD thesis, Department of Materials Science and Engineering, Carnegie Mellon University, 2001.

[94] Wright SI and Larsen RJ, “Extracting twins from orientation imaging microscopy scan data,” Journal of Microscopy, vol. 205, no. Pt 3, pp. 245–252, 2002.

[95] Gregory S. Rohrer, “Fortran programs for calculating the GBCD from 2D or 3D EBSD data and some other programs,”
http://mimp.materials.cmu.edu/~gr20/stereology/,
http://mimp.materials.cmu.edu/~gr20/for_lisa/?C=N;O=D.

[96] Frederick Williams and Peter Monge, “Reasoning with Statistics,” Fifth Edition, Harcourt College Publishers, 2001.

[97] Jae Bon Koo and Duk Yong Yoon, “The dependence of normal and abnormal grain growth in silver on annealing temperature and atmosphere,” Metallurgical and Materials Transactions A, vol. 32, no. 3, pp. 469–475, 2001.

[98] B.J. Duggan, K. Lücke, G. Köhlhoff, and C.S. Lee, “On the origin of cube texture in copper,” Acta Metallurgica et Materialia, vol. 41, no. 6, pp. 1921–1927, 1993.

[99] A.A. Ridha and W.B. Hutchinson, “Recrystallisationmechanisms and the origin of cube texture in copper,” Acta Metallurgica, vol. 30, no. 10, pp. 1929–1939, 1982.

[100] K. Ito, R. Musick, and K. Lücke, "The Influence of Iron Content and Annealing Temperature on the Recrystallization Textures of High-purity Aluminium-Iron Alloys," Acta Metall., vol. 31, no. 12, pp. 2137–2149, 1983.

[101] Niels Hansen and Dorte Juul Jensen, "Deformation and Recrystallization Textures in Commercially Pure Aluminum," Metallurgical and Materials Transactions A, vol. 17, no. 2, pp. 253–259, 1986.

[102] F.J. Humphreys and M. Hatherly, "Recrystallization and Related Annealing Phenomena," Elsevier, vol. Chapter 12, no. Recrystallization textures, pp. 379–413, 2004.

[103] Doherty R.D., Hughes D.A., Humphreys F.J., Jonas J.J., Jensen D.J., Kassner M.E., King W.E., McNelley T.R., McQueen H.J., and Rollett A.D., "Current issues in recrystallization: a review," Materials Science and Engineering: A, vol. 238, no. 2, pp. 219–274, 1997.

[104] J.K. Mackenzie, A.J.W. Moore, J.F. Nicholas, "Bonds broken at atomically flat crystal surfaces—I: Face-centred and body-centred cubic crystals," J. Phys. Chem. Solids, vol. 23, pp. 185–196, 1962.

[105] J.K. Mackenzie, "Second paper on statistics associated with the random disorientation of cubes," Biometrika, vol. 45, pp. 229–240, 1958.

[106] E. Holm, "On misorientation distribution evolution during anisotropic grain growth," Acta Materialia, vol. 49, no. 15, pp. 2981–2991, 2001.

[107] D. Wolf, "Correlation between the energy and structure of grain boundaries in b.c.c metals. I. Symmetrical boundaries on the (110) and (100) planes," Philosophical Magazine B, vol. 59, no. 6, pp. 667–680, 1989.

[108] D. Wolf, "Correlation between the energy and structure of grain boundaries in b.c.c. metals. II. Symmetrical tilt boundaries," Philosophical Magazine A, vol. 62, no. 4, pp. 447–464, 1990.

[109] D. Wolf, "Structure and energy of general grain boundaries in bcc metals," Journal of Applied Physics, vol. 69, no. 1, pp. 185–196, 1991.

[110] H. Beladi and G.S. Rohrer, "The Distribution of Grain Boundary Planes in Interstitial Free Steel," Metallurgical and Materials Transactions A, vol. 44A, pp. 115–124, 2013.

[111] Dierk Raabe and K. Lücke, "Rolling and Annealing Textures of BCC Metals," Materials Science Forum, vol. 157–162, pp. 597–610, 1994.

[112] Tricia A. Bennett, Chang-Soo Kim, Gregory S. Rohrer and Anthony D. Rollett, "Five-Parameter Grain Boundary Character Distribution in Fe-1%Si," Materials Science Forum, vol. 467–470, pp. 727–732, 2004.

[113] MA Tschopp, KN Solanki, F Gao, X Sun, MA Khaleel, "Probing grain boundary sink strength at the nanoscale: Energetics and length scales of vacancy and interstitial absorption by grain boundaries in α-Fe," Phys. Rev. B, vol. 85, p. 064108, 2012.

[114] Hyun-Kyu Kim, Won-Seok Ko, Hyuk-Joong Lee, Seong Gyoon Kim, and Byeong-Joo Lee, "An identification scheme of grain boundaries and construction of a grain boundary energy database," Scripta Materialia, vol. 64, pp. 1152–1155, 2011.

[115] M. I. Mendelev, S. Han, D. J. Srolovitz, G. J. Ackland, D. Y. Sun, and M. Asta, "Development of new interatomic potentials appropriate for crystalline and liquid iron," Philos. Mag., vol. 83, pp. 3977–3994, 2003.

[116] David L. Olmsted, Dorel Buta, Ari Adland, Stephen M. Foiles, Mark Asta, and Alain Karma, "Dislocation-Pairing Transitions in Hot Grain Boundaries," Physical Review Letters, vol. 106, no. 4, p. 046101, 2011.

[117] Seunghwa Ryu and Wei Cai, "Comparison of thermal properties predicted by interatomic potential models," Modelling Simul. Mater. Sci. Eng., vol. 16, p. 085005, 2008.

[118] D. Wolf, "Correlation between structure, energy and surface tension for free surfaces in b.c.c. metals," Philosophical Magazine A, vol. 63, no. 2, pp. 337–361, 1991.

[119] S. Tsurekawa, T. Tanaka, and H. Yoshinaga, "Grain boundary structure, energy and strength in molybdenum," Materials Science and Engineering, vol. A176, pp. 341–348, 1994.

[120] R. Hill, "The Elastic Behaviour of a Crystalline Aggregate," Proc. Phys. Soc. A, vol. 65, p. 349, 1952.

[121] S. Foiles and J. Hoyt, "Computation of grain boundary stiffness and mobility from boundary fluctuations," Acta Materialia, vol. 54, no. 12, pp. 3351–3357, 2006.

[122] H. Sautter, H. Gleiter, and G. Bäro, "The effect of solute atoms on the energy and structure of grain boundaries," Acta Metallurgica, vol. 25, no. 4, pp. 467–473, 1977.

[123] Y. Pang and P. Wynblatt, "Effects of Nb Doping and Segregation on the Grain Boundary Plane Distribution in TiO2," J American Ceramic Society, vol. 89, no. 2, pp. 666–671, 2006.

[124] T. Tsuru, Y. Shibutani, and Y. Kaji, "Fundamental interaction process between pure edge dislocation and energetically stable grain boundary," Phys. Rev. B, vol. 79, p. 012104, 2009.

[125] Jason Gruber, "Interface Texture Development During Grain Growth," PhD thesis, Department of Materials Science and Engineering, Carnegie Mellon University, 2007.

[126] K. Miyazawa, Y. Iwasaki, K. Ito, and Y. Ishida, "Combination Rule of Σ Values at Triple Junctions in Cubic Polycrystals," Acta Cryst., vol. A52, pp. 787–796, 1996.

[127] C. A. Schuh, M. Kumar, and W. E. King, "Universal features of grain boundary networks in FCC materials," Journal of Materials Science, vol. 40, pp. 847–852, 2005.

[128] G. S. Rohrer and H. M. Miller, "Topological characteristics of plane sections of polycrystals," Acta Materialia, vol. 58, no. 10, pp. 3805–3814, 2010.

[129] C. Cayron, "Quantification of multiple twinning in face centred cubic materials," Acta Materialia, vol. 59, pp. 252–262, 2011.

[130] S. Maddali, C. Hefferan, S.F. Li, J. Lind, R. Suter, A. Rollett, and U. Lienert, "Grain Boundary Misorientation Statistics in Polycrystalline Nickel-Bismuth," Scripta Materialia, vol. preprint.

[131] Valerie Randle, "Twinning-related grain boundary engineering," Acta Materialia, vol. 52, no. 14, pp. 4067–4081, 2004.

[132] V. Randle, "Mechanism of twinning-induced grain boundary engineering in low stacking-fault energy materials," Acta Materialia, vol. 47, no. 15–16, pp. 4187–4196, 1999.

[133] Mukul Kumar, Wayne E. King, and Adam J. Schwartz, "Modifications to the microstructural topology in f.c.c. materials through thermomechanical processing," Acta Materialia, vol. 48, no. 9, pp. 2081–2091, 2000.

[134] P. J. Goodhew, "Annealing twin formation by boundary dissociation," Metal Science, vol. 13, no. 3–4, pp. 108–112, 1979.

[135] Mukul Kumar, Adam J. Schwartz, and Wayne E. King, "Microstructural evolution during grain boundary engineering of low to medium stacking fault energy fcc materials," Acta Materialia, vol. 50, pp. 2599–2612, 2002.

[136] J. Gruber, H. M. Miller, T. D. Hoffmann, G. S. Rohrer, and A. D. Rollett, "Misorientation texture development during grain growth. Part I: Simulation and experiment," Acta Materialia, vol. 57, no. 20, pp. 6102–6112, 2009.

[137] Joel Durgavich, "Expansion of the NRL Tight-Binding Method to Include F-Orbitals and Application in Thorium and Actinium," PhD thesis, Graduate Program in Computational Sciences and Informatics, George Mason University, 2012.

[138] Harry Julius Emeléus, A. G. Sharpe, "Advances in inorganic chemistry and radiochemistry," Academic Press, vol. 31, pp. 16–17, 1987.

[139] Gregory S. Rohrer, "Structure and Bonding in Crystalline Materials," Cambridge University Press, 2001.

[140] Alan Russell and Kok Loong Lee, "Structure-Property Relations in Nonferrous Metals," John Wiley & Sons, Inc, pp. 470–471, 2005.

[141] J. Konrad, S. Zaefferer, and D. Raabe, “Investigation of orientation gradients around a hard Laves particle in a warm-rolled Fe3Al-based alloy using a 3D EBSD-FIB technique,” Acta Materialia, vol. 54, no. 5, pp. 1369–1380, 2006.

[142] C.V. Thompson, “Grain Growth in Thin Films,” Annual Review of Materials Research, vol. 20, pp. 245–268, 1990.

[143] E. M. Zielinski, R. P. Vinci, and J. C. Bravman, “Effects of barrier layer and annealing on abnormal grain growth in copper thin films,” Journal of Applied Physics, vol. 76, pp. 4516–4523, 1994.

[144] N.-J. Park, D.P. Field, M.M. Nowell, and P.R. Besser, “Effect of Film Thickness on the Evolution of Annealing Texture in Sputtered Copper Films,” Journal of Electronic Materials, vol. 34, no. 12, pp. 1500–1508, 2005.

[145] N. Setter, and R. Waser, “Electroceramic materials,” Acta Materialia, vol. 48, no. 1, pp. 151–178, 2000.

[146] T. Sano, D. M. Saylor, and G. S. Rohrer, “Surface Energy Anisotropy of SrTiO3 at 1400°C in Air,” Journal of the American Ceramic Society, vol. 86, no. 11, pp. 1933–1939, 2003.

[147] B. Meyer, J. Padilla, and David Vanderbilt, “Theory of PbTiO3, BaTiO3, and SrTiO3 surfaces,” Faraday Discussions, vol. 114, pp. 395–405, 1999.

[148] Xuan Liu, Dooho Choi, Hossein Beladi, Noel T. Nuhfer, Gregory S. Rohrer, and Katayun Barmak, “The five-parameter grain boundary character distribution of nanocrystalline tungsten,” Scripta Materialia, vol. 69, pp. 413–416, 2013.

[149] Myung-Beom Park, Shao-Ju Shih, and David J.H. Cockayne, “The preferred CSL misorientation distribution in polycrystalline SrTiO3,” Journal of Microscopy, vol. 227, pp. 292–297, 2007.

[150] M. Syha, W. Rheinheimer, M. BaÅNurer, E.M. Lauridsen, W. Ludwig, D. Weygand, and P. Gumbsch, “Three-dimensional grain structure of sintered bulk strontium titanate from X-ray diffraction contrast tomography,” Scripta Materialia, vol. 66, pp. 1–4, 2012.

[151] H.-S. Lee, T. Mizoguchi, J. Mistui, T. Yamamoto, S.-J. L. Kang, and Y. Ikuhara, “Defect energetics in SrTiO3 symmetric tilt grain boundaries,” Physical Review B, vol. 83, p. 104110, 2011.

[152] Oliver Kienzle and Frank Emst, “Effect of Shear Stress on the Atomistic Structure of a Grain Boundary in Strontium Titanate,” J. Amer. Ceram. Soc., vol. 80, no. 7, pp. 1639–1644, 1997.

[153] Y.I. Jung, S.Y. Choi, S.J.L. Kang, “Effect of oxygen partial pressure on grain boundary structure and grain growth behavior in BaTiO3,” Acta Materialia, vol. 54, pp. 2849–2855, 2006.

[154] Sung-Yoon Chung, Duk Yong Yoon, and Suk-Joong L. Kang, "Effects of donor concentration and oxygen partial pressure on interface morphology and grain growth behavior in SrTiO3," Acta Materialia, vol. 50, pp. 3361–3371, 2002.

[155] Suk-Joong L. Kang, Min-Gon Lee, and Se-Min An, "Microstructural Evolution During Sintering with Control of the Interface Structure," Journal of the American Ceramic Society, vol. 92, no. 7, pp. 1464–1471, 2009.

[156] C. L. Jia and K. Urban, "Atomic-Resolution Measurement of Oxygen Concentration in Oxide Materials," Science, vol. 303, pp. 2001–2004, 2004.

[157] Zaoli Zhang, Wilfried Sigle, Fritz Phillipp, Manfred Ruhle, "Direct Atom-Resolved Imaging of Oxides and Their Grain Boundaries," Science, vol. 302, pp. 846–849, 2003.

[158] Martin P. Harmer, "Interfacial Kinetic Engineering: How Far Have We Come Since Kingery's Inaugural Sosman Address?," J. Amer. Ceram. Soc., vol. 93, no. 2, pp. 301–317, 2010.

[159] Hak-Sung Lee, Teruyasu Mizoguchi, Takahisa Yamamoto, Suk-Joong L. Kang, and Yuichi Ikuhara, "First-principles calculation of defect energetics in cubic-BaTiO3 and a comparison with SrTiO3," Acta Materialia, vol. 55, pp. 6535–6540, 2007.